Ministère de l'Enseignement Supérieur et de la Recherche Scientifique

جامعة أكلي محند أولحاج - البويرة

Université Akli Mohand Oulhadj Bouira

كلية العلـــــوم التطبيقية

Faculté des Sciences Appliquées

Département de : Génie des procédés

Laboratoire des Matériaux et Développement Durable

THESE DE DOCTORAT

Présentée en vue de l'obtention du grade de Docteur

En : GENIE DES PROCEDES

Spécialité : Génie Chimique

Par :

BRAHMI Aghilas

Intitulée :

Utilisation de matériaux innovants dans le traitement des eaux usées

Soutenue publiquement le **12/06/2025** devant le Jury composé de :

LOUNICI Hakim	Pr	Président	Université de Bouira
ZIANI Salima	Pr	Directeur de Thèse	Université de Bouira
AITALI Salima	MCA	Codirecteur de Thèse	Université de Bouira
HAMMACHE Fadila	MCA	Examinateur	Université de Bouira
YAHIAOUI Idris	Pr	Examinateur	Université de Béjaïa
AZOUANI Rabah	MC	Examinateur	École de Biologie Industrielle, Cergy, France
ZAABAR Aida	Pr	Invité	Université de Bouira

2024/2025

Ministry of Higher Education and Scientific Research

جامعة أكلي محند أولحاج - البويرة

University of Akli Mohand Oulhadj Bouira

كلية العلـــــــوم التطبيقية

Applied Science Faculty

Department of: Process Engineering

Laboratory of Materials and Sustainable Development

DOCTORAL THESIS

Presented to obtain the degree of Doctor

In: PROCESS ENGINEERING

Specialty: Chemical Engineering

By:

BRAHMI Aghilas

Entitled:

Use of innovative materials in wastewater treatment

Publicly defended on **12/06/2025** in front of the Jury composed of:

LOUNICI Hakim	Pr	President	Université de Bouira
ZIANI Salima	Pr	Supervisor	Université de Bouira
AITALI Salima	Dr	Co-Supervisor	Université de Bouira
HAMMACHE Fadila	Dr	Examiner	Université de Bouira
YAHIAOUI Idris	Pr	Examiner	Université de Bejaia
AZOUANI Rabah	Dr	Examiner	Institute of Industrial Biology, Cergy, France
ZAABAR Aida	Pr	Guest	Université de Bouira

2024/2025

This thesis is dedicated to:

My beloved parents,
whose unwavering love, guidance, and sacrifices have shaped me into who I am today.

My dear brother and sisters,
your constant support, encouragement, and affection have been my source of strength and inspiration.

This work is a reflection of your endless belief in me, and I am forever grateful for your presence in my life.

Acknowledgements

I would like to express my sincere appreciation to the **University of Bouira** for providing the financial support that was essential throughout the course of this research.

First, I wish to extend my deepest gratitude to my principal supervisor, Professor **Salima Ziani**, and my co-supervisor, Assistant Professor **Salima Aitali**, for their exceptional guidance, profound insight, and unwavering support throughout my doctoral research. Their invaluable contributions, coupled with their insightful recommendations, have consistently provided clarity and direction. The trust and autonomy they allowed me in formulating and executing my research have been pivotal to my development as an independent researcher. Working under their supervision has been an honor and a truly rewarding experience for which I am deeply grateful.

I am also profoundly thankful to Professor **Hafit Khireddine** and all the members of his laboratory at the ***Laboratoire de Génie de l'Environnement*** **(LGE), Faculté de Technologie, Université A. MIRA, Bejaia, Algérie**, for their exceptional guidance and support throughout my research journey. The opportunity to initiate my research in such a well-equipped and supportive environment was invaluable. Their generosity in providing all the necessary resources and equipment significantly facilitated my work. Furthermore, I am particularly appreciative of their kindness and camaraderie, which fostered a conducive atmosphere for both personal and academic growth.

I would like to extend my sincere gratitude to Mrs. **Katia Bensadi**, the laboratory engineer, for her consistent and professional assistance in managing the official and laboratory requirements throughout my research. Her support has been instrumental in ensuring the efficient execution of my work.

I consider myself fortunate to have had the privilege of undertaking three research visits during the course of my doctoral research: one to the **University of Oulu in Finland**, another to the **Université de Lille in France**, and finally, to **the University of Aveiro in Portugal**. I am particularly grateful to Assistant Professor **Tero Luukkonen**, who served as my supervisor during my internship at **the Fibre and Particle Engineering Research Unit at the University of Oulu**. This experience significantly enhanced my understanding of geopolymer quantification and led to the development of a new matrix based on HAP-MK-GP, a key

contribution to my doctoral thesis. I would also like to express my gratitude to Mr. **Jarno Karvonen** and Mrs. **Elisa Wirkkala**, the laboratory technicians, for their invaluable support during my experimental work at Oulu. Their expertise and assistance were crucial to the successful completion of my research tasks.

I am equally indebted to Assistant Professor **Karima Ben Tayeb** and Professor **Hervé Vezin**, who guided me during my internship at the ***Institut Michel-Eugène Chevreul*****, Université de Lille, France**. Their mentorship has been instrumental in expanding my knowledge of photocatalysis quantification and analysis. I would also like to extend my sincere thanks to **Hania Ahouari** for her considerable assistance in various analytical and characterization processes. Her dedication, coupled with the time she generously devoted to discussing my research, has been greatly appreciated.

I wish to convey my profound gratitude to Professor **Rui M. Novais**, **Nuno P.F. Gonçalves, Ana Caetano** and all the members of their **laboratory at the Department of Materials and Ceramic Engineering, University of Aveiro**, **Portugal,** for their enduring support and insightful guidance throughout my research. Their expertise and encouragement have been pivotal to the advancement of my work.

Finally, I would like to express my sincere gratitude to the following individuals; **Pr. Lounici Hakim, Pr. Zaabar Aida and Dr. Hammache Fadila** from **University of Bouira**, **Pr. YahiaouI Idris** from **University of Bejaia** and **Dr. Azouani Rabah** from **Institute of Industrial Biology, Cergy, France** for their invaluable role in examining and reviewing my thesis.

Abstract

This thesis investigates the potential of new innovative hydroxyapatite (HAP) based materials, synthesized as adsorbents for removing both anionic and cationic dyes from aqueous solutions. It is divided into three main sections. The first section explores a novel approach to enhance HAP's selectivity for cationic dyes. To achieve this, a metakaolin-based geopolymer (MK-GP) was incorporated as a binding agent, giving the HAP enhanced mechanical properties and enabling it to be converted into stable granules. These HAP-MK-GP granules were characterized structurally, morphologically and mechanically, and their adsorption capacities were assessed using batch experiments accompanied by kinetic modelling. The second section focused on optimizing the synthesis parameters of HAP-MK-GP granules, with the aim of improving their surface properties, in particular by increasing their specific surface area and porosity, which result in high adsorption efficiency. For this, a granulation technique incorporating polyethylene glycol (PEG) and sodium dodecyl sulfate (SDS) was used. This resulted in the production of highly porous granules with significant mechanical strength and improved capacity to adsorb organic pollutants, making them suitable for large-scale applications in the wastewater treatment. However, due to the MK-GP surface charge, these granules exhibited limited affinity for anionic dyes. To overcome this limitation, the final section of this study focused on the development of a magnetized hydroxyapatite nanocomposite (HAP-Fe-*Urtica dioica* extract) synthesized via co-precipitation. The incorporation of iron oxide (Fe_3O_4) conferred magnetic properties to the material, while *Urtica dioica* extract induced the formation functional groups to improve adsorption efficiency through the establishment hydrogen bonding and π-π interactions.

Overall, this study highlights the effectiveness of HAP-based materials, including geopolymer-bound granules and magnetic nanocomposites, as promising adsorbents for dye removal in industrial wastewater treatment. It also demonstrates scalable synthesis methods that can be applied to other powdered adsorbents, broadening their potential for environmental remediation.

Keywords: Hydroxyapatite, Geopolymer, iron oxide, *Urtica dioica* extract, Wastewater treatment, Adsorption, response surface methodology.

Résumé

Cette thèse s'intéresse au développement et à l'évaluation de nouveaux matériaux adsorbants innovants à base d'hydroxyapatite (HAP), destinés à l'élimination de colorants anioniques et cationiques dans des milieux aqueux. Le travail est organisé en trois sections principales. La première section propose une stratégie innovante visant à renforcer la sélectivité de l'HAP envers les colorants cationiques. Dans cette optique, un géopolymère à base de métakaolin (MK-GP) a été incorporé en tant qu'agent liant, ce qui a permis d'améliorer les propriétés mécaniques de l'HAP et de le transformer en granulés stables. Ces granulés composites HAP-MK-GP ont fait l'objet d'une caractérisation approfondie aux niveaux structural, morphologique et mécanique. Leur efficacité en adsorption a été examinée par des essais en mode discontinu (batch), associés à une modélisation des cinétiques d'adsorption. La deuxième partie de cette étude a été consacrée à l'optimisation des conditions de synthèse des granulés HAP-MK-GP, dans le but d'améliorer leurs propriétés texturales, en particulier la surface spécifique et la porosité, afin d'augmenter leur efficacité en adsorption. À cet effet, une méthode de granulation assistée par l'ajout de polyéthylène glycol (PEG) et de dodécylsulfate de sodium (SDS) a été mise en œuvre. Cette approche a permis l'obtention de granulés hautement poreux, dotés d'une résistance mécanique accrue et d'une capacité d'adsorption améliorée vis-à-vis des polluants organiques, les rendant potentiellement adaptés à des applications à grande échelle dans le traitement des eaux usées. Toutefois, en raison de la nature chargée du géopolymère MK-GP, ces granulés ont montré une affinité réduite pour les colorants anioniques. Pour pallier cette limitation, la troisième et dernière partie de la thèse s'est orientée vers la synthèse d'un nanocomposite magnétisé à base d'hydroxyapatite (HAP-Fe/extrait d'Urtica dioica) obtenu par co-précipitation. L'incorporation d'oxyde de fer (Fe_3O_4) a conféré au matériau des propriétés magnétiques facilitant sa séparation, tandis que l'introduction de l'extrait végétal a favorisé l'apparition de groupes fonctionnels susceptibles de renforcer les mécanismes d'adsorption via la formation de liaisons hydrogène et d'interactions π-π.

Dans l'ensemble, cette étude met en lumière l'efficacité des matériaux à base d'HAP, y compris les granulés liés au géopolymère et les nanocomposites magnétiques, en tant qu'adsorbants prometteurs pour l'élimination des colorants dans le traitement des eaux usées industrielles. Elle démontre également des méthodes de synthèse évolutives pouvant être appliquées à d'autres adsorbants en poudre, élargissant ainsi leur potentiel pour la dépollution environnementale.

Mots-clés : Hydroxyapatite, Géopolymère, oxyde de fer, extrait d'Urtica dioica, traitement des eaux usées, adsorption, plans d'expériences.

List of Original Publications

This thesis is based on the following publications, which are referred to throughout the text by their Roman numerals:

Publication I. Brahmi, A., Ziani, S., AitAli, S., Benkhaoula, B. N., Yu, Y., Ahouari, H., Khireddine, H., & Luukkonen, T. (2023). Porous metakaolin geopolymer as a reactive binder for hydroxyapatite adsorbent granules in dye removal. *Hybrid Advances*, *5*, 100134. https://doi.org/10.1016/j.hybadv.2023.100134

Publication II. Brahmi, A., Ziani, S., AitAli, S., Khireddine, H., & Luukkonen, T. (2024). Preparation of porous hydroxyapatite–metakaolin geopolymer granules for adsorption applications using polyethylene glycol as porogen agent and sodium dodecyl sulfate as anionic surfactant. *Environmental Science and Pollution Research*, *31*(30), 43262–43280.

https://doi.org/10.1007/s11356-024-34001-6

Publication III. Brahmi, A., Ziani, S., AitAli, S., Lakehal, Z.Y., & Luukkonen, T. (2025). Synthesis of hydroxyapatite-Fe_3O_4 nanocomposite modified with Urtica dioica extract for the removal of anionic dyes from aqueous solutions. Surface and Interface, 106925. https://doi.org/10.1016/j.surfin.2025.106925

Contents

List of abbreviations

Notation	Nomenclature
α_i	The importance weight assigned to each response.
$\alpha_{1/2}$	Separation factor
ANOVA	Analyse of variance
a_R	Redlich–Peterson isotherm constants (L/mg)
ARS	Alzarine red S
B	The full width at half maximum of the peak in radians
B	Redlich–Peterson isotherm constants
BBD	Box-Behnken design
BET	Brunauer-Emmett-Teller
BG	Brilliant green
BJH	Barrett-Joyner-Halenda
b_{jj}	Quadratic terms
b_j	Linear terms
b_0	Value of the fitted response at the center point of the design
b_{uj}	Interaction terms
CCD	Central Composite Design
C_e	Equilibrium concentration in aqueous (mg/L)
C_s	Equilibrium concentration in solid phase (mg/L)
CV	Crystal violet
d	Diameter of granules (mm)
δ	Film thickness (m)
$\Delta G°$	Gibbs free energy (Kj/mol)
$\Delta H°$	Enthalpy (Kj/mol),
$\Delta S°$	Entropy ($Kj/mol.K$)
ΔZ_j	Step size
D_f	Film diffusion coefficient in liquid phase (m^2/s)
d_i	The desirability of each response
D_p	Effective diffusion coefficient (m^2/s)
DR23	Direct red 23
DTG	Differential thermal analysis
ε	Residue
F	Peak force (N)
FTIR	Fourier transform infrared spectroscopy
HAP	Hydroxtapatite
HPDM	Homogeneous particle diffusion model
k	Diffusion rate constant (L/s)
k_1	Pseudo-first-order rate constant (min^{-1})
k_2	Pseudo-second order rate constant (g/(mg×min))
K	Number of factors studied
K_d	Distribution coefficients (L/g)
K_F	Freundlich constants ($mg^{(1-1/n)}×L^{(1/n)}/g$)
K_L	Langmuir adsorption constant (L/mg)
k_p	Diffusion rate constant (L/s)
K_R	Redlich–Peterson isotherm constants (L/g)

$\boldsymbol{\lambda_{max}}$	Maximum emission wavelength (nm)
$\boldsymbol{m}$	Mass of the adsorbent granules (g)
MB	Methylene blue
MK	Metakaolin
MK-GP	Metakaolin geopolymer
MS	Mean of squares
N	Number of experiments
$\boldsymbol{n_0}$	replicate number of the central point
PEG	Polyethylene glycol
$\boldsymbol{pH_{pzc}}$	The point of zero charge
$\boldsymbol{q_e}$	Adsorption capacity at equilibrium (mg/g)
$\mathbf{q_{exp}}$	The calculated adsorption capacities (mg/g)
$\boldsymbol{q_i^{exp}}$	Measured adsorption amounts (mg/g)
$\boldsymbol{q_i^{pred}}$	Predicted values of the adsorption amounts (mg/g)
$\boldsymbol{q_{max}}$	Langmuir monolayer adsorption capacity (mg/g)
$\boldsymbol{q_t}$	Adsorption capacity versus time (mg/g)
R	the universal gas constant (J/(K × mol)
$\boldsymbol{RSM}$	Response Surface Methodology
$\boldsymbol{r_0}$	Radius of the granules (m)
$\boldsymbol{Sc}$	The crystallite size (%)
SDS	Sodium dodecyl sulfate
SEM	Scanning electron microscope
$\boldsymbol{\sigma}$	Compressive strength (MPa)
SSA	Specific surface area (m^2/g)
T	The absolute temperature (K)
θ	The peak diffraction angle
TGA	Thermogravimetric analysis
UV-Vis	Spectroscopy of the ultraviolet-visible range
$\boldsymbol{V}$	Volume of the solution (L)
W	The weight of adsorbent (g)
$\boldsymbol{wi}$	The weight assigned to each response.
$\boldsymbol{x_j}$	Dimensionless variables or coded forms that correspond to Z_j
XRD	X-ray diffraction
XRF	X-ray fluorescence spectroscopy
$\boldsymbol{X_{(t)}}$	The fractional adsorption at given time
$\boldsymbol{y}$	Measured dye removal efficiency response
$\boldsymbol{\hat{y}}$	Predicted dye removal efficiency response
$\boldsymbol{Z_j}$	Dimensionless variables or reel forms
$\boldsymbol{Z_j^0}$	Value of Z_j at the center point of the investigation domain
$\boldsymbol{Z_{jmax}}$	Maximum level of factor *j* in natural units
$\boldsymbol{Z_{jmin}}$	Minimum level of factor *j* in natural units
$\frac{\mathbf{1}}{\mathbf{n}}$	Partitioning coefficient

Overview, Objectives and Thesis outline

1. Overview: General introduction

The rapid pace of industrialization and population growth is intensifying the global demand for freshwater, particularly in regions such as Algeria, where the existing water treatment infrastructure is inadequate to address these mounting challenges. This situation is all the more worrying given that, in many developing economies, industrial activities often lack sufficient wastewater treatment facilities, leading to the annual discharge of millions of cubic meters of untreated effluents into water bodies (Yang et al., 2024). This untreated wastewater significantly contributes to the degradation of freshwater resources, exacerbating the existing challenges associated with water pollution (Wang et al., 2024). Simultaneously, the effects of climate change, including altered precipitation patterns, increasing drought frequency, and erratic weather events, are amplifying water scarcity, further complicating efforts to meet growing water demands (Wang et al., 2023). Moreover, urban expansion, accompanied by increased population concentration, exerts additional pressure on already limited water supplies, culminating in a multifaceted crisis (McGonigle et al., 2013). Taken together, these factors pose a significant threat to access to quality water (clean and potable), compromise the balance of ecosystems and raise major public health concerns.

For this, in such water-scarce and contaminated regions, there is an urgent need for innovative and efficient wastewater treatment solutions. Addressing these interconnected challenges requires a comprehensive, integrated approach. First, the introduction of robust regulatory frameworks and public policies is essential for promoting the rational use of water resources, enhancing industrial water efficiency, and incorporating climate change adaptation strategies. Second, significant investment in water infrastructure is necessary to modernize existing systems, enhance the resilience of distribution networks, and ensure equitable access to high-quality water. Third, the development and optimization of advanced wastewater treatment technologies are critical to improving pollutant removal efficiency, particularly in addressing organic contaminants such as synthetic dyes, which traditional treatment methods often fail to remove. Among promising solutions, adsorption has emerged as an effective technique for eliminating harmful dyes from industrial effluents, offering a viable pathway to mitigate environmental pollution and support the sustainable management of water resources (Megherbi et al., 2024). The coherent integration of these strategies is crucial to achieving long-term, sustainable water management and safeguarding freshwater resources.

A variety of adsorbent materials have been investigated for their efficacy in water treatment, including carbon-based materials, biopolymer-based adsorbents, agro-industrial waste-derived materials, zeolites, double-layered hydroxides, metal-organic frameworks, silica-based materials, geopolymers (GP) and hydroxyapatite (HAP) powders (Cong et al., 2021 ; Billah et al., 2022). These last two have attracted the attention of many researchers due to their affinity for several types of pollutants.

Hydroxyapatite (HAP, $Ca_{10}(PO_4)_6(OH)_2$) is a calcium phosphate mineral compound that can be derived from natural sources rich in calcium and phosphorus, such as eggshells, mussel shells, and animal bones (Agsous et al., 2025). Utilizing these secondary materials not only provides an eco-friendly alternative to synthetic sources but also reduces dependence on phosphate rock, a critical raw material (Hosseinian et al., 2023). In wastewater treatment, HAP is valued for its high adsorption capacity for heavy metals like zinc, lead, and copper (Meski et al., 2019). However, its ability to adsorb organic pollutants, particularly dyes, is limited due to its low electrostatic interactions, porosity, and surface area (Panneerselvam et al., 2019). In contrast, metakaolin-based geopolymers (MK-GP) are three-dimensional inorganic polymeric materials with cross-linked tetrahedral units of [AlO_4] and [SiO_4], stabilized by alkali metal cations (i.e., Na^+, K^+) (Kumar et al., 2021). These alkali-activated binders exhibit exceptional resistance to water dissolution, thermal stability, and durability, making them effective for pollutant removal, especially for cationic organic pollutants like dyes (Luukkonen et al., 2019 ; Gonçalves et al., 2022).

To address HAP limitation, researchers have developed HAP-based materials. This thesis investigates a novel approach by combining HAP with MK-GP materials to enhance its adsorption properties. The integration of HAP with MK-GP results in durable, high-strength materials (i.e. granules, monoliths and filter) that address the challenges of separation and adsorptive capacity loss often associated with fine HAP powders. Furthermore, MK-GP can be tailored to increase porosity and improve pore interconnectivity, optimizing the surface area for enhanced dye adsorption. This combination not only enhances the mechanical strength of HAP but also improves its overall adsorption efficiency. The resulting composite material provides a stable and recoverable solution, enabling more efficient use of HAP in large-scale environmental remediation, particularly in wastewater treatment.

2. Objectives: Aim and scope of the thesis

This thesis is part of an innovative approach to cleaning up industrial effluents by using eco-friendly materials. It aims to explore the development of new hydroxyapatite (HAP)-based materials to enhance the adsorption and removal of organic pollutants, particularly dyes, in wastewater treatment. This research addresses the limitations of unmodified HAP, such as its low affinity for organic compounds and challenges related to recovery and reusability. By combining HAP with geopolymer-based binders and Fe_3O_4 nanoparticles, this study seeks to improve the adsorptive capacity, mechanical stability, and recovery efficiency of HAP composites. This thesis is structured around three publications, each addressing specific objectives related to the development of HAP-based materials for environmental applications:

Publication I. This publication investigates the use of metakaolin-based geopolymer (MK-GP) as a binder for unmodified HAP powder, with hydrogen peroxide (H_2O_2) added at different concentrations (0.0, 5.0, 7.5, and 10.0%) as both a granulation fluid and a foaming agent. The study focuses on improving the mechanical properties of the material by transforming HAP powder into granules, thereby enhancing the adsorption efficiency of the granules for the removal of Brilliant Green (BG) dye from aqueous solutions.

Publication II. This study explores the enhancement of HAP-MK-GP granules by incorporating polyethylene glycol (PEG) as a porogen agent and sodium dodecyl sulfate (SDS) as an anionic surfactant. The objective is to increase the porosity, surface area, and adsorption capacity of the granules for binary cationic dye pollutants (MB and CV), while maintaining high mechanical strength. The study also evaluates the granules' regeneration potential, demonstrating that they can be reused for up to eight cycles without significant loss in adsorption capacity or structural degradation. These results suggest that the porous granules developed in this study have significant potential for industrial wastewater treatment applications.

Publication III. This publication investigates the integration of Fe_3O_4 nanoparticles into the HAP matrix, modified with *Urtica dioica* extract. It serves as a follow-up to the findings in Publications I and II, where the HAP-MK-GP granules showed limited affinity for the adsorption of binary anionic dyes (DR23 and ARS) due to the structure of the MK-GP binder. So, the addition of Fe_3O_4 nanoparticles and *Urtica dioica* extract aims to improve the overall performance of the composite materials for anionic dye removal

3. Thesis outline

This thesis is structured into three chapters, each analysing a key aspect that will help us to understand and evaluate the development of the work carried out.

Chapter I. provides a comprehensive literature review on hydroxyapatite (HAP) materials and geopolymer (GP) alkali-activated materials, focusing on their synthesis, properties, and applications in dye removal. It also discusses the challenges and advancements in these fields, laying the foundation for the research presented in this work.

Chapter II. details the materials and methods used in this study. It describes in detail the synthesis processes and the strategies for modifying the materials, while highlighting their effectiveness in eliminating organic dyes. The chapter also outlines the experimental setup and analytical techniques employed for material characterization and adsorption studies.

Chapter III. presents the experimental results, including materials characterization, adsorption performance, and comparative analysis with existing technologies. The findings are critically examined in relation to the research objectives, highlighting key insights and contributions.

The thesis concludes with a summary of the results obtained and their implications, while also proposing future research directions for further advancements in HAP-based composite materials for innovative environmental applications.

Chapter I. State of the art

Chapter I. State of the art

This chapter provides a critical review of the development and advancements in hydroxyapatite (HAP) and metakaolin-based geopolymer (MK-GP), focusing on their structural properties, synthesis methods, modifications, and applications in adsorption processes. It examines recent progress in enhancing the efficiency of these materials for environmental remediation, addressing both their potential and existing challenges. The discussion also highlights their scientific and technological advancements, limitations, and future research directions essential for optimizing their performance in environmental applications.

I.1. Apatite and hydroxyapatite material

The term '**apatite**' is derived from a Greek word meaning '**deceitful**'. It refers to a family of calcium phosphate minerals with similar structures but varying compositions, generally represented by the formula $Me_{10}\,(XO_4)_6\,Y_2$. In this formula (Pai et al., 2020 ; Manning, 1985) :

- Me represents a divalent cation, often calcium (Ca^{2+}), which can be substituted by other divalent ($Zn^{2+}, Pb^{2+}, Mg^{2+}..$), monovalent ($Na^{+}, Rb^{+}, K^{+}..$), trivalent cations ($Re^{3+}, Al^{3+}, An^{3+}..$), and tetravalent cations ($U^{4+}, Pu^{4+}, Th^{4+}..$);
- XO_4 is tetrahedral anion group, typically phosphate (PO_4^{-3}), which can be substituted by other tetrahedral anion groups (AsO_4^{-3}, GeO_4^{-3}), tetravalent groups (SiO_4^{-4}, GeO_4^{-4}), and bivalent ions (SO_4^{-2}, CO_3^{-2});
- Y is a monovalent ion often $OH\,, Cl, F$, and sometimes a bivalent ion (O^{2-}, CO_3^{-2}).

Stoichiometric hydroxyapatite (HAP), with the chemical formula $(Ca)_{10}(PO_4)_6(OH)_2$, is characterized by a $\frac{Ca}{P}$ ratio ranging from 1.5 to 1.667 (Surmeneva et al., 2019). It has a hexagonal structure with a six-fold *c*-axis perpendicular to three *a*-axes (β = 120°) and belongs to the $P6_3/m$ space group, with lattice parameters $a = b = 9.37$ Å, $c = 6.88$ Å (Balasooriya et al., 2022). HAP contains two distinct calcium sites, $Ca_{(I)}\ and\ Ca_{(II)}$ leading to the general formula $\left(Ca_{(I)4}Ca_{(II)6}\right)(PO_4)_6(OH)_2$. The hydroxyapatite framework is a compact assembly of PO_4 tetrahedra, with each tetrahedron shared by one column, forming a rigid network. This arrangement results in two types of unconnected channels: one with a diameter of 2.5 Å, accommodating $Ca_{(I)}$ ions, and another with a diameter of 3.5 Å, designed for $Ca_{(II)}$ ions (**Fig. I.1**). These channels, though unconnected, are pivotal for the selective ion transport and structural stability of the material. Additionally, the presence of hydroxyl (OH) groups along

the *c*-axis helps neutralize the positive charge of the calcium-rich framework, balancing the overall charge distribution within the crystal (Surmeneva et al., 2019).

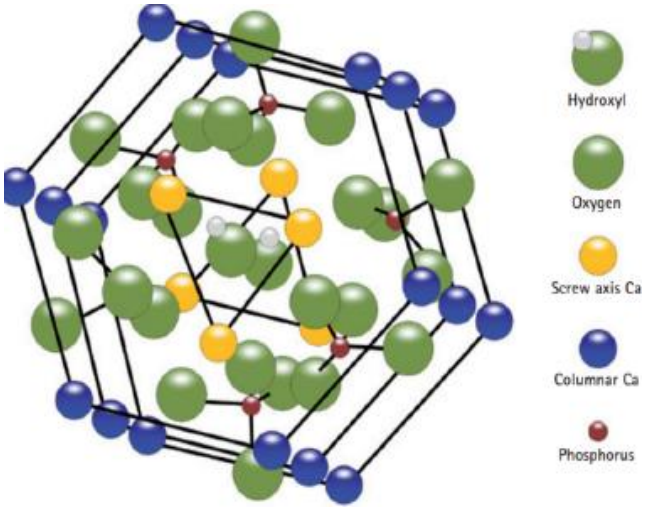

Fig.I.1. The structure of hydroxyapatite (HAP) (Brunton et al., 2013).

Stoichiometric HAP exhibits notable surface adsorption properties due to the presence and exchange of hydroxyls and orthophosphates groups, which play a crucial role in its reactivity. As a member of the calcium orthophosphate family. HAP can appear in different allotropic forms, such as rhombohedral (β-form) or monoclinic (α-form). The phase diagram of calcium phosphates (**Fig. I.2**) is significantly influenced by water pressure. Under anhydrous conditions, hydroxyapatite does not form and decomposes into α-tricalcium phosphate (α-TCP), tetracalcium phosphate (TTCP), and water, depending on water pressure (Anandan & Jaiswal, 2023 ; Alam et al., 2024 ; Lin et al., 2001).

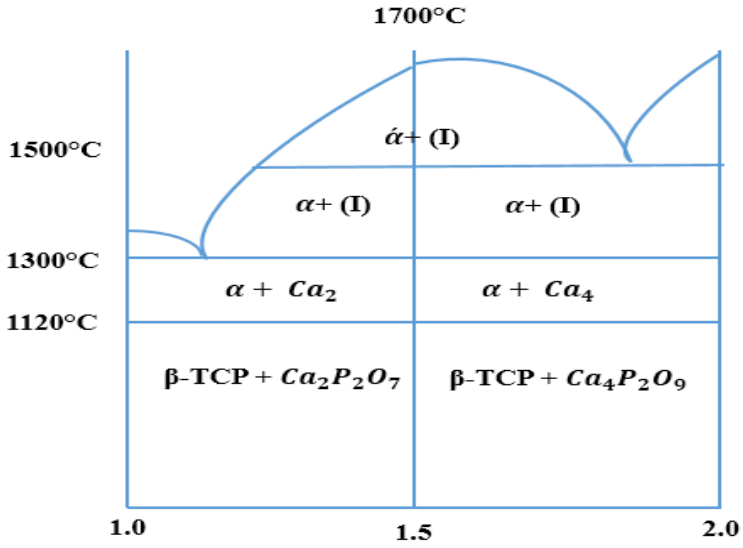

Fig. I.2. Phase diagram of the $CaO - P_2O_5$ system (Welch & Gutt, 1961).

I.1.1. Synthesis of hydroxyapatite

Synthetic HAP can be produced through various methods, classified into dry, wet, and high-temperature techniques. Each method results in HAP particles with distinct characteristics, including variations in size, surface properties (e.g., porosity, surface area), morphologies, and particle agglomeration. These methods also produce different crystalline phases of HAP (Sadat-Shojai et al., 2013 ; Lin et al., 2015). The resulting properties significantly influence the bioactivity, mechanical strength, biological interactions and adsorption capacity of HAP. Therefore, understanding and controlling these properties through appropriate synthesis techniques is crucial for tailoring HAP for specific applications in biomedicine, materials science, and environmental engineering (Kannan, 2015 ; Sidane et al., 2015).

I.1.1.1. Dry method

Dry synthesis of hydroxyapatite (HAP) is based on two main approaches: solid-state and mechanochemical methods. Mechanochemical technique typically mixes dry precursor chemicals, usually calcium and phosphate, and is suitable for large-scale powder production due to its lack of precise conditions (Pu'ad et al., 2020). However, solid-state reactions involve milling and heating a mixture of calcium and phosphate precursors to produce new solids, such as HAP, and gases. The mechanism relies on the diffusion of solid-state ions from the precursors, combined with a high-temperature process to trigger the reaction (Cox et al., 2015).

I.1.1.2. Wet method

The wet method is widely favored for its simplicity, low cost, and ability to produce uniform results. This method encompasses various approaches, such as co-precipitation, hydrothermal, and sol-gel, each its own advantages and limitations depending on the specific application for HAP.

- **Co-precipitation:** this involves the dissolution of calcium and phosphate precursors. The phosphate solution is added drop by drop to the calcium solution, then the pH is adjusted to alkaline levels (pH = 10). The mixture is stirred until the precipitate forms. Afterward, the HAP particles undergo washing, filtering, and drying. This method provides flexibility and control over synthesis conditions, facilitating the production of well-defined HAP particles suitable for diverse applications.
- **Sol-gel method:** this process involves mixing calcium and phosphate precursors in a solvent (e.g., water, ethanol) to form a homogeneous sol, which undergoes hydrolysis and condensation reactions to form a stable gel. The gel is then dried and calcined at high temperatures to obtain the final HAP powder. This method offers advantages by

enhancing chemical homogeneity and achieving HAP of high purity and crystallinity (Paziresh et al., 2021).

- **Hydrothermal method:** this involves dissolving calcium and phosphate precursors and adjusting the pH to 10. The mixture is then heated and pressurized, typically in an autoclave or pressure vessel. This method enhances reactivity and promotes the formation of crystalline hydroxyapatite with fixed Ca/P ratios (Gao et al., 2019).

I.1.1.3. High-temperature method

High-temperature methods like combustion and pyrolysis are widely used for HAP synthesis. However, their use remains limited due to insufficient control over processing parameters and the formation of secondary aggregates.

- **Combustion method:** this involves burning calcium nitrate, diammonium hydrogen phosphate, citric acid, and succinic acid, leading to the formation of carbonated HAP and β-tricalcium phosphate (β-TCP) via rapid exothermic reactions (Sasikumar et al., 2008 ; Najmi & Singh, 2024).
- **Pyrolysis method:** this method involves converting calcium and phosphate precursors into HAP particles by heating them at a temperature of 800°C in the absence of oxygen for a specific period. It is advantageous as it is easier to scale and requires less fuel mixing compared to combustion, making it suitable for continuous production of HAP particles (Fihri et al., 2017). Additionally, pyrolysis can be adapted for aerosol-based methods, where the precursor materials are suspended in a gaseous phase (aerosol) and then subjected to heat, allowing for precise control over particle size and distribution (Mathew et al., 1977).

I.1.2. Recent and future development in hydroxyapatite for environmental applications (adsorption)

The applications of HAP in environmental remediation are extensive due to their attractive physicochemical properties. Their high adsorption capacity, excellent chemical and thermal stability, ion-exchange capacity, non-toxicity, and abundant natural availability make them valuable tools in pollution control (Meski et al., 2019). This section provides an overview of new synthesis methods and improvements in their properties for various environmental remediation applications, including the adsorption of heavy metals and organic molecules (i.e. dye).

I.1.2.1. Heavy metals remediation

Synthetic hydroxyapatite, produced through various synthesis methods using both natural and synthetic sources, has been extensively studied as an adsorbent for heavy metals such as Pb^{2+}, Ni^{2+}, Zn^{2+}, Cu^{2+}, Sr^{2+}, and Cd^{2+}. HAP demonstrates good sorption capacity due to its structural properties (**Table I.1**). The sorption mechanism involves electrostatic attraction, surface complexation, and ion exchange between calcium sites and heavy metal ions. Moreover, HAP exhibits varying degrees of affinity towards different heavy metals. Studies by Errich et al., (2021) and Gupta et al., (2011) showed that HAP's affinity varies among metals, in the following order: $Zn^{2+} > Cu^{2+} > Cr^{2+}$, $Pb^{2+} > Co^{2+} > Ni^{2+}$, and $Pb^{2+} > Cd^{2+} > Ni^{2+}$. This variation is influenced by the hydrated ionic radii (Pb^{2+} (1.2 Å) > Cu^{2+} (0.97 Å) > Cd^{2+} (0.75 Å), the metal ion electronegativity, and the cation/anion state. Additionally, HAP's morphology, microcrystalline size, composition, and structure significantly affect its efficiency and selectivity towards heavy metals.

Table I.1. Comparison of various synthesized HAP and their heavy metals adsorption mechanisms.

Method	SSa (m^2/g)	q_{max} Heavy metals (mg/g)	Adsorption mechanism	References
Microwave assisted	8.08	$q_{Pb^{2+}}$ = 1430	Ion exchange and electrostatic attraction	Jiang et al., 2020
thermal decomposition 900 °C	103.46	$q_{Ni^{2+}}$ = 181.32		Ofudje et al., 2021
N/A	77.00	$q_{Cu^{2+}}$ = 20 and $q_{Cd^{2+}}$ = 25	Surface complexation and co-precipitation	Femane et al., 2008
Double interfacial diffusion method.	188.50	$q_{Sr^{2+}}$ = 45	Surface complexation and ion exchange	Xia et al., 2019
Co-precipitation	26.40	$q_{Zn^{2+}}$ = 330	surface complexation and electrostatic attraction	Ni & Fox., 2019
Precipitation	N/A	$q_{Pb^{2+}}$ = 1352, $q_{Cu^{2+}}$ = 285, $q_{Zn^{2+}}$ = 304 and $q_{Cd^{2+}}$ = 305	Surface adsorption, complexation and ion exchange	Zhou et al., 2021
N/A= not available.				

Due to HAP's high adsorption capacity, it is being used as a precursor in combination with polymers to create membranes with enhanced adsorption properties. For example, Shokri et al., (2021) developed PLA/HAP adsorptive membranes. Pure PLA membranes have low affinity for removing Pb^{2+} and As^{2+}, but when combined with HAP, new membranes with high porosity, hydrophilicity, and permeability are formed, maintaining acceptable mechanical strength. Another study by Gai et al., (2024) analyzed chitosan-gelatin-hydroxyapatite methylcellulose (CS-GEL-HPMC) membranes for Cd^{2+} adsorption. The results showed that the addition of HAP into CS-GEL membranes significantly enhances their adsorption capacity.

I.1.2.2. Organic compounds remediation

Unmodified hydroxyapatite (HAP) exhibits low adsorption affinity for organic compounds like dyes, pharmaceutical molecules, and pesticides in aqueous solutions. To enhance its adsorption properties (surface area, porosity, electrostatic attraction), hybridization processes are employed. These involve combining HAP with materials such as polymers, activated carbon, and Fe_3O_4 through co-precipitation or crosslinking agents. Additionally, doping HAP by substituting different ions (e.g., Fe^{2+}, Al^{3+}A, Co^{2+}, Ag^{+}A) at the Ca^{2+}site under controlled conditions has been practiced (Miyah et al., 2024 ; Mahanty and Shikha, 2023). These methods create new adsorbent materials that are inexpensive, have high adsorption capacity, and are easily regenerated. **Table I.2** provides the adsorption capacity and surface area of various hybridized HAP-based materials for organic pollutant removal.

Sahoo et al., (2019) doped HAP with Fe^{2+} and $Fe^{3+}$to create magnetic hydroxyapatite (M-HAP). The M-HAP exhibited high adsorption capacity for anionic ETB dye by increasing the availability of hydroxyl groups, forming hydrogen bonds with dye molecules, and enhancing dipole-ion interactions. Additionally, the newly adsorbed powder displayed interesting magnetic properties, allowing it to be easily removed using external magnetic fields, thus facilitating straightforward regeneration. However, Guan et al., (2020) developed a polyalcohol-coated HAP nanocomposite using polyvinylanyl (PVA), which showed good adsorption capacity for both anionic MO and CR and cationic MB dyes. This improvement is due to the structural modifications induced by PVA, which increase the porosity and surface characteristics of the HAP nanocomposite. Another study by Pereira et al., (2020) used Amino HAP/chitosan/glutaraldehy for the removal of DC. Additionally, Pereira et al., (2020) found that combining HAP with chitosan (HAP-CS) synergistically improves adsorption properties by increasing active adsorption sites, porosity, and surface area. These new composites are biocompatible and biodegradable, making them suitable for water treatment and biomedical engineering.

Recent research has investigated innovative HAP-based materials by combining HAP powder with metakaolin geopolymer (MK-GP) through granulation to form adsorbent granules .This novel composite matrix has demonstrated several noteworthy properties, including enhanced mechanical strength and significant adsorption capacity for heavy metals and dyes. The advantages of this HAP-MK-GP matrix extend beyond its mechanical and adsorptive capabilities. It exhibits remarkable chemical stability, making it suitable for long-term use in harsh environments. Additionally, the material is cost-effective due to the relatively low price

of raw materials and the straightforward synthesis process. Its porous structure also enhances its surface area, leading to improved adsorption efficiency.

Table I.2. Hydroxyapatite based materials for organic pollutant removal.

Material	**Organic Pollutant**	**Type**	**SSa (m^2/g)**	**q_{max} (mg/g)**	**References**
Magnetic HAP	EBT	Dyes	41.20	$q_{EBT} = 43.47$	Sahoo et al., 2019
Zein/nHAP	CR		73.73	$q_{CR} = 416.71$	Nasab et al., 2018
Polyalcohol-coated HAP	MO, CR and MB		203.18	$q_{MO} = 14.7, q_{CR} = 170.7$ and $q_{MB} = 379.1$	Guan et al., 2018
HAP-chitosan	OG		N/A	$q_{OG} = 20$	Kjidaa et al., 2024
nHAP-biochar	TY, SX	Antibiotic	566.11	$q_{TY} = 160.17$ and $q_{SX} = 140.23$	Li et al., 2020
HAP/Clay	TC		47.65	$q_{TC} = 76.2$	Ersan et al., 2015
Amino HAP/CS/glutaraldehy	DC		50.00	q_{DC} =125	Pereira et al., 2020
HAP-Montmorillonite (HAP-Mt)	Cipro		91.18	q_{Cipro} = 147.51	Laabd et al., 2021
Nano-HAP	Atrazine	Pesticide	N/A	$q_{Atrazine}$ = 0.00995 × 10^{-10}	Randa et al., 2023

N/A= not available, EBT= Eriochrome Black T, CR= Congo red, MO = Methyl orange, MB = Methyl blue, OG = Orange G, TY = Tylosin , SX = Sulfamethoxazole, TC = Tetracycline, DC = Diclofenac , Cipro = Ciprofloxacin.

I.2. Metakaolin-based geopolymers (GP)

The term "**geopolymers**" (GP) was initially coined and developed by Professor Joseph Davidovits in 1972 (Davidovits, 1991). He defined them as green inorganic polymer materials formed by the condensation of aluminosilicate materials in alkali or acid solutions at low temperatures. They are characterised by a three-dimensional network architecture, with an amorphous or semi-crystalline phase. (Davidovits et al., 2019).

The preparation process for GP is simple, typically involving the mixing of various aluminosilicate source materials, such as clay minerals, fly ash, slag, and industrial wastes (**Fig. I.3**), with alkali or acid activator solutions, and curing below 100°C (Bai et al., 2018). Metakaolin (MK) is a preferred raw material for GP formation due to its high mineral activation, large specific surface area, and consistent chemical composition (Panagiotopoulou et al., 2007; Cheng et al., 2012). MK is an anhydrous aluminosilicate formed through the thermal breakdown of kaolin at temperatures above 550°C, resulting in significant atomic rearrangement (Rożek et al., 2019).

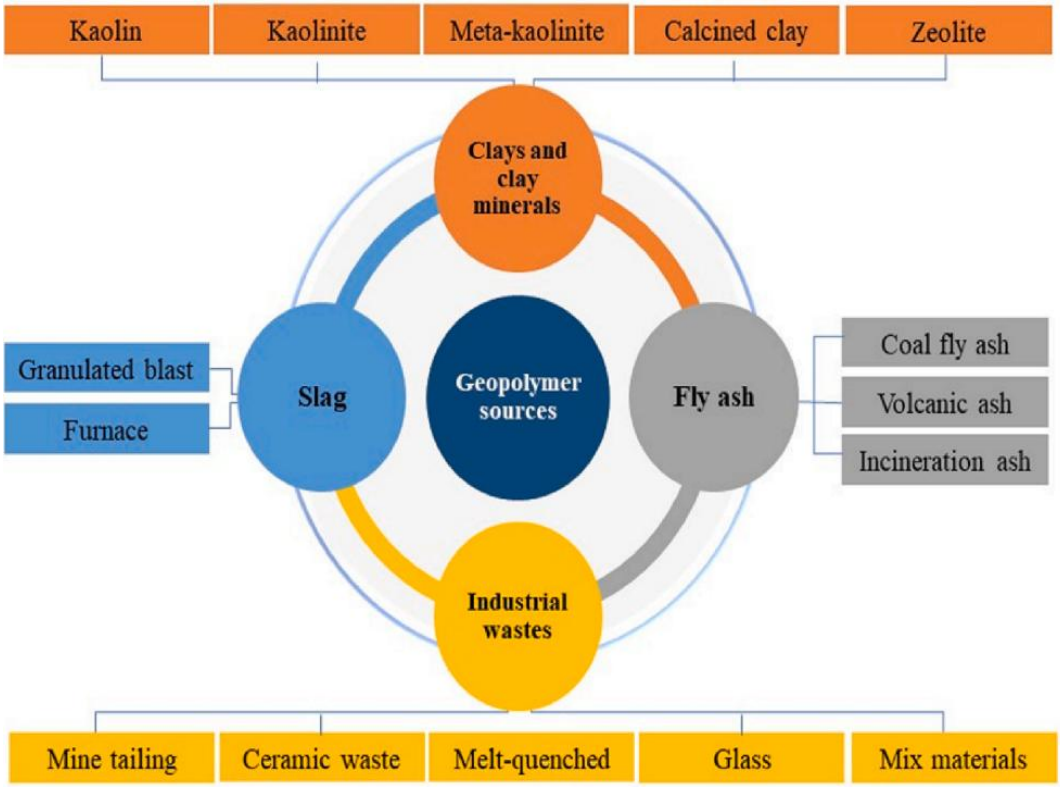

Fig. I.3. Main resources of common aluminosilicate materials used in GP synthesis (Elgarahy et al., 2023).

I.2.1. Geopolymer structure and geopolymerization process

The empirical formula for GP is $M_n[(SiO_2)_zAlO_2]_n.H_2O$, where M is alkali cation (usually Na^+ and K^+), n is the degree of polymerization and z is the molar ratio of $\frac{Si}{Al}$. Based on the $\frac{Si}{Al}$ ratio, geopolymers are classified into three types: poly (sialate) ($\frac{Si}{Al}$ =1), poly (sialate-siloxo) ($\frac{Si}{Al}$= 2), and poly (sialate-disiloxo) ($\frac{Si}{Al}$= 3) (**Table I.3**) (Davidovits, 2002).

Table I.3. Types of GP according of $\frac{Si}{Al}$ ration (Davidovits, 1988)

GP type	$\frac{Si}{Al}$ **ratio**	**Chemical formula**
Polysialate: PS	1	(–) (-Si-O-Al-O-) O O
Polysialate-siloxo:PSS	2	(–) (-Si-O-Al-O-Si-O-) O O O
Polysialate-disiloxo: PSDS	3	(–) (-Si-O-Al-O-Si-O- Si-O-) O O O O

The production process for GP involves dissolving aluminosilicate precursors (such as metakaolin, fly ash, and slag) in alkali hydroxide and/or alkali silicate solutions. The mixture is kept for at least 15 minutes to ensure homogeneity before being poured into a mould. That then polymerizes to form interconnected amorphous gels, which harden under heat (20°C to 100°C) or pressure to create the final geopolymer material (**Fig. I.4**). Increasing the curing temperature accelerates the reaction kinetics and the geopolymerization process (Zhang et al., 2016 ; De Oliveira et al., 2024 ; Ren et al., 2020).

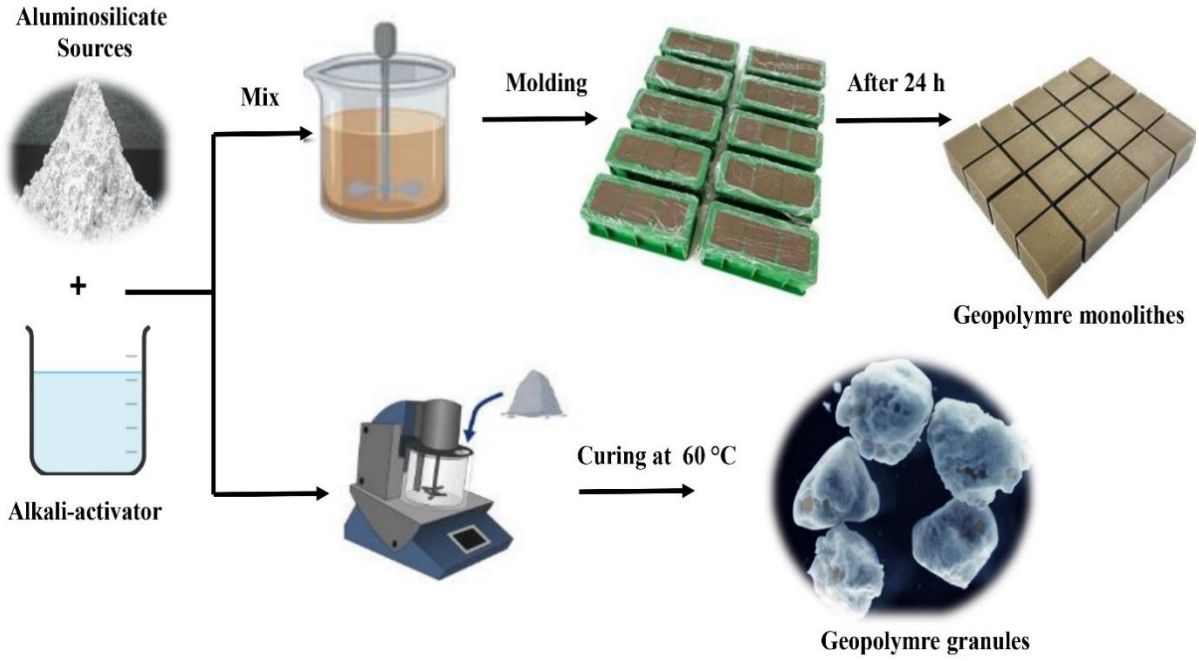

Fig. I.4. Schematic of geopolymer casting formation (Ren et al., 2021)

Glukhovsky in 1994 proposed a reaction mechanism model for alkali-activated silicon-aluminum phase components, structuring the process into four main stages: deconstruction, reconstruction, condensation, and crystallization (**Fig. I.5**). This process can be further detailed into five stages (Krivenko et al., 2007 ; Duxson et al., 2008 ; Ren et al., 2020).

1. Hydrolysis of the precursors, during which the alkali dissociates the chemical bonds in powdered silica-aluminate materials, resulting in the release of $[SiO_4]^{4-}$ and $[AlO_4]^{5-}$ tetrahedral units ;
2. Transition phase characterised by the formation of chemical bonds T-O-T (T = Al or Si) among silicate, aluminate, and aluminosilicate units ;

3. Condensation reaction, where oligomers condense to form a small cross-linked structure under strong alkaline conditions ;
4. Gel formation, where the gelling substances reorganise to generate geopolymer gels or other hydration products ;
5. Formation of a dense material, resulting from further dehydration and condensation, leading to the creation of a compact, dense and hard geopolymer material.

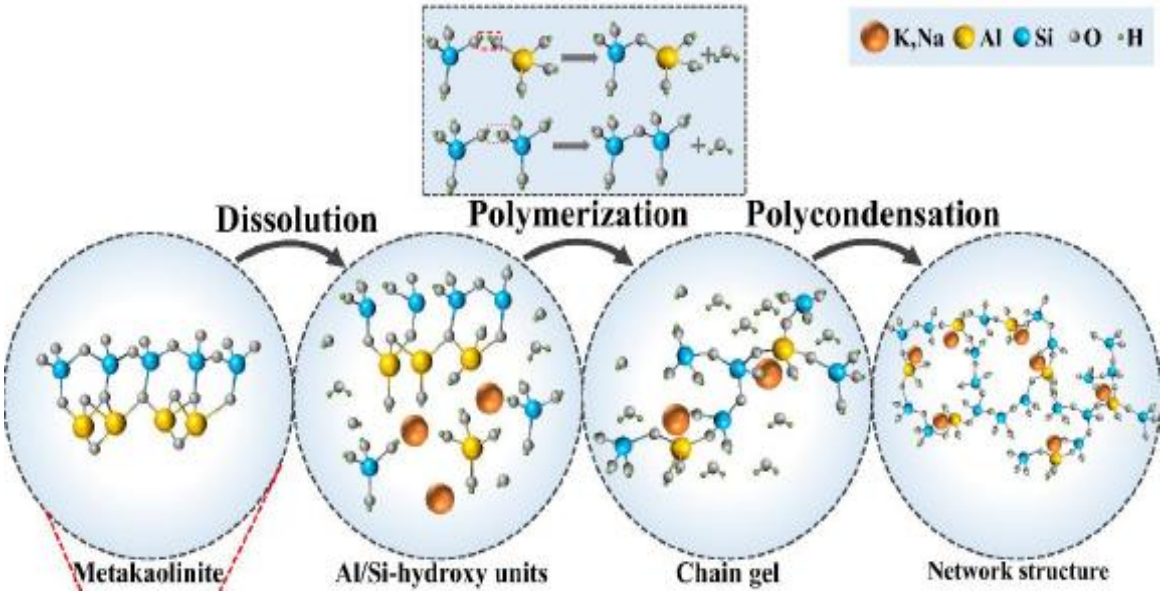

Fig. I.5. Schematic diagram of geopolymerization of metakaolin-based geopolymer (Bai et al., 2024).

I.2.2. Preparation of porous geopolymers

Porous geopolymers, such as spheres, granules, filters, and monoliths, can be synthesized using various methods. However, direct foaming (DF) technique is the more useful and the most effective.

I.2.2.1. Direct foaming (DF) method

The use of foaming agents such as H_2O_2, metal powders such as silicon and aluminium (Papa et al., 2022 ; Ibrahim et al., 2022), as well as other chemical agents such as NaO_2 (Peng et al., 2020), $CaCO_3$ (Rashad et al., 2022) and $NaHBO_4$ (Wattanarach et al., 2022) also leads to the formation of porous geopolymers. During curing, these agents decompose to release oxygen and hydrogen gas (De Oliveira et al., 2024), forming bubbles within the geopolymer matrix and creating its porous structure (Eqs. I-1, 2, 3 and 4) (Bai & Colombo, 2018).

$$2H_2O_2 \rightarrow 2H_2O + O_{2\,(g)} \qquad (\mathbf{I-1})$$

$$Si + 2\,MOH + H_2O \xrightarrow{20\ to\ 100\ ^\circ C} M_2SiO_3 + 2H_{2\,(g)} \qquad (\mathbf{I-2})$$

$$2Al + 2MOH + 2H_2O \xrightarrow{20\ to\ 100\ ^\circ C} 2MAlO_2 + 3H_{2\,(g)} \qquad (\mathbf{I-3})$$

where *M*=K or Na

$$4NaBO_3 + H_2O \rightarrow 2\,NaOH + Na_2B_4O_7 + 2O_{2\,(g)} \qquad (\mathbf{I-4})$$

I.2.3. Recent and future development in Metakaolin-based geopolymer for environmental applications (adsorption)

In recent years, metakaolin-based geopolymers (MK-GP) have garnered significant interest for water treatment applications such as adsorption, degradation, filtration, and solidification/stabilization. This interest stems from their unique properties, including high specific surface area, porous structure, ion-exchange capabilities, low production costs, and abundant availability.

MK-GP materials have proven effective in adsorbing a wide range of pollutants, including cationic organic dyes and heavy metals. These GP's are developed into various shapes, such as spheres, granules, and monoliths, which enhance their practical application in adsorption processes by facilitating easier recycling or regeneration after adsorption (Gonçalves et al., 2023). **Table I.4** details the properties and adsorption capacities of various MK-GP materials for the pollutants mentioned above, underscoring their significant potential in adsorption applications. The data in **Table I.4** show that MK-GP materials exhibit varying degrees of affinity towards different pollutants. This variation is primarily due to their specific surface area and cation exchange capacity. The high surface area provides numerous active sites for adsorption, while the cation exchange capacity facilitates the removal of metal cations through ion exchange mechanisms. Studies by Ge et al., 2015 ; Liu et al., 2022 and Candamanoet al., 2023 have demonstrated that the hierarchical pore structures within these geopolymers enhance the accessibility of pollutants to the adsorption sites, further improving their efficiency. The versatility in shapes and the inherent properties of MK-GP materials make them promising candidates for addressing pollution in diverse environmental settings.

Table I.4. MK-GP materials proprieties and their adsorption capacity for different pollutants.

Shape	Pollutants	SSa (m^2/g)	q_{max} (mg/g)	References
Sphere	Cu^{2+}	53.90	$q_{Cu^{2+}} = 56.20$	Ge et al., 2015
monolith	Pb^{2+}, Ni^{2+}, Cd^{2}	N/A	$q_{Pb^{2+}} = 12.40$, $q_{Ni^{2+}} = 6.80$, $q_{Cd^{2+}} = 6.20$	Liu et al., 2022
Granules	Cs^{+}	53.70	$q_{Cs^{+}} = 192.10$	Xiang et al., 2021
Granules	NH_4^+	39.20	$q_{NH_4^+} = 47$	Sanguanpak et al., 2021
Granules	NH_4^+	25.50	$q_{NH_4^+} = 15$	Yu et al., 2023
Sphere	F^-	N/A	$q_{F^-} = 202.20$	Wei et al., 2023
Granules	MB	N/A	$q_{MB} = 39.50$	Candamanoet al., 2023
Monolith	MB	N/A	$q_{MB} = 7.80$	Kaya-Özkiper et al., 2022
N/A= not available.				

To enhance the properties of MK-GP materials, such as surface area, porosity, and adsorption capacity, various hybridization methods have been developed during their preparation. These methods involve combining MK-GP with additives like activated carbon, zeolite, and Fe_3O_4 or using surfactants such as sodium dodecyl sulfate (SDS) and cetyl trimethylammonium bromide (CTAB). **Table I.5** provides detailed information on the adsorption capacity and surface area of these hybridized MK-GP materials, highlighting their improved performance and efficiency in adsorption applications.

Table I.5. Developed MK-GP based materials proprieties and their adsorption capacity for different pollutants.

MK-GP base material	Shape	Pollutants	SSa (m^2/g)	q_{max}(mg/g)	References
GP/Fe_3O_4 composite	Monolith	AG16	53.40	$q_{Ag13} = 400$	Rossatto et al., 2020
MK-GP zeolite microsphere	Powder	Pb^{2+}	N/A	$q_{Pb^{2+}} = 529.60$	Wei et al., 2022
Diatomite/MK-GP zeolite	Sphere	Sr^{2+}	106	$q_{Sr^{2+}} = 193.70$	Salam et al., 2021
Activated carbon/hydrotalcite/MK-GP	Filter	AOII	66.50	$q_{AOII} = 66.50$	Oliveira et al., 2022
MK-GP-CTAB	Sphere	MB	128.65	$q_{MB} = 183.08$	Bouna et al., 2020
Carbon nanotube/GP	Sphere	MB, Pb^{2+}, Ni^{2+}	73.06	$q_{Pb^{2+}} = 52.74$, $q_{Ni^{2+}} = 8.91$, $q_{MB} = 73.06$	Yan et al., 2022
MB = Methylen blue , AOII= Acid orange II, AG16= Acid green 16, N/A = not variable.					

Rossatto et al. (2020) synthesized MK-GP-based magnetic composites by incorporating soybean oil and hydrogen peroxide (H_2O_2), which demonstrated a strong affinity towards anionic dyes such as Acid Green 16. While MK-GP alone does not exhibit an affinity for anionic dyes, the addition of Fe_3O_4 significantly enhanced the electrostatic interaction between the dye's negatively charged sulfonate group and the functional groups present on the magnetic MK-GP. Furthermore, the inclusion of soybean oil and H_2O_2 further improved the material's overall adsorption capacity. The soybean oil likely aided in the formation of a more porous

structure, while H_2O_2 could have played a role in activating certain functional groups, enhancing the interaction between the material and the dye. The results showed that these new materials possess good magnetic properties, facilitating their separation from the aqueous medium and making them easier to regenerate. On the other hand, Oliveira et al. (2022) developed new materials based on MK-GP by incorporating activated carbon and hydrotalcite for the removal of the organic anionic dye Orange II from water. The incorporation of activated carbon significantly enhanced the surface area of the MK-GP, thereby improving its adsorption capacity towards anionic dyes. A comparative study between two types of materials and three different forms of the MK-GP composites (with and without the incorporation of activated carbon and hydrotalcite) highlighted the differences in adsorption efficiency and mechanical properties. The modified MK-GP composites showed superior adsorption capacity compared to the unmodified ones, demonstrating that combining different materials such as activated carbon and hydrotalcite can optimize both the adsorption properties and mechanical strength of MK-GP for various applications.

Likewise, Yan et al., (2022) developed MK-GP spheres with a hierarchical pore structure and enhanced mechanical properties by incorporating carbon nanotubes (CNTs). This incorporation significantly improved the surface characteristics of the MK-GP spheres, increasing the surface area to 73 m²/g and enhancing porosity, thus providing more sites for adsorption. The modified MK-GP spheres demonstrated a significantly higher adsorption capacity for Pb^{2+}, Ni^{2+} and MB compared to unmodified MK-GP, as detailed in **Table I.5**. This modification not only improved the mechanical strength of the MK-GP spheres but also optimized their effectiveness in removing contaminants from aqueous solutions.

I.3. Conclusion

The integration of HAP and MK-GP in hybrid materials represents an innovative advancement in adsorption technologies, utilizing their complementary physicochemical properties. HAP's high affinity for specific pollutants, especially heavy metals, is attributed to its ion-exchange capacity and surface reactivity. MK-GP, on the other hand, offers mechanical strength, thermal stability, and resistance to chemical degradation, ensuring long-term performance in diverse environmental conditions. Combining these materials in composite adsorbents enhances pollutant removal efficiency by integrating the adsorption capacity of HAP with the durability of MK-GP.

The incorporation of HAP into MK-GP for composite formation was first explored in this thesis, marking a novel approach to address challenges related to HAP powder properties and limitations, particularly in enhancing adsorption capacity for organic pollutants. Since then, other researchers have begun investigating similar systems (Arokiasamy et al., 2024 ; Papa et al., 2024). This matrix system is a key focus of this research, which explores and studies its synthesis, physicochemical characterization, and adsorption performance for environmental remediation.

Chapter II. Material & Methods

Chapter II. Material & Methods

This chapter, divided into four sections, outlines the experimental methodology used in the synthesis, characterization, and evaluation of unmodified HAP, MK-GP and their novel HAP-MK-GP composites. The first section describes synthesis protocols, including raw material selection, chemical precursors, and processing conditions. Special attention is given to HAP-MK-GP hybrid preparation, focusing on composition and conditions of preparation that optimize structural and functional properties. Additionally, it details HAP doping with Fe_3O_4 for magnetic enhancement and modification with *Urtica dioica* extract to introduce organic functional groups for improved adsorption selectivity. The second section presents characterization techniques used to analyze physicochemical properties. These include X-ray diffraction (XRD) for phase identification, Fourier transform infrared spectroscopy (FTIR) for functional group analysis, scanning electron microscopy (SEM) for morphology, and BET/BJH analysis for surface area and porosity. Thermal stability (TGA) and mechanical tests assess structural integrity and durability. The third section details batch adsorption experiments evaluating pollutant removal efficiency. It also studies adsorption kinetics and isotherm models to elucidate interaction mechanisms. The last section of the chapter illustrates the calculation and optimization approaches used to study the adsorption phenomenon, as well as the methodological tools used to exploit and interpret the experimental data.

II.1. Preparation of hydroxyapatite powder

A stoechiometric hydroxyapatite (HAP) powder, with a $\frac{Ca}{P}$ molar ratio of 1.67, was synthesized by the co-precipitation method. First, ammonium phosphate dibasic ($(NH_4)_2HPO_4$, 99.2% assay) and calcium nitrate tetrahydrate ($Ca(NO_3)_2 \cdot 4H_2O$, 99.2% assay) were dissolved in distilled water to form two solutions with concentrations of 0.36 M and 0.6 M respectively. Then the P solution was added dropwise to the Ca solution. The pH of the mixture was adjusted to 10 using NaOH, and the solution was continuously stirred for 12 hours to allow the formation of HAP particles. Finally, the precipitate was then filtered and dried in an oven at 353 K for 24 hours. **Fig. II.1** summarizes the various steps involved in HAP powder synthesis.

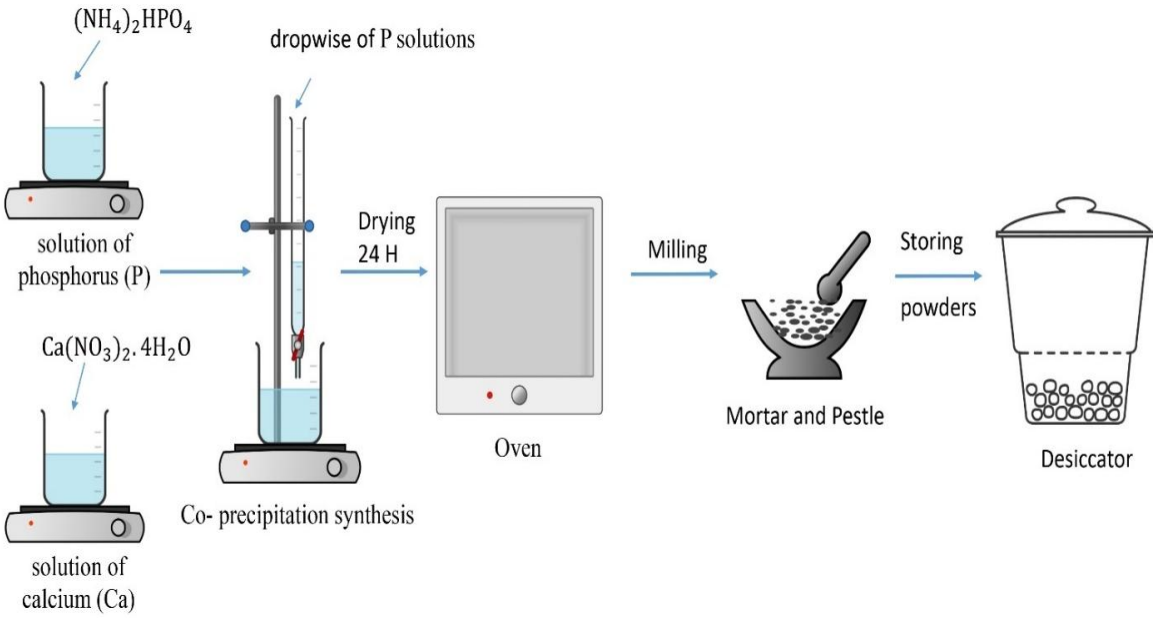

Fig. II.1. Synthesis pathway for hydroxyapatite (HAP) using the co-precipitation method.

II.2. Preparation of different types of HAP-MK-GP granules

II.2.1. HAP-MK-GP granules elaborated using distilled water as a granulation fluid

Hydroxyapatite-based geopolymers granules (HAP-MK-GP) were prepared using a direct forming method (Ren et al., 2021 ; Papa et al., 2022 ; Ibrahim et al., 2022). To optimize the granules' composition and achieve high mechanical properties, various weight percentages of HAP, sodium metasilicate (Na_2O 50.8 wt. %, SiO_2 46.7 wt. %, and H_2O 2.5 wt. %), and metakaolin powders were tested (**Table II.1**). The powders were mixed as dry powders, ground using a disc mill (Retsch RS 200) at 1500 rpm for 5 minutes, and then processed in a high shear granulator (Eirich EL1). Distilled water was added dropwise as a granulation fluid, until visual observation of granule formation. In this step, the granulator pan mixing speed was set to 1200 rpm, the mixer plate speed to 170 rpm, and the granulator-tilting angle to 30°. Finally, the granules formed were recovered and cured at 333 K for 24 hours. The steps followed in the preparation are presented schematically in **Fig. II.2**.

Table II.1. Composition of the elaborated HAP-MK-GP granules.

Granules	(% wt)			Toughness of obtained granules
	HAP	Sodium- Metasilicate	MK	
HAP-MK-GP 1	80	5	15	Not hard
HAP-MK-GP 2	70	7.50	22.50	Not hard
HAP-MK-GP 3	60	10	30	Not hard
HAP-MK-GP 4	55	15	30	Hard
HAP-MK-GP 5	57.40	14.60	28	Hard

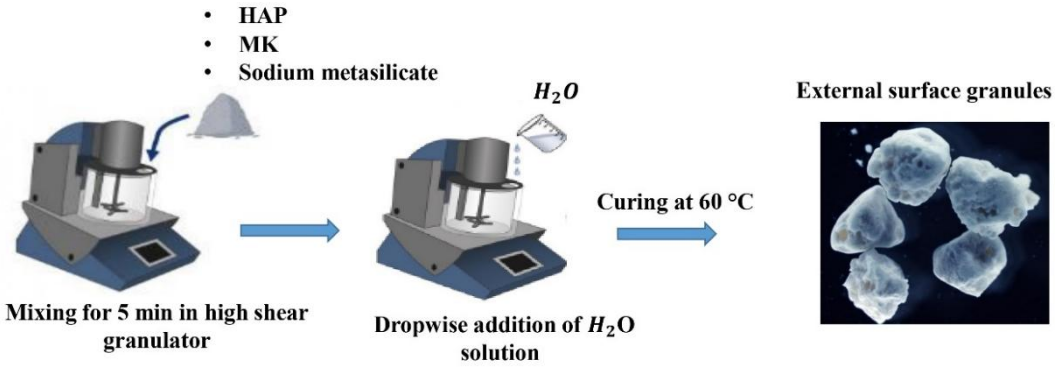

Fig. II.2. Schematic illustration of the preparation steps for HAP-MK-GP granules.

II.2.2. HAP-MK-GP elaborated porous granules

To improve the porosity and mechanical properties of HAP-MK-GP granules, hydrogen peroxide (H_2O_2, 30%) and polyethylene glycol (PEG, 99 %, Mw = 4000 g/mol) were used as porogen agents during the granule elaboration process.

II.2.2.1. HAP-MK-GP elaborated granules using H_2O_2 as a granulation fluid (Publication I)

Hydrogen peroxide (H_2O_2) solution was added dropwise to the optimized powder mixture of 57.4% HAP, 28 % MK and 14.6% sodium metasilicate, until granule formation was visually observed (**Fig. II.3**). Various concentrations of H_2O_2 (0, 5, 7.50, and 10 %) were introduced into the optimized mixture, while maintaining its weight percentage constant at 100% by proportionally adjusting the pecentage of H_2O_2 to that of sodium metasilicate. All this preparation results in granules labeled G_0, G_1, G_2, and G_3 (**Table. II.2**). The granules were cured at 333 K for 24 hours to allow the release of oxygen bubbles from the H_2O_2. Subsequently, they were rinsed with distilled water, dried in an oven at 333 K for 24 hours, sieved to a particle size of 1–4 mm, and stored at room temperature.

Table II.2. Composition of the elaborated HAP-MK-GP granules at various concentrations of H_2O_2.

Granules	(%wt)			
	HAP	MK	Sodium- Metasilicate	H_2O_2
G_0	57.4	28	14.6	0.00
G_1	57.4	28	14.6	5.00
G_2	57.4	28	14.6	7.50
G_3	57.4	28	14.6	10.00

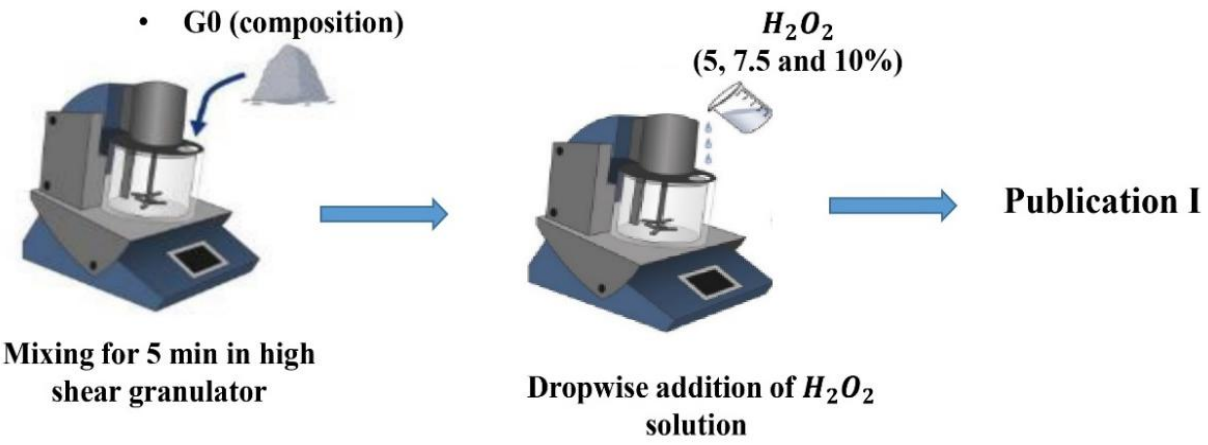

Fig. II.3. Schematic illustration of the preparation steps for the different HAP-MK-GP granules at various concentrations of H_2O_2 .

II.2.2.2. HAP-MK-GP elaborated granules using PEG as a porogen agent (Publication II)

Various weight percentages of polyethylene glycol (PEG), ranging from 0 to 4%, were added to the optimized powder mixture of 57.4% HAP, 28 % MK and 14.6% sodium metasilicate (**Table II.3, Fig. II.4**). the weight percentage of the mixture is kept constant at 100% by proportionally adjusting the percentage of PEG to those of sodium metasilicate and MK. The obtained granules were identified: G-PEG0, G-PEG1, G-PEG2, G-PEG3, and G-PEG4, in reference to the percentage of PEG introduced into their composition. After that, PEG was removed by mixing the granules with distilled water (V = 200 mL) at 358 K and a mixing speed of 150 rpm for 5 hours. This cleaning operation was repeated three times to ensure thorough removal of PEG and the creation of porous granules. Finally, the granules were dried in an oven at 333 K for 24 hours.

Table II.3. Composition of the elaborated HAP-MK-GP granules at various weight percentages of PEG.

Granules	(%wt)				Toughness of obtained granules
	HAP	MK	Sodium- Metasilicate	PEG	
G-PEG0	57.4	14.6	28	0	Hard and not porous
G-PEG1	60	19	20	1	Hard and not porous
G-PEG2	60	19	19	2	Hard and slightly porous
G-PEG3	61	18	18	3	Hard and porous
G-PEG4	61	18	17	4	Not hard and porous

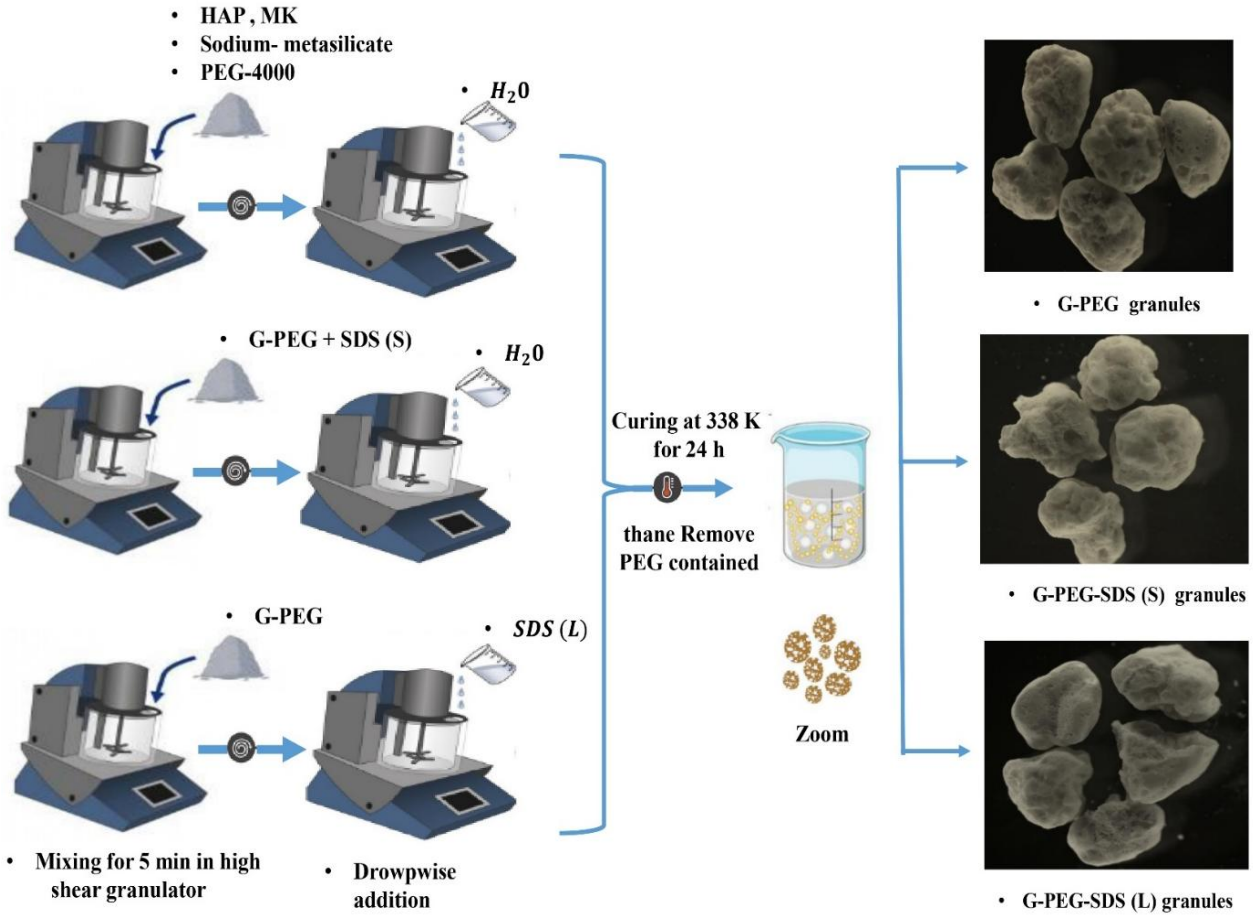

Fig. II.4. Schematic representation of the elaboration HAP-MK-GP granules at different SDS states (S/L).

II.2.3. HAP-MK-GP functionalized granules using SDS (Publication II)

The HAP-MK-GP granules were functionalized by incorporating 1 wt% of sodium dodecyl sulfate (SDS) as anionic surfactant and templating agent to the optimized powder mixture of 60% HAP, 18% MK, 18% sodium metasilicate and 3% PEG (**Table II.4**). The weight percentage of the mixture is kept constant at 100% by proportionally adjusting the percentage of SDS to those PEG, MK and sodium metasilicate. The effect of sodium dodecyl sulfate was then investigated by either incorporating it as a powder directly into the optimized mixture, or dissolving it beforehand in the granulation fluid (L), as shown in **Fig. II.4**. All mixtures result in granules labeled G-PEG, G-PEG/SDS (S) and G-PEG/SDS (L).

Table II.4. Composition of the elaborated HAP-MK-GP granules at different SDS states.

Granules	(%wt)					
	HAP	MK	Sodium- Metasilicate	PEG	SDS (S)	SDS (L)
G-PEG	61	18	18	3	0	0
G-PEG/SDS (S)	60	18	18	3	1	0
G-PEG/SDS (L)	60	18	18	3	0	1

II.3. Functionalization of HAP powder (Publication III)

II.3.1. Synthesis of magnetized hydroxyapatite (HAP-Fe) nanoparticles

Magnetized hydroxyapatite nanoparticles (HAP-Fe) were prepared using the same co-precipitation method as HAP. The Ca solution (0.5 M) was mixed with iron oxide (II, III) (Fe_3O_4, 97 % assay) (0.5g) and continuously stirred for 1 hour. Subsequently, the 0.3 M P solution was added dropwise to the Ca+Fe mixture solution, which was continuously stirred for 12 hours. The precipitate was then filtered and dried in an oven at 353 K for 24 hours.

II.3.2. Synthesis of magnetized hydroxyapatite modified nanoparticles (HAP-Fe-*Urtica dioica* ext)

The *Urtica dioica* leaf extract was prepared using a solid-liquid (diocoxiation) extraction method. First, the *Urtica dioica* leaves, collected in the spring (March) from a woodland located in Bejaia (Amizour-Smaoun)-Algeria, were washed, dried and shielded from light to prevent oxidation reactions that might alter the plant components. Then, 10 g of leaves were added to 250 mL of distilled water and heated to 373 K for 30 minutes. The mixture (V = 150 mL) was filtered, and the organic extracts were reduced to less than 30 mL using a rotary evaporator at 328 K. The resulting *Urtica dioica* extract noted: *Urtica dioica* ext was stored in a refrigerator at 277 K until use.

The HAP-Fe- *dioica* ext nanoparticles were prepared using the same co-precipitation method as HAP and HAP-Fe. However, the Ca solution (0.5 M) was mixed with Fe_3O_4 (0.5g) and *Urtica dioica* ext solution. The mixture was continuously stirred for 1 hour befor adding the P solution.

II.4. Materials characterization

The investigation of functional groups and chemical bonds in the pure HAP powder, the magnetized and functionalized HAP nanoparticles, and the differents elaborated HAP-MK-GP granules was conducted using FTIR analysis. A Bruker VERTEX v80 instrument was used, with samples pulverized to less than 50 µm. The spectra were collected for wavenumbers in the range of 400–4500 cm^{-1} with a resolution of 2 cm^{-1}. However, their phase changes and decomposition were explored by thermogravimetric analysis (TGA) coupled with differential thermal gravimetric analysis (DTG). That was performed using an SDT 650 simultaneous thermal analyzer (a heating rate of 10°C/min under nitrogen atmosphere).

To analyze the composition and structure of samples, a Rigaku Smart Lab 9 kW X-ray diffractometer (XRD) with Co Kα radiation was used. The scan speed was 4°/min, with a range

of 2θ between 10° and 80° and a step width of 0.02°. X'pert HighScore software was used for phase identification. Furthermore, their elemental composition was obtained using an X-ray fluorescence spectrometer (XRF) (PanAnalytical Minipal 4).

The microstructure and chemical composition of both powder and granules were analyzed after carbon-coating to ensure conductivity. Scanning electron microscopy (SEM) with energy-dispersive X-ray spectroscopy (FE-SEM-EDS, Zeiss Ultra Plus) and electron probe microanalysis (EPMA, Jeol JXA-8530F Plus) were used for the analysis. For SEM analysis of the granules, the samples were embedded in epoxy resin (Buehler EpoxiCure 2 Epoxy Resin and Hardener) and polished with silicon carbide grinding papers (P240, P600, P1200). In addition, images of the external and internal surfaces of the granules were captured using an optical microscope (Leica MZ6) equipped with a Leica DFC420 camera.

The surface properties, including mean pore diameter, pore volume, and specific surface area, of the samples were analyzed using the Brunauer-Emmet-Teller (BET) isotherm and Barrett-Joyner-Halenda (BJH) method. Nitrogen (N_2) adsorption and desorption measurements were conducted with a Micromeritics ASAP 2020. The study investigated two types of samples: granules (diameter = 4 mm) and powder (particle sizes < 50 μm). Prior to measurement, the samples were freeze-dried for 48 hours.

The mechanical strength of the granules was determined using a Zwick Roell Z010 (10 kN load cell) instrument with a loading rate of 1 mm/min. The granules selected for the compression test were spherical with a diameter of 4 mm, and measurements were performed for five granules from each batch. The compressive strength (σ, MPa) was calculated using Eq. II-1, where F (N) represents the peak force and d (mm) represents the granule diameter.

$$\sigma = 4 \times \frac{F}{\pi \times d^2} \qquad (\mathbf{II-1})$$

The magnetic properties of the samples were assessed using a vibrating sample magnetometer (VSM, model EV11, MicroSense, USA), while the point of zero charge (pH_{pzc}) determined by preparing a solid/liquid mixture at a ratio of 1 g/L in a 0.01 M NaCl solution. The pH values of the solutions were adjusted between 2 and 12 by adding either 1 M HCl or NaOH, and the mixtures were stirred for 24 hours. The pH_{pzc} was identified as the pH value at which the curve of final pH (pH_{Final} versus $pH_{Initial}$ crosses the line $pH_{Initial} = pH_{Final}$.

II.5. Use of HAP powders and HAP-MK-GP based materials for the removal of cationic and anionic dyes

To assess the performance of the materials developed (HAP powders and HAP-MK-GP based materials), they were tested in a batch reactor for the removal of various anionic and cationic dyes. The cationic dyes used were brilliant green (BG, 99%), crystal violet (CV, 99%) and methylene blue (MB, 99%), while anionic dyes were direct red 23 (DR23, 33%) and alzarine red S (ARS, 99%). Their chemical structures, as well as absorption spectra, are provided in **Fig. II.5**. Adsorption efficiency was analyzed as a function of several parameters, including contact time, initial dye concentration, adsorbent dose, solution pH, etc. These tests made it possible to determine the maximum adsorption capacities of the materials synthetized and elaborated, as well as their selectivity towards the different classes of dyes.

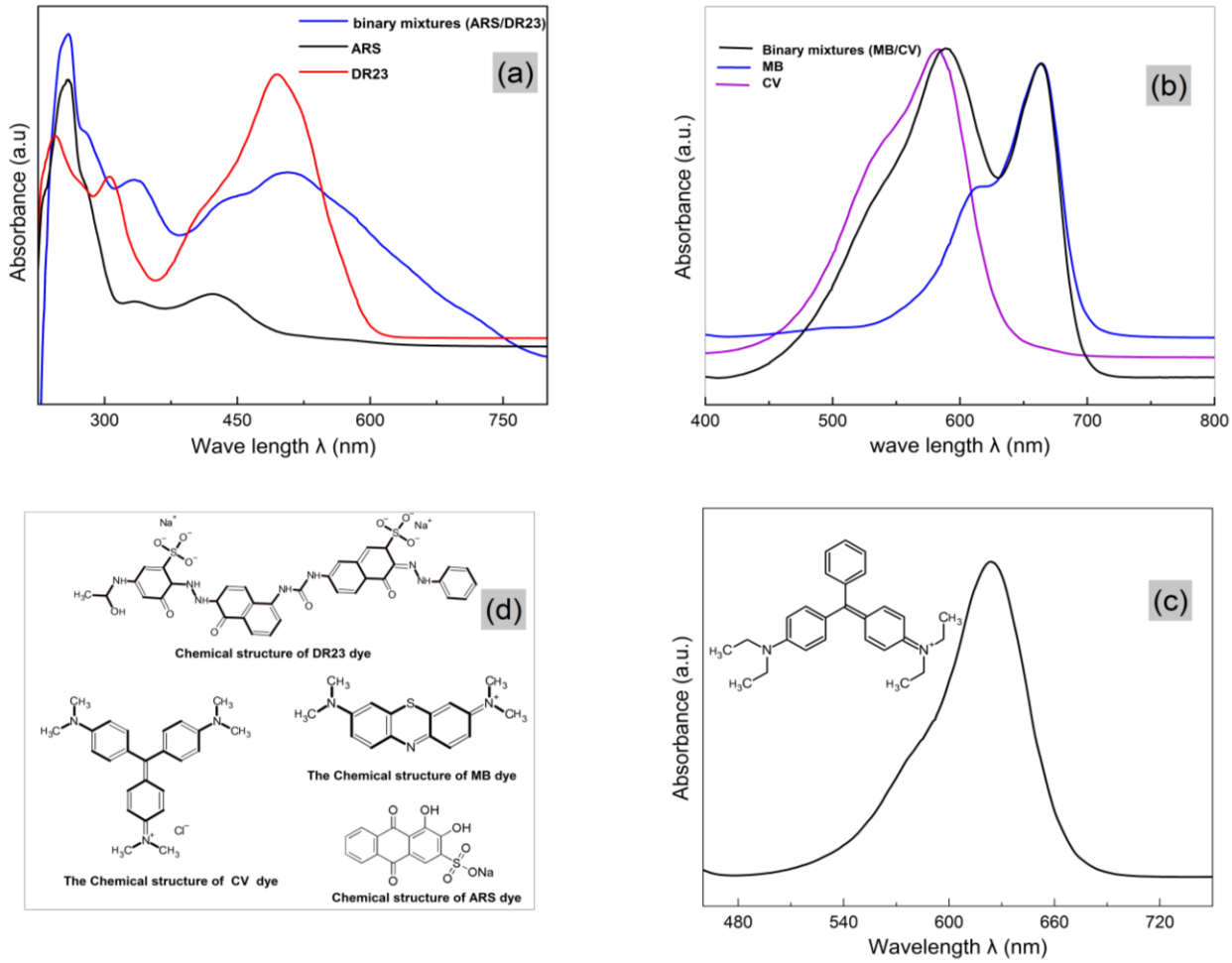

Fig. II.5. Absorption spectra, in single and binary mixture, of (a): ARS and DR23 dyes, (b): MB and CV dyes, (c): Chemical structure of dyes used, and (d): Absorption spectra of BG dye and its chemical structure.

II.5.1. Investigation of brilliant green (BG) dyes removal (Publication I)

A comparative study was conducted to evaluate the adsorption efficiency of the developed granules (i.e. G_0, G_1, G_2, and G_3) at different H_2O_2 concentrations at Conditions: $[BG]_0$ = 15 mg/L, adsorbent dose = 2 g/L, pH = 5, granule diameter = 2 mm, agitation speed = 350 rpm, and T = 298 K. Among these, G_3 was selected for optimization the adsorption parameters due to its high adsorption capacity. The adsorption parameters explored included contact time (0–180 minutes), initial BG dye concentration (10–100 mg/L), stirring speed (150–450 rpm), granule dosage (2–4 g/L), solution pH (3–9), granule diameter (1–4 mm), and temperature (298–338 K).

II.5.2. Investigation of MB and CV cationic dyes removal by using HAP-MK-GP /SDS (L) granules (Publication II)

The initial phase of the study involved a comparative methodology to assess the adsorption efficiency of the raw materials, HAP and MK-GP powders, and developed granules (G_0, G-PEG, G-PEG/SDS (S), G-PEG/SDS (L)). Adsorption studies were carried out using MB and CV dyes individually in aqueous solutions under controlled conditions $[dye]_0 = 25$ mg/L, pH = 7, adsorbedn dose $= 2\ g/L$, $d_{granules} = 4\ mm$, agitation speed = 250 rpm, time = 90 minutes, and T = 298 K. The G-PEG-SDS (L) granules were selected for further study. The adsorption parameters, including contact time (0–180 minutes), granule dosage (1–4 g/L), and solution pH (3–10), were optimized. Subsequently, the selectivity of the granules was assessed using MB and CV dyes at concentrations ranging from 25 to 180 mg/L in aqueous solutions. Additionally, a binary mixture of MB and CV, with both dyes at equal concentrations ranging from 15 to 100 mg/L, was analyzed.

II.5.3. Investigation of ARS and DR23 anionic dyes removal with HAP-Fe- *Urtica dioica* ext powder (Publication III)

A preliminary study was carried out to assess the influence of Fe_3O_4 and *Urtica dioica* extract on the HAP removal efficiency of the anionic dyes ARS and DR23 in aqueous solutions at conditions: pH of dye (i.e., 5.83 for DR23 dye and 4.89 for ARS dye), $[\text{dyes}]_0 = 20$ mg/L, time = 90 minutes, T = 21 °C, agitation speed = 200 rpm and adsorbent dose = 1 g/L. The HAP-Fe-*Urtica dioica* ext, due to its high adsorption capacity, was selected for further selective performance studies. Subsequent selective adsorption experiments were carried out in a batch system using a binary mixture of ARS and DR23 dyes. The adsorption parameters optimized in this part included contact time (0–180 minutes), binary dye

concentration (20–180 mg/L), stirring speed (145–275 rpm), adsorbent dosage (1–3.5 g/L), solution pH (3–7.5), and temperature (294–308 K).

II.5.4. Analytical methodology

Adsorption kinetics were evaluated by monitoring the evolution of residual solution concentration over the contact time between adsorbate (dyes) and adsorbent (elaborated materials). At predefined time intervals, samples were collected with a pipette, centrifuged at 8000 rpm for 5 minutes (Beckman Coulter J326XPI-IM-1), and analyzed using a UV-6300PC spectrophotometer (VWR, China) at a wavelength of $\lambda_{BG} = 624\,nm$, $\lambda_{CV} = 586\,nm$, $\lambda_{MB} = 664\,nm$, $\lambda_{ARS} = 259\,nm$, and $\lambda_{DR23} = 505\,nm$. The dye removal efficiency $y(\%)$ and the adsorption capacity,q_t (mg/g) of the dyes were calculated using Eq. II-2 and Eq. II-3, respectively.

$$y(\%) = \frac{[dye]_0 - [dye]_t}{[dye]_0} \times 100 \qquad (\mathbf{II-2})$$

$$q_t = ([dye]_0 - [dye]_t) \times \frac{V}{m} \qquad (\mathbf{II-3})$$

where $[dye]_0$ and $[dye]_t$ (mg/L) denote the initial concentrations of the dyes (i.e., BG, CV, MB, ARS or DR23) and their concentrations at time *t*, respectively, *V* (L) represents the volume of the solution, and *m* (g) represents the mass of the adsorbent powders or granules.

II.6. Adsorption isotherm, kinetic and thermodynamic studies

Examining adsorption kinetics and isotherms is essential for understanding the adsorption process in wastewater treatment, as it reveals the nature of the process, surface characteristics, and adsorption equilibrium affinity.

II.6.1. Single-dye solution

The equilibrium data obtained for solutions containing a single contaminant were analyzed using pseudo-first-order and pseudo-second-order kinetic models (Eq. II-4 and Eq. II-5, respectively). In addition, the adsorption isotherms were fitted using the non-linear Langmuir (Eq. II-6) and Freundlich (Eq. II-7) models (Yahiaoui et al., 2020).

$$q_t = q_e \times [1 - exp(-k_1 t)] \qquad (\mathbf{II-4})$$

$$q_t = q_e - \frac{q_e}{k_2 q_e t + 1} \qquad (\mathbf{II-5})$$

$$q_e = \frac{q_{max}\ K_L\, C_e}{K_L\, C_e + 1} \qquad (\mathbf{II-6})$$

$$q_e = K_F C_e^{\frac{1}{n}} \qquad (\mathbf{II-7})$$

where k_2 [g/(mg×min)] is the pseudo-second order rate constant, k_1 (min^{-1}) is the pseudo-first order rate constant , C_e (mg/L) is the equilibrium concentration of dye, K_L (L/mg) is the Langmuir adsorption constant, q_{max} (mg/g) is Langmuir monolayer adsorption capacity, K_F ($mg^{1-\frac{1}{n}}.L^{\frac{1}{n}}/g$) and $\frac{1}{n}$ are Freundlich capacity and intensity constants, respectively, related to the surface heterogeneity.

II.6.2. Binary dye mixture solution

The isotherme models developed for single-contaminant solutions cannot accurately describe adsorption behaviour in a binary dye mixture. Therefore, their extended versions are adopted for this analysis. In particular, the extended Langmuir model (Eq. II-8) is applied to interpret the equilibrium data and evaluate the competitive interactions between the adsorbates (Ghemit et al., 2019 ; Djebri et al., 2017).

$$q_{e,i} = \frac{q_{m,i}\, K_{L,i}\, C_{e,i}}{1 + \sum_{j=1}^{N} K_{L,j}\, C_{e,j}} \qquad (\mathbf{II-8})$$

$$\text{with}\quad q_{e,1} = \frac{q_{m,1}\, K_{L,1}\, C_{e,1}}{1+K_{L,1}\, C_{e,1}+K_{L,2}\, C_{e,2}} \quad \text{and}\quad q_{e,2} = \frac{q_{m,2}\, K_{L,2}\, C_{e,2}}{1+K_{L,1}\, C_{e,1}+K_{L,2}\, C_{e,2}}$$

where compounds 1 and 2 present ARS and DR23 dyes or MB, and CV dyes, respectively. $q_{e,1}$ and $q_{e,2}$ are the equilibrium amounts adsorbed (mg/g), $q_{m,1}$ and $q_{m,2}$ (mg/g) are the maximum amounts adsorbed of the extended-Langmuir model, $K_{L,1}$ and $K_{L,2}$ are the Langmuir constants (L/mg), and $C_{e,1}$, $C_{e,2}$ are the dyes (i.e. ARS and DR23 or MB and CV) equilibrium concentrations in the solution (mg/L).

II.6.3. Thermodynamic aspect

To assess the spontaneity of dye adsorption (ARS, DR23, and BG) onto HAP-Fe-*Urtica dioica* ext powder (Publication III) or G_3 granules (Publication I), the thermodynamic quantities Gibbs free energy $\Delta G°$(kJ/mol) , enthalpy $\Delta H°$(kJ/mol) , and entropy $\Delta S°$(kJ/mol. K) , were calculated using Eq. II-9, Eq. II-10, and Eq. II-11, respectively (AitAli et al., 2023).

$$\Delta G^{\circ} = -RT ln\, K_d \qquad (\mathbf{II-9})$$

$$\Delta G^{\circ} = \Delta H^{\circ} - \mathrm{T}\Delta S^{\circ} \qquad (\mathbf{II-10})$$

$$lnK_d = -\frac{\Delta \mathrm{G}^{\circ}}{RT} = \frac{\Delta S^{\circ}}{R} - \frac{\Delta \mathrm{H}^{\circ}}{RT} \qquad (\mathbf{II-11})$$

where R is the universal gas constant (8.314462 J/(K×mol), T is the absolute temperature (K), and K_d is the equilibrium adsorption constant.

II.7. Rate-controlling step of the adsorption dyes

The homogeneous particle diffusion model (HPDM) was utilized to estimate the diffusion coefficient D (m^2/s), as described in Eq. II-13 by Michelson et al., (1975). This model was applied to investigate the selectivity of MB and CV dye adsorption onto G-PEG/SDS (L) granules (Publication II). Furthermore, it was used to examine the effect of temperature and evaluate the diffusion processes governing the adsorption of ARS and DR23 dyes onto HAP-Fe-*Urtica dioica* ext powder (Publication III).

The model identifies the rate-limiting step, typically controlled by either intra-particle diffusion D_p $(\mathrm{Eq.\,II-13})$ or a film diffusion mechanism D_f (Eq. II-14) (Michelson et al., 1975).

$$X_{(t)} = \frac{q_t}{q_e} = 1 - \frac{6}{\pi^2}\sum_{z=1}^{\infty}\frac{1}{Z^2}\exp\left[\frac{-Z^2\pi^2 D_p t}{r_0^2}\right] \qquad (\mathbf{II-12})$$

For $0 < X_{(t)} < 1$ and when adsorption takes place on spherical particles, Eq. II-12 can be simplified to Eq. II-14 and Eq. II-15 (Michelson et al., 1975).

$$X_{(t)} = \left[1 - \exp\left[\frac{-\pi^2 D_p^2 t}{r_0^2}\right]\right]^{0.5} \qquad (\mathbf{II-13})$$

$$-ln\left(1 - {X_{(t)}}^2\right) = 2K_p t = \frac{2\pi^2 D_p}{r_0^2}t \qquad (\mathbf{II-14})$$

where $X_{(t)}$ is the fractional attainment at time t, $D_p = \frac{K_p r_0^2}{\pi^2}$ (m^2/s) is the effective diffusion coefficient, r_0 is the radius of adsorbent assumed to be spherical (6.451×10^{-6}m), Z is an integer, K_p is the diffusion rate constant (L/s), which was used for the calculation of effective intra-particle diffusivity from the experimental data.

If the rate of adsorption is controlled by liquid film diffusion (Michelson et al., 1975), the analogous expression Eq. II-15 may be used.

$$-ln\left(1 - X_{(t)}\right) = K_f t = \left[\frac{3D_f C_e}{r_0 \delta C_s}\right] t \qquad (\mathbf{II - 15})$$

$D_f = \frac{K_f r_0 \delta C_s}{3C_e} (m^2/s)$ is the film diffusion coefficient in liquid phase, K_f is the film diffusion rate constant (L/s), C_e and C_s (mol/L) are equilibrium concentrations of dyes in solution and solid phase, and δ is the film thickness; it is estimated to 10^{-5}(m), according to Liu et *al*. (2018).

II.8. regeneration of the developed adsorbent

The regeneration of developed adsorbents for the removal of contaminants was evaluated through multiple cycles of adsorption and desorption. The regeneration efficiency of G1 granules was tested over five consecutive cycles, each consisting of adsorption equilibration followed by desorption. Adsorption was conducted under conditions of 10 mg/L BG concentration, 3 g/L adsorbent dose, pH 7, 180-minute duration, 2 mm granule diameter, 250 rpm agitation speed, and 298 K temperature. Following adsorption, the granules were washed with distilled water and desorbed in a pH 4 (0.1 mol/L HCl) solution under similar conditions.

In another set of experiments, the regeneration of G-PEG/SDS (L) granules loaded with MB dye was optimized using an acetic acid concentration of 0.72 mol/L, temperature of 323 K, and a contact time of 173.22 minutes. Adsorption was performed under conditions of 20 mg/L MB concentration, 3 g/L adsorbent dose, pH 8, 180-minute duration, 4 mm granule diameter, 250 rpm agitation speed, and 298 K temperature.

Additionally, the reusability of the HAP-Fe-Urtica dioica ext adsorbent was evaluated for the removal of binary DR23 and ARS anionic dyes over seven cycles. Adsorption was carried out under conditions of 20 mg/L initial concentration for both dyes, 120-minute adsorption time, pH 3.15, 2.60 g/L adsorbent dose, 294 K, and 260 rpm agitation speed. After each adsorption cycle, the dye-loaded adsorbent was washed, dried at 100 °C, and desorbed using a 0.1 M NaOH solution.

II.9. Experimental design methodology

Statistical tools, in particular experimental design, and empirical approaches are commonly used in process optimisation procedures. They enable the relationships between input variables and system responses to be modelled, while offering significant advantages such as reducing the number of experimental trials, cutting reagent consumption and optimising laboratory

resources (Boudrahem et al., 2018). However, they also have drawbacks, including long processing times and inaccurate parameters. Response Surface Methodology (RSM), a combination of statistical and mathematical methods, addresses these issues by minimizing the number of trials and translating data into empirical models (AitAli et al., 2023).

RSM techniques based on Box-Behnken Design (BBD) or Central Composite Design (CCD), are frequently used to establish mathematical models, assess factors, and determine optimal conditions for desired outcomes (Koraqi et al., 2024). While both designs are used for similar purposes, CCD is the more versatile and commonly preferred option. It is designed to estimate quadratic models using factorial, axial (star), and center points (Benalia et al., 2024).This flexibility allows CCD to fit various models effectively, though it may require more experimental runs as the number of factors increases. CCD has three variants—circumscribed, inscribed, and face-centered—that offer different geometric configurations, enhancing its adaptability to diverse experimental conditions **(Fig. II.6)** (Chollom et al., 2019).

In contrast, BBD is specifically structured to minimize the number of experimental runs, making it more efficient for experiments with three or four factors. BBD features a spherical design where all points lie on a sphere, combining 2k factorials with incomplete block designs (**Fig. II.6**). While BBD requires fewer treatment combinations than CCD, it shares CCD's limitation of having regions with poor prediction quality and lacks the axial points, which reduces its ability to capture quadratic effects as effectively. Despite this, BBD is often preferred for its cost-effectiveness and practical efficiency, making it a viable alternative to CCD in many experimental scenarios (Koraqi et al., 2024).

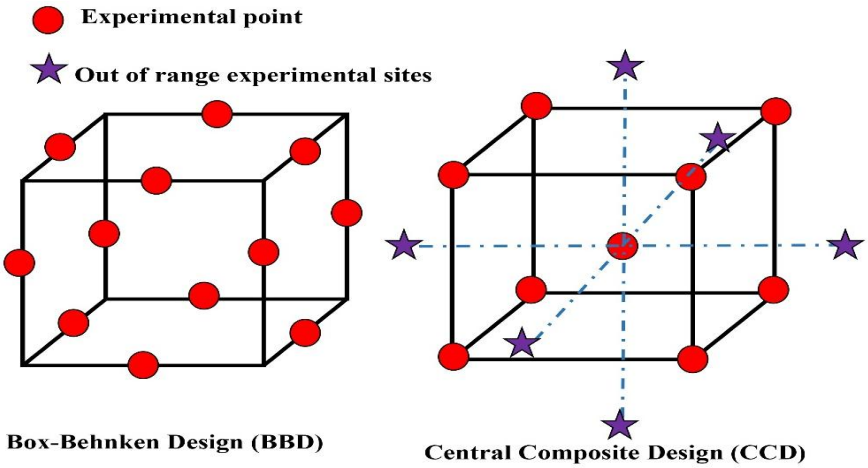

Fig. II.6. Schematic diagram of experimental design of three-factor BBD and CCD (Zhuang et al., 2021).

II.9.1. Box-Behnken Design-Response Surface Methodology approach

BBD-RSM was used to optimize the regeneration process for MB dye adsorption on G-PEG/SDS (L) granules using acetic acid, with the goal of minimizing granule mass loss. Three independent variables were investigated: acetic acid concentration (0.2 to 1 mol/L) (x_1), temperature (294 to 338 K) (x_2), and contact time (30 to 180 minutes) (x_3) (**Publication II**). Regeneration efficiency was evaluated as the weight percentage of desorbed dye, while mass loss was measured after drying the regenerated granules overnight at 313 K.

The number of experiments to be carried out using BBD was calculated based on Eq. II-16 (Dibene et al., 2019).

$$N = 2K(K-1) + n_0 \qquad (\mathbf{II-16})$$

where $K \geq 3$ is the number of factors studied and n_0 is the replicate number of the central point.

II.9.2. Central Composite Design-Response Surface Methodology approach

CCD-RSM was employed to optimize the adsorption efficiencies of ARS and DR23 in a binary dye mixture, as well as the average adsorption efficiency ($y_{avg}(\%)$ Eq. II-17) of ARS and DR23 onto HAP-Fe-*Urtica dioica* ext. The effects of three variables, dose of HAP-Fe-*Urtica dioica* ext (x_1), pH solution (x_2), and the agitation speed (x_3) were investigated **(Publication III)**.

$$y_{avg}(\%) = \frac{y_{ARS}(\%) + y_{DR23}(\%)}{2} \qquad (\mathbf{II-17})$$

To determine the local axial point, the alpha value in the Central Composite Design (CCD) model must be calculated using Eq. II-18 (AitAli et al., 2023). The alpha value can be set as centered, rotatable, or orthogonal. Orthogonality is essential for evaluating linear, quadratic, and interaction effects independently.

$$\alpha = (2^K)^{0.25} \qquad (\mathbf{II-18})$$

The total number of design points N of a rotatable design is calculated (Eq.II-19) (Meski et al., 2011).

$$N = 2^K + 2K + n_0 \qquad (\mathbf{II-19})$$

Chapter III: Results and Discussion

Chapter III. Results and Discussion

This chapter provides a critical analysis of the work carried out during this thesis, structured around the three scientific publications produced. Particular attention is paid to assessing the performance of the materials synthesised (HAP-MK-GP and HAP-Fe-*Urtica dioica* ext), and compared them with the performance of materials described in the literature for the treatment of water contaminated with organic pollutants, in particular textile dyes. This comparative study aims to situate the original contribution of our research to wastewater treatment, by highlighting the advantages, limitations and prospects for improvement of the materials developed. The analysis is based on criteria such as the rate of adsorption of pollutants, the stability of the materials and their potential for reuse. So, through a systematic comparison with recent advances in the field, this chapter not only consolidates current knowledge, but also suggests future research directions for the development of more effective and sustainable water treatment materials.

III.1. Challenges of HAP matrices developed in this study

Hydroxyapatite (HAP), a biocompatible and non-toxic calcium phosphate material, has attracted considerable attention in water treatment applications, particularly for adsorbing organic pollutants. However, the unmodified form of HAP faces significant limitations, including low surface area and porosity, which hinder its adsorption efficiency and selectivity for organic contaminants.

To overcome these challenges, this study proposed an innovative approach based on the incorporation of MK-GP into HAP matrix. This integration aimed to enhance the physicochemical properties of the composite, improving its adsorption potential. In fact, the embedding of HAP within the MK-GP matrix resulted in marked improvements in surface area, porosity, and mechanical stability, transforming the material into a more effective adsorbent. So, the resulting HAP-MK-GP granules exhibited a significantly enhanced adsorption capacities for cationic dyes ((i.e., MB, CV and BG), which is attributed to an increase in the density of surface-active sites and improved structural characteristics of the material. In contrast, their affinity for anionic dyes remained relatively low, highlighting the need for further optimization to extend their adsorption efficiency to a wider range of contaminants.

As a solution to this limitation, functionalizing the HAP surface with bioactive compounds extracted from *Urtica dioica* plant (harvested in the Bejaia region-Algeria) was explored as an innovative strategy. The extract, rich in polyphenols, flavonoid glycosides, phenolic acids,

amino acids, carotenoids, and chlorophyll, provided a variety of reactive functional groups that could enhance adsorption interactions. Immobilization of these bioactive components on the HAP matrix was achieved through complexation with calcium ions (Ca^{2+}) followed by interactions with phosphate groups (PO_4^{3-}), leading to the stable deposition of the extract. This functionalization not only increased the surface reactivity of the material but also improved its affinity for anionic pollutants, thus addressing the previously observed limitations in adsorption selectivity.

Building on these enhancements, the introduction of iron oxide nanoparticles (Fe_3O_4) as a magnetic agent was employed to synthesize a magnetized HAP-Fe composite. The addition of Fe_3O_4 was intended to simultaneously improve the matrix's adsorption efficiency towards anionic dyes and facilitate its recovery by magnetic separation. This modification endowed the composite with multifunctional properties, combining optimized adsorption with easier regeneration and reuse, enhancing its potential for environmental applications.

As a synthesis of the above, the present research provides a comprehensive assessment of the structural, chemical and adsorption improvements achieved through the optimization of HAP-MK-GP granules and HAP-Fe-*Urtica dioica* ext composites. The findings elucidate the mechanisms responsible for improving adsorption performance, highlighting the influence of surface functionalization and magnetization on the effectiveness of the material. Furthermore, this work contributes valuable insights into the development of advanced HAP-based materials, presenting promising solutions for the effective removal of organic contaminants from aqueous environments and paving the way for future innovations in sustainable water treatment technologies.

III.2. Critical review of the elaborated HAP-MK-GP granules performances

This review presents an in-depth comparative analysis of the results from **Publication I** and **Publication II**, highlighting the interactions between the structural modifications induced and their effects on the functional properties of the elaborated HAP-MK-GP granules. Particular attention is paid to the impact of these transformations on structural integrity, chemical stability and improved adsorption performance, thereby providing a better understanding of the underlying mechanisms and guiding the prospects for optimizing the materials studied.

III.2.1. Critical review of Publication I. Porous metakaolin geopolymer as a reactive binder for hydroxyapatite adsorbent granules in dye removal

The study developed porous hydroxyapatite-metakaolin geopolymer (HAP-MK-GP) granules for adsorption of organic pollutants from aqueous solutions. It investigated the use of MK-GP as a binder for unmodified HAP powder, with hydrogen peroxide (H_2O_2) added at different concentrations (0.0, 5.0, 7.5, and 10.0 wt%) as both a granulation fluid and a foaming agent. The study focused on improving the mechanical properties of the material by transforming HAP powder into granules, thereby enhancing the adsorption efficiency of the granules for the removal of Brilliant Green (BG) dye from aqueous solutions.

III.2.1.1. Critical review of chemical functional characterization of HAP-MK-GP granules elaborated using H_2O_2 as granulation fluid

A thorough characterization of the elaborated HAP-MK-GP granules in the presence of various concentrations of H_2O_2 (0.0, 5.0, 7.5, and 10.0 wt%) was carried out in order to assess their structure, chemical composition and physicochemical properties. This analysis involved the use of advanced techniques such as FTIR to identify the functional groups present, BET/BJH isotherm method to calculate specific surface area and porosity, XRF to determine the composition, SEM to observe pores morphology and distribution, as well as the mechanical strength to measure resistance. These investigations have enabled us to gain a better understanding of the impact of H_2O_2 on the modification of HAP-MK-GP granules properties, in particular with regard to its porosity, chemical stability and adsorption capacity, parameters that are crucial for its potential applications in the field of environmental pollution control.

The use of H_2O_2 as a granulation fluid and blowing agent in the synthesis of HAP-MK-GP granules presents a nuanced trade-off between enhancing porosity and maintaining structural integrity. Chemically, the results indicate that the inclusion of HAP in the metakaolin and sodium metasilicate matrix does not disrupt the formation of MK-GP granules at 0 wt.% H_2O_2 (G_0), thereby preserving the structural integrity of the composite material. However, the use of H_2O_2 at concentrations exceeding 5.0 wt.% leads to significant alterations in the material's structure. Specifically, H_2O_2 interacts with HAP, causing notable degradation. Experimental agitation of HAP powder in a 7.5 wt% H_2O_2 solution for 30 minutes results in approximately 20% mass loss of the HAP powder. This interaction is described by the following reactions Eq. III.1 and Eq. III.2.

$$Ca_{10}\,(PO_4)_6(OH)_2 + 8H^+ \rightarrow 9Ca^{2+} + 5HPO_4^{-2} + CaHPO_4 + 2H_2O \qquad (\mathbf{III-1})$$

$$CaHPO_4 + 2H_2O + H^+ \rightarrow Ca^{2+} + H_2PO_4^- + 2H_2O \qquad (\mathbf{III-2})$$

The FTIR analysis shown in **Fig.III.1** highlights changes in the vibrational modes of elongation of the O-H and PO_4^{-3} groups, reflecting the dissolution of calcium and phosphate ions. These observations are corroborated by XRF results (**Table III.1**), which indicate an increase in the Ca/P ratio, a direct reflection of this ionic dissolution. This decrease in the overall calcium and phosphate content thus compromises the structural integrity of the granules.

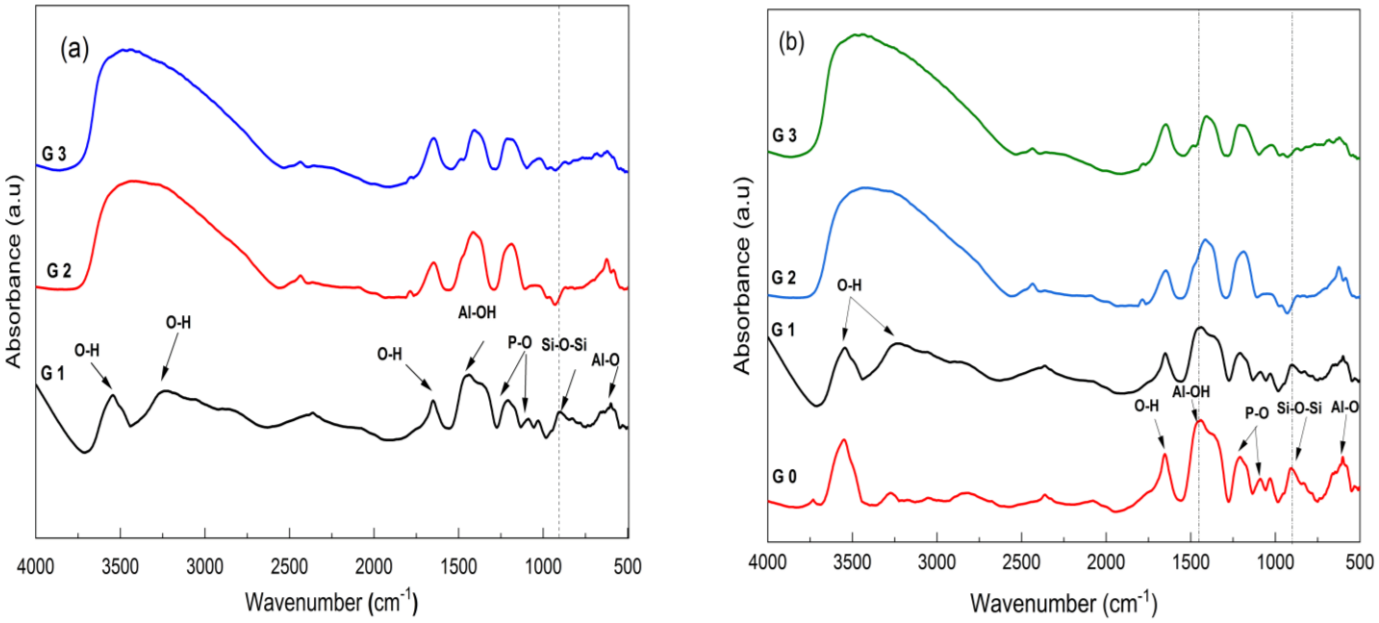

Fig. III.1. FTIR spectrum of (a) raw material HAP and MK, and (b) prepared granules.

Table III.1. XRF results of HAP, MK and prepared granules.

Element (%)	HAP	MK	G_0	G_1	G_2	G_3
O	19.08	47.89	36.95	32.64	32.55	30.39
Na	2.25	0.37	8.74	8.97	9.05	9.71
Al	0	22.20	4.33	3.48	3.21	2.64
Si	0.02	23.50	9.46	8.96	8.82	8.41
P	12.56	0.17	9.46	8.96	7.95	7.20
Ca	21.07	0.29	15.84	15.12	14.75	14.10
Ca/P	1.67	1.70	1.67	1.68	1.85	1.95

Likewise, surface characterization of granules synthesized with H_2O_2 at concentrations of 0, 5, 7.5, and 10 wt% reveals a mesoporous structure, as confirmed by type IV isotherms and H3

hysteresis loops in BET/BJH analysis (**Fig. III.2**). At lower H_2O_2 concentrations (sample G_1), the increase in porosity effectively enhances both interconnected and closed pore structures, as illustrated by SEM analysis (**Fig. III.3**). In fact, the moderate foaming effect induced by the decomposition of H_2O_2 facilitates pore formation without causing structural collapse. This morphological evolution, corroborated by the specific surface area data listed in **Table III.2**, proves advantageous for applications requiring a high active surface area, such as adsorption processes.

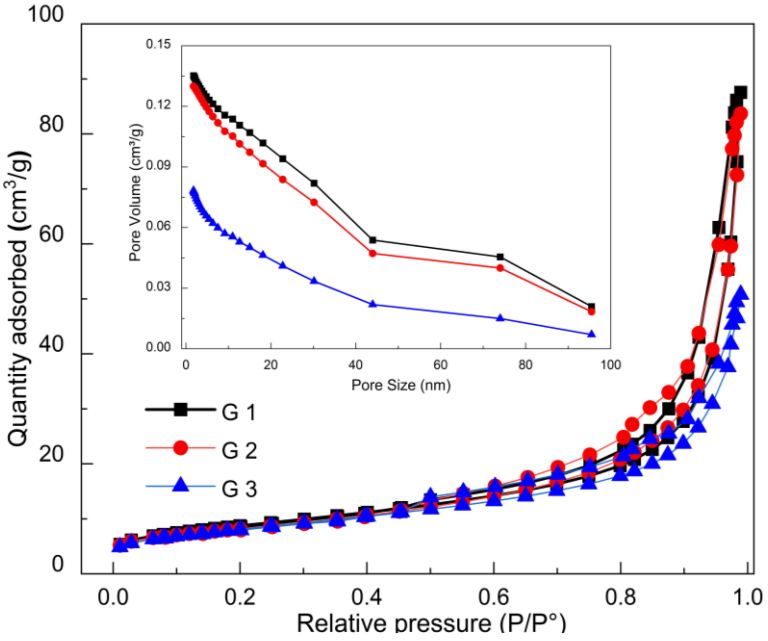

Fig. III.2. BET isotherm of prepared granules and their pore size.

Table III.2. BET/BJH parameters of prepared granules.

Samples	**G_0**	**G_1**	**G_2**	**G_3**
Average diameter d_0 (mm)	2.31	2.23 ± 0.1	2.20 ± 0.1	2.18 ± 0.1
Specific surface area (m^2/g)	22.94	30.86	29.81	28.75
Total pore volume (cm^3/g)	0.051	0.13	0.13	0.07
Mean pore diameter (nm)	9.09	17.37	16.77	10.53

Conversely, at higher H_2O_2 concentrations (samples G_2 and G_3), specifically at 7.5 and 10 wt%, the rapid hardening of the GP restricts pore formation, leading to reductions in both surface area and total pore volume, as evidenced by SEM micrographs and BET/BJH analysis. While the granules maintain a mesoporous structure (2–50 nm), the progressive decline in surface area with increased H_2O_2 concentration highlights the limitations of using this agent at higher levels.

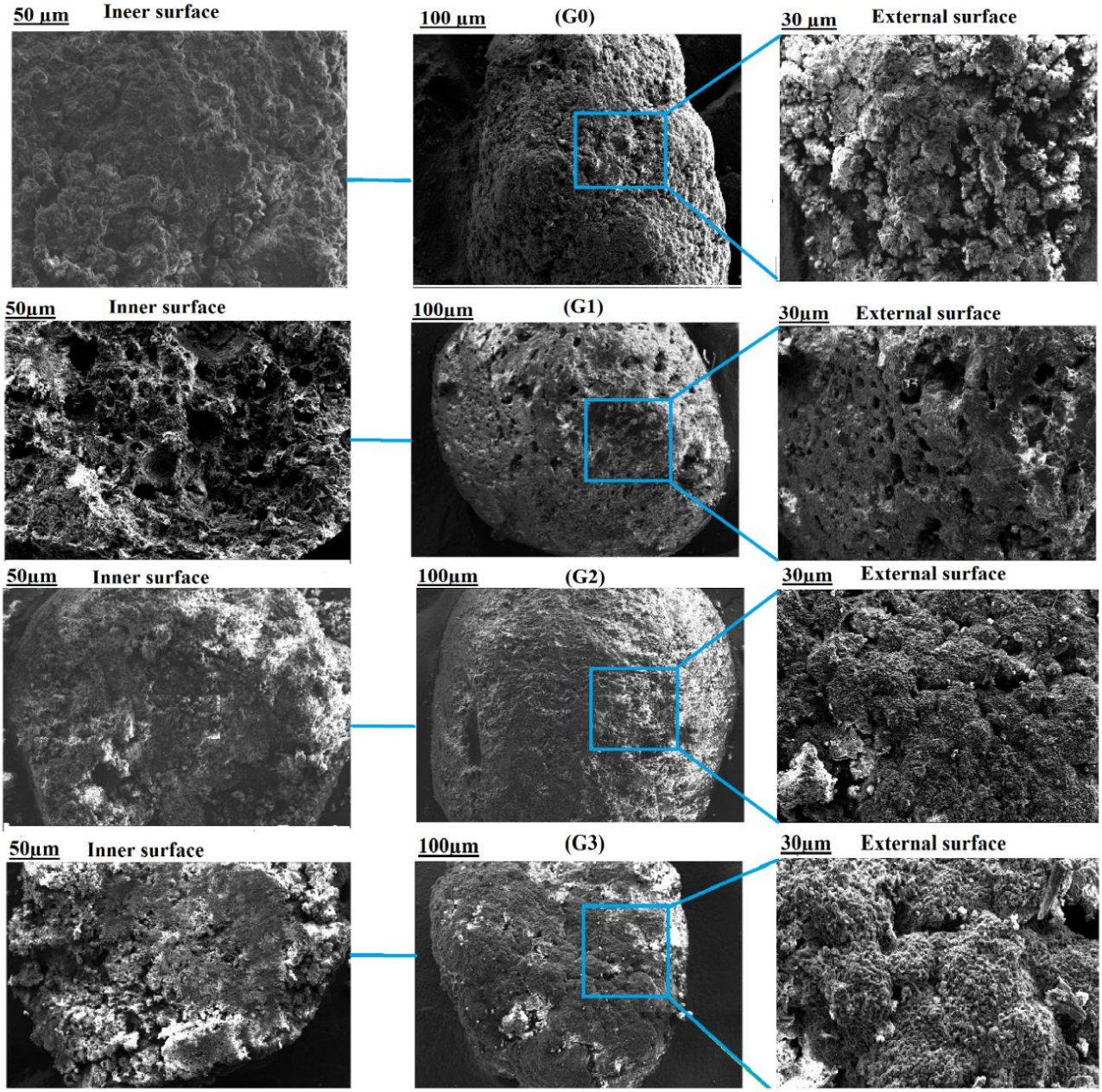

Fig. III.3. SEM image of external and internal surfaces of the prepared granules.

The results of the compressive strength tests depicted in **Table III.3**, reveal that granules with minimal porosity (G_0, G_2, and G_3) exhibit superior mechanical strength. However, this strength is counter balanced by reduced surface area, limiting their effectiveness in adsorption applications. Therefore, the limitations associated with H_2O_2, particularly its detrimental effects on chemical stability and structural integrity; suggest that alternative agents may be more suitable for optimizing granule properties. The use of alternative porogens and surfactants should be explored to balance porosity, mechanical strength, and adsorption efficiency effectively.

Table III.3. Mechanical properties of prepared granules.

Samples	**G_0**	**G_1**	**G_2**	**G_3**
(σ) (MPa)	0.85	0.76	0.77	0.79
Young´s modulus (MPa)	17.01	9.68	11.23	15.56

III.2.1.2. BG dye adsorption experiments

As seen in **Fig. III.4**, the evaluation of the adsorption efficiency highlights a significant performance improvement for the granules prepared in the presence of H_2 O_2 , compared to those obtained without pore-forming agent H_2O_2 (G_0), with G_1 showing the highest adsorption efficiency. This improvement is mainly attributed to its enhanced surface properties and porosity, as demonstrated by the BET/BJH and SEM results.

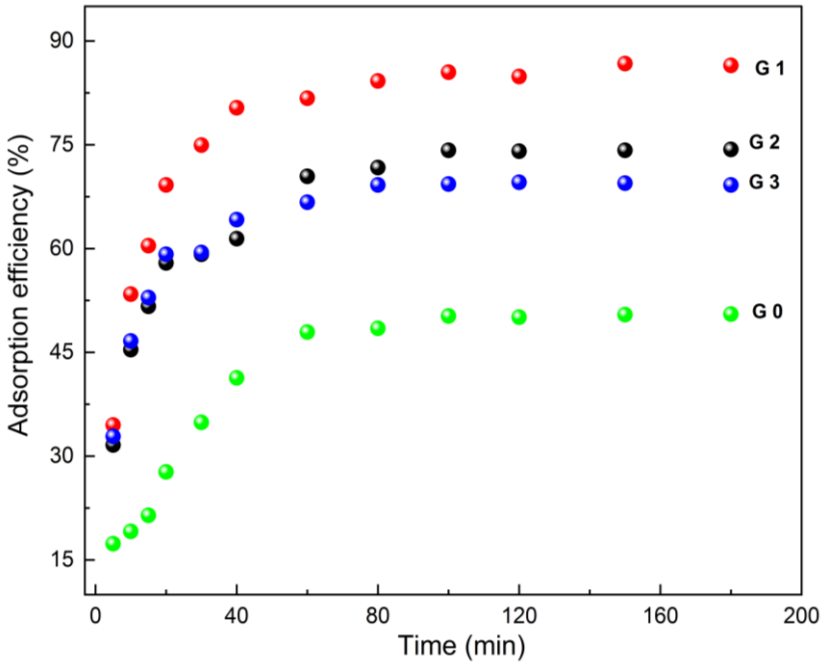

Fig. III.4 The adsorption efficiency of BG dye on the prepared granules.

The influence of several adsorption parameters, namely G_1 adsorbent dose (2 to 4 g/L), agitation speed (150 to 450 rpm), solution pH (3-9), and G_1 diameter (1 to 4 mm) was investigated under experimental conditions set at an initial BG dye concentration of15 mg/L, a temperature of 294 K and a contact time of 180 minutes. The results from this study, presented in **Fig. III.5a** and **Fig. III.5b,** highlight that the optimal dose of the adsorbent G_1 is 2 g/L, with an agitation speed of 250 rpm. This can be explained by the fact that increasing the adsorbent dose boosts adsorption efficiency by providing more available sites for adsorption. Additionally, at moderate agitation speeds (ranging from 150 to 250 rpm), the granules are subject to sufficient

turbulence, which improves mass transfer and adsorption by reducing the boundary layer around the particles. On the other hand, higher speeds (exceeding 350 rpm) introduce shear forces that can cause mechanical damage to the granules, leading to a decrease in their adsorption capacity.

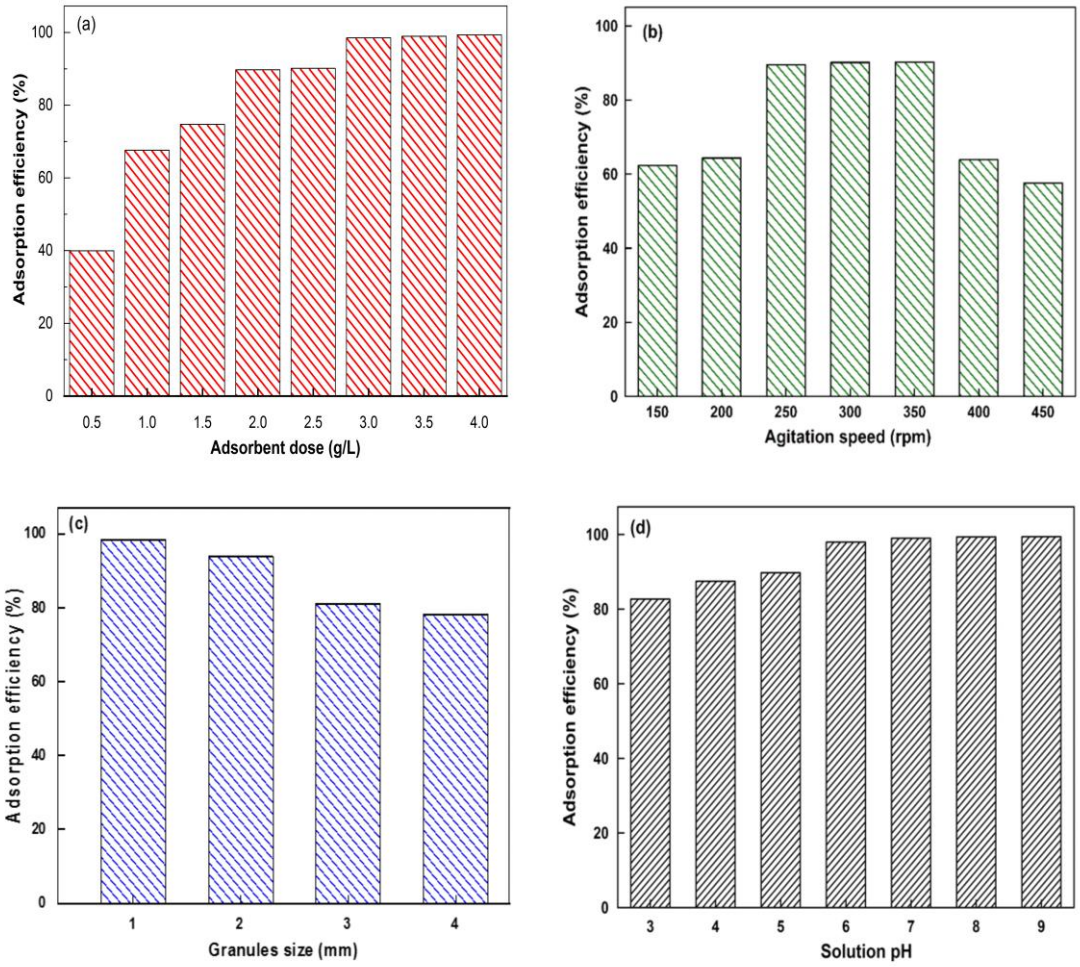

Fig. III.5. Effects of (a) G_1 adsorbent dose, (b) Agitation speed, (c) Granules diameter, and (d) pH of the solution on the adsorption efficiency of BG dye onto G_1.

According to **Fig. III.5c**, the increase in the diameter of the granules leads to a decrease in the adsorption efficiency of the BG dye, probably due to a reduction in both their specific surface area and porosity Consequently, granules with a diameter of 2 mm were selected for the subsequent experiments. Furthermore, **Fig. III.5d** indicates that the optimal pH for BG dye adsorption occurs at pH values greater than or equal to 7, corresponding to the granules' pH_{pzc}. This increased efficiency is attributed to the strengthening of the electrostatic interactions

between the $P-O^-$, $Si-O^-$, and $Al-O^-$ functional groups present on the surface of the granules and the $N-H^+$, groups of the BG dye, thus promoting its adsorption.

III.2.1.3. Kinetic, isotherm modeling, thermodynamic study of adsorption BG dye and proposed mechanism

This section presents the results of adsorption kinetics, isotherms, thermodynamic studies, and FTIR analysis for BG dye onto G_1 granules. Kinetic studies reveal the adsorption rate and mechanisms, while isotherm models describe equilibrium behavior. Thermodynamic analysis provides insights into the feasibility, spontaneity, and energy changes associated with the adsorption process. However, FTIR analysis identifies the functional groups involved and suggests the adsorption mechanism, providing further understanding of the efficiency and selectivity of the granules for dye removal.

The kinetic results presented in **Fig. III.6a and Fig. III.6b** indicate that the pseudo-second-order (PSO) model (R^2 value of 0.99) provided a better fit to the experimental data than the pseudo-first-order model. Furthermore, the isotherm analysis (**Fig. III.7)** shows that the Langmuir model best describes the adsorption of BG dye onto G_1 granules, suggesting a homogeneous adsorbent surface, characterized by equivalent active sites, each capable of adsorbing a single BG molecule. This behavior implies monolayer adsorption without significant interaction between molecules adsorbed on adjacent sites.

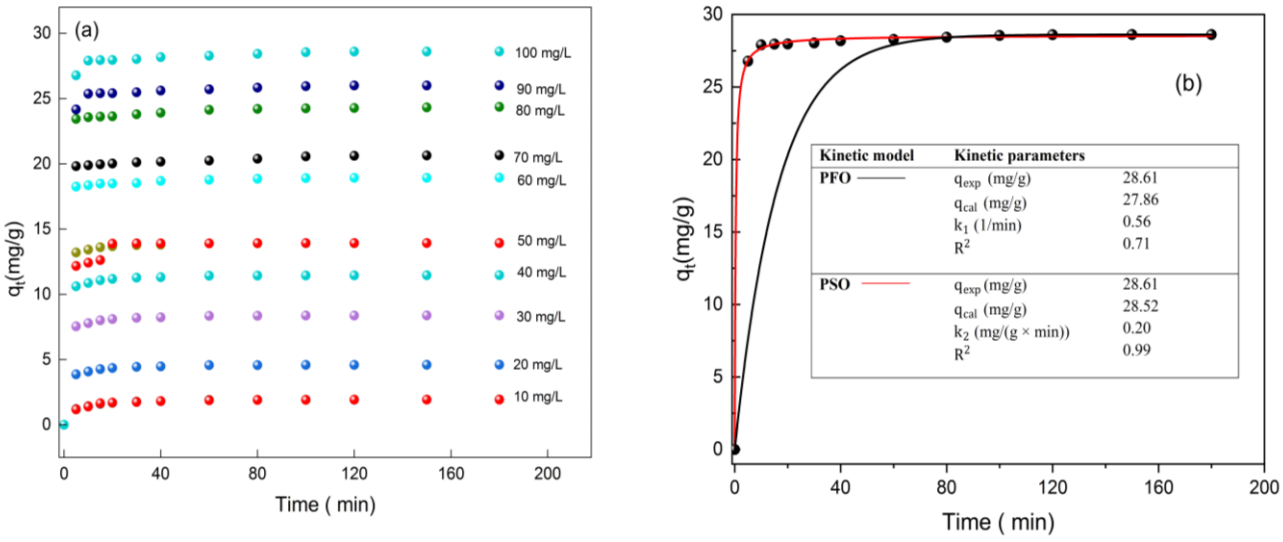

Fig. III.6. (a) Effect of BG dye concentration on its adsorption efficiency onto G_1 granules. (b) Kinetic data fitting for BG adsorption. Conditions: G_1 adsorbent dose = 3 g/L, pH = 7, time = 180 minutes, G_1 diameter = 2 mm, agitation speed = 250 rpm, and T = 298 K.

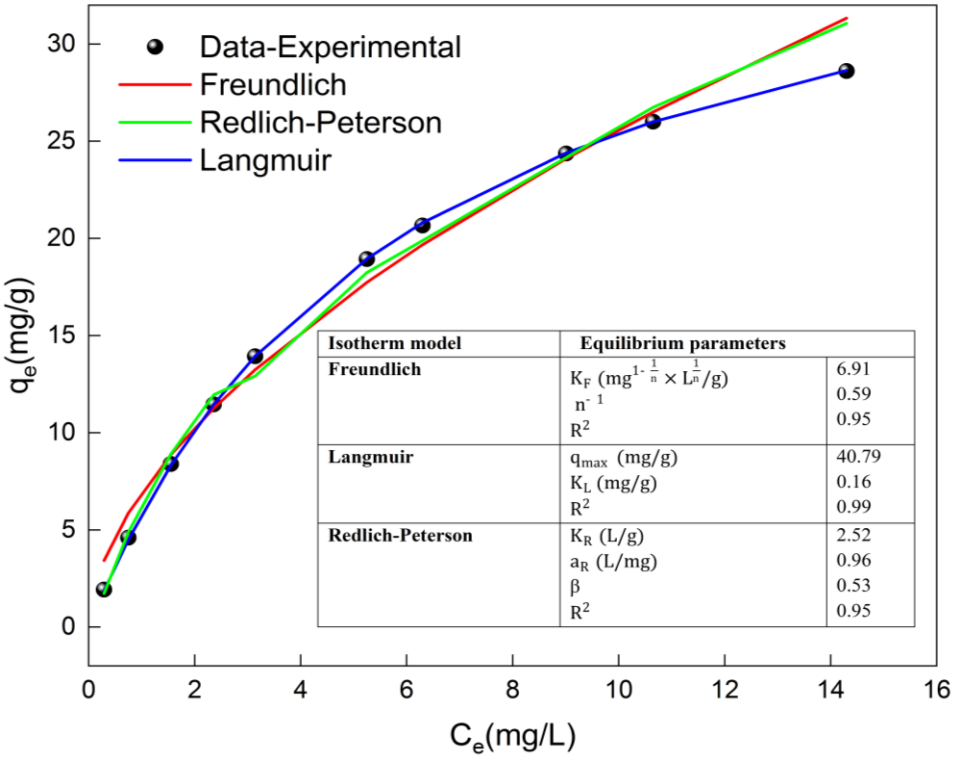

Fig. III.7. Isotherm models fitting to the experimental adsorption data of BG onto G_1 granules. Conditions: G_1 dose = 3 g/L, pH = 7, time = 180 minutes, granule diameter = 2 mm, agitation speed = 250 rpm, and T = 298 K.

Fig.III.8 illustrates the impact of temperature on the BG dye adsorption process onto G_1 under the optimized conditions. As the temperature increased, the adsorption rate became faster. Additionally, the rate constant (k_2) significantly increased at higher temperatures, which can be attributed to the higher kinetic energy of the molecules. This boost in energy led to more effective collisions between the BG dye and the G_1 granule surface, thereby accelerating the adsorption process. Moreover, the thermodynamic parameters listed in **Table III.4** indicate that the BG dye adsorption process is spontaneous, physisorption process and endothermic, with an optimal temperature of 298 K.

Table III.4. Thermodynamic parameters of the BG adsorption onto G_1 granules.

T(K)	ΔG° (kJ/ mol)	ΔH° (kJ/mol)	ΔS° (J/(mol×K))	E_a (J/mol)
298	-3.96	6.76	27.62	27196.0
308	-4.38			
318	-4.57			
328	-5.03			
338	-5.45			

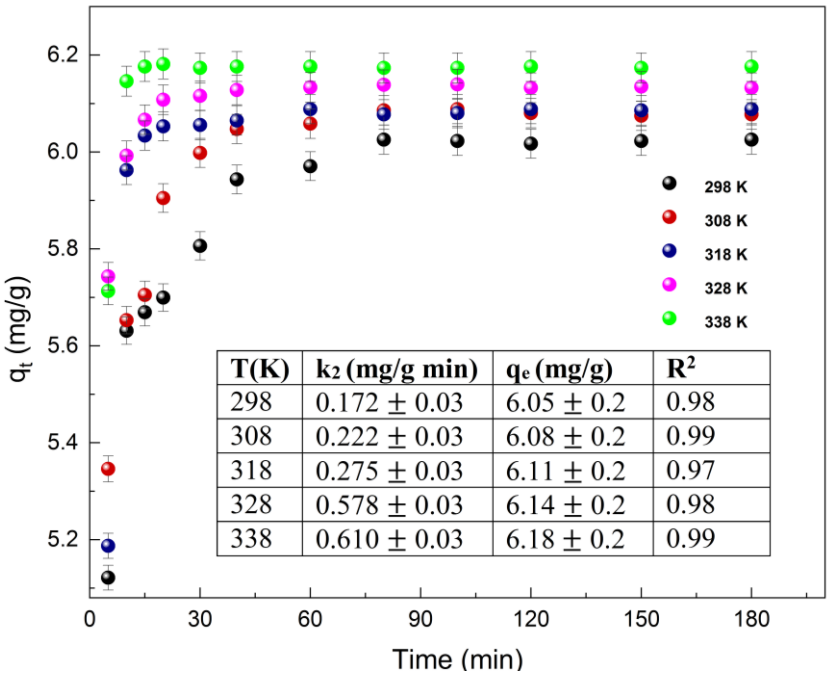

T(K)	k_2 (mg/g min)	q_e (mg/g)	R^2
298	0.172 ± 0.03	6.05 ± 0.2	0.98
308	0.222 ± 0.03	6.08 ± 0.2	0.99
318	0.275 ± 0.03	6.11 ± 0.2	0.97
328	0.578 ± 0.03	6.14 ± 0.2	0.98
338	0.610 ± 0.03	6.18 ± 0.2	0.99

Fig. III.8. Effect of temperature on the adsorption of BG onto G_1. Conditions: $[BG]_0$= 20 mg/L and optimal condition determined below.

The FTIR spectra depicted in **Fig. III.9** reveal changes in the adsorption bands of G_1 granules after BG dye adsorption. The slight shifts in the P-O bands from 1440 to 1490 cm^{-1}, 1204 to 1233 cm^{-1}, and 1028 to 992 cm^{-1}, can be attributed to electrostatic interactions between the PO_4^{-3} groups and the N-H groups of the BG dye. Additionally, the decrease in intensity of the O-H groups at 3262 cm^{-1} is likely due to interactions between the O-H group and the N-H groups, resulting in the formation of hydrogen bonds. Furthermore, the Al-O band in tetrahedral $[AlO_4]^-$ sites may interact electrostatically with the N-H groups. New bands that appeared at 1414 cm^{-1} and 625 cm^{-1} after adsorption may be linked to the C-H and C-N stretching vibrations within the aromatic structure of the BG dye (Baidya & Kumar., 2020).

Based on SEM and BET/BJH results (**Fig. III.2** and **Table III.2**), G_1 exhibits a porous, mesoporous structure that facilitates the mass transfer of the BG dye from the bulk solution into the mesopores. Within the mesopores, the pore filling mechanism plays a significant role in the adsorption of the BG dye. The proposed mechanism is illustrated in **Fig.III.10**.

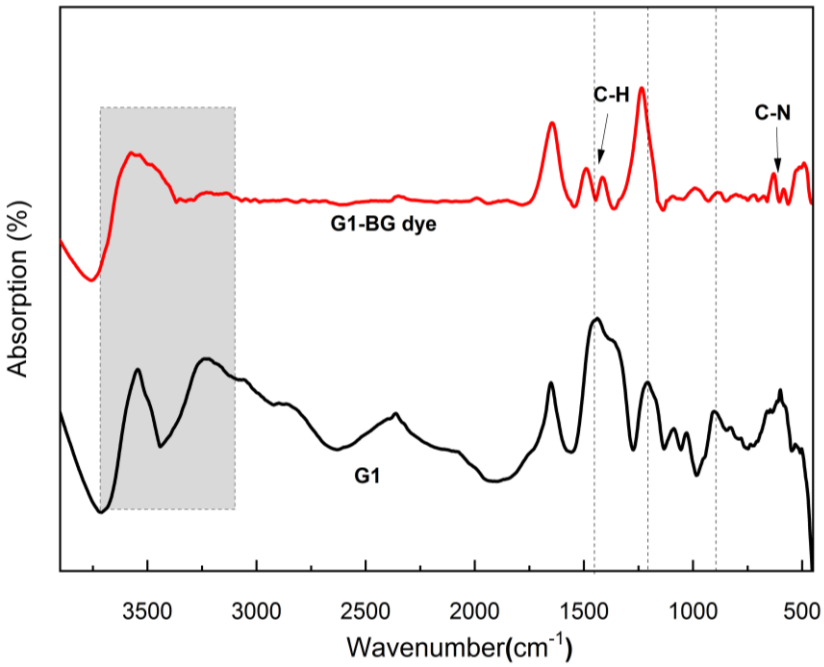

Fig. III.9. FTIR spectra of G_1 granules before and after adsorption BG dye.

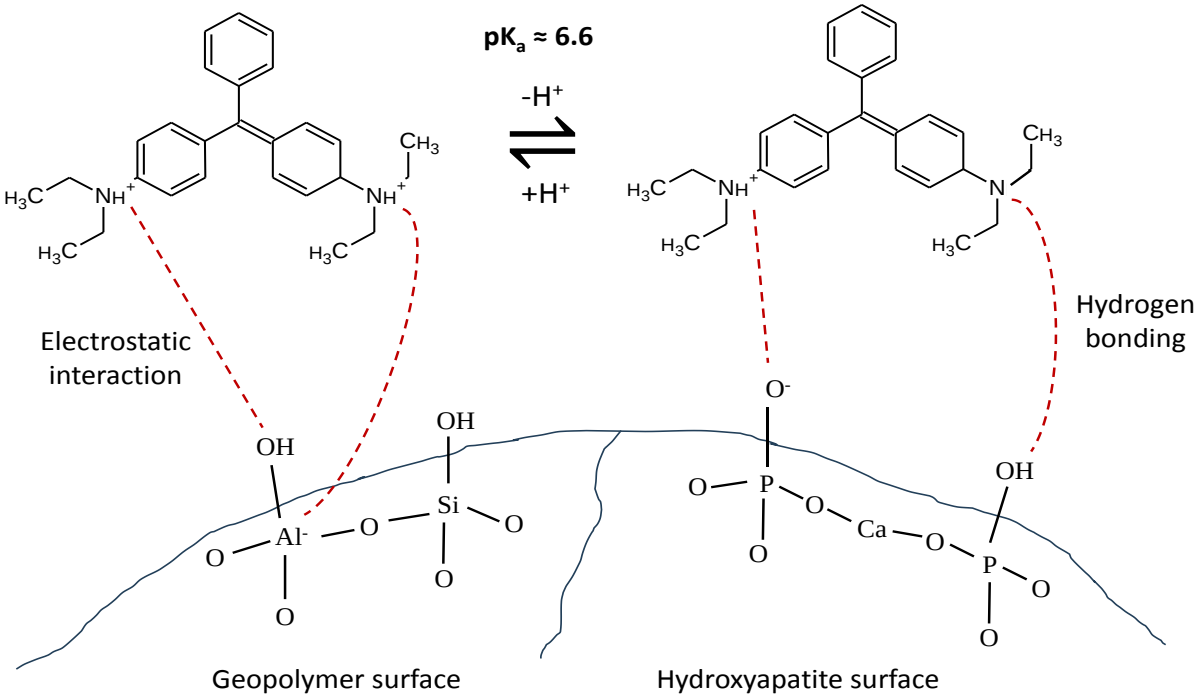

Fig. III.10. Proposed BG dye adsorption mechanism onto G_1 granules.

III.2.1.4. Critical review of use HAP-MK-GP granules elaborated using H_2O_2 as adsorbent

Publication I highlights the promising performance of HAP-MK-GP granules as an adsorbent, demonstrating a maximum adsorption capacity of 41 mg/g for dye removal. This capacity was achieved under optimal conditions of pH 7, an initial BG dye concentration of 100 mg/L, an adsorbent dose of 3 g/L, an agitation speed of 250 rpm, a contact time of 30 minutes, and a temperature of 298 K. Compared to other adsorbents listed in **Table III.5**, such as Areca nut husk (18.21 mg/g) (Baidya and Kumar, 2020) and ZSM-5/CuF/CE NC (9.66 mg/g) (Katowah and Alzahrani, 2023), HAP-MK-GP granules exhibit superior adsorption capacity. This enhanced performance can be attributed to its well-optimized structural and compositional characteristics, suggesting its potential for more effective and efficient dye removal.

Although modified MOF-5 (Dahlan et al., 2024) shows a higher adsorption capacity of 30.22 mg/g, its efficiency is limited to more stringent operating conditions. On the other hand, Fe_3O_4-activated carbon (Singh et al., 2023) with a remarkable adsorption capacity of 773 mg/g, UTP (Vithalkar et al., 2022) reaching 101.01 mg/g and HAP-CS (Ragab et al., 2019) displaying 49.1 mg/g, exhibit notable performance. Nevertheless, the HAP-MK-GP stands out for its optimal compromise between efficiency and less restrictive operating conditions. Its granule form, characterized by high porosity and promising mechanical properties (compressive strength of 0.8 MPa and Young's modulus of 10 MPa), potentially makes it suitable for large-scale adsorption columns. This is in contrast to powder-based adsorbents, which often face practical challenges such as difficult separation from water and regeneration issues.

In industrial applications, granular or fibrous adsorbents are preferred over powders due to these practical difficulties. HAP-MK-GP's advantage lies in its effective performance combined with a relatively simple and cost-effective preparation method. Its substantial adsorption capacity at moderate pH and concentration levels makes it suitable for practical and scalable applications. Additionally, the use of MK-GP as a reactive binder enhances cost-efficiency and sustainability, aligning with the industry's need for economically viable and environmentally friendly solutions. Therefore, HAP-MK-GP granules represents a compelling option for industrial dye removal, offering competitive adsorption capacity and practical preparation processes while overcoming some of the limitations associated with other adsorbents.

Table III.5. Comparison of HAP-MK-GP granules with other adsorbents for BG dye removal.

Adsorbent	Type	q_{max} (mg/g)	Adsorption conditions	Reference
HAP-MK-GP	Granules	41	pH = 7,$[BG]_0$ = 100 mg/L, adsorbent dose = 3 g/L, agitation speed = 250 rpm, time = 30 minutes, and T = 298 K.	**Publication I**
Areca nut husk	Powder	18.21	pH of 7, adsorbent dose = 10 g/L, $[BG]_0$ = 100 mg/L, agitation speed = 200 rpm, and T = 298 K.	Baidya and Kumar, 2020
ZSM-5/CuF/CE NC	Powder	9.66	pH = 8, adsorbent dose = 1 g/L, $[BG]_0$ = 200 mg/L, time = 120 minutes and T= 298K.	Katowah and Alzahrani, 2023
Modified MOF-5	Powder	30.22	pH = 5 , adsorbent dose = 1.4 g/L, $[BG]_0$ = 20 mg/L**,** gitation speed of 200 rpm and time = 120 minutes.	Dahlan et al., 2024
Fe_3O_4-activated carbon	Powder	773	pH of 8, adsorbent dose = 0.5 g/L, $[BG]_0$ = 400 mg/L and time = 120 minutes.	Singh et al., (2023
UTP	Powder	101.01	pH = 6, adsorbent dose = 0.1 g/L, $[BG]_0$ = 100 mg/L and time = 60 minutes.	Vithalkar et al., 2022
HAP-CS	Powder	49.1	pH = 7, adsorbent dose = 0.9 g/L, $[BG]_0$ =80 mg/L, time = 60 minutes, T = 298 K.	Ragab et al., 2019
AGSC	Powder	80.50	pH = 9, AGSC dose of 0.8 g/L, $[BG]_0$ = 100 mg/L, time = 30 minutes and T= 298 K.	Mansour et al., 2020
CTAB-$NiFe_2O_4$	Powder	250	pH = 6, adsorbent dose = 0.6 g/L and time = 170 minutes.	Jsrotia et al., 2022

ZSM-5/CuF/CE NC = nanocomposites-based cellulose derivatives-$CuFe_2O_4$-zeolite, MOF-5 = metal-organic frameworks, UTP= used-tea-powder, HAP-CS= Hydroxyapatite/Chitosan composite, AGSC= activated carbon derived from guava seeds

III.2.2. Critical review of Publication II. Preparation of porous hydroxyapatite–metakaolin geopolymer granules for adsorption applications using polyethylene glycol as porogen agent and sodium dodecyl sulfate as anionic surfactant

The study focuses on advancements achieved in the development of HAP-MK-GP granules, incorporating polyethylene glycol (PEG) as a porogen agent and sodium dodecyl sulfate (SDS) as an anionic surfactant. This approach not only preserves the chemical functional groups of HAP-MK-GP granules but also significantly improves surface area, porosity, and adsorption potential, without sacrificing mechanical strength. Taken together, these properties enabled the granules to have a high adsorption efficiency for the CV and MB dyes in single and binary aqueous solutions. Moreover, this research also evaluates the granules' regeneration potential, demonstrating that they can be reused for up to eight cycles without significant loss in adsorption capacity or structural degradation. These results suggest that the porous granules developed in this study have significant potential for industrial wastewater treatment applications.

III.2.2.1. Critical review of chemical functional characterization of HAP-MK-GP granules using PEG and SDS as a porogen agent and an anionic surfactant, respectively

This investigation examines the effect of polyethylene glycol (PEG) as a pyrogenic agent, used alone or in synergy with sodium dodecyl sulfate (SDS), in solid (S) or dissolved (L) form, in the formulation of HAP-MK-GP granules (G_0). The use of polyethylene glycol (PEG) as a porogen agent and sodium dodecyl sulfate (SDS) as an anionic surfactant in **Publication II** represents a significant advancement over the H_2O_2-based methods described in **Publication I**. PEG and SDS collectively address the challenges posed by H_2O_2, particularly the dissolution of calcium and phosphate ions, which compromises the chemical and structural integrity of HAP-MK-GP granules. By employing PEG, which induces porosity without altering the chemical functional groups of HAP or MK-GP, this method ensures better preservation of the material's chemical composition, as validated by XRF (**Table III.6**) and FTIR analyses (**Fig. III.11**). Furthermore, the addition of SDS introduces a dual functionality: it not only promotes porosity but also enhances pollutant removal, thanks to its hydrophilic and hydrophobic groups, which interact effectively with organic compounds and cationic pollutants.

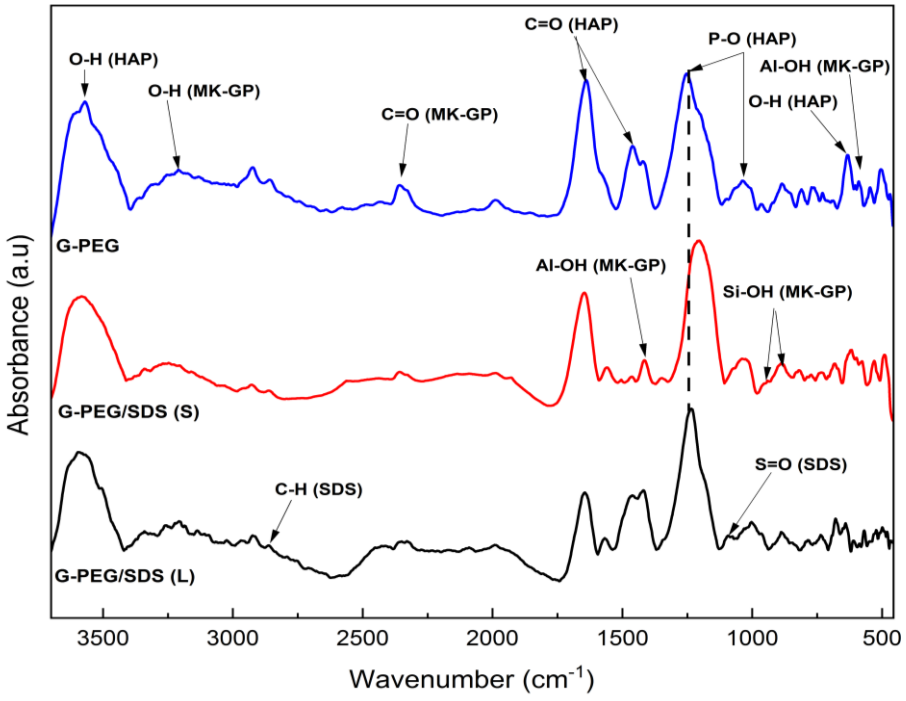

Fig. III.11. FTIR spectrum prepared granules (i.e., G-PEG, G-PEG/SDS(S) and G-PEG/SDS (L)).

Table III.6. XRF results of HAP, MK and prepared granules; G-PEG and G-PEG/SDS(S/L) granules.

Element (%)	G-PEG	G-PEG/SDS (S)	G-PEG/SDS (L)
CaO	21.08	20.65	20.10
P_2O_5	15.66	13.20	14.96
Al_2O_3	13.44	12.45	12.98
Si_2O_2	33.00	33.01	34.78
Na_2O	6.44	6.65	6.54

A critical aspect of this approach lies in the form of sodium dodecyl sulfate (SDS) used during granule synthesis. The study reveals that using SDS in its solid powder form (S) leads to a noticeable shift in the PO_4^{-3} stretching vibrations within HAP as demonstrated by FTIR (**Fig. III. 11**), indicating some degree of chemical interaction. This interaction is associated with a slight reduction in phosphorus content, as evidenced by XRF analysis (**Table III.6**). Conversely, dissolving SDS into the granulation fluid as a liquid may better preserve the structural integrity of the granules. This observation underscores the importance of optimizing SDS application, whether in solid or liquid form, to achieve an effective balance between enhancing porosity and maintaining chemical stability. Proper optimization of SDS usage is essential to maximize the benefits of porosity while mitigating potential adverse effects on the material's structural properties.

Structural analyses using SEM (**Fig. III.12**) and BET (**Fig. III.13**) methods substantiate the effectiveness of employing sodium dodecyl sulfate (SDS) in its liquid form (SDS-L). Granules prepared with SDS-L exhibit a substantial increase in surface area, ranging from 16 to 45% **(Table III.7),** compared to those prepared with SDS in its solid form (SDS-S), as well as to granules prepared without SDS or polyethylene glycol (PEG) (G_0) from **Publication I**. This improvement is evidenced by the mesoporous structure of the granules, confirmed by type IV isotherms and H3 hysteresis loops.

Table III.7. BET/BJH data of HAP, MK, and the prepared G-PEG and G-PEG/SDS(S/L) granules.

Granules	G-PEG	G-PEG/SDS (S)	G-PEG/SDS (L)	HAP	MK
Average diameter d_0 (mm)	4.2 ± 0.1	4.1 ± 0.1	4.2 ± 0.1	-	-
Specific surface area (m^2/g)	73.08	85.25	97.89	31.20	10.74
Total pore volume (cm^3/g)	0.30	0.33	0.32	0.065	0.05
Mean pore diameter (nm)	16.79	15.89	13.27	11.82	21.82

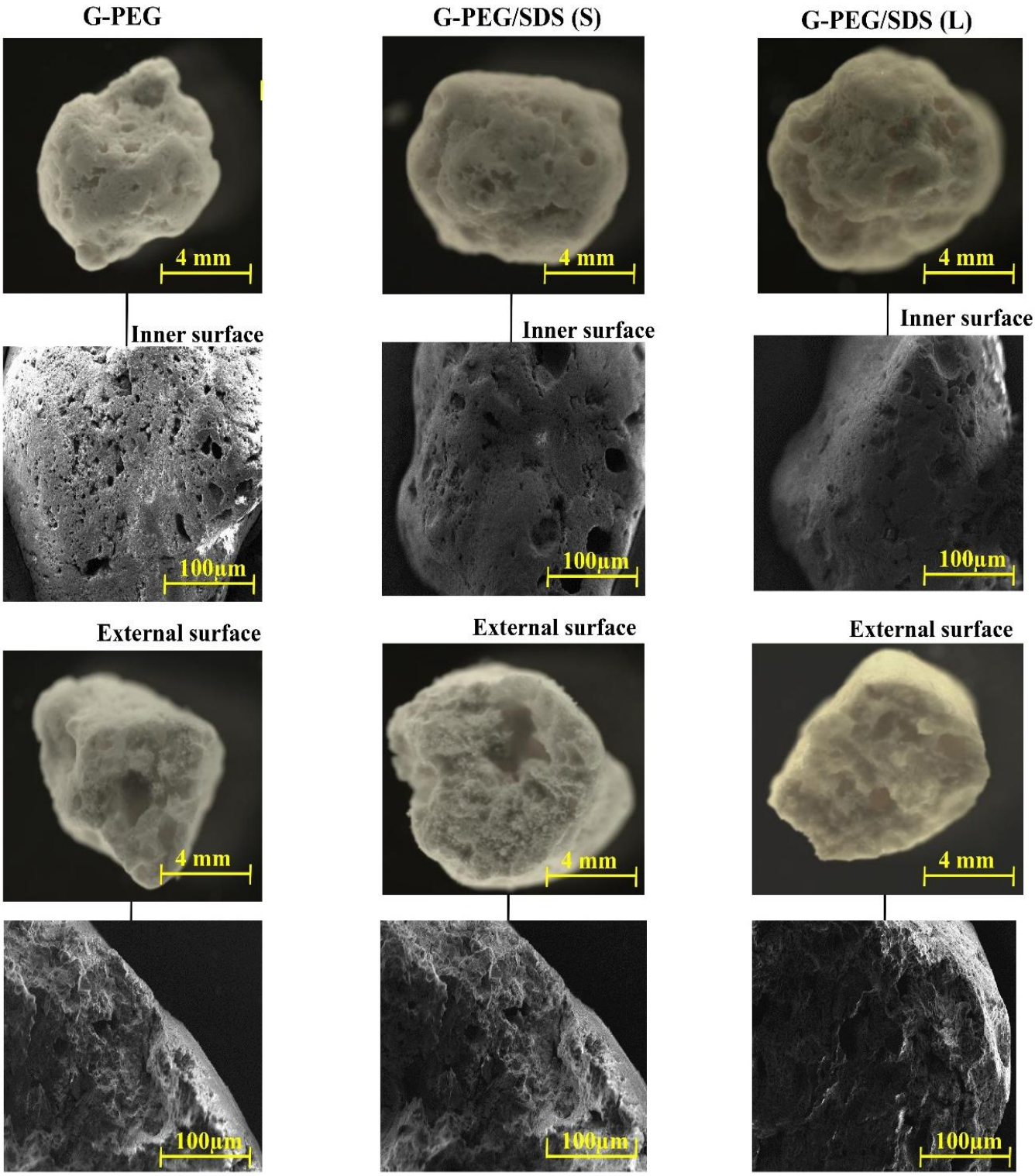

Fig. III.12. SEM and optical microscope photographs of G-PEG and G-PEG/SDS(S/L) granules.

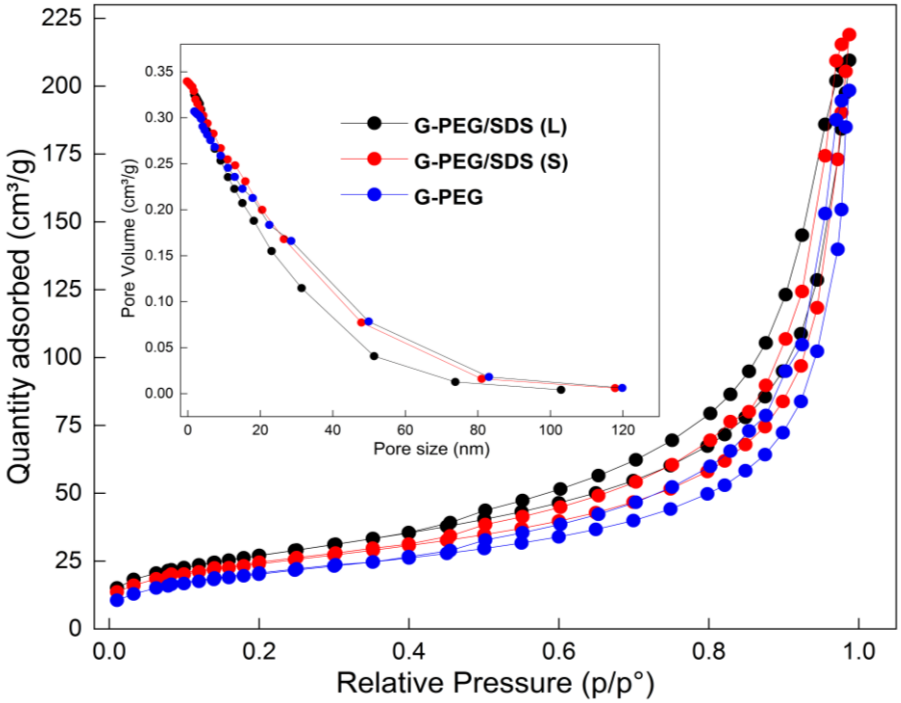

Fig. III.13. BET isotherm of prepared G-PEG and G-PEG/SDS(S/L) granules and their pore size.

Despite a slight reduction in mechanical strength associated with the use of SDS (**Table III.8**), the method strikes a favorable balance between maintaining structural integrity and enhancing adsorption capacity. Compressive strength tests confirm that while SDS-L slightly diminishes the granules' strength, the increased surface area substantially boosts their adsorption potential. The combination of PEG and SDS-L offers a more controlled and effective approach for optimizing both porosity and functional performance of HAP-MK-GP granules, overcoming the limitations H_2O_2 based methods and presenting an improved solution for applications demanding enhanced surface area and adsorption efficiency.

Table III.8. Mechanical parameters of HAP, MK, and the prepared G-PEG and G-PEG/SDS(S/L) granules.

Granules	**G-PEG**	**G-PEG/SDS (S)**	**G-PEG/SDS (L)**	**HAP**	**MK**
Compressive strength (σ) (MPa)	0.91 ± 0.2	0.85 ± 0.4	0.81 ± 0.1	-	-
Young´s modulus (MPa)	16.69 ± 0.3	15.23 ± 0.2	15.08 ± 0.4	-	-

The thermal behavior and decomposition processes of the elaborated granules were analyzed using TGA/DSC (**Fig.III.14**) techniques. The results revealed that incorporating SDS into G-PEG granules, both in solid and liquid forms, led to an increased decomposition rate of the granules. This was primarily due to the loss of the long alkyl chain from the SDS molecules at temperature range [300-350°C] (Lun et al., 2014). Based on these observations, the study recommends utilizing chemical methods to regenerate G-PEG/SDS granules in order to preserve the integrity of SDS and prevent its degradation. These findings are crucial for improving the reliability and performance of the granules in industrial applications, particularly within regeneration strategies. This approach could help optimize the functionality of the granules and extend their lifespan in practical uses.

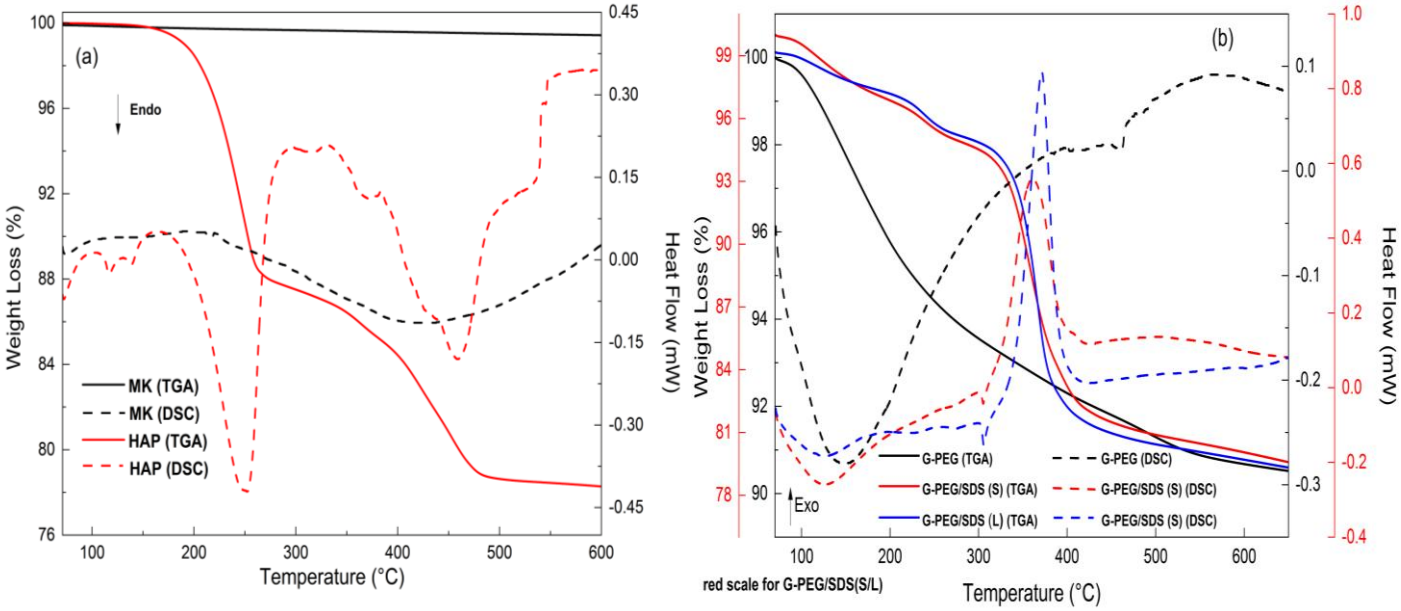

Fig. III.14.TGA and DSC of (a) raw material and (b) prepared granules; G-PEG, G-PEG/SDS (S/L).

III.2.2.2. Adsorption of MB and CV onto HAP-MK-GP/SDS (L) granules: Optimization and selectivity analysis

The results of the batch adsorption experiments using HAP, MK-GP, and the prepared granules are presented in **Fig. III.15**. HAP demonstrated very low affinity for adsorption of organic pollutants (MB and CV dyes), while MK-GP exhibited higher adsorption capacity. Introducing HAP into MK-GP to form G-PEG granules led to a decrease in it adsorption efficiency. This decline is likely due to the reduced MK-GP content in the granules, which resulted in fewer

active sites available for adsorbing MB and CV dyes. On the other hand, incorporating SDS into the G-PEG granules, whether in solid or liquid form, significantly enhanced their adsorption capacity for both MB and CV, with G-PEG/SDS (L) showing the highest adsorption performance. Due this, it was selected for the next of the adsorption experiments.

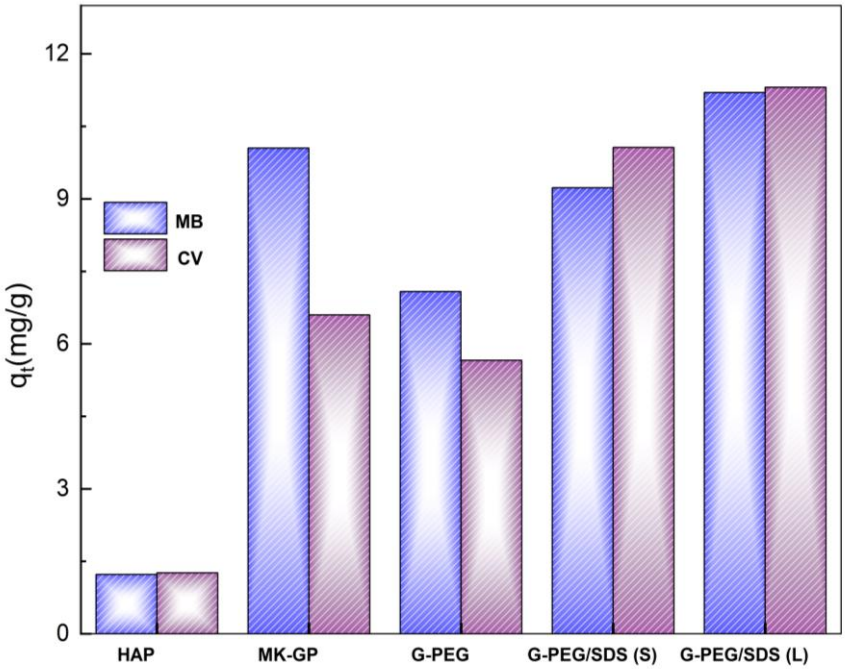

Fig. III.15. Adsorption capacity of HAP, MK-GP, and elaborated granules for MB and CV dyes. Conditions: $[dye]_0$ = 25 mg/L, adsorbed dose = 2g/L, granules diameter = 4 mm, agitation speed = 250 rpm, time = 90 minutes, and T = 298 K.

The optimization results for the adsorption parameters of MB and CV dye, considering the effects of solution pH and granule dose, are presented in **Fig. III.16**. The findings indicate that the optimal G-PEG/SDS(L) dose is 2.5 g/L, and the ideal solution pH is 8. This is consistent with the pH_{pzc}= 7.23 (**Fig. III.16c**), which suggests enhanced electrostatic attraction between the negatively charged groups on the surface of G-PEG/SDS(L) granules and the positively charged N-H groups in the MB and CV molecules.

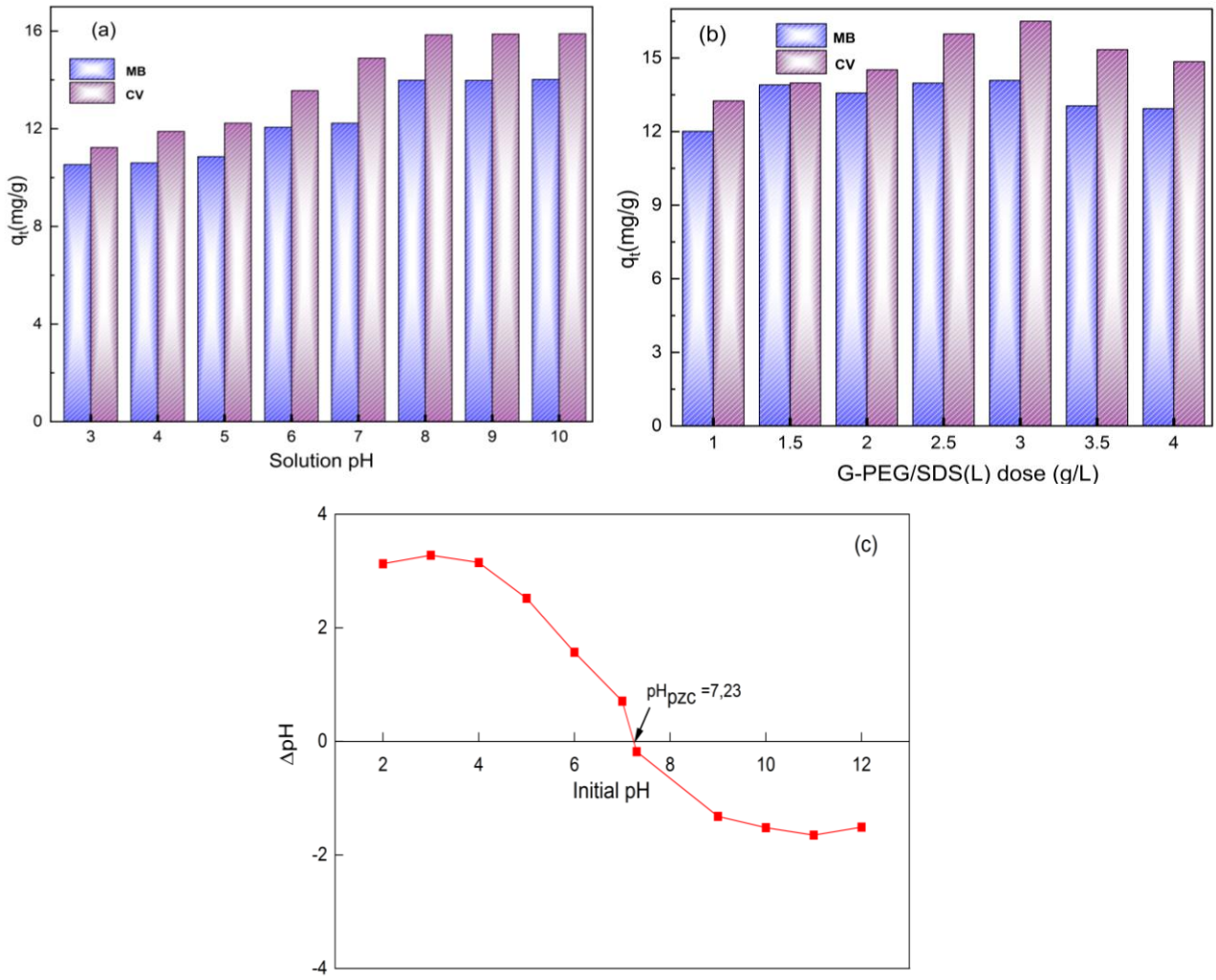

Fig. III.16. (a) and (b) Optimization the adsorption parameters under conditions $[dye]_0$ = 50 mg/L, granules diameter = 4 mm, agitation speed = 250 rpm, time = 90 minutes, and T = 298 K, and (c) pH_{pzc} of G-PEG/SDS(L)

Fig. III.17a illustrates the effect MB and CV concentration on their adsorption capacity by G-PEG/SDS(L) granules, while **Fig. III.17b** presents the adsorption selectivity of these granules in MB/CV binary solutions at different concentrations. As seen, the results indicate that the adsorption capacity for both dyes increased with higher initial concentrations. Below 50 mg/L, the granules exhibited similar selectivity for both dyes, as they had the same diffusion coefficients (**Table III.9**). However, above 50 mg/L, the diffusion coefficient of CV decreases relative to MB, making it more difficult for MB molecules to reach the granule surface, resulting in a higher selectivity for CV adsorption in the binary mixture.

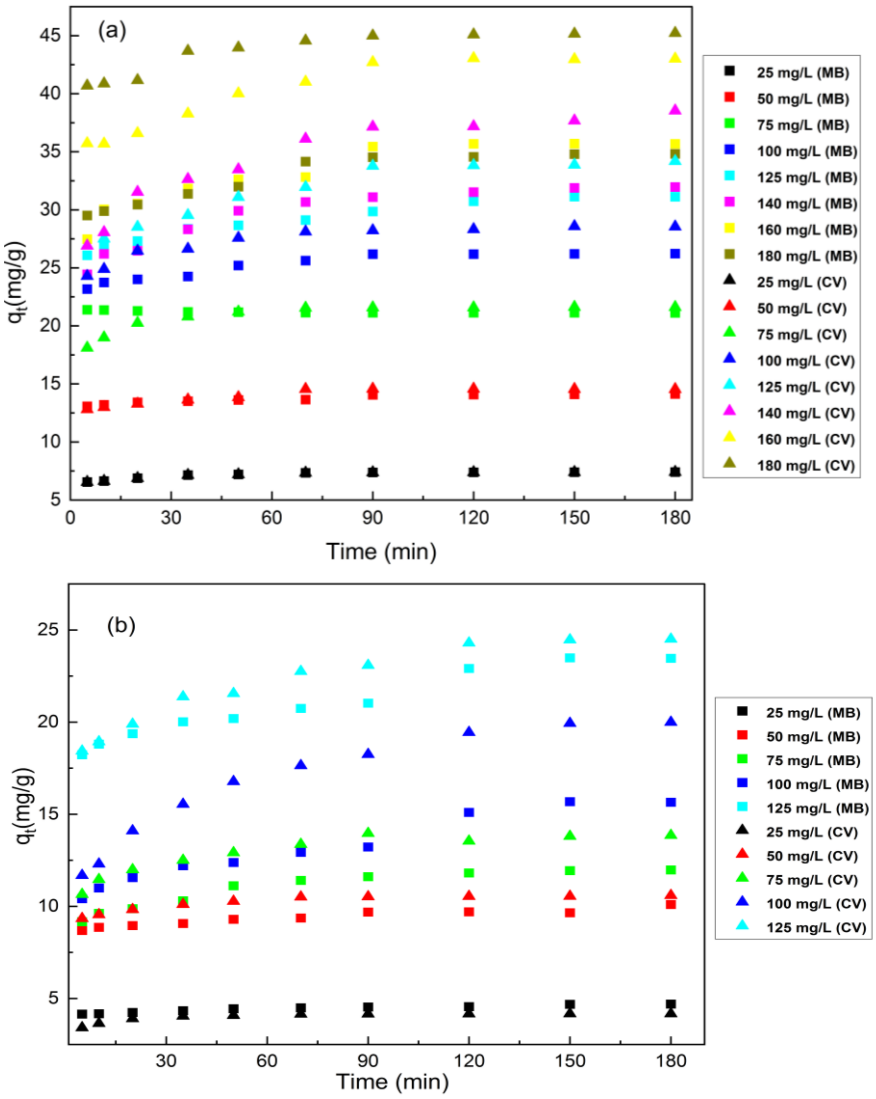

Fig. III.17. Effect of initial concentration dyes on the adsorption amount onto G-PEG/SDS (L) granules. (a) single dye system and (b) binary dye mixture following the optimal Conditions.

Table III.9. Fitting of the HPDM model to the adsorption data of G-PEG/SDS (L) granules with different concentration of MB and CV dyes in binary mixtures.

[MB] (mg/L)	**Particule diffusion**	D_p (m^2/s)	**Film diffusion**	D_f (m^2/s)
25	0.034t+0.090, R^2 =0.99	5.51×10^{-10}	0.015t+0.192, R^2 = 0.98	5.21×10^{-11}
50	0.012t+0.072, R^2 = 0.98	1.94×10^{-10}	0.024t+0.231, R^2 =0.99	8.96×10^{-11}
75	0.061t+0.043, R^2 = 0.97	9.89×10^{-10}	0.012t+0.051, R^2 = 0.98	4.97×10^{-11}
100	0.023t+0.063, R^2 = 0.98	3.73×10^{-10}	0.042t+0.037, R^2 = 0.97	5.53×10^{-10}
125	0.018t+0.075, R^2 = 0.95	2.92×10^{-10}	0.053t+0.156, R^2 = 0.96	2.34×10^{-10}
[CV] (mg/L)				
25	0.001t+0.058, R^2 = 0.93	1.62×10^{-13}	0.001t+0.031, R^2 = 0.97	5.01×10^{-11}
50	0.002t+0.062, R^2 = 0.99	3.24×10^{-13}	0.015t+0.090, R^2 = 0.96	7.2×10^{-11}
75	0.006t +0.071, R^2 =0.92	9.73×10^{-13}	0.091t+0.054, R^2 = 0.98	4.65×10^{-11}
100	0.001t-0.043, R^2 =0.93	1.78×10^{-13}	0.060t+0.025, R^2 = 0.95	2.4×10^{-11}
125	0.001t+0.095, R^2 = 0.90	1.62×10^{-13}	0.034t+0.084, R^2 = 0.95	1.37×10^{-11}

III.2.2.3. Adsorption Kinetics and Isotherms of MB and CV onto G-PEG/SDS(L) Granules and Proposed Mechanism

Fig. III.17 and **Table III.10** show that the adsorption of MB and CV dyes, either individually or in a binary mixture, follows the PFO kinetic model and Langmuir and Redlich–Peterson isotherms. These findings indicate that the surface of the G-PEG/SDS(L) granules is homogeneous, with all sites being equivalent. Each site can hold at most one cationic dye molecule, suggesting monolayer coverage and no interactions between adsorbate molecules on adjacent sites.

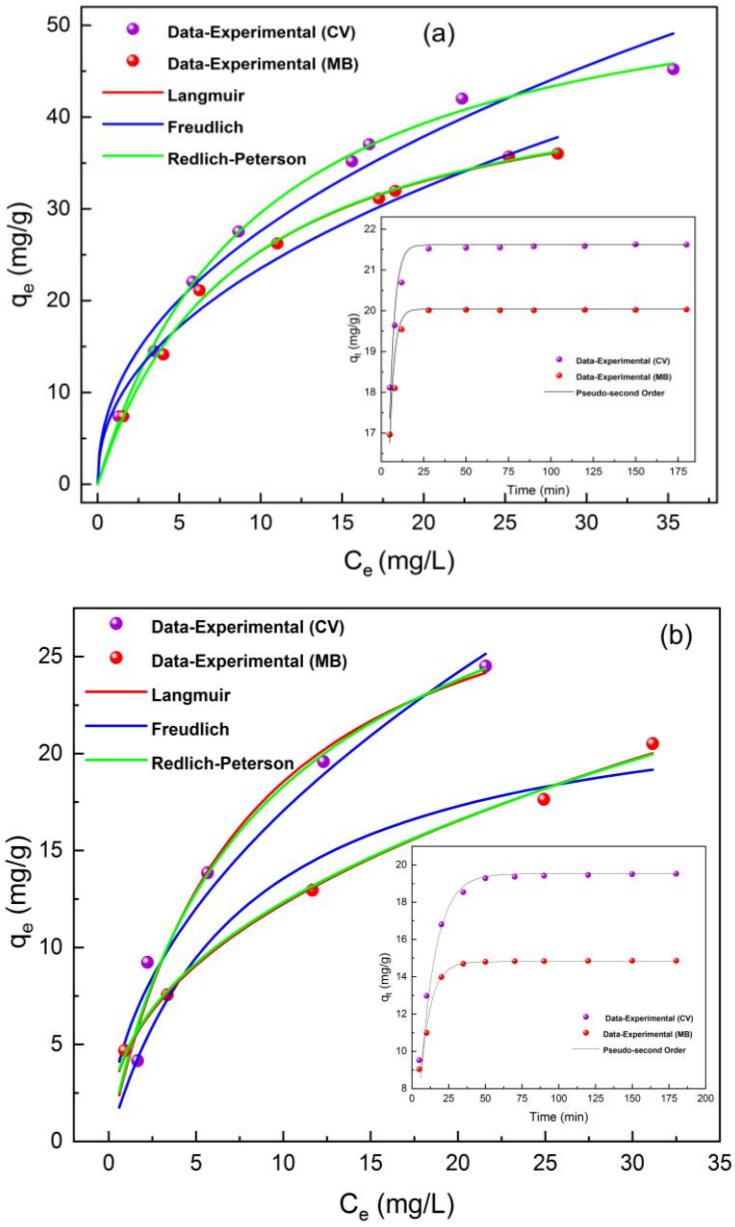

Fig. III.17. Isotherm and kinetic models fitting to experimental data for MB and CV dyes (a) individually in aqueous solution and (b) in binary mixture, following the optimal conditions.

Table III.10. Kinetic and isotherm parameters for MB and CV dyes individually and in binary mixtures, following the optimal conditions.

Kinetic model	**Kinetic parameters**				
		MB	**MB/CV**	**CV**	**CV/MB**
Pseudo-first-order	q_{exp} (mg/g)	20.083	14.879	21.612	20.596
	q_{cal} (mg/g)	19.683	14.135	21.160	28.669
	k_1 (min^{-1})	0.373	0.162	0.350	0.116
	R^2	0.973	0.943	0.956	0.963
Pseudo-second-order	q_{exp}(mg/g)	20.083	14.879	21.612	20.596
	q_{cal} (mg/g)	20.123	14.799	21.792	20.510
	k_2 (mg/(g×L))	0.053	0.017	0.039	0.081
	R^2	0.992	0.995	0.990	0.994
Isotherm model		**Equilibrium parameters**			
Freundlich	$K_F(mg^{1-\frac{1}{n}}.L^{\frac{1}{n}}/g)$	8.216	4.531	9.634	5.328
	n^{-1}	0.457	0.436	0.451	0.550
	R^2	0.913	0.861	0.893	0.903
	RMSEC	0.383	0.170	0.623	0.210
Langmuir	K_L (mg/g)	0.116	0.136	0.102	0.130
	q_{max} (mg/g)	47.130	28.826	58.068	32.712
	R^2	0.992	0.991	0.997	0.998
	RMSEC	0.094	0.105	0.032	0.071
Redlich–Peterson	K_R (L/g)	5.510	2.897	5.618	4.765
	a_R (L/mg)	0.220	0.193	0.078	0.10
	B	0.983	0.884	1.001	0.992
	R^2	0.991	0.993	0.991	0.992
	RMSEC	0.194	0.189	0.138	0.081
MB/CV; MB in binary mixtures (MB/CV) and CV/MB; CV in binary mixtures (MB/CV).					

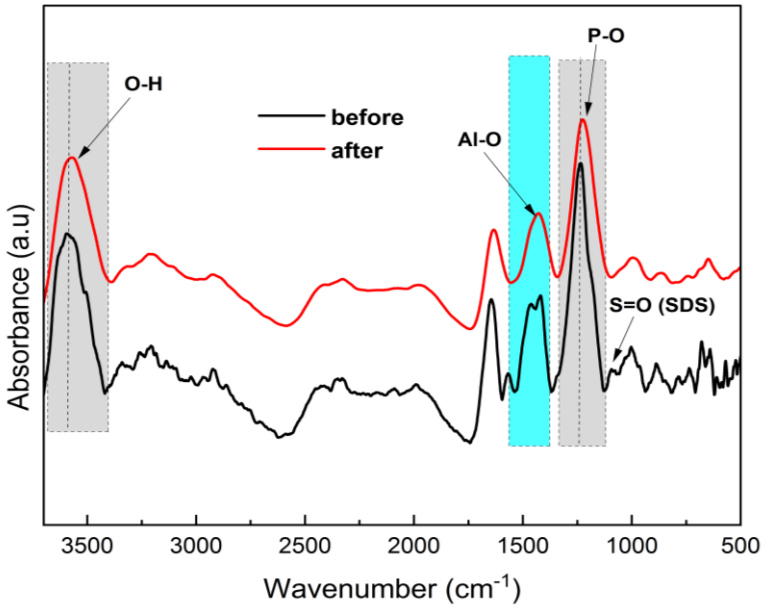

Fig. III.18. FTIR spectrum of G-PEG/SDS (L) granules before and after adsorption MB and CV dyes.

The FTIR spectra in **Fig. III.18** reveal significant changes in the adsorption bands of G-PEG/SDS (L) granules after MB and CV dye adsorption. The P-O, C=O, and O-H bands shift to lower wavenumbers, suggesting alterations in the molecular environment of these functional groups due to interactions with the dye molecules. Specifically, the P-O, C=O groups likely interact electrostatically with the N-H groups in the MB and CV dyes, while the O-H bond forms hydrogen bonds with these N-H groups.

Additionally, SEM and BET/BJH results (**Fig. III.12** and **Table III.7**) reveal that G-PEG/SDS (L) granules have a highly porous, mesoporous structure that enhances the accessibility and uptake of dye molecules. Within the mesopores, a pore filling mechanism plays a crucial role in the adsorption of MB and CV dyes. The proposed adsorption mechanism is illustrated in **Fig. III.19**, outlining the stepwise process of dye adsorption into the mesoporous structure of the granules.

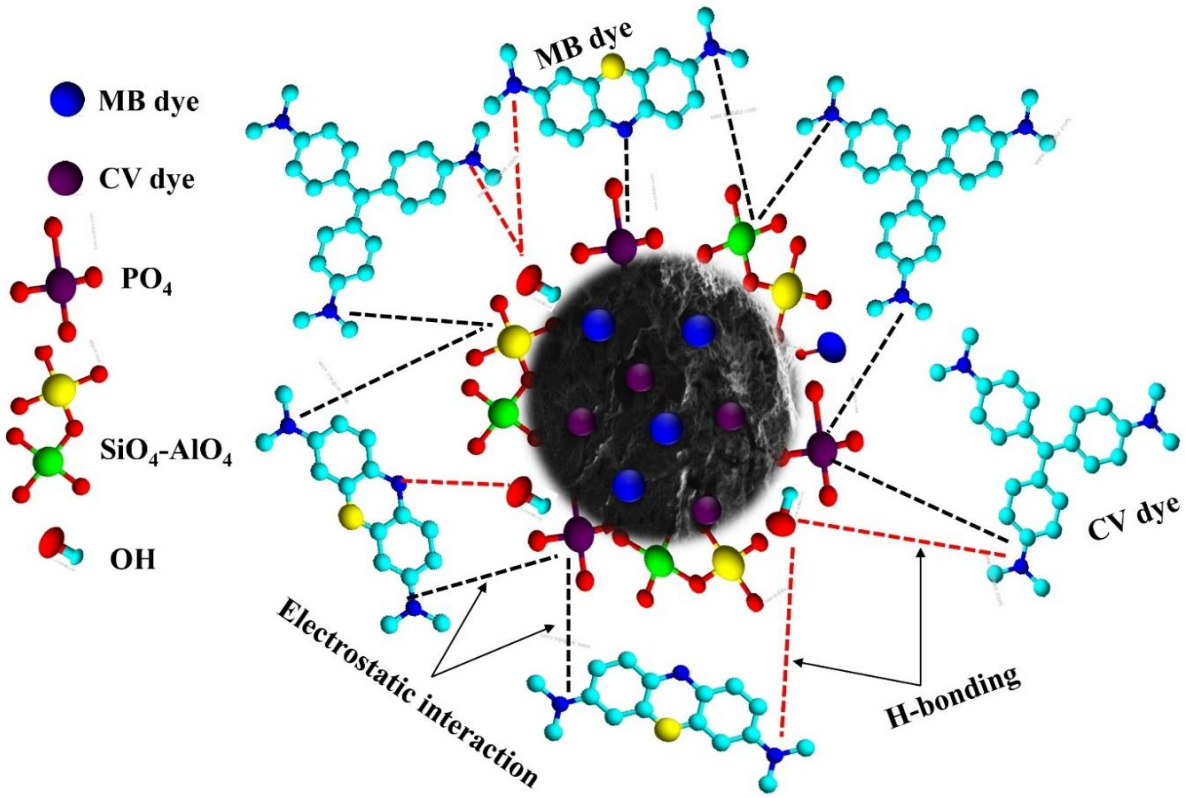

Fig. III.19. Proposed MB and CV dyes adsorption mechanism into G-PEG/SDS(L) granules.

III.2.2.4. Critical review of use HAP-MK-GP granules elaborated using PEG and SDS as adsorbent

Publication II critically highlights the potential of HAP-MK-GP/SDS (L) granules as a robust adsorbent for industrial dye removal, offering an adsorption capacity of 35 mg/g for methylene

blue (MB) and 45 mg/g for crystal violet (CV). These values, obtained under relatively mild conditions: pH 8, adsorbent dose of 3 g/L, granule size of 4 mm, agitation speed of 250 rpm, contact time of 180 minutes, and temperature of 298 K, underscore the practical viability of this adsorbent for large-scale operations. Although other materials, such as montmorillonite/magnetic $NiFe_2O_4$-amine-functionalized chitosan (Gomaa et al., 2022), exhibit higher adsorption capacities (**Table III.9**), HAP-MK-GP/SDS (L) demonstrates significant operational advantages, particularly for continuous flow systems in industrial applications.

An advantage of HAP-MK-GP/SDS (L) lies in its granule form, which offers superior mechanical stability and ease of separation from water compared to traditional powder adsorbents. This is a crucial factor for industrial-scale operations, where the use of powder adsorbents often results in challenges like clogging, difficult recovery, and regeneration issues. The granule size of 4 mm and high porosity ensure not only efficient adsorption but also ease of integration into column-based systems, which are widely used in industry for continuous treatment processes.

The use of sodium dodecyl sulfate (SDS) as an anionic surfactant in the formulation of HAP-MK-GP/SDS (L) appears to be a highly effective strategy, further enhancing adsorption performance by increasing surface hydrophilicity and providing additional active sites for dye interaction. This contributes to balanced adsorption efficiency across different dye types, making HAP-MK-GP/SDS (L) versatile for various wastewater treatment applications, including those involving complex dye mixtures.

From an economic standpoint, HAP-MK-GP/SDS (L) offers a more cost-effective solution compared to advanced nanocomposites, which, although exhibiting higher adsorption capacities, require complex and costly synthesis methods. The use of MK-GP as a binder simplifies the preparation process and aligns with sustainable and environmentally friendly practices, which are increasingly prioritized in industrial sectors.

Compared to other adsorbents listed in **Table III.11**, such as biochar-supported HAP and unmodified HAP powders, the HAP-MK-GP/SDS (L) granules stand out for their moderate adsorption capacities coupled with operational simplicity. This combination of efficient adsorption, mechanical durability, and ease of handling makes HAP-MK-GP/SDS (L) highly suitable for large-scale dye removal processes, where practical implementation and cost-efficiency are critical.

Table III.11. Comparison of G-PEG/SDS (L) granules adsorption capacities with the previously developed adsorbents in the literature.

Adsorbent	**Type**	**Dyes**	q_{max} **(mg/g)**	**Adsorption conditions**	**References**
HAP-MK-GP/SDS (L)	Granules (4 mm)	MB	35	pH = 8, adsorbent dose= 3 g/L, agitation speed = 250 rpm, t = 180 minutes, $[MB]_0$ = 180 mg/L, T = 298 K	**Publication II**
		CV	45		
Metakaolin	Powder	MB	5	120 (298 K)	Feng et al., 2021
MK-GP	Solid monolith	MB	276.90	pH = 4.5, adsorbent dose = 1.5 g/L, T=328 K, t = 120 minutes.	Barbosa et al., 2018
HAP	Powder	MB	38	pH = 10, adsorbent dose = 1.0 $[MB]_0$= 45 mg/L, t = 20 minutes, T=298 K	Aaddouz et al., 2023
Biochar-HAP nanoparticles	Powder	MB	21.1	pH = 8.0, adsorbent dose = 1.0 g/L, t= 600 minutes, T=313K	Li et al., 2018
Bio-HAP/MgO	Powder	MV	42.81	pH= 8, adsorbent dose= 2 g/L, $[MB]_0$= 10 mg/L, t =40 minutes,T= 303 K	Foroutan et al., 2020
Unmodifed HAP	Powder	GV	1.03	pH = 12, $[CV]_0$ = 3 mg/L, adsorbent dose = 1 g/L, t = 90 minutes, T=298 K	Ali et al., 2023
Palm kernel fiber	Powder	CV	78.90	pH = 7.20, adsorbent dose = 1.0 g/L, $[CV\ and\ MB]_0$=160 mg/L, T=298K	El-Sayed, 2011
		MB	95.40		
Modified $ZrSiO_4$ nanoparticles	Powder	CV	39.3	pH = 10, adsorbent dose = 1.0 g/L, $[CV\ and\ MB]_0$= 40 mg/L, t= 40 minutes, T=298K	Mahmoud et al., 2019
		MB	38.5		
Montmorillonite/magnetic Ni-Fe_2O_4- amine-functionalized chitosan	Powder	CV	118	pH = 7, adsorbent dose = 1.0 g/L, $[CV\ and\ MB]_0$= 200 mg/L, t= 30 minutes, T=298K	Gomaa et al., 2022
		MB	137		
CaO/g-C_3N_4 based nanocomposite	Powder	CV	1227.8	pH = 10, $[CV\ and\ MB]_0$= 2000 mg/L, t= 1440 minutes.	Younis et al., 2016
		MB	1915.8		

III.3. Comparison and advancements of the elaborated HAP-MK-GP granules

III.3.1. Structural characteristics and performance evaluation

Comparing the findings of **Publications I** and **II** reveals significant advancements and improvements in the development of HAP-MK-GP granules. **Publication I** underscores the limitations associated with the use of high concentrations of hydrogen peroxide (H_2O_2), inducing structural degradation by dissolution of calcium and phosphate ions. This phenomenon alters the integrity of the granules and reduces their adsorption capacity, thus compromising their effectiveness in the targeted applications. In fact, the dissolution of these

components results in reduced porosity and mechanical strength, highlighting the challenges of balancing porosity enhancement with chemical stability. In contrast, **Publication II** introduces polyethylene glycol (PEG) and sodium dodecyl sulfate (SDS) as effective alternatives to H_2O_2. The use of PEG as a porogen agent maintains the chemical functionality of HAP-MK-GP granules while enhancing their porosity. SDS, particularly in its liquid form (SDS-L), further improves the surface area and adsorption potential of the granules without the adverse effects observed with H_2O_2. This approach not only resolves the issues identified in **Publication I** but also presents a more stable and efficient method for optimizing granule properties.

Together, **Publications I** and **II** contribute to a deeper understanding of the chemical functional characterization and enhancement of HAP-MK-GP granules. **While Publication I** highlights the challenges posed by high H_2O_2 concentrations, **Publication II** offers practical solutions with PEG and SDS. These advancements represent a significant step forward in optimizing HAP-MK-GP granules, particularly for applications in water treatment, by improving both structural integrity and adsorption capabilities.

III.3.2. Regeneration and reusability aspects

Regeneration is essential for the reusability and long-term effectiveness of HAP-MK-GP granules. In **Publication I**, BG dye was desorbed using a 0.1 M HCl solution, which initially facilitated dye removal by protonating the granule surface. However, after five regeneration cycles, the adsorption-desorption efficiency sharply declined due to HAP dephosphorization (Rao et al., 2015) and MK-GP dealumination (Xia et al., 2011), leading to partial granule disintegration. This limited the granules' usability to one to three cycles **(Fig. III.20).** In contrast, in **Publication II**, desorption was carried out using acetic acid, with optimization based on Response Surface Methodology (RSM) and Box-Behnken Design (BBD). This approach achieved a regeneration efficiency of 93.86 ≈ 94% at optimal conditions of 0.72 M acetique acide concentration, 323 K temperature, and 173 minutes contact time, and maintained granule integrity for up to eight cycles **(Fig. III.20)** before degradation occurred due to HAP dissolution. A comparative analysis between these studies reveals the inherent challenges in maintaining the structural stability of HAP-MK-GP granules across multiple regeneration cycles. While dilute HCl in **Publication I** caused rapid disintegration, the optimized acetic acid method in **Publication II** offered greater durability. Nonetheless, both approaches exhibited limitations in long-term use, particularly as granule dissolution occurred after several cycles. Future research should focus on alternative regeneration agents or solvent-free methods to enhance the reusability of these granules. Additionally, optimizing regeneration conditions to

balance desorption efficiency with structural preservation remains a significant challenge for scaling up the use of HAP-MK-GP granules in industrial adsorption processes.

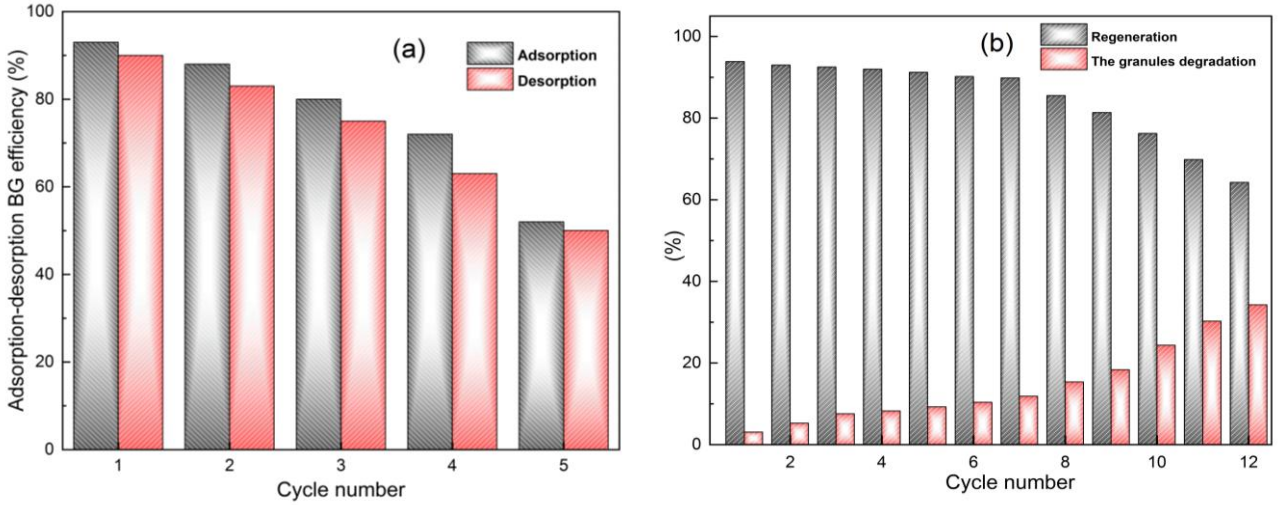

Fig.III.20. Regeneration and reusability of (a) G1 and (b) G-PEG/SDS(L) granules.

III.4. Critical review of the elaborated HAP-MK-GP granules performances

The integration of hydroxyapatite (HAP) with metakaolin-based geopolymer (MK-GP) materials has demonstrated significant potential in developing an effective adsorbent matrix for the removal of organic pollutants. While the results showed high efficiency in adsorbing cationic dyes, the material exhibited limited affinity for anionic dyes. To overcome this limitation, **Publication III** focused on improving the properties of HAP powder by optimizing its surface structure, porosity and adsorption efficiency for anionic organic pollutants, including dyes (i.e. ARS and DR23 dye).

III.5. Publication III. Synthesis of hydroxyapatite-Fe magnetized nanocomposite modified with *Urtica dioica* extract for the removal of anionic dyes from aqueous solutions.

The research investigates the integration of Fe_3O_4 nanoparticles into the HAP matrix, modified with *Urtica dioica* extract, to enhance the adsorption of anionic dyes. It is focused on improving the properties of HAP powder by optimizing its surface structure, porosity and adsorption efficiency for anionic organic pollutants, including dyes (i.e. ARS and DR23). For this, *Urtica dioica* extract (collected from Bejaia-Algeria), rich in bioactive antioxidants such as polyphenols, flavonoid glycosides, phenolic acids, amino acids, carotenoids, and chlorophyll,

was used for its strong chemical reactivity. These compounds were immobilized on the HAP surface through complexation with calcium ions (Ca^{+2}) (Alorku et al., 2020), which then interacted with phosphate precursors (PO_4^{-3}), facilitating the deposition of the extract onto the HAP matrix. To further enhance the functionality and versatility of the adsorbent, iron oxide nanoparticles (Fe_3O_4) are incorporated as a magnetic agent, forming a HAP-Fe composite that offers dual benefits: improved adsorption performance and easy recovery and separation via magnetic means.

III.5.1. Critical review of chemical functional characterization of HAP-Fe-*Urtica dioica* ext powder

The structural and chemical characterization of hydroxyapatite (HAP) modified with Fe_3O_4 and *Urtica dioica* extract (HAP-Fe-*Urtica dioica* ext) has been thoroughly evaluated, shedding light on the effects of these additives on HAP's properties. FTIR analysis depicted in **Fig. III.22** confirms the effective deposition of antioxidants from *Urtica dioica* onto the HAP surface via the formation of chelates or complexes with calcium ions. Concurrently, XRD data **(Fig. III.23)** indicate that the introduction *of Urtica dioica* extract promotes the deposition of Fe ions into the HAP structure, as evidenced by the shift in HAP peaks as well as the increase in the intensity of Fe_3O_4 peaks in HAP-Fe-*Urtica dioica* ext sample. These observations highlight the potential of *Urtica dioica* extract in improving Fe deposition and the functional properties of HAP-based materials.

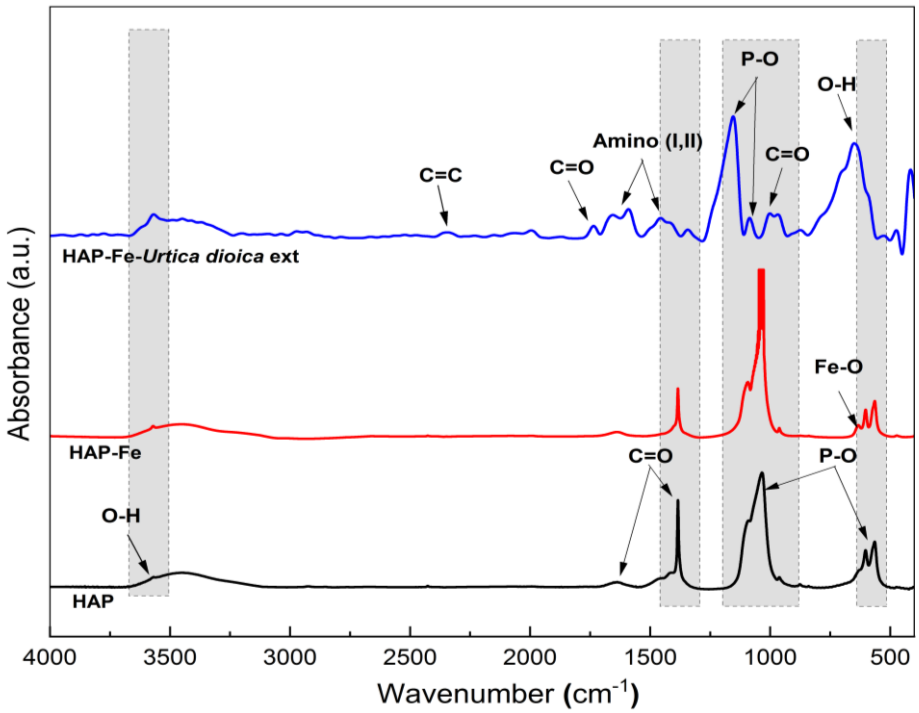

Fig. III.22. FTIR spectra of HAP, HAP-Fe and HAP-Fe-*Urtica dioica* ext.

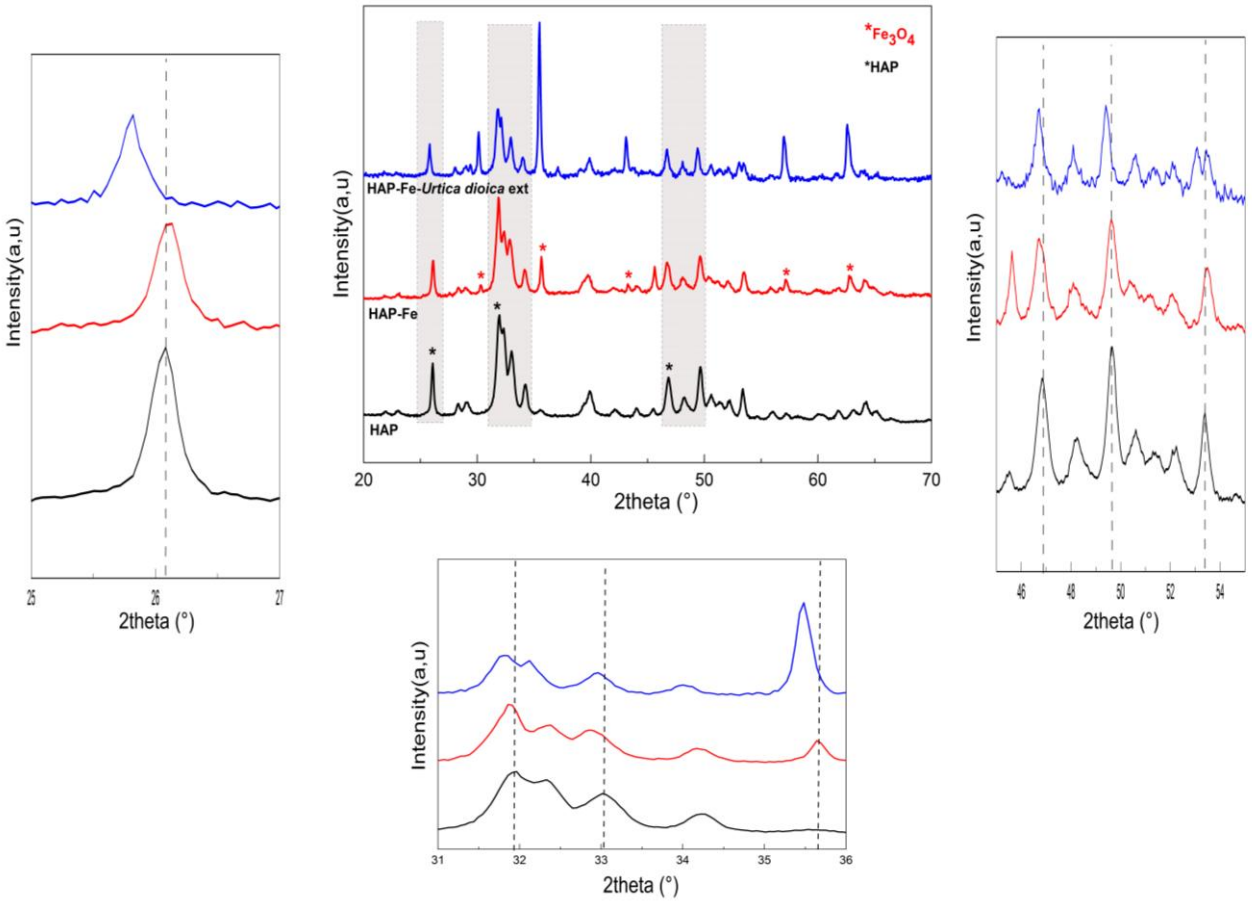

Fig. III.23. XRD diffractograms of HAP, HAP- HAP-Fe and HAP-Fe-*Urtica dioica* ext.

SEM images illustrated in **Fig. III.24** reveal irregular and rough surface morphologies for HAP and HAP-Fe matrices. HAP-Fe-*Urtica dioica* ext sample demonstrates particles with more defined shapes and larger sizes, which is due to the incorporation of *Urtica dioica* extract in HAP structure and its magnetized with Fe_3O_4. This enhancement is attributed to the successful deposition of Fe_3O_4 in the crystal surface of HAP and the interaction of polyphenol groups from *Urtica dioica* extract, which increase steric hindrance and electrostatic repulsion, thereby minimizing particle aggregation.

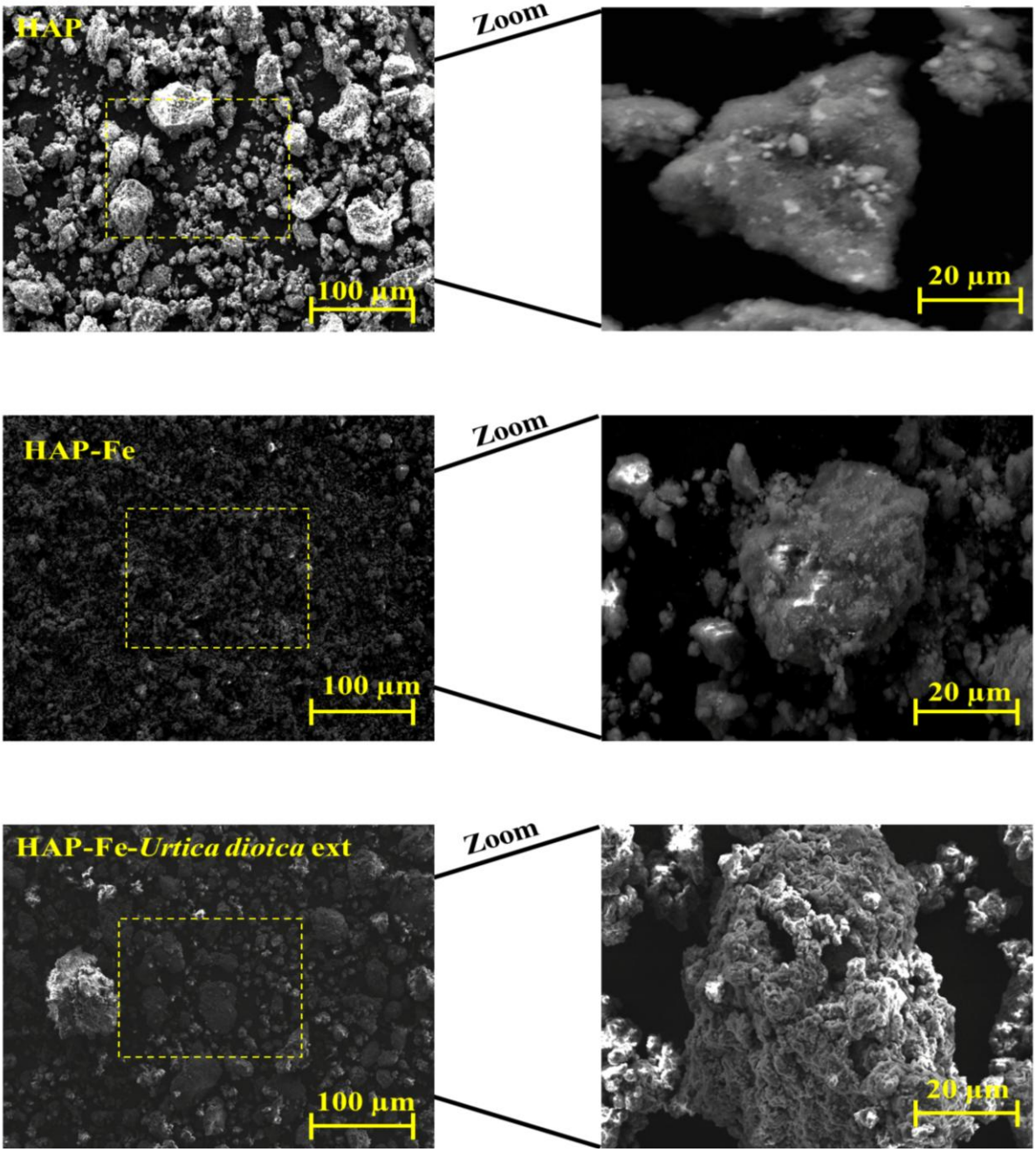

Fig. III.24. SEM images of HAP, HAP-Fe, and HAP-Fe-*Urtica dioica* ext.

To confirms the successful magnetization of HAP, VSM analysis was conducted. According to **Fig. III.25**, both HAP-Fe- and HAP-Fe-*Urtica dioica* ext exhibited superparamagnetic behavior (Wei et al., 2020), with saturation magnetization values of 10.32 emu/g and 10.92 emu/g, respectively. These results reflect a high magnetic susceptibility as well as ease of magnetization, giving the materials a strong potential for post-adsorption recovery with a view to their regeneration.

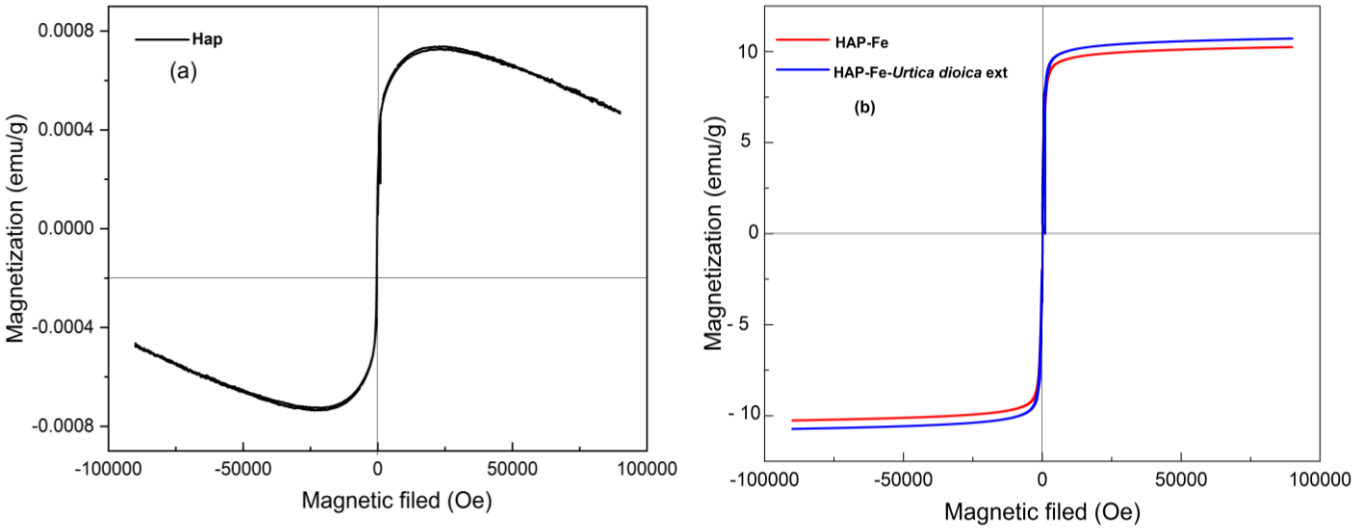

Fig. III.25. Magnetization curve of (a) HAP, (b) HAP-Fe, and HAP-Fe-*Urtica dioica* ext.

Moreover, the combination of *Urtica dioica* extract and magnetic Fe_3O_4 nanoparticles in HAP structure allows the development of a high specific surface area, rising from 30.12 m^2/g for the HAP material to 59.98 m^2/g for HAP-Fe-*Urtica dioica* ext **(Table III.12)**, a significant increase of about 30 m^2/g. Indeed, this natural bi-modification strategy used in this study offers an eco-friendly alternative to synthetic methods, aligning with green chemistry while boosting adsorption efficiency. The rise in SSA enhances the number of active sites, directly improving contaminant adsorption. However, while the total pore volume (0.30 cm^3/g) is comparable to materials like FHAP-CS (0.22 cm^3/g) (Brahmi et al., 2024), it remains lower than advanced adsorbents, which could limit its overall capacity. The larger pore diameter (19.89 nm) indicates improved mesoporous structure, though it is smaller than some other materials, suggesting further optimization is needed.

Compared to high-performance adsorbents like MCM-48 (Ali et al., 2023) **(Table III.12)**, HAP-Fe-*Urtica dioica* ext offers moderate SSA but excels in cost-effectiveness, sustainability, and biocompatibility, making it a more practical solution for large-scale use. While its performance is promising, further refinement in pore structure and surface properties is

necessary to fully compete with top-tier materials like zeolites and MOFs in high-performance adsorption applications.

Table III.12. Comparing HAP-Fe-*Urtica dioica* ext surface characterization with other developed HAP based materials and other materials.

Adsorbent	**SAA(m^2/g)**	**Total pore volume (cm^3/g)**	**Mean pore diameter (nm)**	**References**
HAP	32.12	0.09	11.20	**This work**
HAP-Fe	53.85	0.32	0.30	
HAP-Fe-*Urtica dioica* ext	59.98	0.30	19.89	
FHAP-CS	101.41	0.22	27.36	Brahmi et al., 2024
HAP-CS	59.39	0.11	14.69	
FHAP	59.69	0.15	0.22	
HAP	16.70	0.137	24.94	
HAP-1% GO	35.61	0.054	6.08	Ozder et al., 2023
Ag/Mg/Zn-HAP	0.63	N/A	2.06	Mahanty and Shikha, 2024
MCM-48	1420	1.2	3.7	Ali et al., 2023
ZAB	729.93	0.378	1	Maiti et al., 2022
Activated carbon/γ-Fe_2O_3 nano-composite	347.8	N/A	N/A	Fayazi et al., 2015
Carbon-bridge-doped g-C_3N_4/Fe_3O_4	62.98	0.31	17.75	Zhang et al., 2021

GO = graphene oxide, ZAB= $ZnCl_2$ Activated Biochar, MCM-48 = Silica mesoporous, MOFs = Metal–organic framework-based materials

III.5.2. Adsorption of ARS and DR23 dyes onto HAP-Fe-*Urtica dioica* ext: Selectivity and optimization through CCD-RSM analysis

The adsorption efficiency of HAP and the modified HAP materials for removing ARS and DR23 dyes in both single and binary dye mixture is illustrated in **Fig.III.26**. The results indicate that HAP-Fe −*Urtica dioica* ext outperforms both HAP-Fe and HAP in single dye system. As depicted in **Fig. III.26b**, HAP-Fe-*Urtica dioica* ext exhibits high selectivity for DR23 over ARS in binary mixture, likely due to the stronger charges associated with DR23. Additionally, the presence of DR23 enhances the adsorption of ARS, possibly through electrostatic interactions between the HAP-Fe −*Urtica dioica* ext and both dyes.

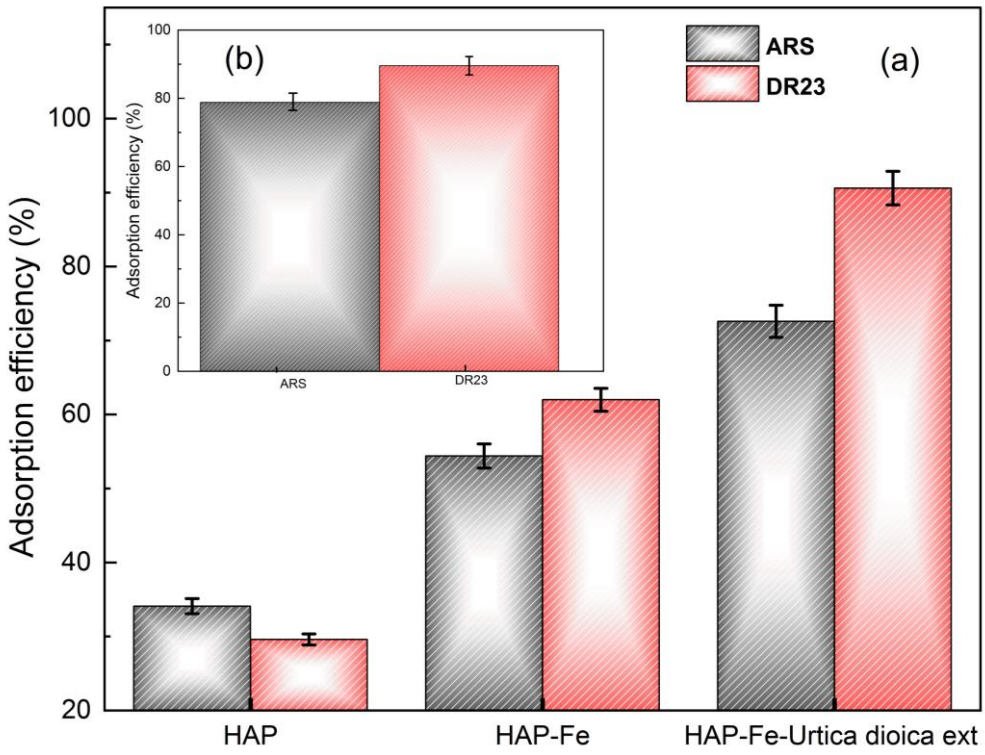

Fig. III.26. Adsorption of ARS and DR23 dye (a) individually, and (b) in binary dye mixture solution using HAP-*Fe-Urtica dioica* ext. Conditions pH of dye, $[\,\mathrm{ARS}\,]_0 = [\mathrm{DR23}\,]_0 = 20\ \mathrm{mg/L}$, time = 90 minutes, T = 294 K, agitation speed = 200 rpm, and adsorbent dose = 1 g/L.

The optimization of the adsorption parameters (i.e., HAP-$Fe-$*Urtica dioica* ext dose (x_1), solution pH (x_2), and agitation speed (x_3)) on adsorption efficiency for ARS and DR23 in a binary dye mixture solution was conducted using the CCD-RSM method. A novel approach was introduced, focusing on comparing the validity of the models by evaluating the adsorption efficiency of ARS and DR23 dyes in the binary mixture onto HAP-$Fe-$*Urtica dioica* ext, in comparison to the average adsorption efficiency of ARS and DR23. This approach enables the direct optimization of the binary mixture of two dyes with similar characteristics.

The validity of the average model for predicting the adsorption efficiency of ARS and DR23 in a binary mixture solution was confirmed through ANOVA (**Table.III.13**). The statistical results (p-values < 0.0001 and high F-values) show that the models are well-fitted and significant, accurately representing the data. Strong correlations between measured and predicted values, with R^2 values of 99.5% further validate the models. Furthermore, residual analysis depicted in **Fig. III.27** showed no correlation, confirming the models' predictive accuracy and robustness.

Table III.13. ANOVA analysis for adsorption efficiency quadratic models of ARS and DR23 dyes onto HAP-Fe-*Urtica dioica* ext.

Case	Coefficients	Estimate	t-Ration	F-Ration	Prob>|t|	Second-Order Model Analysis of Variance		
ARS in mixture	b_0	74.82	88.57	7.84	< 0.05		**Model**	**Error**
	b_1	5.29	9.34	99.95	< 0.05	**DF**	11	8
	b_2	-21.81	-38.45	1678.00	< 0.05	**SS**	8401.24	30.24
	b_3	4.34	7.65	66.44	< 0.05	**MS**	763.75	3.78
	b_{12}	1.53	2.09	4.97	0.07	**F-Ration**	202.03	N/A
	b_{13}	0.55	0.75	0.64	0.47	R^2	0.99	N/A
	b_{23}	-0.81	-1.11	1.40	0.30	R^2_{adj}	0.97	N/A
	b_{11}	-7.48	-13.13	195.55	< 0.05			
	b_{22}	-7.11	-12.47	176.63	< 0.05			
	b_{33}	-2.54	-4.47	22.62	< 0.05			
DR23 in mixture	b_0	84.65	102.86	11.52	< 0.05		**Model**	**Error**
	b_1	4.37	7.92	62.79	< 0.05	**DF**	11	8
	b_2	-19.27	-34.88	1216.83	< 0.05	**SS**	6769.57	32.58
	b_3	3.09	5.6	31.30	< 0.05	**MS**	615.41	4.07
	b_{12}	1.77	2.48	6.16	0.03	**F-Ration**	151.09	N/A
	b_{13}	-0.58	-0.83	0.68	0.43	R^2	0.99	N/A
	b_{23}	-0.01	-0.02	0.00	0.98	R^2_{adj}	0.98	N/A
	b_{11}	-7.66	-13.8	190.55	< 0.05			
	b_{22}	-6.88	-12.39	153.20	< 0.05			
	b_{33}	-0.96	-1.73	2.99	0.12			
Average adsorption efficiency in binary dye mixture	b_0	79.25	186.2	23.07	< 0.05		**Model**	**Error**
	b_1	4.69	16.41	219.60	< 0.05	**DF**	11	8
	b_2	-20.24	-70.83	3957.74	< 0.05	**SS**	7332.45	11.37
	b_3	3.87	13.56	129.49	< 0.05	**MS**	684.76	1.42
	b_{12}	1.55	4.21	15.36	< 0.05	**F-Ration**	481.51	N/A
	b_{13}	0.56	1.52	0.00	< 0.05	R^2	0.99	N/A
	b_{23}	0.01	-0.01	0.96	0.16	R^2_{adj}	0.99	N/A
	b_{11}	-7.40	-25.78	532.71	0.99			
	b_{22}	-6.70	-23.33	454.45	< 0.05			
	b_{33}	-1.52	-5.32	28.53	< 0.05			
SS: sum of squares, **MS**: mean of squares, **DF :** degree of freedom								

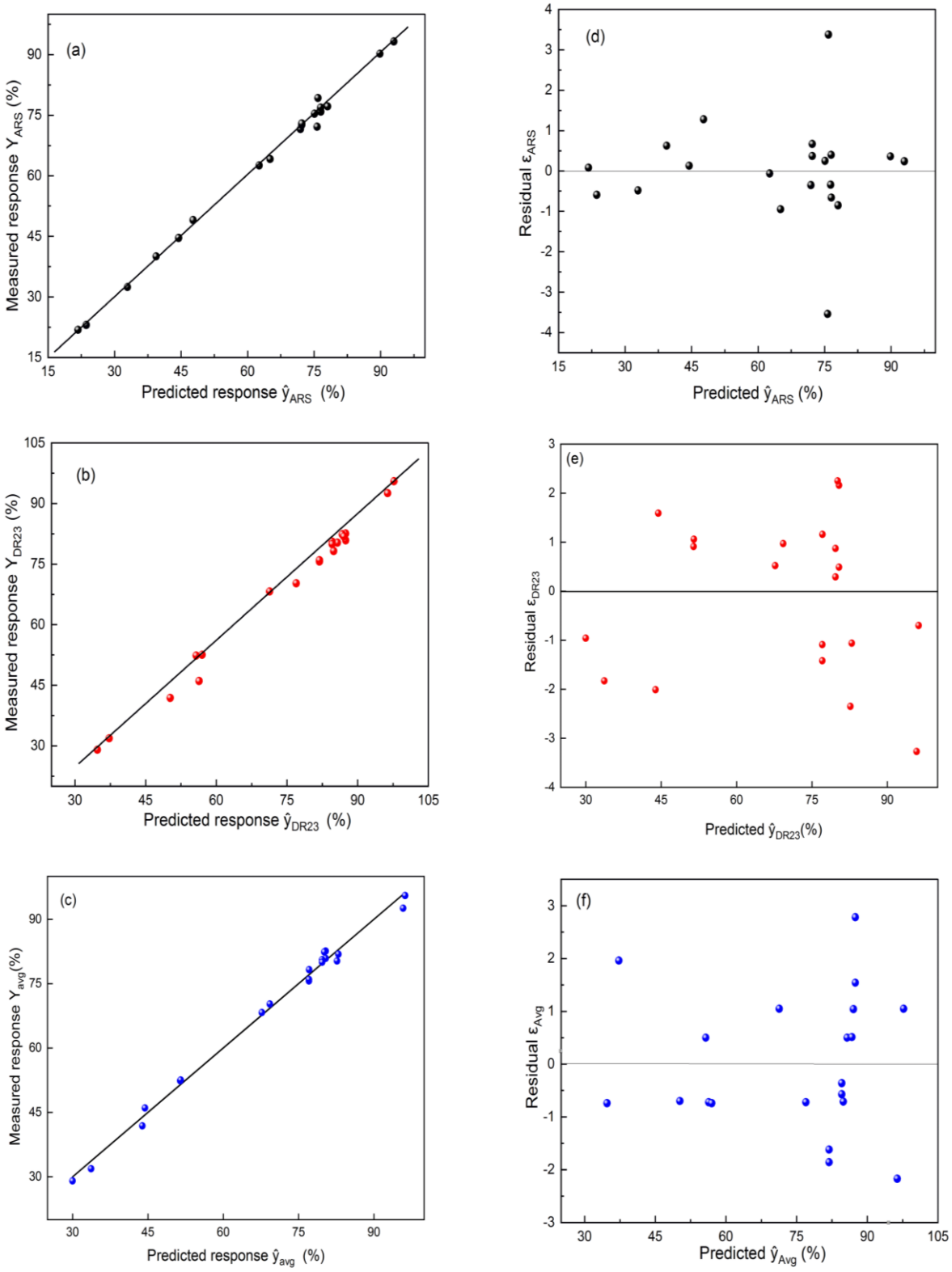

Fig. III.27. (a), (b) and (c) Correlations between experiments and predicted adsorption efficiency, (d), (e), and (f) Residuals versus predicted response for ARS, DR23, and their average adsorption efficiency in the binary dye solution onto HAP-Fe-*Urtica dioica* ext.

The combination of the experimental batch adsorption (**Fig. III.28**) results and the regression models (Eqs. III.1, 2, and 3) highlights consistent findings regarding the factors influencing adsorption efficiency. Both the experimental results and the regression models demonstrate that the pH of the solution has a negative effect on adsorption, indicating that higher pH values reduce ARS/DR23 dye adsorption efficiency.

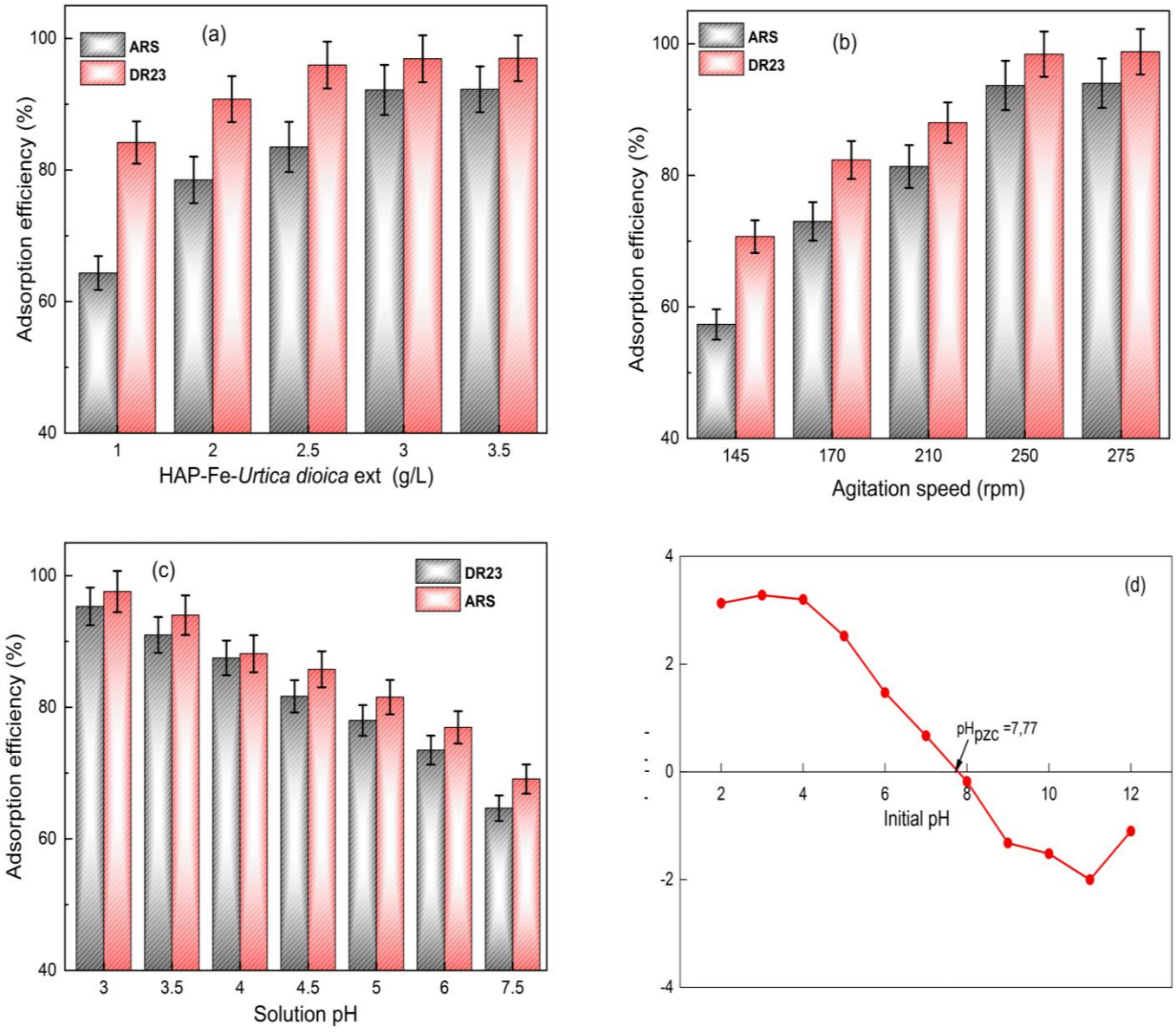

Fig. III.28. Effects of (a) HAP-Fe-*Urtica dioica* ext dose , (b) Agitation speed, (c) pH solution and (d) pH_{pzc}, on the adsorption efficiency of ARS and DR23 in the binary dye mixture onto HAP-Fe-*Urtica dioica* ext . Conditions: $[\,ARS\,]_0 = [DR23\,]_0 = 20$ mg/L, t = 90 minutes, and T = 294 K.

$$\hat{y}_{ARS} = 74.82 + 5.29\,x_1 - 21.81\,x_2 + 4.34\,x_3 - 7.48\,x_1^2 - 7.11\,x_2^2 - 2.54\,x_3^2 \qquad (\boldsymbol{III.1})$$

$$\hat{y}_{DR23} = 84.65 + 4.37\,x_1 - 19.27\,x_2 + 3.09\,x_3 + 1.77\,x_1\,x_2 - 7.66\,x_1^2 - 6.88\,x_2^2 \qquad (\boldsymbol{III.2})$$

$$\hat{y}_{Avg} = 79.74 + 4.84\,x_1 - 20.54\,x_2 + 3.27\,x_3 + 1.65\,x_1x_2 - 7.57\,x_1^2 - 6.99\,x_2^2 - 1.75\,x_3^2 \qquad (\boldsymbol{III.3})$$

Additionally, both the experiments and models show that the HAP-Fe-*Urtica dioica* ext dose and agitation speed have a positive influence on ARS/DR23 dye adsorption efficiency. Increasing the HAP-Fe-*Urtica dioica* ext and agitation speed enhances adsorption due to a higher number of available adsorption sites and increased turbulence, which lead to more effective collisions between the dye molecules and the adsorbent surface. The optimal conditions derived from both the experimental results and the regression models were consistent, with a HAP-Fe-*Urtica dioica* ext dose of 2.5 g/L, agitation speed of 250 rpm and solution pH of 3. Analysis using three-dimensional (3D) response surfaces and two-dimensional (2D) contour plots (**Fig. III.29**) enabled the interactions between operating parameters and adsorption efficiency to be visualised, revealing that the highest adsorption efficiency (> 90%) were achieved under specific optimum conditions of pH 3.15, agitation speed of 260 rpm and HAP-Fe-*Urtica dioica* ext of 2.60 g/L. The consistency of the results obtained from both the batch mode adsorption tests and the regression models confirms the reliability and accuracy of these approaches for predicting optimum dye adsorption conditions.

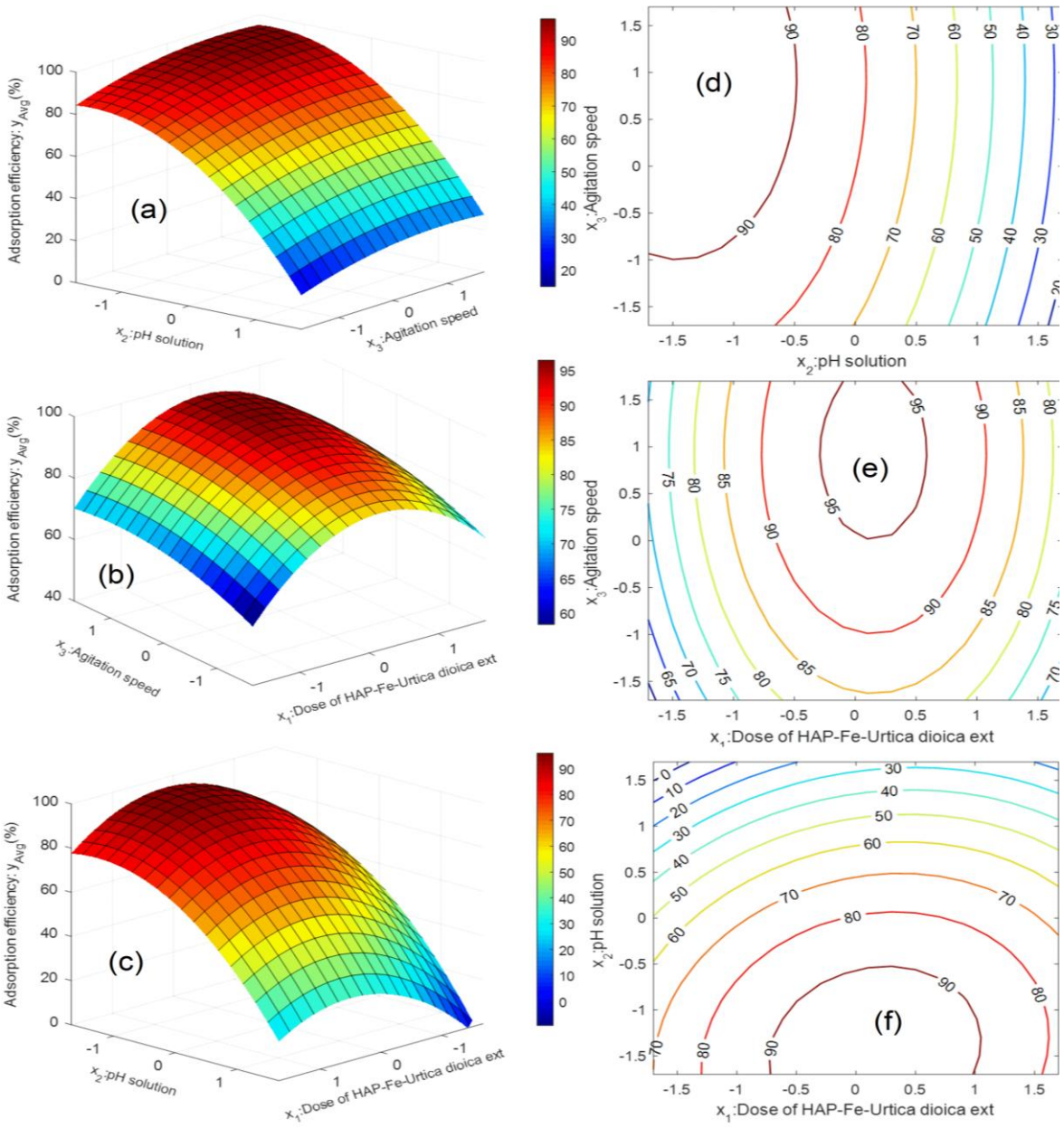

Fig. III.29. 2D contour plots and 3D response surfaces of adsorption efficiency of ARS and DR23 in binary mixture onto HAP-Fe-*Urtica dioica* ext. Conditions:$[\text{dyes}]_0 = 20$ mg/L, t = 120 minutes, pH solution = 3.15, HAP-Fe-*Urtica dioica* ext ext dose = 2.60 g/L, T = 294 K, and agitation speed = 260 rpm.

III.5.3. Adsorption kinetics and isotherms of ARS and DR23 onto HAP-Fe-*Urtica dioica* ext and proposed mechanism

The effect of the initial concentrations of ARS and DR23 in a binary dye mixture as a function of time is shown in **Fig. III.30a**. The findings show that at concentrations between 20 and 100 mg/L, both ARS and DR23 dyes demonstrate similar adsorption efficiencies. However, at

concentrations exceeding 100 mg/L, HAP-Fe-*Urtica dioica* ext exhibits a greater affinity for DR23 dye, likely due to the stronger electrostatic interactions resulting from its higher number of SO_3 groups in comparison to the ARS dye.

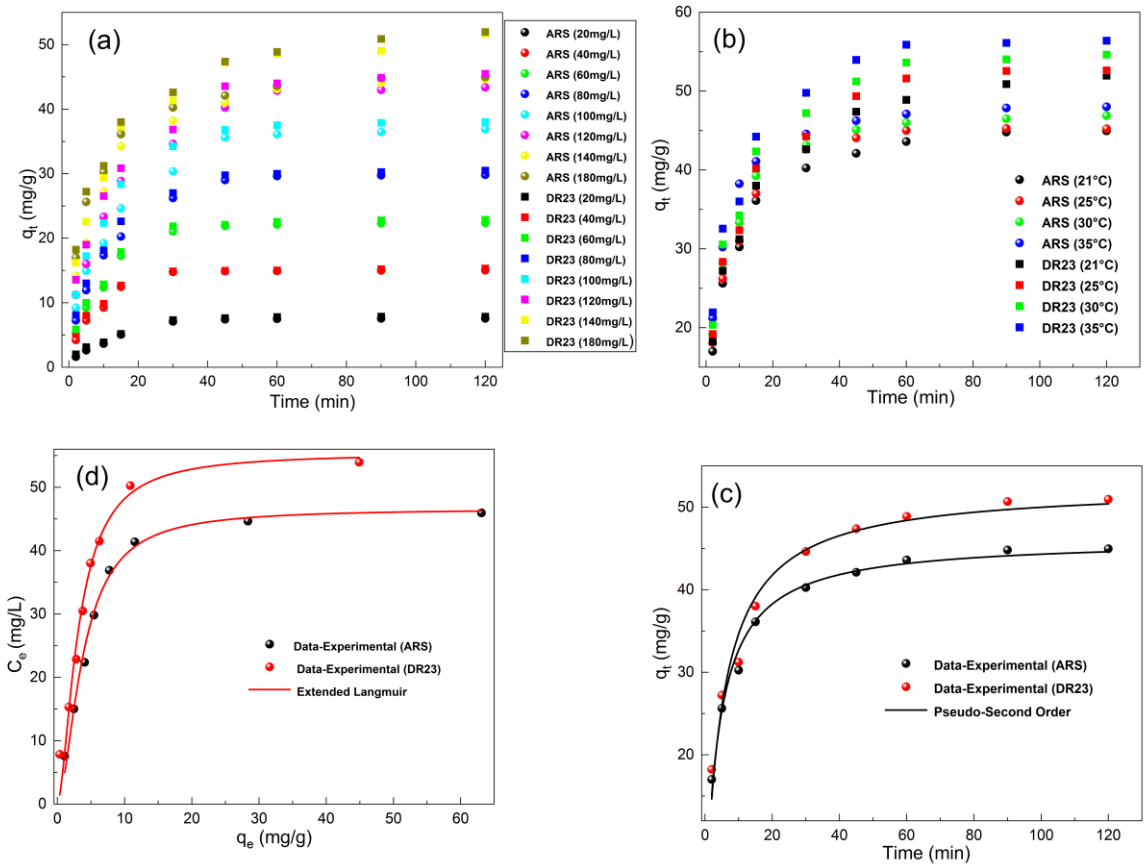

Fig. III.30. (a) Effect of initial concentrations of ARS and DR23 dye in binary mixture solution, (b) Effect of the temperature's (c) Isotherm and (d) kinetic models fitting to experimental data for ARS and DR23 dyes in binary solution at the optimal condition determined by CCD-RSM.

On the other hand, **Fig. III.30b** demonstrates the effect of temperature on the adsorption of ARS and DR23 dyes onto HAP-Fe- *Urtica dioica* ext under optimized CCD-RSM conditions. The results show that increasing temperature enhances the diffusion of both dyes into the adsorbent, leading to improved adsorption capacity. Thermodynamic analysis listed in **Table III.14** reveals that the adsorption process is both spontaneous and endothermic for both dyes. Notably, DR23 exhibits chemisorption behavior, reflected by its higher $\Delta H°$ values, while ARS follows a physisorption process with lower $\Delta H°$ values, indicating distinct adsorption mechanisms for the two dyes (AitAli et al., 2023). Kinetic and extended Langmuir isotherm

models (**Fig. III.30c and d**) further confirm that the adsorption of both dyes adheres to the PSO kinetic model and the extended Langmuir isotherm, suggesting a homogeneous monolayer adsorption process where each site holds one anionic dye molecule. This process occurs on identical sites without lateral interactions or steric hindrance, characterized by constant enthalpies and sorption activation energy.

Table III.14. Kinetic and isotherm parameters of ARS and DR23 dyes in binary solution.

Kinetic model	**Kinetic parameters**	**dye**		**Isotherm model**	
		ARS	**DR23**	**Extended-Langmuir (ARS)**	
Pseudo-First Order	q_{exp} (mg/g)	44.960	51.052	q_m(mg/g)	59.013
	q_{cal} (mg/g)	41.579	48.139	$K_{L,1}$(L/mg)	0.057
	k_1 (min^{-1})	0.141	0.133	$K_{L,2}$(L/mg)	0.201
	Δq (mg/g)	3.381	2.913	$R_{L,1}$	0.495
	R^2	0.91	0.88	$R_{L,2}$	0.199
				R^2	0.991
Pseudo-Second Order	q_{exp}(mg/g)	44.960	51.052	**Extended-Langmuir (DR23)**	
	q_{cal} (mg/g)	45.122	52.113	q_m(mg/g)	64.416
	Δq (mg/g)	-0.162	-1.061	$K_{L,1}$(L/mg)	0.020
				$K_{L,2}$(L/mg)	0.261
	k_2 (mg/(g×L))	0.003	0.005	$R_{L,1}$	0.714
	R^2	0.993	0.991	$R_{L,2}$	0.160
				R^2	0.993

In order to gain a better understanding of the adsorption mechanism involved, FTIR analysis of HAP-Fe- *Urtica dioica* ext before and after the adsorption of DR23 and ARS dyes was carried out. The finding reported in **Fig. III.31** show a shift in the P-O band from 1146 cm^{-1} to 1165 cm^{-1}, along with a reduction in intensity at 1069 cm^{-1}. The decreased intensity of the C=O groups is likely due to interactions between PO_4^{-3} and C=O groups with functional groups like O-H, SO_3^-, and N-H groups in the ARS and DR23 dyes, involving hydrogen bonding and electrostatic interactions (Jiang et al., 2021 ; Normi et al., 2022). Furthermore, the calcium ions (Ca^{2+}) on the HAP surface can form chelate complexes with the C=O and SO_3^- groups of the dyes (Moriguchi et al., 2003). Additionally, Fe_3O_4 can form hydrogen bonds with functional groups like SO_3^- and O-H in the dye molecules and participate in electrostatic interactions with

the azo bonds (-N=N-) and amino (NH) groups in the DR23 dye (Wang at al., 2021 ; Chaudhary, 2013). The proposed adsorption mechanism is illustrated in **Fig. III.32**.

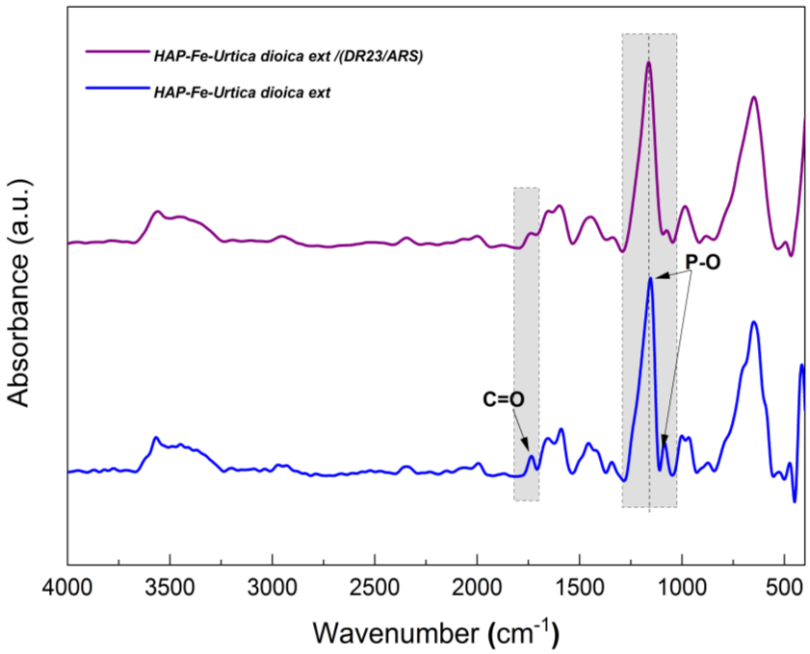

Fig. III.31. FTIR spectra of HAP-Fe- *Urtica dioica* ext before and after the adsorption of DR23 and AS dyes.

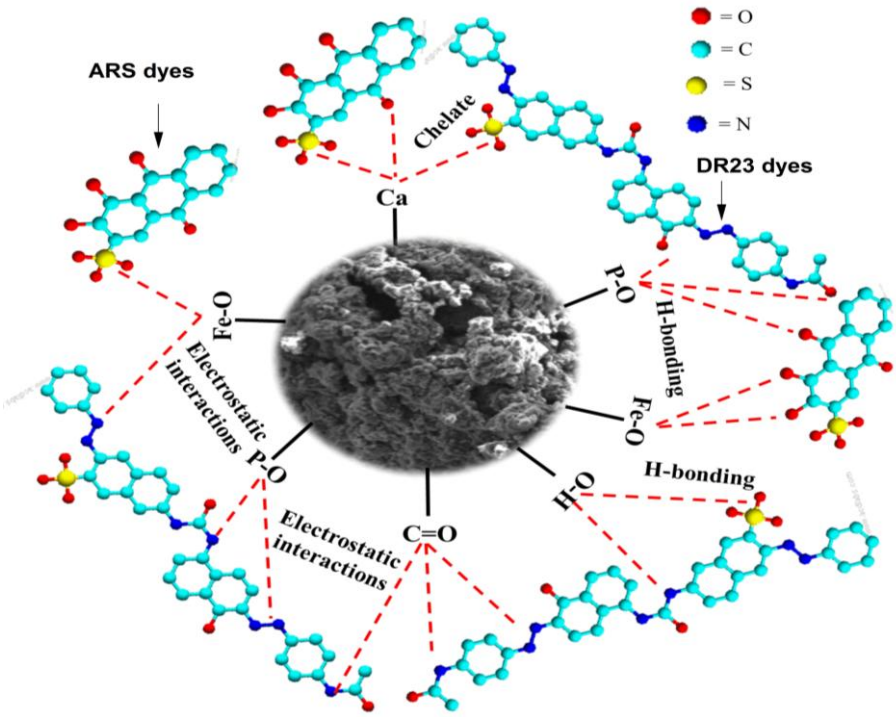

Fig. III.32. Proposal mechanism of adsorption of DR23 and ARS dyes HAP-Fe- *Urtica dioica* ext.

III.5.4. Critical review of use HAP-Fe-*Urtica dioica* ext powder as adsorbent

The utilization of HAP-Fe- *Urtica dioica* ext ext powder as an adsorbent presents a compelling strategy for environmental remediation, capitalizing on the unique structural, surface, chemical, and magnetic properties achieved through the incorporation of *Urtica dioica* extract and Fe_3O_4 with hydroxyapatite (HAP). This composite material exhibited high surface area and porosity with the magnetic characteristics of Fe_3O_4, thereby enhancing adsorption capacity while facilitating convenient recovery from aqueous environments.

The adsorption experiments conducted with HAP-Fe- *Urtica dioica* ext in binary mixture of anionic dyes, specifically ARS and DR23, underscore its efficacy in contaminant removal. The study reveals maximum adsorption capacities of 56.15 mg/g for DR23 and 47.96 mg/g for ARS under optimized conditions of: pH = 3.15, adsorbent dose = 2.60 g/L, T = 308 K, agitation speed = 260 rpm, and t = 120 minutes.

A notable advantage of HAP-Fe- *Urtica dioica* ext lies in its magnetic properties, which enable facile separation post-adsorption. This feature streamlines the recovery process of the adsorbent, significantly enhancing operational efficiency in practical applications. Moreover, the reactive nature of Fe_3O_4 contributes to improved adsorption kinetics and selectivity, particularly in the removal of anionic contaminants, positioning HAP-Fe- *Urtica dioica* ext as a viable alternative to traditional adsorbents. When comparing HAP-Fe- *Urtica dioica* ext extract to other materials in the literature (**Table III.15**), it demonstrates competitive performance, albeit with certain limitations. Specifically, while HAP-Fe- *Urtica dioica* ext is effective in removing anionic dyes, materials such as nanoclay (with an adsorption capacity of 166.6 mg/g for DR23) and sludge biochar-based adsorbents (SBA) (111.98 mg/g) show superior capacities under varying conditions. Additionally, polyaniline-coated activated carbon achieves an adsorption capacity of 109.8 mg/g for DR23, underscoring the efficacy of hybrid materials that combine high surface area and functional coatings. Despite these comparisons, the unique advantages of HAP-Fe- *Urtica dioica* ext, particularly its ease of recovery and distinctive magnetic properties, support its potential for environmental remediation applications. Furthermore, its performance in treating binary ARS/DR23 dye mixtures highlights its practical utility in addressing real-world wastewater treatment challenges.

Table III.15. Comparative insights into the adsorption efficiency and surface characteristics of HAP-Fe- *Urtica dioica* ext and other advanced adsorbents.

Comparing DR23 dye adsorption capacity of HAP-Fe-*Urtica dioica* ext and other adsorbents				
Adsorbent	**q_{max} (mg/g)**	**pH solution**	**Equilibrium time (minutes)**	**Reference**
HAP-Fe-*Urtica dioica* ext	56.15	pH = 3.15	60	**Publication III**
Nanoclay	166.6	pH = 2	30	Mahvi and Dalvand, 2019
Cationized sawdust	65.8	pH=5.5	90	Hebeish et al., 2011
Polyaniline coated activated carbon	109.8	pH = 3	90	Gopal et al., 2014
Corn stalk	52	pH=3	10	Fathi et al., 2014
Sludge biochar-based adsorbent (SBA)	111.98	pH =6.5	190	Jiang et al., 2021
Comparing ARS dye adsorption capacity of HAP-Fe-*Urtica dioica* ext and other adsorbents				
HAP-Fe_3O_4-*Urtica dioica* ext	47.96	pH = 3.15	60	**Publication III**
Activated clay modified by iron oxide (Fe-clay)	32.7			Fu et al., 2011
Untreated Typha Grass	77.99	8	120	Muhammad and Musa, 2022
Ni-Fe-CO_3 layered double hydroxide	69.9	7	120	Ahmed et al., 2023
biomass-based activated carbon	91.69	3	120	Bhomick et al., 2019
Magnetite talc (Fe_3O_4@Talc) nanocomposit	11.76	3	60	Nayl ar al., 2022
Fe_2O_3@BC-KC composite	174.9	2	150	Ohale et al., 2023
Grafted vermiculite (APTES)	18.2	1	40	Ali et al., 2020

III.5.6. Review on the regeneration and reusability of HAP-Fe-*Urtica dioica* ext

The regeneration and reusability of HAP-Fe- *Urtica dioica* ext have been explored to assess its potential for long-term use in dye removal applications. The findings indicate that while the adsorbent remains effective for up to four cycles (**Fig. III.33**), its adsorption efficiency gradually declines thereafter. This decline is primarily attributed to pore blockage caused by the accumulation of residual ARS and DR23 dyes, which obstruct the available adsorption sites and hinder the diffusion of new dye molecules. As these dye molecules become more embedded within the adsorbent matrix, their removal during desorption becomes increasingly difficult, which impacts the material's reusability. Additionally, the interactions between the functional groups of HAP-Fe-*Urtica dioica* ext and the dye molecules, as well as possible chemical transformations, further exacerbate the reduction in adsorption capacity.

Alternative regeneration techniques, such as thermal degradation or advanced chemical treatments, have shown promise in breaking down the accumulated dyes and preventing pore

clogging, thus enhancing the material's longevity. While these methods offer potential solution to extend the lifespan of the adsorbent, further research is necessary to refine these regeneration methods and minimize the negative effects of dye accumulation and adsorbent degradation. The sustainability and cost-effectiveness of HAP-Fe-*Urtica dioica* ext in practical applications can be significantly improved by optimizing regeneration processes, enabling its effective reuse for multiple adsorption cycles.

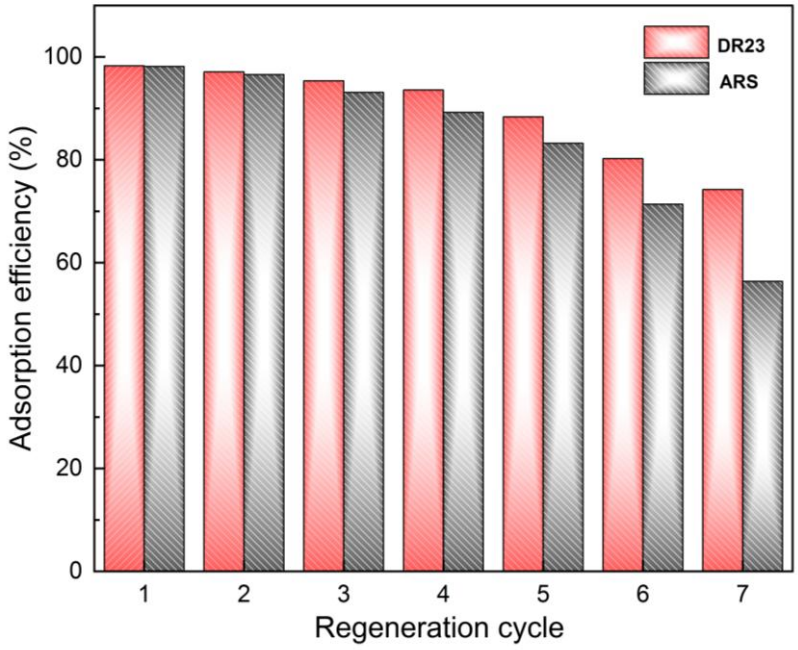

Fig. 1II.33. Regeneration and reusability of HAP-Fe- *Urtica dioica* ext adsorbent for the adsorption of binary DR23 and ARS dyes.

Conclusion and Future Work

IV. Conclusion

This thesis investigates the development of novel Hydroxyapatite (HAP)-based materials with enhanced adsorption properties for environmental remediation, specifically wastewater treatment applications. The co-precipitation method, utilizing NaOH for pH adjustment, was selected for HAP synthesis due to its superior surface characteristics, eco-friendliness, and clear advantages over conventional ammonium-based methods, as detailed in the existing literature.

While the synthesized HAP exhibited relatively limited adsorption capacity for organic pollutants, particularly anionic and cationic dyes, several innovative strategies were employed to address these limitations and maximize the potential of HAP-based materials. Three distinct approaches were proposed and rigorously tested to optimize the adsorption properties of these materials.

The first approach involved the incorporation of MK-GP as a binder to overcome the limitations of direct foaming methods, which had shown suboptimal adsorption efficiency for cationic dyes. By embedding MK-GP onto HAP as an adsorbed powder, the resulting HAP-MK-GP granules demonstrated significant improvements in surface properties, mechanical integrity, and adsorption performance. These granules outperformed GP materials and other HAP-based materials reported in the literature, as evidenced in Publication I.

In Publication II, a novel strategy was introduced by combining polyethylene glycol (PEG) with sodium dodecyl sulfate (SDS) to further enhance the properties of the HAP-MK-GP matrix. This combination effectively mitigated the limitations associated with hydrogen peroxide (H_2O_2) as a foaming agent and led to improvements in the granules' surface morphology, textural properties, mechanical strength, and adsorption capacity. The optimized granules, with a diameter of 4 mm, exhibited superior adsorption efficiency and remarkable regeneration potential, maintaining their performance over eight cycles without any degradation.

Despite these advancements, the HAP-MK-GP matrix still showed limited adsorption efficiency for anionic dyes, attributable to the negative surface charge of MK-GP, as discussed in both Publications I and II. To address this issue, an alternative strategy was employed by doping the HAP matrix with magnetized Fe_3O_4 and *Urtica dioica extract*. The resulting HAP-Fe-*Urtica dioica ext* composite exhibited a marked enhancement in adsorption efficiency for anionic dyes, underscoring its potential for more effective wastewater treatment.

In conclusion, this research makes a substantial contribution to the field of HAP-based materials, offering innovative strategies for improving their adsorption capacities and long-term stability, particularly for environmental applications. The findings provide valuable insights into the development of advanced materials for sustainable wastewater treatment solutions and suggest promising avenues for further research.

V. Future Work

Future research could focus on optimizing of use the HAP-Fe-*Urtica dioica ext* composites for the adsorption of organic pollutants (i.e., cationic dyes) and heavy metals. A key aspect of this would be evaluating the performance of these composites in column adsorption tests to assess their efficacy for both dye pollutants and heavy metals under real-world conditions. Furthermore, scaling up the synthesis of these materials for large-scale industrial applications in wastewater treatment should be considered.

Another promising direction is the integration of HAP-Fe -Urtica dioica extract with MK-GP to create hybrid materials that combine the strengths of each component. This approach could enhance the adsorption capacities, mechanical stability, and regeneration potential of the materials, thereby improving their practical use in environmental remediation. This integration could also potentially expand the materials' ability to tackle a broader range of environmental contaminants.

Additionally, the potential of HAP-MK-GP composites for heavy metal adsorption warrants further investigation. By targeting multiple environmental pollutants, these composites could provide a versatile solution for various types of contamination. Long-term studies are essential to evaluate their regeneration cycles and performance stability, ensuring their reliability and effectiveness in real-world applications.

Lastly, assessing the environmental impact of these materials after prolonged use and multiple regeneration cycles is crucial to ensure their sustainability and long-term effectiveness. Expanding this research to explore the integration of these advanced materials into broader environmental treatment systems could further enhance their applicability and provide new solutions for addressing diverse environmental challenges.

List of references

Aaddouz M., Azzaoui K., Akartasse N., Mejdoubi E., Hammouti B., Taleb M., Sabbahi R., Alshahateet S. F., (2023). Removal of methylene blue from aqueous solution by adsorption onto hydroxyapatite nanoparticles. *Journal of Molecular Structure* 1288: 135807. https://doi.org/10.1016/j.molstruc.2023.135807.

Agsous, M., Hafit, K., Yala, S., Oktay, B., Bingöl, A. B., Şenel, İ., & Üstündağ, C. B., (2025). Anti- tumoural activity of 3D printed fluorohydroxyapatite–polylactic acid scaffolds combined with graphene oxide and doxorubicin. *Polymer International* 74: 277-285. https://doi.org/10.1002/pi.6743.

Ahmed, I. M., Abd-Elhamid, A. I., Aly, A. A., Bräse, S., & Nayl, A. A., (2023). Synthesis of Ni-Fe-CO_3 layered double hydroxide as Effective Adsorbent to remove Cr(VI) and ARS-dye from aqueous media. *Environmental Technology & Innovation*, 31 : 103214. https://doi.org/10.1016/j.eti.2023.103214.

AitAli, S., Ziani, S., Yahiaoui, I., Brahmi, A., Boudrahem, F., & Aissani-Benissad, F., (2023). Application of central composite design and response surface methodology for the study of extraction of gentian violet dye in aqueous solution by polystyrene membrane modified with oleic acid. *Environmental Progress & Sustainable Energy*, 42: e14200. https://doi.org/10.1002/ep.14200.

Alam, M. K., Hossain, M. S., Kawsar, M., Bahadur, N. M., & Ahmed, S., (2024). Synthesis of nano-hydroxyapatite using emulsion, pyrolysis, combustion, and sonochemical methods and biogenic sources: a review. *RSC Advances*, 14: 3548–3559. https://doi.org/10.1039/d3ra07559a.

Ali D. A., Saad F. A., Elsawy H. A., (2023). Kinetics and Isotherm Studies for Adsorption of Gentian Violet Dye from Aqueous Solutions Using Synthesized Hydroxyapatite (T Liu, Ed.). *Journal of Environmental and Public Health*, 1–15. https://doi.org/10.1155/2023/7418770 .

Ali, N. S., Harharah, H. N., Salih, I. K., Saady, N. M. C., Zendehboudi, S., & Albayati, T. M., (2023). Applying MCM-48 mesoporous material, equilibrium, isotherm, and mechanism for the effective adsorption of 4-nitroaniline from wastewater. *Scientific Reports*, 13*: 9837*. https://doi.org/10.1038/s41598-023-37090-4.

Ali, N., Ali, F., Said, A., Begum, T., Bilal, M., Rab, A., Sheikh, Z.A., Iqbal, H.M.N., Ahmad, I., (2020). Characterization and deployment of surface-engineered cobalt ferrite nanospheres as photocatalyst for highly efficient remediation of alizarin red S dye from aqueous solution. *Journal of Inorganic Organometaterial Polymer Materrials*, 30 : 5063–5073. https://doi.org/10.1007/s10904-020-01654-y.

Alorku, K., Manoj, M., & Yuan, A. (2020). A plant-mediated synthesis of nanostructured hydroxyapatite for biomedical applications: a review. *RSC Advances*. 10*:* 40923–40939. https://doi.org/10.1039/d0ra08529d.

Al-Qodah Z., Al-Zghoul T. M., Jamrah A., (2024). The performance of pharmaceutical wastewater treatment system of electrocoagulation assisted adsorption using perforated electrodes to reduce passivation. *Environmental Science and Pollution Research*. 31*:* 20434–20448.https://doi.org/10.1007/s11356-024-32458-z.

Anandan, D., & Jaiswal, A. K., (2023). Synthesis methods of hydroxyapatite and biomedical applications: an updated review. *Journal of the Australian Ceramic Society*, 60*:* 663–679. https://doi.org/10.1007/s41779-023-00943-2.

Bai, C., & Colombo, P., (2018). Processing, properties and applications of highly porous geopolymers: A review. *Ceramics International*, 44 *:* 16103–16118. https://doi.org/10.1016/j.ceramint.2018.05.219.

Baidya, K. S., & Kumar, U., (2020). Adsorption of brilliant green dye from aqueous solution onto chemically modified areca nut husk. *South African Journal of Chemical Engineering*, *35*: 33–43. https://doi.org/10.1016/j.sajce.2020.11.001.

Balasooriya, I. L., Chen, J., Gedara, S. M. K., Han, Y., Wickramaratne, M. N., (2022). Applications of Nano Hydroxyapatite as Adsorbents: A Review. *Nanomaterials*, 12*:* 2324. https://doi.org/10.3390/nano12142324.

Barbosa T. R., Foletto E. L., Dotto G. L., Jahn S. L., (2018). Preparation of mesoporous geopolymer using metakaolin and rice husk ash as synthesis precursors and its use as potential adsorbent to remove organic dye from aqueous solutions. *Ceramics International* 44: 416–423. https://doi.org/10.1016/j.ceramint.2017.09.193.

Benalia, A., Baatache, O., Derbal, K., Khalfaoui, A., Amrouci, Z., Pizzi, A., & Panico, A., (2024). The use of central composite design (CCD) to optimize and model the coagulation-

flocculation process using a natural coagulant: Application in jar test and semi-industrial scale. *Journal of Water Process Engineering*, 57: 104704. https://doi.org/10.1016/j.jwpe.2023.104704.

Bhagawan D., Poodari S., Chaitanya N., Ravi S., Rani Y. M., Himabindu V., Vidyavathi S., (2017). Industrial solid waste landfill leachate treatment using electrocoagulation and biological methods. Desalination Water and Treatment, 68:137–142. https://doi.org/10.5004/dwt.2017.20335.

Bhomick, P. C., Supong, A., Baruah, M., Pongener, C., Gogoi, C., & Sinha, D., (2019). Alizarin Red S adsorption onto biomass-based activated carbon: optimization of adsorption process parameters using Taguchi experimental design. *International Journal of Environmental Science and Technology*, 17: 1137–1148. https://doi.org/10.1007/s13762-019-02389-1.

Billah, R. E. K., Zaghloul, A., Ahsaine, H. A., BaQais, A., Khadoudi, I., Messaoudi, N. E., Agunaou, M., Soufiane, A., & Jugade, R., (2022). Methyl orange adsorption studies on glutaraldehyde cross-linking chitosan/fluorapatite-based natural phosphate composite. *International Journal of Environmental & Analytical Chemistry*, 104: 5840–5856. https://doi.org/10.1080/03067319.2022.2130690.

Boudrahem, F., Ziani, S., & Aissani-Benissad, F., (2018). Application of response surface methodology based on central composite design for optimization of yellow bezacryl sorption on shoe soles waste. *Environmental Progress & Sustainable Energy*, 38:S412-S421. https://doi.org/10.1002/ep.13073.

Bouna, L., Fakir, A. E., Benlhachemi, A., Draoui, K., Ezahri, M., Bakiz, B., Villain, S., Guinneton, F., & Elalem, N., (2020). Synthesis and characterization of mesoporous geopolymer based on Moroccan kaolinite rich clay. *Applied Clay Science*, 196: 105764. https://doi.org/10.1016/j.clay.2020.105764.

Brahmi, A., Agsous, M., Benkhaoula, B. N., Ziani, S., Khireddine, H., AitAli, S., Abdullah, M. M., Chai, B. X., & Belaadi, A. (2024). Fluoro-hydroxyapatite/chitosan composites as an eco-friendly adsorbent for direct red 23 dye removal: Optimization through response surface methodology. *Journal of Molecular Structure*, 1321: 140212. https://doi.org/10.1016/j.molstruc.2024.140212.

Brunton, P. A., Davies, R. P. W., Burke, J. L., Smith, A., Aggeli, A., Brookes, S. J., & Kirkham, J., (2013). Treatment of early caries lesions using biomimetic self-assembling peptides – a clinical safety trial. *British Dental Journal*, 215, E6. https://doi.org/10.1038/sj.bdj.2013.741.

Cai, G., Sun, J., Kang, F., Lv, Q., Liu, J., Wang, J., Gao, Z., & Ren, X., (2024). Chitosan Gel Hydroxypropyl Methylcellulose Membranes: A Novel Approach for the Remediation of Cadmium in Aqueous Solutions and Soils. *Coatings*, 14: 421. https://doi.org/10.3390/coatings14040421.

Candamano, S., Coppola, G., Mazza, A., Caranqui, J. C., Bhattacharyya, S., Chakraborty, S., Alexis, F., & Algieri, C., (2023). Batch and fixed bed adsorption of methylene blue onto foamed metakaolin-based geopolymer: A preliminary investigation. *Chemical Engineering Research & Design*, 197: 761–773. https://doi.org/10.1016/j.cherd.2023.08.014

Chaudhary, G. R., Saharan, P., Kumar, A., Mehta, S. K., Mor, S., & Umar, A., (2013). Adsorption Studies of Cationic, Anionic and Azo-Dyes via Monodispersed Fe_3O_4 Nanoparticles. *Journal of Nanoscience and Nanotechnology*, 13: 3240–3245. https://doi.org/10.1166/jnn.2013.7152.

Cheng, T. W., Lee, M. L., Ko, M. S., Ueng, T. H., Yang, S. F., (2012). The heavy metal adsorption characteristics on metakaolin-based geopolymer. Applied Clay Science, 56: 90–96. https://doi.org/10.1016/j.clay.2011.11.027.

Chiroma, T. M., Ebewele, R. O. & Hymore, F. K., (2014). Comparative Assessment of heavy metal levels in soil, vegetables and urban grey water used for irrigation in Yola and Kano. *International Refereed Journal of Engineering and Science*, 3: 1–9. https://www.irjes.com/Papers/vol3-issue2/A03020109.pdf.

Chollom, M. N., Rathilal, S., Swalaha, F. M., Bakare, B. F., & Tetteh, E. K., (2019). Comparison of response surface methods for the optimization of an upflow anaerobic sludge blanket for the treatment of slaughterhouse wastewater. *Environmental Engineering Research*, 25: 114–122. https://doi.org/10.4491/eer.2018.366.

Cong, P., & Cheng, Y. (2021). Advances in geopolymer materials: A comprehensive review. *Journal of Traffic and Transportation Engineering*, 8: 283–314. https://doi.org/10.1016/j.jtte.2021.03.004.

Cox, S. C., Walton, R. I., & Mallick, K. K., (2015). Comparison of techniques for the synthesis of hydroxyapatite. *Bioinspired, Biomimetic and Nanobiomaterials*, 4: 37–47. https://doi.org/10.1680/bbn.14.00010.

Dahlan, I., Obi, C. C., Razaman, N. S., & Hasan, H. Y. A., (2024). Adsorptive decolorization of brilliant green dye in aqueous media using various modified MOF-5 adsorbents. *Groundwater for Sustainable Development*, *26*: 101228. https://doi.org/10.1016/j.gsd.2024.101228.

Davidovits, J., (1991). Geopolymers: Inorganic polymeric new materials *Journal of Thermal Analysis*, 37: 1633–1656. https://doi.org/10.1007/bf01912193.

Davidovits, J., (1988). Geopolymer chemistry and properties. *Proceedings of the 1st International Conference on Geopolymer '88,* Compiegne, 1: 25–48.

Davidovits, J., Huaman, L., & Davidovits, R., (2019). Ancient geopolymer in south-American monument. SEM and petrographic evidence. *Materials Letters*, 235: 120–124. https://doi.org/10.1016/j.matlet.2018.10.033.

Davidovits. J., (2020). Geopolymer Chemistry and Applications, 5th Edition, Institut Geopolymère, France. ISBN: 9782954453118.

Davidovits. J., (2002). years of successes and failures in geopolymer applications. Market trends and potential breakthroughs, Geopolymer 2002 conference, Geopolymer Institute Saint Quentin, France; 836 Melbourne, Australia.

De Oliveira, K. G., Jokipii-Lukkari, S., & Luukkonen, T. (2024). Assessing alkali activation of waste stone wool from greenhouses combined with direct foaming or granulation to obtain recycled plant substrate. *Open Research Europe*, *4*: 26. https://doi.org/10.12688/openreseurope.17101.1.

Dibene, K., Yahiaoui, I., Aitali, S., Khenniche, L., Amrane, A., & Aissani-Benissad, F., (2019). Central composite design applied to paracetamol degradation by heat-activated peroxydisulfate oxidation process and its relevance as a pretreatment prior to a biological treatment. *Environmental Technology*, 42*:* 905–913. https://doi.org/10.1080/09593330.2019.1649308

Djebri, N., Boutahala, M., Chelali, N., Boukhalfa, N., & Larbi, Z., (2017). Adsorption of bisphenol A and 2,4,5-trichlorophenol onto organo-acid-activated bentonite from aqueous solutions in single and binary systems. *Desalination and Water Treatment*, 66: 383–393. https://doi.org/10.5004/dwt.2017.20220.

Duxson, P., Provis, J.L., (2008). Designing precursors for geopolymer cements. Journal American Ceramic Society. 91: 3864–3869. https://doi.org/10.1111/j.1551-2916.2008.02787.x.

Elgarahy, A. M., Maged, A., Eloffy, M., Zahran, M., Kharbish, S., Elwakeel, K. Z., & Bhatnagar, A., (2023). Geopolymers as sustainable eco-friendly materials: Classification, synthesis routes, and applications in wastewater treatment. *Separation and Purification Technology*, 324: 124631. https://doi.org/10.1016/j.seppur.2023.124631.

El-Sayed G. O., (2011). Removal of methylene blue and crystal violet from aqueous solutions by palm kernel fiber. *Desalination*, 272: 225–232. https://doi:10.1016/j.desal.2011.01.025.

Errich, A., Azzaoui, K., Mejdoubi, E., Hammouti, B., Abidi, N., Akartasse, N., Benidire, L., Hajjaji, S. E., Sabbahi, R., & Lamhamdi, A., (2021). Toxic heavy metals removal using a hydroxyapatite and hydroxyethyl cellulose modified with a new Gum Arabic. *Indonesian Journal of Science and Technology*, 6: 41–64. https://doi.org/10.17509/ijost.v6i1.31480.

Ersan, M., Guler, U. A., Acıkel, U., & Sarioglu, M., (2015). Synthesis of hydroxyapatite/clay and hydroxyapatite/pumice composites for tetracycline removal from aqueous solutions. *Process Safety and Environmental Protection/Transactions of the Institution of Chemical Engineers. Part B, Process Safety and Environmental Protection/Chemical Engineering Research and Design/Chemical Engineering Research & Design*, *96*: 22–32. https://doi.org/10.1016/j.psep.2015.04.001.

Fathi, Asfaram, A., & Farhangi, A., (2014). Removal of Direct Red 23 from aqueous solution using corn stalks: Isotherms, kinetics and thermodynamic studies. *Spectrochimica Acta Part a Molecular and Biomolecular Spectroscopy*, *135*: 364–372. https://doi.org/10.1016/j.saa.2014.07.008.

Fayazi, M., Ghanei-Motlagh, M., & Taher, M. A., (2015). The adsorption of basic dye (Alizarin red S) from aqueous solution onto activated carbon/γ-Fe_2O_3 nano-composite: Kinetic and

equilibrium studies. *Materials Science in Semiconductor Processing*, 40: 35–43. https://doi.org/10.1016/j.mssp.2015.06.044.

Feng X., Yan S., Jiang S., Huang K., Ren X., Du X., Xing P., (2021). Green Synthesis of the Metakaolin/slag Based Geopolymer for the Effective Removal of Methylene Blue and Pb (II). *Silicon*, 14: 6965–6979. https://doi.org/10.1007/s12633-021-01439-z .

Fernane, F., Mecherri, M., Sharrock, P., Hadioui, M., Lounici, H., & Fedoroff, M., (2008). Sorption of cadmium and copper ions on natural and synthetic hydroxylapatite particles. *Materials Characterization*, 59: 554–559. https://doi.org/10.1016/j.matchar.2007.04.009.

Fihri, A., Len, C., Varma, R. S., & Solhy, A., (2017). Hydroxyapatite: A review of syntheses, structure and applications in heterogeneous catalysis. *Coordination Chemistry Reviews*, *347*: 48–76. https://doi.org/10.1016/j.ccr.2017.06.009.

Foroutan R., Peighambardoust S. J., Aghdasinia H., Mohammadi R., Ramavandi B., (2020). Modification of bio-hydroxyapatite generated from waste poultry bone with MgO for purifying methyl violet-laden liquids. *Environmental Science and Pollution Research*, 27: 44218–44229. https://doi.org/10.1007/s11356-020-10330-0.

Fu, F., Gao, Z., Gao, L., & Li, D., (2011). Effective Adsorption of Anionic Dye, Alizarin Red S, from Aqueous Solutions on Activated Clay Modified by Iron Oxide. *Industrial & Engineering Chemistry Research*, 50: 9712–9717. https://doi.org/10.1021/ie200524b.

Gao, M., Wang, W., Yang, H., & Ye, B. C., (2019). Hydrothermal synthesis of hierarchical hollow hydroxyapatite microspheres with excellent fluoride adsorption property. *Microporous and Mesoporous Materials*, 289: 109620. https://doi.org/10.1016/j.micromeso.2019.109620.

Ge, Y., Cui, X., Kong, Y., Li, Z., He, Y., & Zhou, Q., (2015). Porous geopolymeric spheres for removal of Cu(II) from aqueous solution: Synthesis and evaluation. *Journal of Hazardous Materials*, 283: 244–251. https://doi.org/10.1016/j.jhazmat.2014.09.038.

Ghemit, R., Makhloufi, A., Djebri, N., Flilissa, A., Zerroual, L., & Boutahala, M., (2019). Adsorptive removal of diclofenac and ibuprofen from aqueous solution by organobentonites: Study in single and binary systems. *Groundwater for Sustainable Development*, *8*: 520–529. https://doi.org/10.1016/j.gsd.2019.02.004.

Glukhovsky, V.D., (1994). Ancient, modern and future concretes. *Proceedings of the 1st International Conference on Alkaline Cements and Concretes*, Company, Kiev, Ukraine, pp. 1–9.

Gomaa H., Abd El-Monaem E. M., Eltaweil A. S., Omer A. M., (2022). Efficient removal of noxious methylene blue and crystal violet dyes at neutral conditions by reusable montmorillonite/$NiFe_2O_4$@amine-functionalized chitosan composite. *Scientific Reports*, 12: 15499. https://doi.org/10.1038/s41598-022-19570-1.

Gonçalves, N. P., Olhero, S. M., Labrincha, J. A., & Novais, R. M., (2022). 3D-printed red mud/metakaolin-based geopolymers as water pollutant sorbents of methylene blue. *Journal of Cleaner Production*, 383: 135315. https://doi.org/10.1016/j.jclepro.2022.135315.

Gopal, N., Asaithambi, M., Sivakumar, P., & Sivakumar, V., (2014). Adsorption studies of a direct dye using polyaniline coated activated carbon prepared from Prosopis juliflora. *Journal of Water Process Engineering*, 2: 87–95. https://doi.org/10.1016/j.jwpe.2014.05.008.

Guan, Y., Cao, W., Guan, H., Lei, X., Wang, X., Tu, Y., Marchetti, A., & Kong, X., (2018). A novel polyalcohol-coated hydroxyapatite for the fast adsorption of organic dyes. *Colloids and Surfaces. A, Physicochemical and Engineering Aspects*, *548*: 85–91. https://doi.org/10.1016/j.colsurfa.2018.03.054.

Gupta, N., Kushwaha, A. K., & Chattopadhyaya, M., (2012). Adsorptive removal of Pb2+, Co^{2+} and Ni^{2+} by hydroxyapatite/chitosan composite from aqueous solution. *Journal of the Taiwan Institute of Chemical Engineers*. 43: 125-131. https://doi.org/10.1016/j.jtice.2011.07.009.

Hebeish, A., Ramadan, M. A., Abdel-Halim, E., & Abo-Okeil, A., (2011). An effective adsorbent based on sawdust for removal of direct dye from aqueous solutions. *Clean Technologies and Environmental Policy*, 13: 713–718. https://doi.org/10.1007/s10098-010-0343-z.

Mahvi, A. H., & Dalvand, A., (2019). Kinetic and equilibrium studies on the adsorption of Direct Red 23 dye from aqueous solution using montmorillonite nanoclay. *Water Quality Research Journal*, 55: 132–144. https://doi.org/10.2166/wqrj.2019.008.

Hosseinian, A., Pettersson, A., Ylä-Mella, J., & Pongrácz, E., (2023). Phosphorus recovery methods from secondary resources, assessment of overall benefits and barriers with focus on

the Nordic countries. *Journal of Material Cycles and Waste Management*, *25*: 3104–3116. https://doi.org/10.1007/s10163-023-01747-z.

Ibrahim, M., Ibrahim, W.M.W., Al Bakri Abdullah, M.M., Sauffi, A.S., Vizureanu, P., (2022). Effect of Solid-To-Liquids and Na2SiO3-To-NaOH Ratio on Metakaolin Membrane Geopolymers. Archives of Metallurgy and Materials, 67: 695–702. https://doi.org/10.24425/amm.2022.137808.

Jasrotia, R., Singh, J., Mittal, S., & Singh, H., (2022). Synthesis of CTAB modified ferrite composite for the efficient removal of brilliant green dye. *International Journal of Environmental & Analytical Chemistry*, 104: 1–17. https://doi.org/10.1080/03067319.2022.2098485.

Jiang, J., Long, Y., Hu, X., Hu, J., Zhu, M., & Zhou, S., (2020). A facile microwave-assisted synthesis of mesoporous hydroxyapatite as an efficient adsorbent for Pb2+ adsorption. *Journal of Solid State Chemistry*, *289*:121491. https://doi.org/10.1016/j.jssc.2020.121491.

Jiang, R., Yu, G., Ndagijimana, P., Wang, Y., You, F., Xing, Z., & Wang, Y., (2021). Effective adsorption of Direct Red 23 by sludge biochar-based adsorbent: adsorption kinetics, thermodynamics and mechanisms study. *Water Science & Technology*, 83: 2424–2436. https://doi.org/10.2166/wst.2021.126.

Kannan, M., (2015). Hydroxyapatite coating on biodegradable magnesium and magnesium-based alloys. In *Elsevier eBooks*, 289–306. https://doi.org/10.1016/b978-1-78242-033-0.00013-4.

Katowah, D. F., & Alzahrani, H. K., (2023). A New ternary nanocomposites-based cellulose derivatives-CuFe2O4-Zeolite with ultra-high adsorption capacity for Brilliant Green dye treatment and removal from the aquatic environment. *Journal of Saudi Chemical Society*, 27: 101764. https://doi.org/10.1016/j.jscs.2023.101764**.**

Kaya-Özkiper, K., Uzun, A., & Soyer-Uzun, S., (2022). Tuning adsorption, structure and compressive strength of sepiolite- and metakaolin-based alkali activated monoliths for methylene blue removal from waste water. *Surfaces and Interfaces*, *33*: 102110. https://doi.org/10.1016/j.surfin.2022.102110.

Kjidaa, B., Mchich, Z., Aziz, K., Saffaj, N., Saffaj, T., & Mamouni, R., (2024). Flexible Synthesis of Bio-Hydroxyapatite/Chitosan Hydrogel Beads for Highly Efficient Orange G Dye

Removal: Batch and Recirculating Fixed-Bed Column Study. *ACS Omega*, 9: 8543–8556. https://doi.org/10.1021/acsomega.3c10054.

Koraqi, H., Aydar, A. Y., Khalid, W., Ercisli, S., Rustagi, S., Ramniwas, S., & Pandiselvam, R., (2024). Ultrasound-assisted extraction with natural deep eutectic solvent for phenolic compounds recovery from Rosa damascene Mill.: Experimental design optimization using central composite design. *Microchemical Journal*, *196*: 109585. https://doi.org/10.1016/j.microc.2023.109585.

Krivenko, P. V., Kovalchuk, G.Y., (2007). Directed synthesis of alkaline aluminosilicate minerals in a geocement matrix. Journal of Materials Science, 42: 2944–2952. https://doi.org/10.1007/s10853-006-0528-3.

Kumar, A., Saravanan, T.J., Bisht, K., Kabeer, K.I.S.A., (2021). A review on the utilization of red mud for the production of geopolymer and alkali activated concrete. Construction and Building Materials, 302: 124170 https://doi.org/10.1016/J. CONBUILDMAT.2021.124170.

Laabd, M., Brahmi, Y., Ibrahimi, B. E., Hsini, A., Toufik, E., Abdellaoui, Y., Oualid, H. A., Ouardi, M. E., & Albourine, A., (2021). A novel mesoporous Hydroxyapatite@Montmorillonite hybrid composite for high-performance removal of emerging Ciprofloxacin antibiotic from water: Integrated experimental and Monte Carlo computational assessment. *Journal of Molecular Liquids*, *338*: 116705. https://doi.org/10.1016/j.molliq.2021.116705.

Li Y., Zhang Y., Zhang Y., Wang G., Li S., Han R., Wei W., (2018). Reed biochar supported hydroxyapatite nanocomposite: Characterization and reactivity for methylene blue removal from aqueous media. *Journal of Molecular Liquids*, 263: 53–63. https://doi.org/10.1016/j.molliq.2018.04.132 OK.

Lin, F. H., Liao, C. J., Chen, K. S., Sun, J. S., & Lin, C. P., (2001). Petal-like apatite formed of the surface of tricalcium phosphate ceramic after soaking in distilled water. Biomaterials, 22: 2981–2992. https://doi.org/10.1016/s0142-9612(01)00044-8.

Lin, K., & Chang, J., (2015). Structure and properties of hydroxyapatite for biomedical applications. In *Elsevier eBooks*, 3–19. https://doi.org/10.1016/b978-1-78242-033-0.00001-8.

Liu, D., Shi, Q., Liu, C., Sun, Q., & Zeng, X., (2023). Effects of Endocrine-Disrupting Heavy Metals on Human Health. *Toxics*, 11: 322. https://doi.org/10.3390/toxics11040322.

Liu, N., Wang, H., Weng, C. H., & Hwang, C. C., (2018). Adsorption characteristics of Direct Red 23 azo dye onto powdered tourmaline. *Arabian Journal of Chemistry*, *11:* 1281–1291. https://doi.org/10.1016/j.arabjc.2016.04.010.

Liu, Y., Meng, Y., Qiu, X., Zhou, F., Wang, H., Zhou, S., Yan, C., (2022). Novel porous phosphoric acid-based geopolymer foams for adsorption of Pb(II), Cd(II) and Ni(II) mixtures: Behavior and mechanism. Ceramics International, 49: 7030-7039. https://doi.org/10.1016/j.ceramint.2022.10.164.

Lun H, Ouyang J, Yang H., (2014). Enhancing dispersion of halloysite nanotubes via chemical modification. Phys Chem Minerals, 41:281–288. https://doi.org/10.1007/s00269-013-0646-9.

Luukkonen, T., Heponiemi, A., Runtti, H., Pesonen, J., Yliniemi, J., & Lassi, U., (2019). Application of alkali-activated materials for water and wastewater treatment: a review. *Reviews in Environmental Science and Bio/Technology*, 18: 271–297. https://doi.org/10.1007/s11157-019-09494-0.

Mahanty, A., & Shikha, D., (2024). Design of a new Ag/Mg/Zn alloyed doped hydroxyapatite hybrid biomaterial. *Materials Chemistry and Physics*, 311: 128553. https://doi.org/10.1016/j.matchemphys.2023.128553.

Mahmoud M. E., Nabil G. M., Khalifa M. A., El-Mallah N. M., Hassouba H. M., (2019). Effective removal of crystal violet and methylene blue dyes from water by surface functionalized zirconium silicate nanocomposite. *Journal of Environmental Chemical Engineering*, 7: 103009.https://doi.org/10.1016/j.jece.2019.103009.

Maiti, P., Siddiqi, H., Kumari, U., Chatterjee, A., & Meikap, B., (2023). Adsorptive remediation of azo dye contaminated wastewater by $ZnCl_2$ modified bio-adsorbent: Batch study and life cycle assessment. *Powder Technology*, 415: 118153. https://doi.org/10.1016/j.powtec.2022.118153.

Mansour, R., Simeda, M. G., & Zaatout, A., (2020). Adsorption studies on brilliant green dye in aqueous solutions using activated carbon derived from guava seeds by chemical activation

with phosphoric acid. *Desalination and Water Treatment*, 202: 396–409. https://doi.org/10.5004/dwt.2020.26147.

Mansourri, G., & Madani, M., (2016). Examination of the Level of Heavy Metals in Wastewater of Bandar Abbas Wastewater Treatment Plant. *Open Journal of Ecology*, 6*:* 55–61. https://doi.org/10.4236/oje.2016.62006.

Mathew, M., Schroeder, L. W., Dickens, B., & Brown, W. E., (1977). The crystal structure of α-Ca3(PO4)2. *Acta Crystallographica. Section B, Structural Crystallography and Crystal Chemistry*, 33*:* 1325–1333. https://doi.org/10.1107/s0567740877006037.

McGonigle, D. F., Burke, S. P., Collins, A. L., Gartner, R., Haft, M. R., Harris, R. C., Haygarth, P. M., Hedges, M. C., Hiscock, K. M., & Lovett, A. A., (2014). Developing Demonstration Test Catchments as a platform for transdisciplinary land management research in England and Wales. *Environmental Science Processes & Impacts*, 16: 1618–1628. https://doi.org/10.1039/c3em00658a.

Medri V., Papa E., Lizion J., Landi E., (2020) Metakaolin-based geopolymer beads: Production methods and characterization. *Journal of Cleaner Production*, 244: 118844. https://doi.org/10.1016/j.jclepro.2019.118844 118844.

Megherbi, H., Runtti, H., Tuomikoski, S., Heponiemi, A., Hu, T., Lassi, U., & Reffas, A., (2024). The effect of phosphoric acid on the properties of Activated Carbons made from Myrtus communis Leaves: Textural characteristics, surface chemistry, and capacity to adsorb Methyl orange. *Journal of Molecular Structure*,1321: 140038. https://doi.org/10.1016/j.molstruc.2024.140038.

Meski, S., Ziani, S., & Khireddine, H., (2010). Removal of Lead Ions by Hydroxyapatite Prepared from the Egg Shell. *Journal of Chemical and Engineering Data/Journal of Chemical & Engineering Data*, 55; 3923–3928. https://doi.org/10.1021/je901070e.

Meski, S., Ziani, S., Khireddine, H., Boudboub, S., & Zaidi, S., (2011). Factorial design analysis for sorption of zinc on hydroxyapatite. *Journal of Hazardous Materials*, 186: 1007–1017. https://doi.org/10.1016/j.jhazmat.2010.11.087.

Meski, S., Ziani, S., Khireddine, H., Yataghane, F., & Ferguene, N., (2011). Elaboration of the hydroxyapatite with different precursors and application for the retention of the lead. *Water Science & Technology*, 63*:* 2087–2096. https://doi.org/10.2166/wst.2011.210.

Michelsen, D. L., Gideon, J. A., Griffith, G. P., Pace, J. E., & Kutat, H. L., (1975). *Removal of soluble mercury from waste water by complexing techniques*. Bultin 74. http://hdl.handle.net/10919/25731.

Moriguchi, T., Yano, K., Nakagawa, S., & Kaji, F., (2003). Elucidation of adsorption mechanism of bone-staining agent alizarin red S on hydroxyapatite by FT-IR microspectroscopy. *Journal of Colloid and Interface Science*, 260: 19–25. https://doi.org/10.1016/s0021-9797(02)00157-1.

Muhammad, N. a. A., & Musa, N. S., (2022). Study on Adsorption of Alizarin Red S and Eriochrome Black T Dyes by Untreated Typha Grass as a Low Cost Adsorbent. *UMYU Scientifica*, 1 : 155–165. https://doi.org/10.56919/usci.1122.020.

Nasab, S. G., Semnani, A., Teimouri, A., Kahkesh, H., Isfahani, T. M., & Habibollahi, S., (2018). Removal of Congo Red from Aqueous Solution by Hydroxyapatite Nanoparticles Loaded on Zein as an Efficient and Green Adsorbent: Response Surface Methodology and Artificial Neural Network-Genetic Algorithm. *Journal of Polymers and the Environment*, 26: 3677–3697. https://doi.org/10.1007/s10924-018-1246-z.

Nayl, A.A., Abd-Elhamid, A.I., Ahmed, I.M., Brase, S., (2022). Preparation and characterization of magnetite talc (Fe_3O_4@Talc) nanocomposite as an effective adsorbent for Cr(VI) and alizarin red S dye. *Materials*, 15: 3401. https://doi.org/10.3390/ma15093401.

Ni, P., & Fox, J. T., (2019). Synthesis and appraisal of a hydroxyapatite/pectin hybrid material for zinc removal from water. *RSC Advances*, 9: 21095–21105. https://doi.org/10.1039/c9ra03710a.

Normi, N. I., Abdulhameed, A. S., Jawad, A. H., Surip, S. N., Razuan, R., & Ibrahim, M. L., (2022). Hydrothermal-Assisted Grafting of Schiff base Chitosan by Salicylaldehyde for Adsorptive Removal of Acidic Dye: Statistical Modeling and Adsorption Mechanism. *Journal of Polymers and the Environment*, 31:1925–1937. https://doi.org/10.1007/s10924-022-02730-9.

Ofudje, E. A., Adedapo, A. E., Oladeji, O. B., Sodiya, E. F., Ibadin, F. H., & Zhang, D., (2021). Nano-rod hydroxyapatite for the uptake of nickel ions: Effect of sintering behaviour on adsorption parameters. *Journal of Environmental Chemical Engineering*, 9: 105931. https://doi.org/10.1016/j.jece.2021.105931.

Ohale, P. E., Chukwudi, K., Ndive, J. N., Michael, M. E., Abonyi, M. N., Chukwu, M. M., Obi, C. C., Onu, C. E., Igwegbe, C. A., & Azie, C. O., (2023). Optimization of Fe2O3@BC-KC composite preparation for adsorption of Alizarin red S dye: Characterization, kinetics, equilibrium, and thermodynamic studies. *Results in Surfaces and Interfaces*, *13*: 100157. https://doi.org/10.1016/j.rsurfi.2023.100157.

Oliveira, K. G., Botti, R., Kavun, V., Gafiullina, A., Franchin, G., Repo, E., & Colombo, P., (2022). Geopolymer beads and 3D printed lattices containing activated carbon and hydrotalcite for anionic dye removal. *Catalysis Today*, 390–391: 57–68. https://doi.org/10.1016/j.cattod.2021.12.002.

Ozder, M. N., Ciftci, F., Rencuzogullari, O., Arisan, E. D., & Ustündag, C. B., (2023). In situ synthesis and cell line studies of nano-hydroxyapatite/graphene oxide composite materials for bone support applications. *Ceramics International*, 49 : 14791–14803. https://doi.org/10.1016/j.ceramint.2023.01.075.

Panagiotopoulou, C., Kontori, E., Perraki, T., Kakali, G., (2007). Dissolution of aluminosilicate minerals and by-products in alkaline media. Journal of Materials Science, 42: 2967–2973. https://doi.org/10.1007/s10853-006-0531-8.

Papa, E., Landi, E., Miccio, F., Medri, V., (2022). K_2O-metakaolin-based geopolymer foams: production, porosity characterization and permeability test. *Materials,* 15: 1-14. https://doi.org/10.3390/ma15031008 .

Peng, X., Li, H., Shuai, Q., Wang, L., (2020). Fire resistance of alkali activated geopolymer foams produced from metakaolin and Na2O2. Materials (Basel). 13: 1–8. https://doi.org/10.3390/ma13030535.

Panneerselvam, K., Arul, K. T., Warrier, A. R., Asokan, K., & Dong, C., (2019). Rapid adsorption of industrial pollutants using metal ion doped hydroxyapatite. *AIP Conference Proceedings*. 2117: 020004, https://doi.org/10.1063/1.5114584.

Pereira, M., França, D., Araújo, R. C., Filho, E. C. S., Rigaud, B., Fonseca, M., & Jaber, M., (2020). Amino hydroxyapatite/chitosan hybrids reticulated with glutaraldehyde at different pH

values and their use for diclofenac removal. *Carbohydrate Polymers*, 236: 116036. https://doi.org/10.1016/j.carbpol.2020.116036.

Pu'ad, N. M., Haq, R. A., Noh, H. M., Abdullah, H., Idris, M., & Lee, T., (2020). Synthesis method of hydroxyapatite: A review. *Materials Today: Proceedings*, 29: 233–239. https://doi.org/10.1016/j.matpr.2020.05.536.

Ragab, A., Ahmed, I., & Bader, D., (2019). The Removal of Brilliant Green Dye from Aqueous Solution Using Nano Hydroxyapatite/Chitosan Composite as a Sorbent. *Molecules*, 24 *:* 847. https://doi.org/10.3390/molecules24050847.

Rahman, M. A., Habib, M. L., Chisty, A. H., Mallik, A. K., Khan, M. N., Haque, P., & Rahman, M. M., (2021). Organic–Inorganic Polymer Hybrids for Water and Wastewater Treatment. In *Environmental footprints and eco-design of products and processes*, 29–54. https://doi.org/10.1007/978-981-16-5916-4_2.

Rao, C. V., Giri, A. S., Goud, V. V., & Golder, A. K., (2015). Studies on pH-dependent color variation and decomposition mechanism of Brilliant Green dye in Fenton reaction. *International Journal of Industrial Chemistry*, 7: 71–80. https://doi.org/10.1007/s40090-015-0060-x.

Rashad, A.M., Gharieb, M., Shoukry, H., Mokhtar, M.M., (2022). Valorization of sugar beet waste as a foaming agent for metakaolin geopolymer activated with phosphoric acid. Construction and Building Materials, 344: 128240. https://doi.org/10.1016/j.conbuildmat.2022.128240.

Ren, B., Zhao, Y., Bai, H., Kang, S., Zhang, T., & Song, S., (2021). Eco-friendly geopolymer prepared from solid wastes: A critical review. *Chemosphere*, 267 : 128900. https://doi.org/10.1016/j.chemosphere.2020.128900.

Renda, C. G., De Oliveira Ruellas, T. M., Malafatti, J. O. D., Araújo, C. S. S., Da Silva, G. L., Figueira, B. a. M., Quaranta, S., & Paris, E. C., (2023). A "Zero-Cost" Adsorbing Hydroxyapatite-Based Material from Amazon Fishery Waste for Water Remediation and Nutrient Release for Agriculture. *Physchem*, 3: 34–60. https://doi.org/10.3390/physchem3010004.

Rossatto, D., Netto, Jahn, S., Mallmann, E., Dotto, G., & Foletto, E., (2020). Highly efficient adsorption performance of a novel magnetic geopolymer/Fe3O4 composite towards removal of aqueous acid green 16 dye. *Journal of Environmental Chemical Engineering*, 8: 103804. https://doi.org/10.1016/j.jece.2020.103804.

Rożek, P., Król, M., & Mozgawa, W., (2019). Geopolymer-zeolite composites: A review. *Journal of Cleaner Production*, 230, 557–579. https://doi.org/10.1016/j.jclepro.2019.05.152.

Sadat-Shojai, M., Khorasani, M. T., Dinpanah-Khoshdargi, E., & Jamshidi, A., (2013). Synthesis methods for nanosized hydroxyapatite with diverse structures. *Acta Biomaterialia*, 9: 7591–7621. https://doi.org/10.1016/j.actbio.2013.04.012.

Sahoo, J. K., Konar, M., Rath, J., Kumar, D., & Sahoo, H., (2019). Magnetic hydroxyapatite nanocomposite: Impact on eriochrome black-T removal and antibacterial activity. *Journal of Molecular Liquids*, 294: 111596. https://doi.org/10.1016/j.molliq.2019.111596.

Shini, J. J. P., Prabu, H. J., Sahayaraj, A. F., Johnson, I., Thaninayagam, E., Gopi, R., & Snowlin, V., (2024). Synthesis of hydroxyapatite (HAp) from eggshells via thermal decomposition method for the application of dye adsorption. *Journal of the Indian Chemical Society*, 101: 101321. https://doi.org/10.1016/j.jics.2024.101321.

Salam, M. A., Mokhtar, M., Albukhari, S. M., Baamer, D. F., Palmisano, L., & Abukhadra, M. R., (2021). Insight into the role of the zeolitization process in enhancing the adsorption performance of kaolinite/diatomite geopolymer for effective retention of Sr (II) ions; batch and column studies. *Journal of Environmental Management*, 294: 112984. https://doi.org/10.1016/j.jenvman.2021.112984.

Sanguanpak, S., Wannagon, A., Saengam, C., Chiemchaisri, W., & Chiemchaisri, C., (2021). Porous metakaolin-based geopolymer granules for removal of ammonium in aqueous solution and anaerobically pretreated piggery wastewater. *Journal of Cleaner Production*, 297: 126643. https://doi.org/10.1016/j.jclepro.2021.126643.

Sasikumar, S., & Vijayaraghavan, R., (2008). Solution combustion synthesis of bioceramic calcium phosphates by single and mixed fuels—A comparative study. *Ceramics International*, 34 :1373–1379. https://doi.org/10.1016/j.ceramint.2007.03.009.

Shokri, E., Khanghahi, B., Esmizadeh, E., & Etemadi, H., (2021). Biopolymer-based adsorptive membrane for simultaneous removal of cationic and anionic heavy metals from water.

International Journal of Environmental Science and Technology, 19: 4167–4180. https://doi.org/10.1007/s13762-021-03592-9.

Singh, S., Mandal, M., Mishra, T., Angayarkanni, A., Veldurthi, N. K., & Pati, S. S., (2023). facile synthesis of citric acid functionalized Fe_3O_4@activated carbon magnetic nanocomposite for efficient adsorption of brilliant green dye from wastewater. *Chemistry Select*, 8: e202205045. https://doi.org/10.1002/slct.202205045.

Surmeneva, M.A., Ivanova, A.A., Tian, Q., Pittman, R., Jiang, W., Lin, J., Liu, H.H., Surmenev, R.A., (2019). Bone marrow derived mesenchymal stem cell response to the RF magnetron sputter deposited hydroxyapatite coating on AZ91 magnesium alloy. Materials Chemistry and Physics, 221: 89–98. https://doi: 10.1016/j.matchemphys.2018.09.030

Vithalkar, S., Jugade, R. M., & Saravanan, D., (2022). Adsorption of brilliant green dye by used-tea-powder: equilibrium, kinetics and thermodynamics studies. *Journal of Water Supply Research and Technology—AQUA*, 71*:* 1148–1158. https://doi.org/10.2166/aqua.2022.076 .

Wang, J., Chen, W., Zhang, M., Zhou, R., Li, J., Zhao, W., & Wang, L., (2021). Optimize the preparation of Fe3O4-modified magnetic mesoporous biochar and its removal of methyl orange in wastewater. *Environmental Monitoring and Assessment*, 193: 179. https://doi.org/10.1007/s10661-021-08971-w .

Wang, R., Tang, H., Yang, R., & Zhang, J., (2024). Emerging contaminants in water environments: progress, evolution, and prospects. *Water Science & Technology*, 89: 2763–2782. https://doi.org/10.2166/wst.2024.151.

Wang, S., Nam, H., & Nam, H., (2020). Preparation of activated carbon from peanut shell with KOH activation and its application for H_2S adsorption in confined space. *Journal of Environmental Chemical Engineering*, 8: 103683. https://doi.org/10.1016/j.jece.2020.103683.

Wang, X., Wang, Z., Jiang, S., Jordan, R. W., & Gu, Y., (2023). Bioenrichment preference and human risk assessment of arsenic and metals in wild marine organisms from Dapeng (Mirs) Bay, South China Sea. *Marine Pollution Bulletin*, 194: 115305. https://doi.org/10.1016/j.marpolbul.2023.115305.

Wattanarach, S., Supothina, S., Thavorniti, P., (2022). Preparation and properties of metakaolin-based porous geopolymer formed with sodium perborate. Journal of Asian Ceramic Societies, 10: 567–574. https://doi.org/10.1080/21870764.2022.2088755.

Wei, E., Wang, K., Muhammad, Y., Chen, S., Dong, D., Wei, Y., & Fujita, T., (2022). Preparation and conversion mechanism of different geopolymer-based zeolite microspheres and their adsorption properties for Pb^{2+}. *Separation and Purification Technology*, 282: 119971. https://doi.org/10.1016/j.seppur.2021.119971.

Wei, H., Yi, M., Li, X., Shao, L., Gao, F., Cui, X., & Wang, K., (2023). Preparation of metakaolin-based geopolymer microspheres (MK@GMs) and efficient adsorption of F- from acidic wastewater. *Separation and Purification Technology*, 310: 123159. https://doi.org/10.1016/j.seppur.2023.123159.

Wei, X., Wang, Y., Chen, J., Liu, Z., Xu, F., He, X., Li, H., & Zhou, Y., (2020). Fabrication of di-selective adsorption platform based on deep eutectic solvent stabilized magnetic polydopamine: Achieving di-selectivity conversion through adding $CaCl_2$. *Chemical Engineering Journal*, 421: 127815. https://doi.org/10.1016/j.cej.2020.127815.

Welch, J. H., & Gutt, W., (1961). 874. High-temperature studies of the system calcium oxide–phosphorus pentoxide. *Journal of the Chemical Society (Resumed)*, 0*;* 4442–4444. https://doi.org/10.1039/jr9610004442.

Wt, X., Zd, R., Yf, Gao., (2011) Removal of phosphorus from high phosphorus iron ores by selective HCl leaching method, *Journal of Iron and Steel Research International*, 18: 1–4, https://doi. org/10.1016/S1006-706X(11)60055-1.

Xia, X., Shen, J., Cao, F., Wang, C., Tang, M., Zhang, Q., & Wei, S., (2019). A facile synthesis of hydroxyapatite for effective removal strontium ion. *Journal of Hazardous Materials*, *368*: 326–335. https://doi.org/10.1016/j.jhazmat.2019.01.040.

Xiang, Y., Hou, L., Liu, J., Li, J., Lu, Z., & Niu, Y., (2021). Adsorption and enrichment of simulated 137Cs in geopolymer foams. *Journal of Environmental Chemical Engineering*, 9: 105733. https://doi.org/10.1016/j.jece.2021.105733.

Tanizawa.Y., (2005) Reaction characteristics of a tooth-bleaching agent containing H_2O_2 and NaF: in vitro study of crystal structure change in treated hydroxyapatite and chemical states of

incorporated fluorine, *International Journal of cosmetic science*, 27: 253-254 https://doi.org/10.1111/j.0142-5463.2005.00276_2.x.

Yahiaoui, K., Boudrahem, F., Ziani, S., Yahiaoui, I., & Aissani-Benissad, F., (2020). Removal studies of Pb (II) ions by carbon powder prepared from polyethylene terephthalate (PET) bottles. *International Journal of Environmental & Analytical Chemistry*, 102: 6670–6683. https://doi.org/10.1080/03067319.2020.1814272.

Yan, S., Ren, X., Zhang, F., Huang, K., Feng, X., & Xing, P., (2022). Comparative study of Pb^{2+}, Ni^{2+}, and methylene blue adsorption on spherical waste solid-based geopolymer adsorbents enhanced with carbon nanotubes. *Separation and Purification Technology*, 284: 120234. https://doi.org/10.1016/j.seppur.2021.120234.

Yang, Q., Chen, J., Liu, Y., Li, Y., Zhang, H., Zhang, J., Sun, X., Lu, M., Ma, R., & Wu, Y., (2024). Analysis of changes in water quality and treatment effectiveness of seven major river basins in China from 2001 to 2020. *Frontiers in Environmental Science*, 12: 1-22. https://doi.org/10.3389/fenvs.2024.1340994.

Younis S. A., Abd-Elaziz A., Hashem A. I., (2016). Utilization of a pyrrole derivative based antimicrobial functionality impregnated onto CaO/g-C_3N_4 for dyes adsorption. *RSC Advances* 6: 89367–89379. https://doi.org/10.1039/C6RA10143G.

Yu, Y., Perumal, P., Corfe, I. J., Paul, T., Illikainen, M., & Luukkonen, T., (2023). Combined granulation–alkali activation–direct foaming process: A novel route to porous geopolymer granules with enhanced adsorption properties. *Materials & Design*, 227:111781. https://doi.org/10.1016/j.matdes.2023.111781.

Zafar, A., Yasir, M. & Khalid, M., (2024). Development of Piperine-Loaded Soft Binary Ethosomal Gel to Improve Transdermal Delivery: Box-Bhekhen Design Optimization, Ex-Vivo Permeation, and Antimicrobial Evaluation. *Journal of Cluster Science*, 35: 311–325 https://doi.org/10.1007/s10876-023-02479-8.

Zhang, X., Ren, B., Li, X., Liu, B., Wang, S., Yu, P., Xu, Y., & Jiang, G., (2021). High-efficiency removal of tetracycline by carbon-bridge-doped g-C_3N_4/Fe_3O_4 magnetic heterogeneous catalyst through photo-Fenton process. *Journal of Hazardous Materials*, 418: 126333. https://doi.org/10.1016/j.jhazmat.2021.126333.

Zhang, Z., Zhu, H., Zhou, C., & Wang, H., (2015). Geopolymer from kaolin in China: An overview. *Applied Clay Science*, 119*:* 31–41. https://doi.org/10.1016/j.clay.2015.04.023.

Zhou, C., Wang, X., Wang, Y., Song, X., Fang, D., & Ge, S., (2021). The sorption of single- and multi-heavy metals in aqueous solution using enhanced nano-hydroxyapatite assisted with ultrasonic. *Journal of Environmental Chemical Engineering*, *9*: 105240. https://doi.org/10.1016/j.jece.2021.105240.

Zhuang, Y., Guo, Y., Li, J., Jiang, K., Zhang, H., & Meng, D., (2021). Study on process and parameter optimisation of selective laser sintering of thermoplastic polyurethane/carbon nanotube powder. *The International Journal of Advanced Manufacturing Technology*, 116*:* 993–1001. https://doi.org/10.1007/s00170-021-07482-9.

Annex

Hybrid Advances 5 (2024) 100134

Contents lists available at ScienceDirect

Hybrid Advances

journal homepage: www.journals.elsevier.com/hybrid-advances

Research Article

Porous metakaolin geopolymer as a reactive binder for hydroxyapatite adsorbent granules in dye removal

Aghilas Brahmi [a,b], Salima Ziani [a,c], Salima AitAli [a,c], Bachir Nadir Benkhaoula [d], Yangmei Yu [b], Hania Ahouari [e,f], Hafit Khireddine [c], Tero Luukkonen [b,g,*]

[a] Laboratoire des Matériaux et Développement Durable (LMDD), Département de Génie des Procédés, Faculté des Sciences et Sciences Appliquées, Université A.M.O, Bouira, 10000, Algeria
[b] University of Oulu, Fibre and Particle Engineering Research Unit, P.O. Box 4300, FI-90014, Finland
[c] Laboratoire de Génie de L'Environnement (LGE), Faculté de Technologie, Université A. MIRA, Route de Targua Ouzemour, 06000, Bejaia, Algeria
[d] Laboratoire de Physico-Chimie des Matériaux, Catalyse et Environnement-LPCM-CE, Université des Sciences et de La Technologie D'Oran Mohamed Boudiaf (USTO-MB), BP 1505, El M'naouer, 31000, Oran, Algeria
[e] Institut Michel-Eugène Chevreul, Université de Lille, FR2638, 59655, Lille, France
[f] Laboratoire de Spectroscopie pour Les Interactions, La Réactivité et L'environnement, Université de Lille, CNRS, LASIRE UMR 8516, F-59000, Lille, France
[g] Department of Chemical Engineering Technology, University of Johannesburg, P.O. Box 17011, Doornfontein, 2088, South Africa

ARTICLE INFO

Keywords:
Adsorption
Brilliant green
Geopolymer
Granulation
Hydroxyapatite
Wastewater treatment

ABSTRACT

In this study, porous hydroxyapatite-metakaolin geopolymer (HAP-MK-GP) granules were prepared with a novel method for adsorption of organic pollutants from aqueous solutions, using brilliant green dye as a model compound. The preparation involved combining finely powdered hydroxyapatite, metakaolin, and solid sodium metasilicate in a high-shear granulator. Then, hydrogen peroxide (H_2O_2) was added at different concentrations (0.0, 5.0, 7.5, or 10.0%) as a combined granulation fluid and blowing agent. In the resulting granules, metakaolin geopolymer bound the powdered hydroxyapatite as granules and contributed to the adsorption capacity. To determine their structural, morphological, and mechanical properties, the granules were characterized with infrared spectroscopy, X-ray fluorescence, scanning electron microscopy, specific surface area and porosity analysis, and compressive strength tests. The granules had a high porosity and promising compressive strength and Young's modulus of 0.8 and 10 MPa, respectively, potentially enabling their use in large-scale adsorption columns. The monolayer adsorption mechanism of brilliant green dye onto HAP-MK-GP granules was confirmed by fitting the obtained batch adsorption data to the Langmuir isotherm model which showed that the adsorption capacity was approximately 41 mg/g. The optimum conditions were: pH of 7, initial dye concentration of 100 mg/L, adsorbent dose of 3 g/L, agitation speed of 250 rpm, contact time of 30 min, and temperature of 298 K. The adsorption kinetic data indicated that the adsorption followed the pseudo-second-order kinetic model. The thermodynamic parameters, including Gibbs free energy, enthalpy, entropy, and activation energy, indicated that adsorption was spontaneous, endothermic, and was based on physisorption. The rate-limiting step was film diffusion. Based on the results, HAP-MK-GP granules could be a feasible adsorbent for the removal of dyes from industrial wastewater. Moreover, the facile granulation method presented here could be applied to other powdered adsorbents as well to prepare adsorbent granules.

1. Introduction

The textile industry is a significant user of dyes, and the dyeing process requires large amounts of water, energy, and chemicals. Consequently, large quantities of wastewater are formed containing pollutants such as heavy metals, organic compounds, and salts that can be harmful to aquatic life and human health [1–4]. An example of a typical synthetic cationic dye used in the textile industry is brilliant green (BG), which can cause ecosystem risks at concentration above 50 mg/L [5]. It has also been suspected that BG could be genotoxic and carcinogenic due to the chemical similarity with some other triphenylmethane dyes, malachite green or crystal violet [6]. Thus, methods to

* Corresponding author. University of Oulu, Fibre and Particle Engineering Research Unit, P.O. Box 4300, FI-90014, Finland.
E-mail address: tero.luukkonen@oulu.fi (T. Luukkonen).

https://doi.org/10.1016/j.hybadv.2023.100134
Received 8 November 2023; Received in revised form 14 December 2023; Accepted 21 December 2023
Available online 30 December 2023

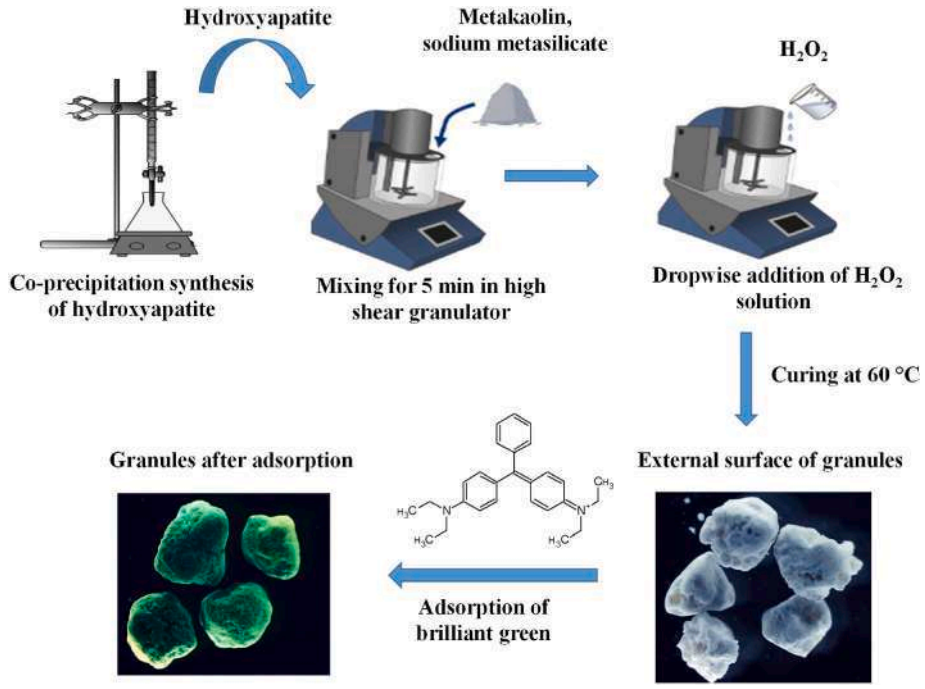

Fig. 1. Schematic representation of the preparation of HAP-MK-GP granules and adsorption experiments.

efficiently remove dyes from industrial wastewaters are needed and one actively studied approach is to use adsorption technology.

Adsorbents are commonly used in industrial processes to remove impurities or target substances from gases or liquids. Frequently used adsorbents include activated carbon, silica gel, alumina, and zeolites while new experimental adsorbent materials are being developed at an increasing pace [7,8]. Typically, new adsorbent materials are developed initially in the form of powders. However, the use of powdered adsorbents can be difficult in practice due to the difficult separation from water or cumbersome regeneration. To mitigate these problems, granular adsorbents are generally preferred in industrial applications [9]. Thus, widely applicable methods to granulate powdered adsorbents would be required to enable up-scaling and commercialization of new adsorbent materials.

Hydroxyapatite (HAP) and metakaolin geopolymer (MK-GP) are two types of adsorbents that have been studied extensively for their ability to remove contaminants from water [10]. HAP is a naturally occurring mineral, similar in composition to the mineral component of bone and teeth (i.e., $Ca_5(PO_4)_3(OH)$) [11]. It has a high adsorption capacity for metals, low water solubility, high stability under reducing and oxidizing conditions, good availability, and low cost [12]. MK-GP, on the other hand, is produced from calcined kaolin clay (i.e., metakaolin) by mixing it with an alkali-activator solution (frequently sodium silicate) under ambient conditions [13]. MK-GP consists of an amorphous aluminosilicate network, which resembles a zeolite structure. MK-GP has a high capacity to adsorb a variety of impurities, including metals, cationic dyes, or ammonium from water [14,15]. It is also used as a cementitious binder.

The aim of this research was to develop a method to prepare porous granules from powdered adsorbent using MK-GP as a reactive binder, which would also provide synergistic adsorption properties. This study involved combining HAP, metakaolin and sodium metasilicate powder in a granulator and adding H_2O_2 as a blowing agent and granulation fluid at different concentrations (0.0, 5.0, 7.5, or 10.0%). The obtained hydroxyapatite–metakaolin geopolymer (HAP-MK-GP) granules were comprehensively characterized and used in adsorption of BG dye from aqueous solutions in a batch reactor at different conditions. In addition, comparative adsorption experiments with different types of dyes (crystal violet, Congo red, methyl orange, and rhodamine b) were performed.

The objectives of the study were to (i) demonstrate the suitability of the combined granulation–alkali activation–direct foaming method to prepare highly porous granules from powdered HAP, (ii) optimize the adsorption conditions of BG and compare those to the adsorption of other types of dyes, and (iii) determine the adsorption mechanism by fitting the adsorption data to isotherm, kinetic, and thermodynamic models. This study provides new insights to the development of adsorbent materials by providing a widely applicable method to produce granular adsorbents from powdered materials.

2. Materials and methods

2.1. Chemicals

The raw materials to prepare HAP were $Ca(NO_3)_2{\cdot}4H_2O$ (99% assay) and $(NH_4)_2HPO_4$ (99.2% assay) from Biochem Chemopharma (Canada) and Analar Normapur (Belgium), respectively. Brilliant green (BG) (99.1%) crystal violet (CV) (96.5%), Congo red (CR) (97.%), methyl orange (MO) (98.1%) and rhodamine b (Rhb) (98.3%) were obtained from Sigma-Aldrich (Canada). HCl (0.1 M) and NaOH (0.1 M) solutions (VWR, Belgium) were used to adjust pH. The raw materials used for the preparation of porous geopolymer granules were metakaolin (MetaMax, BASF, USA), solid anhydrous sodium metasilicate (Na_2O 50.8 wt%, SiO_2 46.7 wt%, and H_2O 2.5 wt%; VWR Alfa Aesar, Germany), and H_2O_2 solution (30%, VWR, Belgium).

2.2. Preparation of HAP powder

The HAP powder was synthesized by the co-precipitation method using aqueous solutions containing 0.6 mol/L of Ca and 0.34 mol/L of P (prepared by dissolving $Ca(NO_3)_2.4H_2O$ and $(NH_4)_2HPO_4$ in ultrapure water). The P solution was added dropwise to the Ca solution to obtain the $\frac{Ca}{P}$ molar ratio of 1.67. Then, the solution was continuously stirred for 45 min before adjusting pH to 10 with NaOH (0.1 M). After 12 h of stirring at room temperature, the HAP particles were formed. The precipitate was filtered and dried in an oven at 353 K for 24 h.

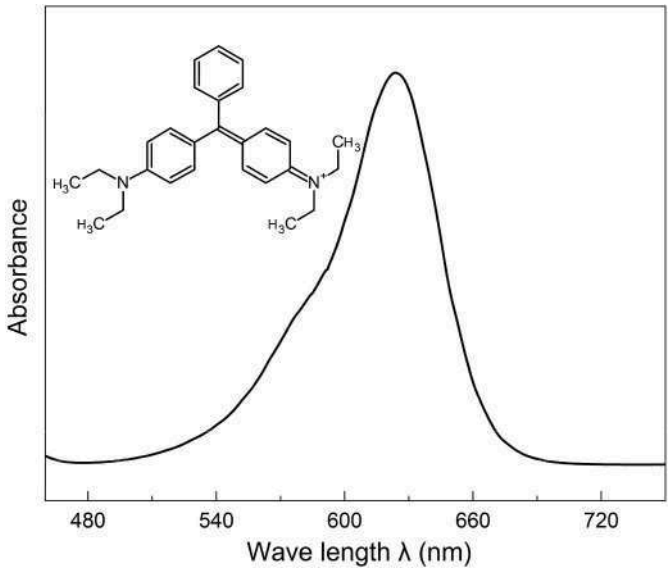

Fig. 2. Chemical structure and absorption spectrum of brilliant green dye.

Table 1
Properties of the dyes in the comparative adsorption experiment and the wavelengths used for their spectrophotometric determination.

Dye	Formula	Nature	Wavelength (nm)
Crystal violet	$C_{25}N_3H_{30}Cl$	Cationic	498
Congo red	$C_{32}N_6H_{22}Na_2O_6S_2$	Anionic	586
Methyl orange	$C_{14}H_{14}N_3NaO_3S$	Anionic	462
Rhodamine b	$C_{28}H_{31}ClN_2O_3$	Cationic	554

2.3. Preparation of HAP-MK-GP granules

The HAP-MK-GP granules were prepared by applying the previously reported method by Yu et al. [16]. First, the target amounts of HAP (57.4 wt%), sodium metasilicate (14.6 wt%), and metakaolin (28.0 wt %) were mixed as dry powders, ground using a disc mill (Retsch RS 200) at a speed of 1500 rpm for 5 min, and then placed in a high shear granulator (Eirich EL1). H_2O_2 solutions with concentrations of 5, 7, and 10% (w/w) were used as a granulation fluid and blowing agent. The amount of added H_2O_2 was approximately 18 wt% of the solids in the granulator. H_2O_2 solution was added dropwise until the granules were formed by a visual observation. The granulator pan mixing speed was 1200 rpm, granulator mixer plate speed was 170 rpm, and granulator tilting angle was 30°. The granules are identified with names G0, G1, G2 and G3 according to the concentration of H_2O_2 added (0.0, 5.0, 7.5, or 10.0%, respectively). They were cured at 333 K for 24 h to release the oxygen bubbles from the H_2O_2. The granules were then rinsed with distilled water and dried in an oven at 333 K for 24 h. They were sieved into particle size of 1–4 mm and stored at room temperature. The steps followed in the preparation are presented schematically in Fig. 1.

2.4. Characterization of material microstructure and mechanical strength

The functional groups of the samples were identified by Fourier transform infrared spectroscopy (FTIR, range: 400-4000 cm^{-1}, spectral resolution: 200). Analyses were performed using a Bruker Vertex v80 instrument equipped with a Harrick Praying Mantis DRIFT cell.

Specific surface area and pore size were determined using a Micromeritics ASAP2020 instrument and calculated using the Brunauer-Emmett-Teller (BET) isotherm and the Barrett-Joyner-Halenda (BJH) method. Before the measurement, samples were degassed at 70 °C for 24 h.

The microstructural morphology and composition of the samples were determined using a field emission scanning electron microscope equipped with an energy dispersive X-ray spectroscope (FE-SEM-EDS, Zeiss Ultra Plus). The surface and inner sections of the granules were imaged from unbroken and crushed granules, respectively. Before the analysis, the samples were placed on a two-sided tape and coated with carbon.

The mechanical strength of granules was determined with a Zwick Roell Z010 (10 kN load cell) universal testing instrument using a 1 mm/min loading rate. The granules selected for compression were spherical with a similar diameter and the measurement of each batch of granules was repeated three times. Compressive strength σ was calculated using Eq (1).

$$\sigma = 4 \times \frac{F_{max}}{\pi \times d^2} \tag{1}$$

where σ (MPa) is compressive strength, F_{max} (N) is peak force, and d (mm) is diameter of granules.

2.5. Point of zero charge determination

The point of zero charge (pH_{pzc}) of the granules was determined by using solutions containing 0.5 g of 2 mm diameter granules in 50 mL of 0.01 M NaCl. Their pH values were adjusted between 2 and 12 with the addition of 0.1 M HCl or NaOH solutions and then stirred for 24 h. The pH_{PZC} value is the point where the curve pH_{Final} versus $pH_{Initial}$ crosses the line $pH_{Initial} = pH_{Final}$.

2.6. Batch adsorption experiments

The adsorption parameters, contact time (0–180 min), BG dye concentration (10–100 mg/L), stirring speed (150–450 rpm), doses of granules (2–4 g/L), solution pH (3–9), granule diameter (1–4 mm), and temperature (298–338 K) were studied. Water samples were collected after each adsorption experiment using a pipette, centrifuged (using Beckman Coulter J326XPI-IM-1) at 8000 rpm for 2 min, and analyzed using a UV-6300PC spectrophotometer (VWR, China) at wavelength of 624 nm (Fig. 2). A calibration curve was created in a concentration range of 0.5–17 mg/L.

The percentage of the adsorbed BG dye and adsorption amount per adsorbent mass were calculated using Eqn (2) and (3), respectively.

$$y(\%) = \frac{C_0 - C_t}{C_0} \times 100 \tag{2}$$

$$q_t = (C_0 - C_t) \times \frac{V}{W} \tag{3}$$

Where $y(\%)$ is the adsorbed fraction of BG dye, C_0 (mg/L) and C_t (mg/L) are the initial BG concentration and its concentration at time t, respectively, q_t (mg/g) is the amount of BG adsorbed per adsorbent mass at time t, V (L) is the volume of BG dye solution, and W (g) is the weight of adsorbent granules.

To evaluate the behavior and selectivity of HAP-MK-GP (using the G1 granule composition) towards other dyes, namely CV, CR, MO, and Rhb, a comparative removal study was conducted under the optimal adsorption conditions of BG dye (i.e., initial dye concentration = 15 mg/L, contact time = 60 min, adsorbent dose = 3 g/L, pH = 7, granule diameter = 2 mm, agitation speed = 250 rpm, and T = 298 K). The wavelength used for quantifying their concentration and the formula of each dye are presented in Table 1.

2.7. Modeling of kinetic and isotherm data

The experimental kinetic data were fitted to the pseudo-first order and pseudo-second-order kinetic models (Eqn (4) and (5), respectively)

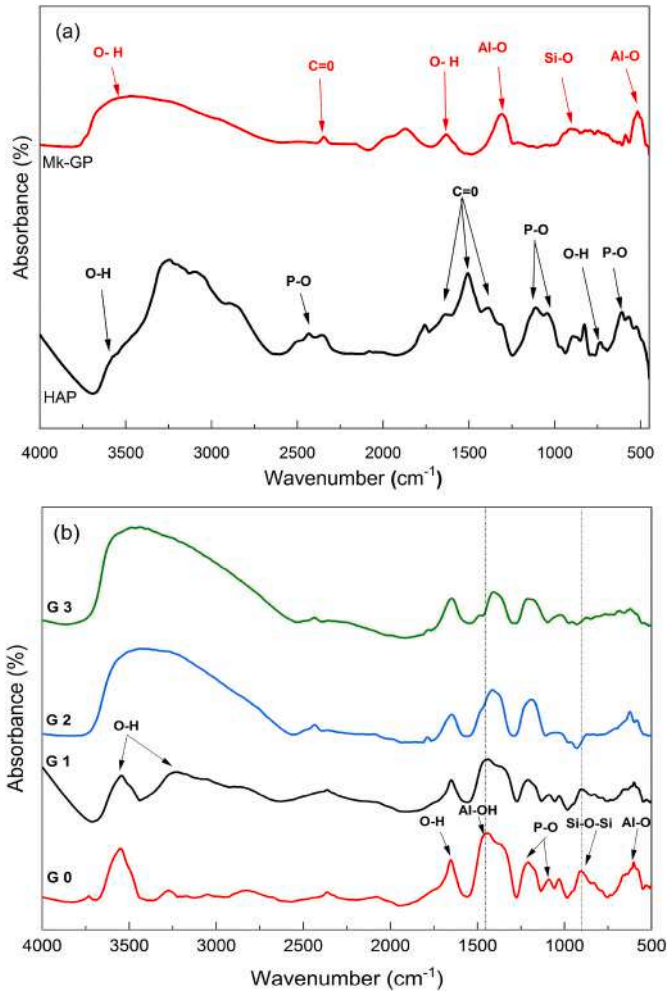

Fig. 3. FTIR spectra of (a) HAP and MK, and (b) HAP-MK-GP granules: G0, G1, G2, and G3.

Table 2
The main elements (by XRF, as atomic-%) of raw materials (HAP and MK) and HAP-MK-GP granules (G0, G1, G2, and G3).

Element (%)	HAP	MK	G0	G1	G2	G3
O	19.08	47.89	36.95	32.64	32.55	30.39
Na	2.25	0.37	8.74	8.97	9.05	9.71
Al	0	22.20	4.33	3.48	3.21	2.64
Si	0.02	23.50	9.46	8.96	8.82	8.41
P	12.56	0.17	9.46	8.96	7.95	7.20
Ca	21.07	0.29	15.84	15.12	14.75	14.10

[17]:

$$q_t = q_e \times [1 - exp(-k_1 t)] \tag{4}$$

$$q_t = q_e - \frac{q_e}{k_2 q_e t + 1} \tag{5}$$

where q_e (mg/g) is the amount of BG adsorbed at equilibrium, k_1 (1/min) is the pseudo-first order rate constant, k_2 [g/(mg.min)] is the pseudo-second order rate constant.

Three non-linear adsorption isotherm models, Langmuir, Freundlich, and Redlich-Peterson, were utilized to interpret the equilibrium data. The equations of Langmuir, Freundlich, and Redlich-Peterson isotherms are presented in Eqn (6)–(8), respectively [17,18]:

$$q_e = \frac{q_{max}\ K_L\ C_e}{K_L\ C_e + 1} \tag{6}$$

$$q_e = K_F C_e^{\frac{1}{n}} \tag{7}$$

$$q_e = \frac{K_R\ C_e}{a_R C_e^{\beta} + 1} \tag{8}$$

where C_e (mg/L) is the equilibrium concentration of BG dye, q_{max} (mg/g) is Langmuir monolayer adsorption capacity, K_L (L/mg) is the Langmuir adsorption constant, K_F $\left(mg^{1-\frac{1}{n}}.L^{\frac{1}{n}}/g\right)$ and $\frac{1}{n}$ are Freundlich capacity and intensity constants, respectively, related to the surface heterogeneity. K_R (L/g), a_R (L/mg), and β are Redlich–Peterson isotherm constants.

2.8. Thermodynamic study

To evaluate the spontaneity of the BG dye adsorption onto HAP-MK-GP granules, as well as the effect of temperature on its progress, thermodynamic parameters, Gibbs free energy (ΔG°), enthalpy change (ΔH°), and entropy change (ΔS°), were calculated using Eqn (9)–(11), respectively [17].

$$\Delta G^\circ = -RTln\ K_d \tag{9}$$

$$\Delta G^\circ = \Delta H^\circ - T\Delta S^\circ \tag{10}$$

$$lnK_d = -\frac{\Delta G^\circ}{RT} = \frac{\Delta S^\circ}{R} - \frac{\Delta H^\circ}{RT} \tag{11}$$

where R is the universal gas constant (8.314462 J/(K × mol)), T is the absolute temperature (K), and K_d is the equilibrium adsorption constant.

The optimum temperature (T_{opt}), at which the standard free energy is zero, predicts the feasibility of the adsorption process of BG dye into HAP-MK-GP granules. It was calculated using Eqn (12) [19].

$$T_{opt} = \frac{\Delta H^\circ}{\Delta S^\circ} \tag{12}$$

The activation energy (E_a) of the BG and G1 adsorption system was determined using the Arrhenius Equation (Eq (13)). Moreover, the Clausius-Clapeyron equation (Eq (14)) was used to calculate the isosteric heat of adsorption [20,21].

$$\ln(k_2) = \ln(A) - \frac{E_a}{RT} \tag{13}$$

$$\ln\ (C_e)_{qe} = \frac{\overline{\Delta H}}{RT} + Const \tag{14}$$

Where E_a is the activation energy (J/mol), A is the pre-exponential factor related to molecular collision (unitless), and $\overline{\Delta H}$ (J/mol) is the isosteric heat of adsorption.

To be able to interpret the effect of temperature on the adsorption, the diffusion coefficient D (m^2/s) of the BG into G1 granules was calculated at different temperatures using the film-pore diffusion model, describing the movement of a solute within a spherical particle Eq (15) [22].

At boundary conditions:

$$t = 0, q_t = 0, C_t = 0;\ r = 0, \frac{\partial C_t}{\partial r} = 0;\ r = R_p;\ D_p \frac{\partial C_t}{\partial r} = k_f (C_t - C_0)\Big).$$

$$\varepsilon_F \frac{\partial C_t}{\partial t} + \rho_p \frac{\partial q_t}{\partial r} = \frac{D_p}{r^2} \frac{\partial}{\partial r}\left(r^2 \frac{\partial C_t}{\partial r}\right) \tag{15}$$

where D_p is the diffusion coefficient (m^2 /s), ρ_p is the particle density (g/cm^3), ε_F is the particle porosity, r is the radial distance for mass

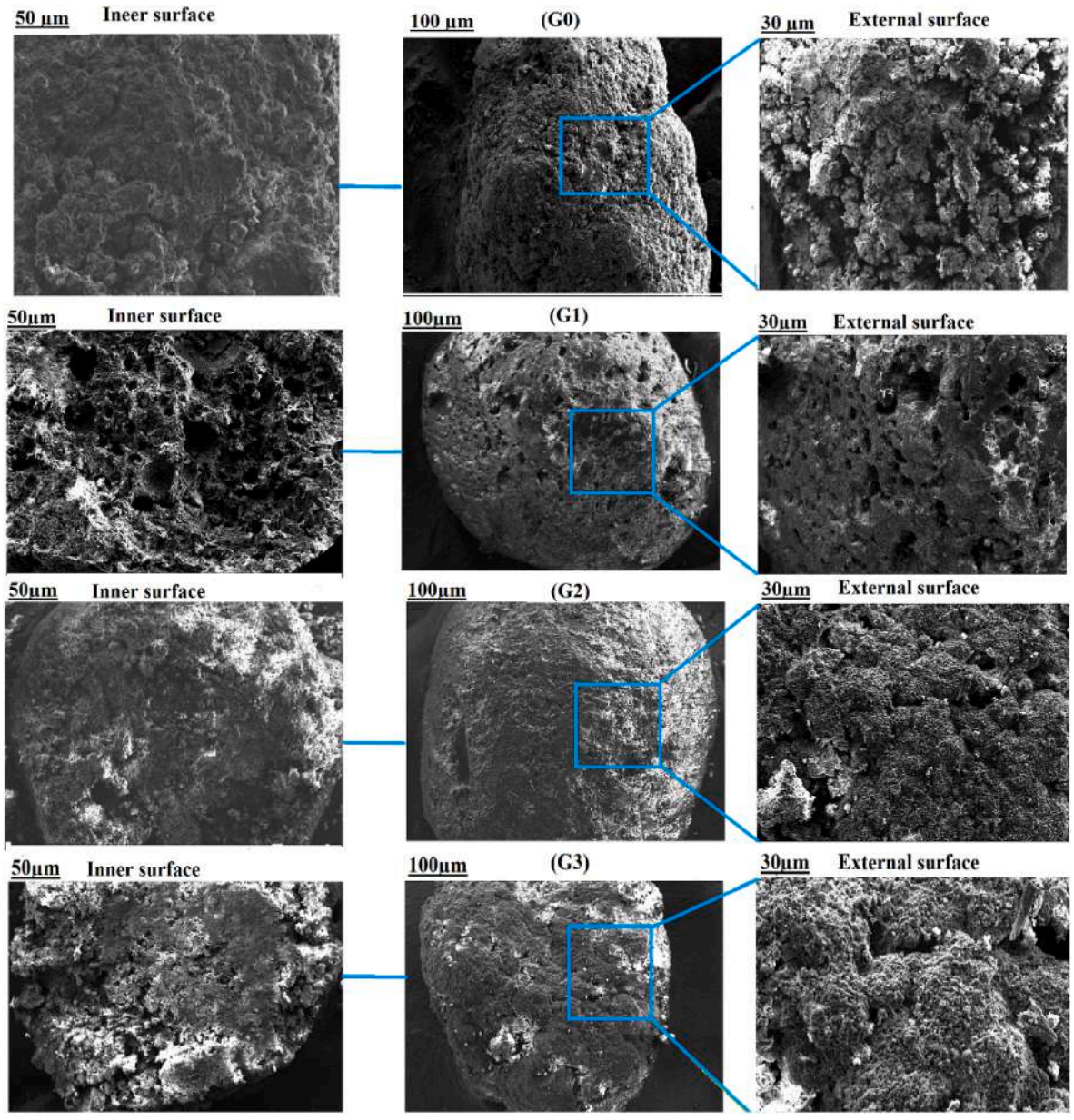

Fig. 4. SEM micrographs photographs of HAP-MK-GP granules: G0, G1, G2, and G3 (external and internal surfaces).

transfer in the granule (mm), R_p is the particle radius (mm), and k_f is the external mass transfer coefficient (cm/s).

The conservation equation, and initial condition at $t = 0$ and $c = c_0$, for a batch contactor are given as Eq (16) (where V is the solution volume (cm^3), and m is the mass of particles (g)) [22].

$$\frac{dC_t}{dt} = \frac{3k_f W}{R_p V}(C_t - C_0) \tag{16}$$

As the initial uptake of solute is controlled by external mass transfer resistance, k_f can be estimated from experimental $\frac{C_t}{C_0}$ obtained during the initial uptake. Eq (17) was used to calculate the change in fluid phase concentration during the first period based on the $\frac{C_t}{C_0}$ values [22].

$$\frac{C_t}{C_0} = 1 - \frac{3k_f m}{\rho_p R_p V} t \tag{17}$$

2.9. Regeneration experiments

The regeneration efficiency was evaluated through five consecutive cycles, each beginning with an adsorption equilibration followed by desorption. The adsorption experiments were conducted using the conditions of $[BG]_0 = 10$ mg/L, adsorbent dose = 3 g/L, pH = 7, t = 180 min, granule diameter = 2 mm, agitation speed = 250 rpm, and T = 298 K. After adsorption, the granules were washed with distilled water to remove non-adsorbed BG and then transferred to a pH 4 ([HCl] = 0.1 mol/L] solution for desorption (t = 180 min, agitation speed = 250 rpm, and T = 298 K). Samples were collected after each adsorption and desorption experiment using a pipette, centrifuged (using Beckman Coulter J326XPI-IM-1) at 8000 rpm for 2 min, and analyzed using a UV-6300PC spectrophotometer (VWR) to determine the final concentration.

3. Results and discussion

3.1. Characterization of the HAP-MK-GP granules obtained at different concentrations of H_2O_2

The FTIR spectra of raw materials and granules prepared using different concentrations of H_2O_2 are displayed in Fig. 3

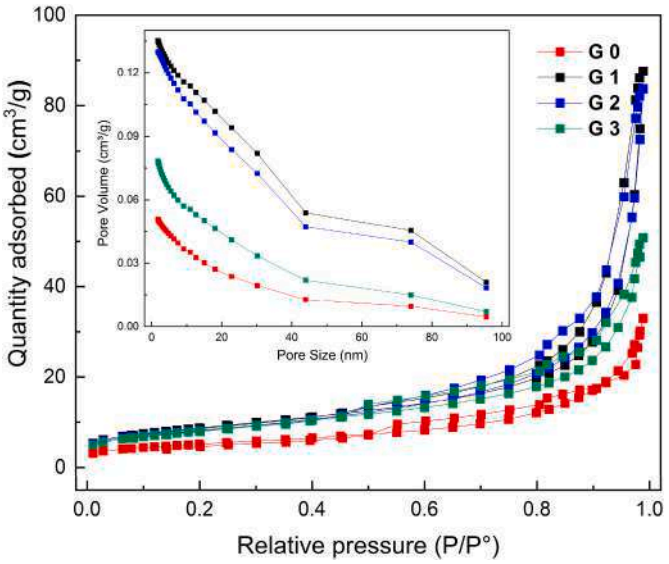

Fig. 5. N_2 adsorption-desorption isotherm of HAP-MK-GP granules (G0, G1, G2, and G3) and their pore size distribution curves as a function of cumulative pore volume.

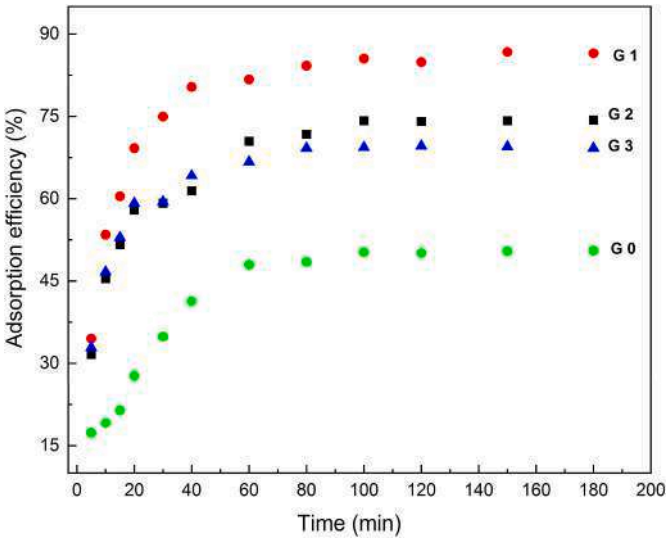

Fig. 6. The effect of H_2O_2 concentration and contact time on the adsorption efficiency of BG dye on the HAP-MK-GP granules. Conditions: $[BG]_0$ = 15 mg/L, adsorbent dose = 2 g/L, pH = 5, granule diameter = 2 mm, agitation speed = 350 rpm, and T = 298 K.

Table 3
BET/BJH parameters and mechanicals properties of G0, G1, G2, and G3 granules.

Samples	G0	G1	G2	G3
BET/BJH parameters				
Average diameter d_0 (mm)	2.31 ± 0.1	2.23 ± 0.1	2.20 ± 0.1	2.18 ± 0.1
Specific surface area (m^2/g)	22.59	30.86	29.81	28.75
Total pore volume (cm^3/g)	0.05	0.13	0.13	0.07
Mean pore diameter (nm)	9.09	17.37	16.77	10.53
Mechanical properties				
F_{max} (N)	42.50	39.96	24.44	41.81
Compressive strength (σ) (MPa)	0.85	0.76	0.77	0.79
dL at F_{max} (mm)[a]	0.23	0.55	0.49	0.29
(%) Deformation at F_{max}	3.20	6.80	5.37	3.64
Young's modulus (MPa)	17.01	9.68	11.23	15.56

[a] The deformation of material under maximum force.

The FTIR spectra of the granules G0, G1, G2, and G3 (Fig. 3b) contained the characteristic absorption bands of HAP and MK-GP (Fig. 3a). According to Meski et al. [10] and Ziani et al. [11], the bands at 2033, 1218 and 1100 cm^{-1} correspond to the bending vibrations of PO_4 tetrahedral units, which are the building blocks of HAP. The bands at 3547 and 620 cm^{-1} correspond to the O–H stretching vibration of hydroxyl groups in the HAP structure. The bands observed at about 1380–1450 cm^{-1} and 1620 cm^{-1} could be assigned to carbonates [12]. Moreover, the band at 1308 cm^{-1} is related to the Al–OH bending vibration that occurs in the OH groups of MK-GP, and the band at 591 cm^{-1} corresponds to the Al–O bending vibration, which is a characteristic of the AlO_4 tetrahedra found in MK-GP [23]. The band from 900 to 950 cm^{-1} is associated to the silanol stretching (Si–OH) group. The bands registered at 3274 and 1630 cm^{-1} are due to the stretching vibration of the O–H groups present on the surface of MK-GP [16,24,25]. The band at 2400 cm^{-1} is associated with the asymmetric stretching of carbonate likely due to the atmospheric CO_2 reacting with the surface alkalinity of MK-GP [16]. The results indicated that the inclusion of HAP in the reaction mixture of metakaolin and sodium metasilicate does not hinder the formation of MK-GP. The amount of Si–OH or Al–OH groups on the MK-GP surface contributes to its ability to interact with cations. On the other hand, the tetrahedral $[AlO_4]^-$ sites are thought to be the main surface sites providing reversible ion-exchange capacity for cations.

Furthermore, the findings of the experiments indicate that high concentrations of H_2O_2 (> 5.0 weight-%) can cause variations in the vibrational modes of chemical bands in HAP and MK-GP components. These variations were observed in the absorption bands at 1644, 1630–1191, and 1218 cm^{-1}, connected to the stretching vibrations of O–H in MK-GP and the flexural vibrations of PO_4 tetrahedral units in HAP, respectively. The shift at 1445 cm^{-1} band towards 1415 and 1403 cm^{-1} observed in the spectra of G2 and G3 may be associated to the interaction between Al–OH bonds in the MK-GP structure and H_2O_2. The shift at 904 cm^{-1} band towards 880 cm^{-1} observed in the spectra of G2 and G3 may be associated to the breaking of some Si–O–Si bonds in the MK-GP structure. These results indicate that increasing the concentration of H_2O_2 may influence the chemical structure of the HAP-MK-GP granules.

The XRF results of the main elements for HAP, MK-GP, and HAP-MK-GP granules prepared at different concentrations of H_2O_2 are presented in Table 2.

The atomic element (%) indicated that increasing the concentration of H_2O_2 raised the $\frac{Ca}{P}$ ratio of HAP in the G1, G2 and G3 granules, which is most likely owing to the chemical interaction that happens between H_2O_2 and HAP. When H_2O_2 is introduced into HAP, it reacts with the calcium and phosphate present in the mineral and can dissolve them [26]. As a result, the proportion of Ca and P in the HAP-MK-GP granules decreased.

The appearance of internal and external surfaces of granules G0, G1, G2, and G3 are shown in Fig. 4. As can be seen, the SEM micrographs indicated that granules prepared with H_2O_2 exhibited enhanced porosity (connected and closed pores) as compared to nonporous granules (G0). However, the increase in H_2O_2 concentration (i.e., samples G2 and G3) in the granulation fluid decreased the porosity of both the inner and outer surfaces of the granules, as well as the pore size and depth. This result agrees with Yu et *al.* [16], since using too highly concentrated H_2O_2 as the granulation fluid may induce too rapid hardening of the geopolymer gel due to heat release, which prevents pore formation.

The N_2 adsorption/desorption isotherms of HAP-MK-GP granules Fig. 5 exhibit a type IV hysteresis loop with mesoporous structure. The results of specific surface area, total pore volume, and the pore size

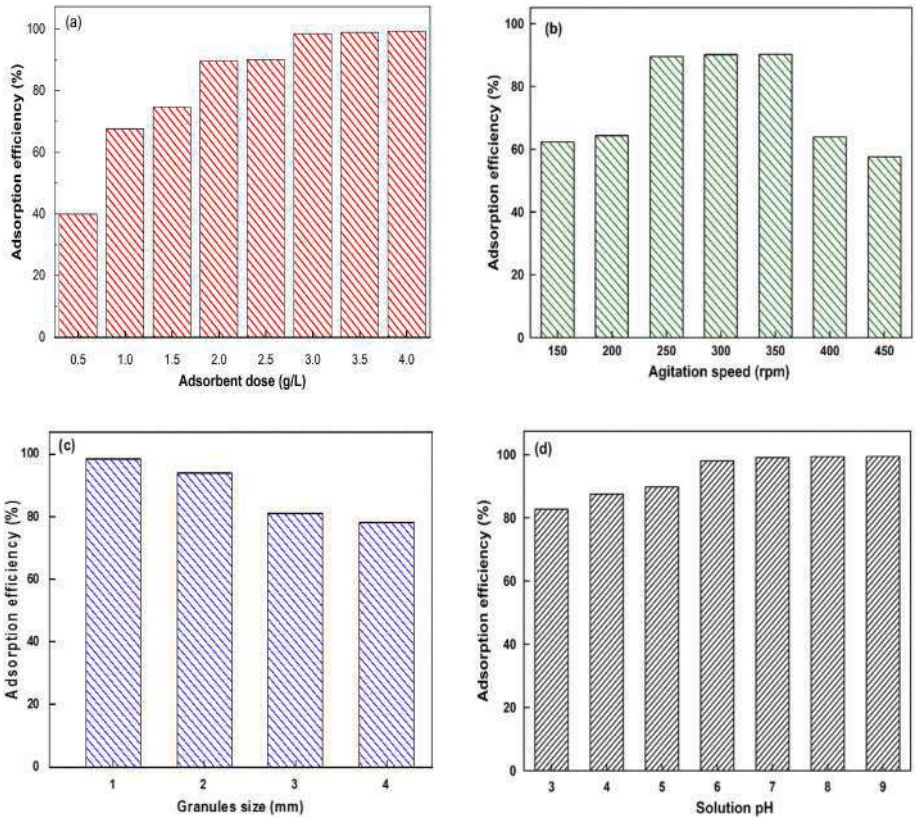

Fig. 7. Effects of (a) adsorbent dose, (b) agitation Speed, (c) granules size, and (d) pH of the solution on the adsorption efficiency of BG dye onto G1 granules. Conditions: $[BG]_0$ = 15 mg/L, t = 180 min, and T = 298 K.

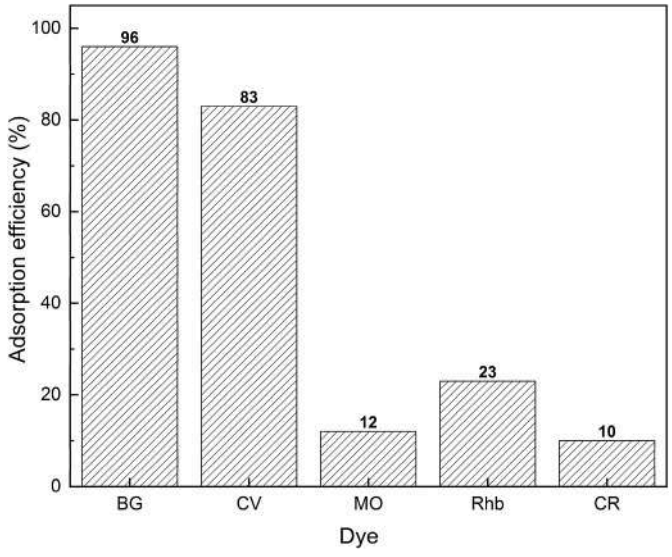

Fig. 8. Comparative study of the adsorption efficiency of HAP-MK-GP (G1) with respect to five different dyes. Conditions: $[dyes]_0$ = 15 mg/L, time = 60 min, adsorbent dose = 3 g/L, pH = 7, granule diameter = 2 mm, agitation speed = 250 rpm, and T = 298 K.

distribution (Fig. 5 and Table 3) demonstrated that the granules prepared with H_2O_2 exhibited higher porosity and surface area than the control sample prepared using water (i.e., G0). Most of the pore volume of granules is between 2 and 50 nm which represents mesopores, which are also called medium capillary pores when describing the transport of ions in pore networks.

Furthermore, the results indicated a slight reduction in the specific surface area of granules, as well as decreased total pore volume and pore diameter with increasing the H_2O_2 concentration. These results also support the above observations that lower H_2O_2 concentrations are beneficial for the granule microstructure. For instance, the decrease in the specific surface area and volume of pores was supported by the SEM micrographs, which showed a decrease in the number of μm-sized pores upon increasing the H_2O_2 concentration.

The results of compressive strength testing of the granules are shown in Table 3. The G0 and G3 granules exhibited the highest strength contrary to the G1 and G2 granules, indicating that G0 and G3 granules had the lowest porosity as also confirmed by the BET/BJH results and SEM micrographs.

3.2. Adsorption experiments

To investigate the effect of H_2O_2 concentration and contact time on the adsorption of BG dye onto HAP-MK-GP granules (G0, G1, G2, and G3), the experiments were conducted at the pH of 5 with contact times ranging from 0 to 180 min. The initial BG dye concentration and the granules dose were fixed at 15 mg/L and 2 g/L, respectively. The results of this experiment, shown in Fig. 6, indicate that the granules prepared with H_2O_2 exhibited higher adsorption efficiency than G0 due to their higher porosity and surface area. Moreover, the high concentrations of H_2O_2 (> 5.0 %) reduced the adsorption efficiency of the granules towards the BG dye. This may be due to the reduction in the porosity of the granules at higher H_2O_2 concentrations (Table 3). Moreover, the XRF findings indicated that using a too high H_2O_2 concentration can cause leaching of calcium and phosphate ions from HAP. This phenomenon can negatively influence the stability of the functional groups on the surface of the HAP-MK-GP granules. The adsorption mechanism was assumed to involve electrostatic interactions, hydrogen bonding, and

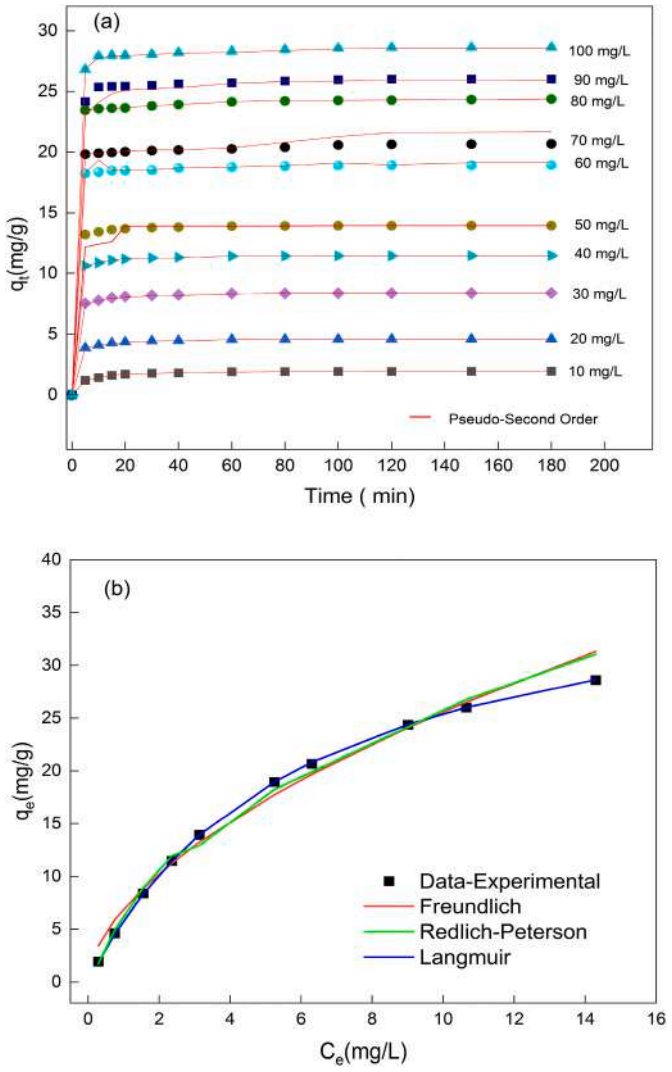

Fig. 9. (a) Kinetic models and (b) isotherm models fitting to the experimental data of BG adsorption on the HAP-MK-GP granules. Conditions: adsorbent dose = 3 g/L, pH = 7, t = 180 min, granule diameter = 2 mm, agitation speed = 250 rpm, and T = 298 K.

van der Waals forces between the BG dye and functional groups present on the surface of the HAP-MK-GP adsorbent. More specifically, the calcium- and aluminum-containing groups in HAP and MK-GP could connect electrostatically with the amine groups of BG, while phosphate and carbonate form hydrogen bonds with the hydroxyl and amine groups of BG (see Fig. 12 below). The decrease of numbers of these groups in the granule surface results in a lower adsorption efficiency. Because of the lower adsorption performance of G2 and G3 towards BG dye, G1 was chosen for further experiments.

3.3. *Optimization of the parameters affecting the adsorption*

The adsorption efficiency in a batch reactor depends largely on the amount of adsorbent used, as well as the adsorbent particle size and the concentration of the adsorbate. Furthermore, the agitation speed is critical in promoting the mass transfer between the solution and the adsorbent, regulating both the film diffusion and the pore diffusion processes [27,28]. To study all these, experiments were carried out to optimize the adsorption process. The first experiment was performed with different sizes of G1 granules, ranging from 1 to 4 mm at pH = 5 and $[BG]_0$ = 15 mg/L. Next, several agitation speeds, ranging from 150 to 450 rpm, were examined using the optimum granule particle size.

Table 4
Kinetic and isotherm parameters for BG adsorption onto G1 granules. Conditions: adsorbent dose = 3 g/L, pH = 7, t = 180 min, granule diameter = 2 mm, agitation speed = 350 rpm, and T = 298 K.

Kinetic model	Kinetic parameters	
Pseudo-First Order	q_{exp} (mg/g)	28.61
	q_{cal} (mg/g)	27.86
	k_1 (1/min)	0.56
	R^2	0.91
Pseudo-Second Order	q_{exp} (mg/g)	28.61
	q_{cal} (mg/g)	28.52
	k_2 (mg/(g. min))	0.20
	R^2	0.99
Isotherm model	**Equilibrium parameters**	
Freundlich	$K_F\left(mg^{1-\frac{1}{n}}.L^{\frac{1}{n}}/g\right)$	6.91
	n^{-1}	0.59
	R^2	0.95
Langmuir	q_{max} (mg /g)	40.79
	K_L (L /g)	0.16
	R^2	0.99
Redlich-Peterson	K_R (L /g)	2.52
	a_R (L /mg)	0.96
	β	0.53
	R^2	0.95

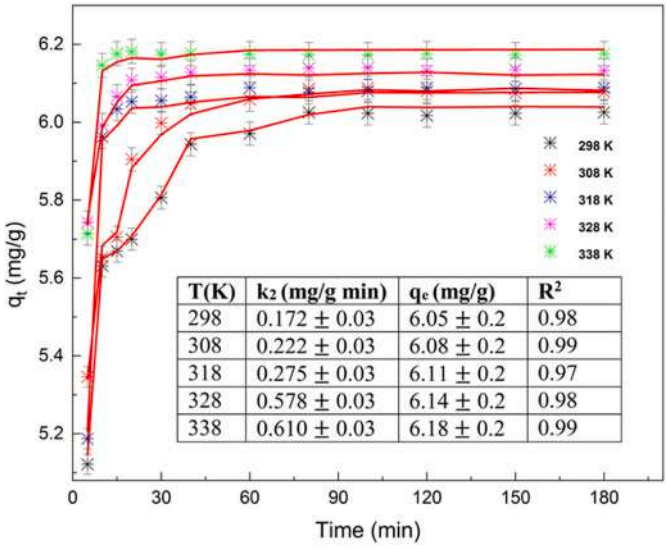

Fig. 10. Effect of temperature on the adsorption of BG onto G1 granules and the fitting of the pseudo-second-order model to the data. Conditions: $[BG]_0$ = 20 mg/L, adsorbent dose = 3 g/L, pH = 7, granule diameter = 2 mm, and agitation speed = 250 rpm. The error bars represent standard deviation of three repeated experiments.

Table 5
The diffusion coefficients and thermodynamic parameters of the BG adsorption onto G1 granules.

T (K)	D (m^2/s) × 10^{-10}	ΔG° (kJ/mol)	ΔH° (kJ/mol)	ΔS° (J/(mol × K))	$T^{\circ}(K)$	$\overline{\Delta H^{\circ}}$ (kJ/mol)	E_a (KJ/mol)
298	0.64	−3.96	6.76	27.62	244.56	6.84	27.19
308	0.83	−4.38					
318	1.37	−4.57					
328	1.93	−5.03					
338	2.02	−5.45					

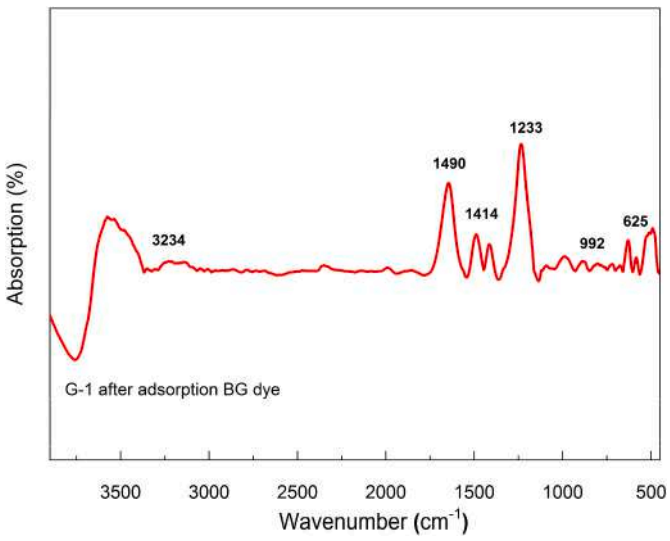

Fig. 11. FTIR spectrum of the G1 granules after the adsorption of BG dye.

Finally, the effect of adsorbent dose, ranging from 2 to 4 g/L, and the effect of pH of the solution, ranging from 3 to 9, were studied. The results of these experiments are displayed in Fig. 7. A significant improvement in the adsorption efficiency of BG dye was observed as the HAP-MK-GP dose, stirring speed, and pH of the solution were increased up to 3 g/L, 250 rpm, and 7, respectively. Moreover, the granule diameter smaller than 3 mm was the optimum.

The increase in the adsorbent dose resulted in a higher adsorption efficiency due to the increase in available adsorption sites (Fig. 7a). Additionally, an increase in the stirring speed from 150 to 250 rpm increased the adsorption efficiency from 62 to 90%, which then remained constant up to an agitation of 350 rpm (Fig. 7b). In this range of moderate agitation, the particles of the granulated material are subjected to moderate turbulence causing more collisions with the BG molecules and, consequently, improved mass transfer. This is because the film boundary enclosing the particles is reduced. However, at high agitation speeds beyond 350 rpm, the granulated material particles may be exposed to shear stresses, causing mechanical deterioration, which decrease the mass transfer between the adsorbate and the adsorbent, and thus the adsorption efficiency. Similar results have been reported earlier [29] when investigating the effect of stirring speed on the adsorption of dyes from aqueous solutions using activated carbon granules prepared of coconut shell as adsorbent material.

It should be noted that the granules of 1 mm of diameter exhibited a BG removal rate of 98% compared to those of 2 mm (94%) (Fig. 7c). However, granules with a diameter of 2 mm are easier to obtain during synthesis than granules with a diameter of 1 mm. Therefore, granules with a diameter of 2 mm were chosen for the subsequent experiments. The size of granules above 3 mm resulted in reduced adsorption efficiency, which is explained by a decrease in the specific surface area and porosity of the granules. The specific surface area of 2 and 3 mm-sized granules was 30.86 and 19.52 m^2/g, respectively.

The pH of the solution has a strong influence on the adsorption mechanism, as it determines the charge of the adsorbent surface as well as the ionization of the adsorbates. The effect of solution pH on the adsorption behavior of BG dye onto HAP-MK-GP granules was studied under the optimized conditions (Fig. 7d). The adsorption efficiency was much higher (99.3 %) at pH values equal to or greater than 7, which corresponded to the pH_{pzc} of granules. This can be due to the more negative charge of phosphate, silanol, and aluminol groups on the HAP-MK-GP granule surface causing enhanced electrostatic interactions with the positively charged amine groups of BG dye. Samiyammal et al. [30] and Duarte et al. [31] also investigated the effect of solution pH on the adsorption of BG dye from aqueous solutions using HAP derived from Pirarucu (*Arapaima gigas*). The decreased adsorption efficiency at pH < 6 also coincides with the pK_a value of BG (see Fig. 11), and thus the change in the BG speciation likely contributed for the decreased efficiency.

The results of the comparative adsorption study with different dyes (Fig. 8) revealed that HAP-MK-GP (G1) granules have a higher selectivity to remove cationic dyes (CV and BG) with adsorption efficiency higher than 80 % compared to anionic dyes at the optimized conditions. This is an expected result since the surface charge of MK-GP and HAP are both negative as illustrated in Fig. 12. The difference between BG and CV can be explained by slightly different chemical structure (both belong to the triarylmethane dyes) and size of the molecule.

3.4. Kinetic and isotherm modeling

Fig. 9 shows the fitting of the non-linear equations to the kinetic data and adsorption amounts at equilibrium. Most of the adsorption of BG occurred during the first 5 min for all BG dye concentrations and after 30 min, the equilibrium was reached. The quick equilibration time can

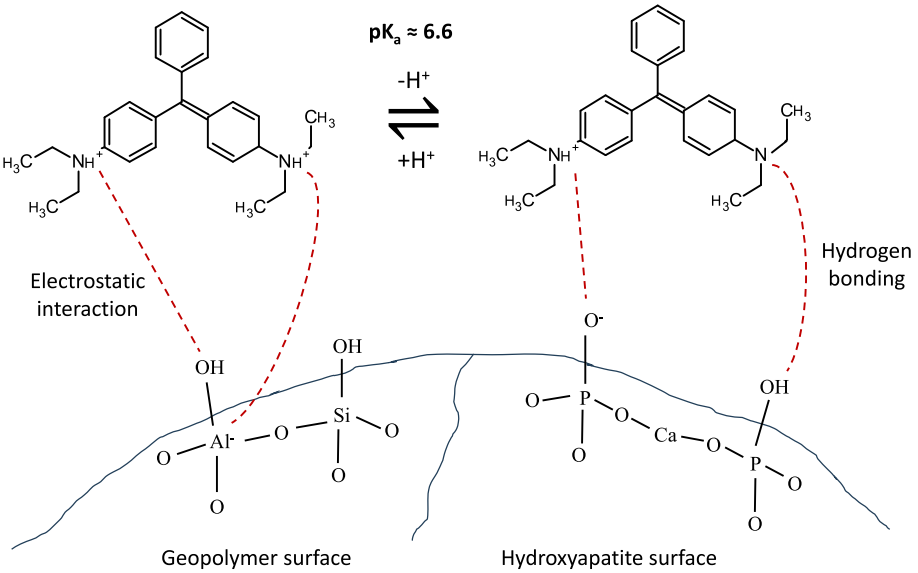

Fig. 12. A schematic presentation about the interactions between the HAP-MK-GP surface and BG molecules.

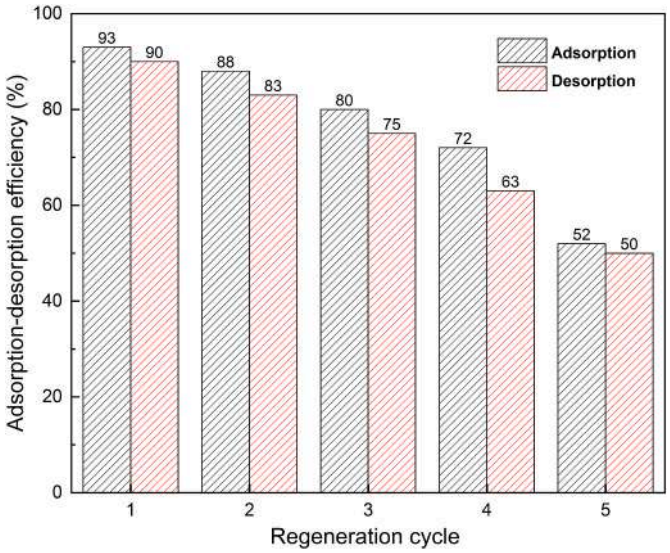

Fig. 13. Regeneration of the G1 granules with 0.1 mol/L HCl solution. Adsorption Conditions: $[BG]_0$ = 10 mg/L, adsorbent dose = 3 g/L, pH = 7, t = 180 min, granule diameter = 2 mm, agitation speed = 250 rpm, and T = 298 K. Desorption Conditions: pH = 4, agitation speed = 250 rpm, t = 180 min, and T = 298 K. Adsorption efficiency refers to removal% of BG by granules.

be explained by the high porosity (as demonstrated by the SEM and BET/BJH data). It should be noted that reaching equilibrium in 30 min for an adsorbent particle with a diameter of 2 mm is excellent performance. The pseudo-second-order model represented a better fit than the pseudo-first order model on kinetic data as indicated by the difference between the experimental and calculated adsorption amount (Table 4). The results in Table 4 and Fig. 9b show that the Langmuir isotherm resulted in a better fit (R^2 = 0.99) of the equilibrium adsorption data than the Freundlich or Redlich-Peterson isotherms (R^2 = 0.95). These findings indicate that the surface of HAP-MK-GP granules exhibit uniformity, all surface sites are identical, capable of accommodating one molecule of BG (i.e., limited to a monolayer coverage), and there are no interactions between sorbate molecules on neighboring sites [32].

3.5. Effects of temperature and thermodynamic studies

The effect of temperature on the adsorption on the G1 granules (Fig. 10 and Table 5) was studied in the conditions optimized above. As the temperature increased, the time required to reach the adsorption equilibrium decreased. At temperature of 338 K, the adsorption equilibrium was achieved within 20 min, whereas at lower temperatures, it took over 30 min. At high temperature, the rate constant (k_2) increased significantly. This is due to the increase in the kinetic energy of the molecules, promoting efficient collisions and faster reaction between BG and the surface of the G1 granules, ultimately resulting in faster adsorption on the granules.

All the obtained values indicated that the diffusion boundary layer formed between the BG dye solution and the G1 adsorbent granules was reduced by the effect of temperature. As a result, the reduction in the diffusion resistance allowed BG molecules to move freely throughout the system, increasing the likelihood of them randomly encountering the granule surface [33]. Table 5 lists the results of the thermodynamic modelling of the BG and G1 granules adsorption system. ΔG° Values were negative and fell steadily as the temperature rose. This suggests that the adsorption process is spontaneous. The value of ΔH° is less than 40 kJ /*mol* and the value of activation energy (E_a) is less than 27.19 kJ/mol, implying that the adsorption process of BG dye onto G1 granules is based on physical adsorption (i.e., physisorption). The low E_a value indicated that the BG adsorption on the G1 granules proceeded with low energy barriers and can be achieved at relatively low temperature. The positive value of ΔH° indicated that the adsorption is endothermic in nature with an optimal temperature of 244.56 K [20,34]. Moreover, a positive ΔS° value suggested increased disorder of the system as BG molecules attached to the adsorbent surface.

Fig. 11 displays the FTIR spectra of the G1 granules before and after the adsorption of BG dye. A slight shift of the P–O bands, characteristic of HAP, occurred from 1440 to 1490 cm^{-1}, 1204 to 1233 cm^{-1}, and 1028 to 992 cm^{-1}. These results can be explained by the interaction between the PO_4^{3-} groups of the HAP with the amine groups of BG dye (Fig. 12). Furthermore, the reduction observed in the intensity of the band at 3262 cm^{-1} can be attributed to an interaction between the hydroxyl groups O–H of MK-GP and the amine of BG dye Fig. 12. Moreover, the two new bands developed at 1414 cm^{-1} and 625 cm^{-1} after adsorption, are attributed, respectively to the C–H stretching vibration of benzene and the aromatic *C*–N stretching vibrations and to flexion or torsion vibrations of C–H bonds present in the aromatic structure of the BG dye [35,36].

3.6. Regeneration of granules

The desorption of BG dye was studied with a 0.1 mol/L HCl solution, which makes the surface of the adsorbent protonated displacing the adsorbed dyes. Adsorption and desorption performance of the G1 granules decreased during five reuse cycles (Fig. 13). Thus, the granules appeared to be practically suitable for one to three times use only. One possible reason for the decreased adsorption-desorption efficiency over repeated cycles could be dephosphorization of the hydroxyapatite surface [37] and dealumination of geopolymer surface [38] due to the regenerant solution (0.1 mol/L HCl) – even though the acid solution is rather dilute. It was observed during the repeated adsorption-desorption cycles that some of granules disintegrated. Specific surface area of granules increased slightly during the five cycles (to 35.6 m^2/g) while pore volume and average pore diameter remained approximately unchanged (at 0.13 cm^3/g and 15.7 nm, respectively). An alternative regeneration strategy could be to thermally degrade the adsorbed dye.

4. Conclusions

This study demonstrates a new method to prepare granular materials from powdered adsorbents utilizing porous geopolymer as a reactive and synergistic binder. Hydroxyapatite–metakaolin geopolymer (HAP-MK-GP) granules were prepared, characterized, and studied as an adsorbent to remove brilliant green dye from water. It was observed that a low concentration of H_2O_2 (i.e., 5 wt%) in the granule preparation was the optimum since it did not affect the chemical composition of hydroxyapatite and resulted higher porosity. The mechanical properties of granules indicate that they could be appropriate for use in a large-scale adsorption column extending over many meters in height. The batch adsorption experiments of BG dye from aqueous solutions by the optimum granules demonstrated a very promising adsorption capacity (approx. 41 mg/g as predicted by the Langmuir isotherm) and fast equilibration (< 30 min) for a granular material, likely due to the highly porous structure. The adsorption capacity and equilibration time compared favorably to other adsorbents studied for BG dye removal [39–42]. Furthermore, the granules had their highest adsorption capacity at near-neutral conditions in terms of pH, which enables their use in practical wastewater treatment scenarios. According to the thermodynamic modelling, the adsorption was spontaneous, endothermic, and occurred via physisorption. Overall, this study demonstrates that the developed method of preparing porous adsorbent granules using metakaolin geopolymer as a reactive binder is feasible for practical applications in water and wastewater treatment.

CRediT authorship contribution statement

Aghilas Brahmi: Conceptualization, Formal analysis, Investigation, Methodology, Validation, Visualization, Writing – original draft. **Salima Ziani:** Methodology, Supervision, Writing – review & editing, Conceptualization. **Salima AitAli:** Conceptualization, Methodology, Supervision, Writing – review & editing. **Bachir Nadir Benkhaoula:** Conceptualization, Writing – review & editing. **Yangmei Yu:** Investigation, Methodology, Writing – review & editing. **Hania Ahouari:** Conceptualization, Writing – review & editing. **Hafit Khireddine:** Conceptualization, Writing – review & editing. **Tero Luukkonen:** Conceptualization, Funding acquisition, Methodology, Resources, Supervision, Writing – review & editing.

Declaration of competing interest

The authors declare that they have no known competing financial interests or personal relationships that could have appeared to influence the work reported in this paper.

Acknowledgement

This research received financial support from the University of Oulu and the Research Council of Finland (Profi5 326291).

References

[1] N. Mohammed, A.P.K. Aftab, M.A. Abdullah, K.H. Jae, Exploring rapid photocatalytic degradation of organic pollutants with porous CuO nanosheets: synthesis, dye removal, and kinetic studies at room temperature, ACS Omega 6 (2021) 2601–2612, https://doi.org/10.1021/acsomega.0c04747.

[2] X. Peng, W. Chen, Z. He, D. Li, H. Liu, H. Jin, G. Zhou, F. Xu, Removal of Cu(II) from wastewater using doped HAP-coated-limestone, J. Mol. Liq. 293 (2019) 111502, https://doi.org/10.1016/j.molliq.2019.111502.

[3] K. Panneerselvam, K.T. Arul, A.R. Warrier, Rapid adsorption of industrial pollutants using metal ion doped hydroxyapatite, AIP Conf. Proc. 2117 (2019) 020004, https://doi.org/10.1063/1.5114584.

[4] K. Yahiaoui, F. Boudrahem, S. Ziani, F. Aissani-Benissad, Removal studies of Pb (II) ions by carbon powder prepared from polyethylene terephthalate (PET) bottles, Int. J. Environ. Anal. Chem. 102 (2020) 1–14, https://doi.org/10.1080/03067319.2020.1814272.

[5] A.C. Enache, C. Cojocaru, P. Samoila, V. Ciornea, R. Apolzan, G. Predeanu, V. Harabagiun, Adsorption of brilliant green dye onto a mercerized biosorbent: kinetic, thermodynamic, and molecular docking studies, Molecules 28 (2023) 4129, https://doi.org/10.3390/molecules28104129.

[6] M. Oplatowska, R.F. Donnelly, R.J. Majithiya, D.G. Kennedy, C.T. Elliott, The potential for human exposure, direct and indirect, to the suspected carcinogenic triphenylmethane dye Brilliant Green from green paper towels, Food Chem. Toxicol. 49 (2011) 1870–1876, https://doi.org/10.1016/j.fct.2011.05.005.

[7] N. Liu, H. Wang, C. Weng, C. Hwan, Adsorption characteristics of Direct Red 23 azo dye onto powdered tourmaline, Arab. J. Chem. 11 (2018) 1281–1291, https://doi.org/10.1016/j.arabjc.2016.04.010.

[8] A. Al Natsheh, A. Gray, T. Luukkonen, Drivers and barriers for productization of alkali-activated materials in environmental technology, in: T. Luukkonen (Ed.), Alkali-Activated Materials in Environmental Technology Applications, Woodhead Publishing, Sawston, 2022, pp. 407–426, https://doi.org/10.1016/B978-0-323-88438-9.00008-9.

[9] T.M. Ting, M.M. Nasef, D. Aravindan, M.A. Ahmad, M. Mokhtar, N.A. Kamarudin, A.F. Abd Rahman, Comparative modelling analysis of boron dynamic adsorption on fibrous adsorbent prepared using radiation grafting versus granular resin, J. Environ. Chem. Eng. 9 (2021) 105208, https://doi.org/10.1016/j.jece.2021.105208.

[10] D.C. Manatunga, R.M. De Silva, K.M.N. De Silva, N. De Silva, E.V.A. Premalal, Metal and polymer-mediated synthesis of porous crystalline hydroxyapatite nanocomposites for environmental remediation, 171557, Royal Society Open Science, 2018, pp. 1–15, https://doi.org/10.1098/rsos.171557.

[11] B. Huang, D. Xiong, T. Zhao, H. He, X. Pan, Adsorptive removal of PPCPs by biomorphic HAP templated from cotton, Water Sci. Technol. 74 (2016) 276–286, https://doi.org/10.2166/wst.2016.209.

[12] Y. Chen, Y. Guo, G. Feng, K. Urasaki, G. Guo, Y. Qin, K. Kubota, Y.Y. Li, Key factors improving the stability and the loading capacity of nitrogen removal in a hydroxyapatite (HAP)-enhanced one-stage partial nitrification/anammox process, Chem. Eng. J. 452 (2023) 139589, https://doi.org/10.1016/j.cej.2022.139589.

[13] X. Zhang, C. Bai, Y. Qiao, X. Wang, D. Jia, H. Li, P. Colombo, Porous geopolymer composites: a review, Composites Part A 150 (2021) 106629, https://doi.org/10.1016/j.compositesa.2021.106629.

[14] J. Laukkanen, S. Ojala, T. Luukkonen, U. Lassi, Effect of material age on the adsorption capacity of low-, medium-, and high-calcium alkali-activated materials, Applied Surface Science Advances 12 (2022) 100345, https://doi.org/10.1016/j.apsadv.2022.100345.

[15] T. Luukkonen, E. Olsen, A. Turkki, E. Muurinen, Ceramic-like membranes without sintering via alkali activation of metakaolin, blast furnace slag, or their mixture: characterization and cation-exchange properties, Ceram. Int. 49 (2023) 10645–10651, https://doi.org/10.1016/j.ceramint.2022.11.252.

[16] Y. Yu, P. Perumal, I.J. Corfe, T. Paul, M. Illikainen, T. Luukkonen, Combined granulation–alkali activation–direct foaming process: a novel route to porous geopolymer granules with enhanced adsorption properties, Mater. Des. 227 (2023) 111781, https://doi.org/10.1016/j.matdes.2023.111781.

[17] S. Aitali, S. Ziani, I. Yahiaoui, A. Brahmi, F. Boudrahem, F. Aissani-Benissad, Application of central composite design and response surface methodology for the study of extraction of gentian violet dye in aqueous solution by polystyrene membrane modified with oleic acid, Environ. Prog. Sustain. Energy 42 (2023) e14200, https://doi.org/10.1002/ep.14200.

[18] F. Boudrahem, F. Aissani-Benissad, F. Audonnet, C. Vial, Effects of acid-basic treatments of date stones on lead (II) adsorption, Separ. Sci. Technol. 54 (2019) 1–15, https://doi.org/10.1080/01496395.2018.1538240.

[19] K.M. Doke, E.M. Khan, Adsorption thermodynamics to clean up wastewater; critical review, Rev. Environ. Sci. Biotechnol. 12 (2013) 25–44, https://doi.org/10.1007/s11157-012-9273-z.

[20] N. Liu, H. Wang, C. Weng, C. Hwang, Adsorption characteristics of Direct Red 23 azo dye onto powdered tourmaline, Arab. J. Chem. 11 (2018) 1281–1291, https://doi.org/10.1016/j.arabjc.2016.04.010.

[21] T. Saeed, A. Naeem, I.U. Din, M. Farooq, I.W. Khan, M. Hamayun, T. Malik, Synthesis of chitosan composite of metal-organic framework for the adsorption of dyes; kinetic and thermodynamic approach, J. Hazard Mater. 427 (2022) 127902, https://doi.org/10.1016/j.jhazmat.2021.127902.

[22] G. Yuan, B. Zhao, K.H. Chu, Adsorption of fluoride by porous adsorbents: estimating pore diffusion coefficients from batch kinetic data, Environmental Engineering Research 25 (2020) 645–651, https://doi.org/10.4491/eer.2019.205.

[23] T. Luukkonen (Ed.), Alkali-activated Materials in Environmental Technology Applications, Woodhead publishing, Sawston, 2022.

[24] W.K.W. Lee, J.S.J. Van Deventer, Use of infrared spectroscopy to study geopolymeri- zation of heterogeneous amorphous aluminosilicates, Langmuir 19 (2003) 8726–8734, https://doi.org/10.1021/la026127e.

[25] Y. Zhang, G. Ye, Z. Yang, Pore size dependent connectivity and ionic transport in saturated cementitious materials, Construct. Build. Mater. 238 (2020) 117680, https://doi.org/10.1016/j.conbuildmat.2019.117680.

[26] Y. Tanizawa, Reaction characteristics of a tooth-bleaching agent containing H_2O_2 and NaF: in vitro study of crystal structure change in treated hydroxyapatite and chemical states of incorporated fluorine, Int. J. Cosmet. Sci. (2005) 253–254, https://doi.org/10.1111/j.0142-5463.2005.00276_2.x.

[27] S. Aitali, O. Kebiche-Senhadji, M. Benamor, Performance of an acidic extractant (D2EHPA) incorporated in IM used for extraction and separation of methylene blue and Rhodamin B, Membrane Water Treatment 7 (2016) 521–537, https://doi.org/10.12989/mwt.2016.7.6.521.

[28] R. Khosravi, M. Fazlzadehdavil, B. Barikbin, A.A. Taghizadeh, Removal of hexavalent chromium from aqueous solution by granular and powdered Peganum Harmala, Appl. Surf. Sci. 292 (2014) 670–677, https://doi.org/10.1016/j.apsusc.2013.12.031.

[29] P. Samiyammal, A. Kokila, L. Arul Pragasan, R. Rajagopal, R. Sathya, S. Ragupathy, M. Krishnakumar, V. Reddy, M. Reddy, Adsorption of brilliant green dye onto activated carbon prepared from cashew nut shell by KOH activation: studies on equilibrium isotherm, Environ. Res. 212 (2022) 113497, https://doi.org/10.1016/j.envres.2022.113497.

[30] E.D.V. Duarte, G.V. Brião, N.F.P. Ribeiro, M.G.C. da Silva, M.G.A. Vieira, S.M.L. de Carvalho, Ternary adsorption of Auramine-O, Rhodamine 6G, and Brilliant Green onto Arapaima gigas scales hydroxyapatite: adsorption mechanism investigation using CCD and DFT studies, Sustain. Materials and Technol. 31 (2022) e00391, https://doi.org/10.1016/j.susmat.2022.e00391.

[31] J.E. Burkell, J.W.T. Spinks, Measurements of self-diffusion in aqueous solutions of sodium dihydrogen phosphate, Can. J. Chem. 30 (1952) 311–319, https://doi.org/10.1139/v52-042.

[32] F. Boudrahem, S. Ziani, F. Aissani-Benissad, Application of response surface methodology based on central composite design for optimization of yellow bezacryl sorption on shoe soles waste, Environ. Prog. Sustain. Energy 38 (2018) S412–S421, https://doi.org/10.1002/ep.13073.

[33] K. Sharma, S. Sharma, V. Sharma, P.K. Mishra, A. Ekielski, V. Sharma, V. Kumar, Methylene blue dye adsorption from wastewater using hydroxyapatite/gold nanocomposite: kinetic and thermodynamics studies, Nanomaterials 11 (2021) 1403, https://doi.org/10.3390/nano11061403.

[34] R. Prakash, N.S.G. Usha, K. Karpagalakshmi, L. Piramuthu, Brilliant green decorated graphene oxide for the detection of cucurbituril, Int. J. Innovative Technol. Explor. Eng. 9 (2019) 227–231, https://doi.org/10.35940/ijitee.B1188·1292S219.

[35] J. Cheriaa, M. Khaireddine, M. Rouabhia, A. Bakhrouf, Removal of triphenylmethane dyes by bacterial consortium, Sci. World J. 512454 (2012) 1–9, https://doi.org/10.1100/2012/512454.

[36] C.V. Rao, A.S. Giri, V.V. Goud, A.K. Golder, Studies on pH-dependent color variation and decomposition mechanism of Brilliant Green dye in Fenton reaction, Int. J. Integrated Care 7 (2016) 71–80, https://doi.org/10.1007/s40090-015-0060-x.

[37] Wt Xia, Zd Ren, Yf Gao, Removal of phosphorus from high phosphorus iron ores by selective HCl leaching method, J. Iron Steel Res. Int. 18 (2011) 1–4, https://doi.org/10.1016/S1006-706X(11)60055-1.

[38] Z. Tišler, K. Hrachovcová, E. Svobodová, J. Šafář, L. Pelíšková, Acid and thermal treatment of alkali-activated zeolite foams, Minerals 9 (2019) 719, https://doi.org/10.3390/min9120719.
[39] S. Kamal, K. Upendra, Adsorption of brilliant green dye from aqueous solution onto chemically modified areca nut husk, S. Afr. J. Chem. Eng. 35 (2021) 33–43, https://doi.org/10.1016/j.sajce.2020.11.001.
[40] B.K. Nandi, A. Goswami, M.K. Purkait, Adsorption characteristics of brilliant green dye on kaolin, J. Hazard Mater. 161 (2009) 387–395, https://doi.org/10.1016/j.jhazmat.2008.03.110.
[41] Venkat S. Mane, P.V. Vijay Babu, Studies on the adsorption of Brilliant Green dye from aqueous solution onto low-cost NaOH treated saw dust, Desalination 273 (2011) 321–329, https://doi.org/10.1016/j.desal.2011.01.049.
[42] N. Laskar, U. Kumar, Removal of Brilliant Green dye from water by modified Bambusa Tulda: adsorption isotherm, kinetics and thermodynamics study, Int. J. Environ. Sci. Technol. 16 (2019) 1649–1662, https://doi.org/10.1007/s13762-018-1760-5.

Environmental Science and Pollution Research
https://doi.org/10.1007/s11356-024-34001-6

RESEARCH ARTICLE

Preparation of porous hydroxyapatite–metakaolin geopolymer granules for adsorption applications using polyethylene glycol as porogen agent and sodium dodecyl sulfate as anionic surfactant

Aghilas Brahmi[1,2] · Salima Ziani[1,3] · Salima AitAli[1,3] · Hafit Khireddine[3] · Tero Luukkonen[2,4]

Received: 29 February 2024 / Accepted: 11 June 2024

Abstract

This study investigated the elaboration of novel porous absorbent granules by mixing powdered hydroxyapatite, metakaolin, sodium metasilicate, polyethylene glycol, and sodium dodecyl sulfate (SDS), an anionic surfactant. The effect of sodium dodecyl sulfate (SDS) was then studied by introducing it as a powder to the powdered mixture or dissolved into the granulation fluid. Characterization of the granules indicated that the incorporation of SDS dissolved in the granulation fluid into the G-PEG granules improved their specific surface area (97.9 m^2/g) and porosity, resulting in a synergistic increase in the adsorption of crystal violet and methylene blue dyes compared to G-PEG granules and hydroxyapatite or metakaolin geopolymer alone. Moreover, the granules exhibited satisfactory compressive strength of 0.81 MPa, making them suitable for large-scale adsorption columns. Finally, the regeneration process of the granules was modeled and optimized by using surface response methodology based on Box–Behnken design. The granules could be regenerated for eight cycles under optimum conditions of acetic acid concentration of 0.72 mol/L, a temperature of 323 K, and a contact time of 173.22 min, without a significant loss in the adsorption capacity or degradation of the granules. These results suggest that the porous granules prepared in this study have potential to be used in industrial wastewater treatment.

Keywords Adsorbent granulation · Hydroxyapatite · Geopolymers · Box–Behnken design · Wastewater treatment

Abbreviations

$\alpha_{1/2}$	Separation factor
a_R	Redlich–Peterson isotherm constants (L/mg)
ΔZ_j	Step size
β	Redlich–Peterson isotherm constants
b_0	Value of the fitted response at the center point of the design
b_j	Linear terms
b_{jj}	Quadratic terms
b_{uj}	Interaction terms
BBD	Box–Behnken design
BET	Brunauer-Emmett-Teller
BJH	Barrett-Joyner-Halenda
CCD	Central composite design
C_e	Equilibrium concentration in aqueous (mg/L)
C_s	Equilibrium concentration in solid phase (mg/L)
CV	Crystal violet
d	Diameter of granules (mm)
D_f	Film diffusion coefficient in liquid phase (m2/s)
D_p	Effective diffusion coefficient (m2/s)
DF	Degrees of freedom
DTG	Differential thermal analysis
DSC	Differential scanning calorimetry
ε	Residue
F	Peak force (N)

Responsible Editor: Guilherme Luiz Dotto

Highlights

- A novel, straightforward, and scalable method was developed for the preparation of porous hydroxyapatite–metakaolin geopolymer using polyethylene glycol as a porogen agent.
- The incorporation of sodium dodecyl sulfate (SDS) dissolved in the granulation fluid probably enhanced geopolymer formation by reducing water surface tension.
- The granules prepared with SDS demonstrated significantly enhanced proprieties and synergistic adsorption capacity compared with those prepared solely with HAP or MK-GP and those prepared without SDS.
- Modelization and optimization of the regeneration process parameters of HAP-MK-GP granules using response surface methodology based on Box–Behnken design.
- The obtained granules exhibit enduring, high-stress, and Young's modulus characteristics, making them suitable for use in large-scale adsorption columns.

Extended author information available on the last page of the article

FTIR	Fourier transform infrared spectroscopy
δ	Film thickness (m)
HAP	Hydroxyapatite
HPDM	Homogeneous particle diffusion model
k	Diffusion rate constant (L/s)
k_1	Pseudo-first-order rate constant (min−1)
k_2	Pseudo-second-order rate constant (g/(mg × min))
K_d	Distribution coefficients (L/g)
K_F	Freundlich constants (mg(1–1/n) × L(1/n)/g)
K_L	Langmuir adsorption constant (L/mg)
k_p	Diffusion rate constant (L/s)
K_R	Redlich–Peterson isotherm constants (L/g)
λ_{max}	Maximum emission wavelength (nm)
m	Mass of the adsorbent granules (g)
MB	Methylene blue
MK	Metakaolin
MK-GP	Metakaolin geopolymer
MS	Mean of squares
N	Number of experiments
OFAT	One-factor-at-a-time
PEG	Polyethylene glycol
q_e	Adsorption capacity at equilibrium (mg/g)
q_i^{exp}	Measured adsorption amounts (mg/g)
q_i^{pred}	Predicted values of the adsorption amounts (mg/g)
q_{max}	Langmuir monolayer adsorption capacity (mg/g)
q_t	Adsorption capacity versus time (mg/g)
r_0	Radius of the granules (m)
RMSEC	Root mean square error
RSM	Response surface methodology
SSA	Specific surface area
SEM	Scanning electron microscope
SDS	Sodium dodecyl sulfate
σ	Compressive strength (MPa)
SS	Sum of squares
TGA	Thermogravimetric analysis
UV-Vis	Spectroscopy of the ultraviolet–visible range
V	Volume of the solution (L)
x_j	Dimensionless variables or coded forms that correspond to Z_j
$X_{(t)}$	The fractional adsorption at given time
XRF	X-ray fluorescence spectroscopy
y	Measured dye removal efficiency response
$\hat{y}$	Predicted dye removal efficiency response
Z_j	Dimensionless variables or reel forms
Z_j^0	Value of Z_j at the center point of the investigation domain
Z_{jmax}	Maximum level of factor j in natural units
Z_{jmin}	Minimum level of factor j in natural units
$\frac{1}{n}$	Partitioning coefficient

Introduction

Hydroxyapatite (HAP), a major component of teeth and bones, is the most extensively investigated calcium phosphate ceramic both in biomedical and environmental fields (Meski et al. 2011). HAP exhibits remarkably versatile properties, enabling its use in various applications depending on its microstructure, making it useful in dental implants, scaffolds for tissue engineering, and as an adsorbent in water treatment. HAP can be synthesized using natural resources such as eggshells, shells, fish bones and scales, animal bones, and algae (Teymouri 2018; Ziani et al. 2014). In wastewater treatment, HAP can be used to separate several pollutants with very promising equilibrium adsorption capacities (q_e) such as lead (q_e = 698 mg/g) (Meski et al. 2011), zinc (q_e = 450 mg/g) (Meski et al. 2010), copper (q_e = 91 mg/g) (Wang et al.2017), dyes (methylene blue (q_e = 328 mg/g)) (Peng et al. 2019), Congo red (q_e = 48 mg/g) (Panneerselvam et al. 2019), and acid yellow (q_e = 213 mg/g) (Manatunga et al. 2018). Furthermore, HAP is effective in adsorbing emerging pollutants, such as ofloxacin (q_e = 27 mg/g) and triclosan (q_e = 130 mg/g) (Huang et al. 2016). However, most existing studies have been conducted using powdered HAP, and there is little research on HAP-based granules as adsorbents (Chen 2023).

Geopolymers (GPs) are ceramic-like amorphous aluminosilicates, formed by mixing an aluminosilicate precursor (e.g., metakaolin) with an alkali-activator solution (e.g., sodium silicate). They have been extensively studied in water and wastewater treatment as adsorbents, membrane materials, filtration media, and catalyst support and for solidification/stabilization of solid residues (Al Natsheh et al. 2022; Luukkonen et al. 2020, 2019). Porous GP composites can be produced through direct foaming (i.e., introduction of a blowing agent to produce gas bubbles), addition of lightweight fillers, additive manufacturing, reactive emulsion templating, particle compaction, or mixed approaches (Zhang et al. 2021).

Recent research has explored the possibility of combining HAP powder with a metakaolin GP (MK-GP) via granulation to form adsorbent granules (Brahmi et al. 2024), improving their feasibility for practical water treatment applications. In this study, a novel method for introducing porosity to HAP-MK-GP granules is proposed by using polyethylene glycol (PEG) as a templating agent and sodium dodecyl sulfate (SDS) as an anionic surfactant. This approach aims to enhance the adsorption and surface properties of HAP-MK-GP granules using the anionic structure of SDS, which has hydrophobic and hydrophilic functional groups, allowing it to interact with organic compounds and cationic pollutants, facilitating their removal from aqueous

solutions. In addition, this study investigates the most effective approach to employ SDS, either as powder or as an aqueous granulation fluid to reduce water surface tension during the granulation process, which can enhance the even distribution of water within the granulation mixture components, ultimately improving the granule formation process.

The developed granules are demonstrated as potential adsorbents for dye removal using cationic dyes, methylene blue (MB), and crystal violet (CV), as model adsorbates (either alone or from a binary solution), and their low-cost regeneration is demonstrated and optimized using statistical design of experiments based on response surface methodology (RSM) with Box–Behnken design (BBD).

Materials and methods

Chemicals

The raw materials used to prepare HAP were $Ca(NO_3)_2{\bullet}4H_2O$ (99% assay) and $(NH_4)_2HPO_4$ (99.2% assay) obtained from Biochem Chemopharma (Canada) and Analar Normapur (Belgium), respectively. CV and MB dyes were obtained from Sigma-Aldrich (China). HCl (0.1 N) and NaOH (0.1 N) solutions used to adjust pH were obtained from VWR (Belgium). The raw materials used to prepare porous MK-GP granules were metakaolin (MetaMax, BASF, USA), solid anhydrous sodium metasilicate (Na_2O (50.8 wt%), SiO_2 (46.7 wt%), and H_2O (2.5 wt%); VWR Alfa Aesar, Germany), SDS obtained from SIGM (China), and PEG with an average molar mass of 4000 g/mol obtained from Merck (Germany). Acetic acid (1.0 N) obtained from Sigma-Aldrich (Germany) was used for the regeneration studies.

Preparation of HAP powder

The HAP powder was synthesized using the co-precipitation method described previously in the literature (Brahmi et al. 2024).

Preparation of porous HAP-MK-PEG/SDS granules

Three batches of granules were prepared, which are referred to as G-PEG (i.e., with PEG and without SDS), G-PEG-SDS (S) (i.e., with PEG and SDS added as a solid powder), and G-PEG-SDS (L) (i.e., with PEG and SDS added as an aqueous solution). The performance of reference granules without PEG and SDS has been represented in a previous study by the authors (Brahmi et al. 2024). First, HAP, PEG, sodium metasilicate, metakaolin, and SDS (SDS only in the G-PEG-SDS (S) granules) were mixed as dry powders (Table 1), ground using a disc mill (Retsch RS 200) at a speed of 1500 rpm for 5 min, and then placed in a high-shear granulator (Eirich EL1). Afterward, deionized water (35 mL for a dry solid mass of 80 g) was used as a granulation fluid by adding it dropwise to the granulator using a granulator pan mixing speed of 1200 rpm, granulator mixer plate speed of 170 rpm, and granulator tilting angle of 30°. Granulation was stopped when the granules were formed by visual observation. The G-PEG-SDS (L) granules were prepared by dissolving SDS (Table 1) in the volume of the deionized water ($V = 35$ mL), which was used as a granulation fluid.

Finally, the granules were cured at 333 K for 24 h. They were then cleaned by mixing with distilled water ($V = 200$ mL) at 358 K and a mixing speed of 150 rpm for 5 h to remove PEG contained in the granules (the operation was repeated three times). Subsequently, they were dried in an oven at 333 K for 24 h.

Characterization of granules

The functional groups of the as-prepared granules were identified using Fourier transform infrared spectroscopy (FTIR) in the range of 400–4000 cm^{-1}, with a spectral resolution of 200. Analyses were performed using a Bruker Vertex v80 instrument fitted with a Harrick Praying Mantis DRIFT cell. In addition, the elemental composition of granules was obtained using an X-ray fluorescence spectrometer (XRF) (PanAnalytical Minipal 4).

Thermogravimetric analysis (TGA) and differential thermal gravimetric (DTG) analysis for the HAP and MK powders and elaborated granules were performed using an SDT 650 simultaneous thermal analyzer (a heating rate of 10 °C/min under nitrogen atmosphere).

The specific surface area and pore size were determined using a Micrometrics ASAP2020 instrument and calculated using the Brunauer–Emmett–Teller (BET) isotherm and the Barrett–Joyner–Halenda (BJH) method.

The microstructural morphology and composition of the samples were determined using a field emission scanning electron microscope equipped with an energy dispersive

Table 1 Composition of the elaborated granules

Samples	HAP (g)	MK (g)	Sodium metasilicate (g)	PEG (g)	SDS (g)	H_2O (mL)
G-PEG	61	18	18	3	0	35
G-PEG-SDS (S)	60	18	18	3	1	35
G-PEG-SDS (L)	60	18	18	3	1	35

X-ray spectroscope (FE-SEM–EDS, Zeiss Ultra Plus). In addition, the cross-sections of the granules were imaged using an optical microscope (Leica MZ6 equipped with a Leica DFC420 camera).

The mechanical strength of the granules was determined using a Zwick Roell Z010 (10 kN load cell) instrument with a loading rate of 1 mm/min. The granules selected for the compression test were spherical with a diameter of 4 mm, and measurements were performed for five granules from each batch. The compressive strength (σ, MPa) was calculated using Eq. (1), where F (N) represents the peak force and d (mm) represents the granule diameter.

$$\sigma = 4 \times \frac{F}{\pi \times d^2} \tag{1}$$

Batch adsorption studies

First, a comparative study was conducted for the adsorption efficiency of the granules and HAP and MK-GP powders. Adsorption studies were conducted using MB and CV dyes individually in aqueous solutions under the following conditions: $[\text{dye}]_0 = 25\,\text{mg/L}, \text{pH}=7, \text{granule mass per water volume} = 2\,\text{g/L}, d_{\text{granules}} = 4\,\text{mm}$, agitation speed = 250 rpm, time = 90 min, and $T = 298$ K. After the comparative study, the G-PEG-SDS (L) granules were used subsequently, because they have higher adsorption capacity than the other granules.

The adsorption parameters (i.e., contact time (0–180 min), mass of granules (1–4 g/L), and solution pH (3–10)) were optimized. Then, the selectivity of the granules was evaluated using MB and CV dyes at concentrations ranging from 25 to 180 mg/L in aqueous solutions. In addition, a binary mixture of MB and CV at different concentrations (ranging from 15 to 100 mg/L, with both dyes having the same concentration) was examined. The conditions in the experiments assessing selectivity were as follows: pH of 8, granule diameter of 4 mm, granule mass per water volume of 3 g/L, agitation speed of 250 rpm, contact time up to 180 min, and temperature of 298 K.

After each experiment, the water samples were centrifuged (Beckman Coulter J326XPI-IM-1) at 8000 rpm for 5 min, and the supernatant was collected and analyzed using a UV-6300PC spectrophotometer (VWR, China) at the following wavelengths: $\lambda_{MB} = 664$ nm and $\lambda_{\text{CV}} = 586$ nm. The calibration curves for MB and CV are shown in Figs. S1 and S2 (supporting information). The dye removal efficiency y (%) and the adsorption capacity, q_t (mg/g), of the dyes were calculated using Eqs. (2) and (3), respectively.

$$y(\%) = \frac{[\text{dye}]_0 - [\text{dye}]_t}{[\text{dye}]_0} \times 100, \tag{2}$$

$$q_t = \left([\text{dye}]_0 - [\text{dye}]_t\right) \times \frac{V}{m}, \tag{3}$$

where $[\text{dye}]_0$ and $[\text{dye}]_t$ (mg/L) denote the initial concentrations of the dyes (i.e., MB or CV) and their concentrations at time t, respectively; V (L) represents the volume of the solution; and m (g) represents the mass of the adsorbent granules.

The selectivity of G-PEG/SDS (L) granules toward the two dyes in a binary solution was evaluated using the separation factor ($\alpha_{1/2}$, Eq. (4)), which is defined as the ratio of the equilibrium adsorption constants for the two components (Shen et al. 2018).

$$\alpha_{\frac{1}{2}} = \frac{K_{d,1}}{K_{d,2}} \text{and } K_d = \frac{q_e}{C_e} \tag{4}$$

In Eq. (4), $K_{d,1}$ and $K_{d,2}$(L/g) denote the distribution coefficients of the dyes between the adsorbent surface and solution at the equilibrium, respectively; q_e (mg/g) denotes the adsorption capacity; and C_e (mg/L) denotes the concentration of the MB or CV dyes at equilibrium.

Rate-controlling step of the adsorption of dyes

Homogeneous particle diffusion model (HPDM)

The HPDM shown in Eq. (5), originally introduced by Boyd et al. (Boyd et al. 1947), describes the rate-limiting step, which can be controlled using either an intra-particle or film diffusion mechanism (Benamor et al. 2008).

$$X_{(t)} = \frac{q_t}{q_e} = 1 - \frac{6}{\pi^2} \sum_{z=1}^{\infty} \frac{1}{Z^2} \exp\left[\frac{-Z^2 \pi^2 D_p t}{r_0^2}\right]. \tag{5}$$

To describe the adsorption onto spherical particles and when $0 < X_{(t)} < 1$, Eqs. (6) and (7) are used as simplified equations derived from Eq. (5) (Liu et el. 2008).

$$X_{(t)} = \left[1 - \exp\left[\frac{-\pi^2 D_p^2 t}{r_0^2}\right]\right]^{0.5}, \tag{6}$$

$$-ln\left(1 - X_{(t)}{}^2\right) = 2k_p t = \frac{2\pi^2 D_p}{r_0^2} t, \tag{7}$$

$$\text{with } D_p = \frac{k_p r_0^2}{\pi^2},$$

where $X_{(t)}$ denotes the fractional adsorption at time t, D_p (m^2/s) denotes the effective diffusion coefficient, r_0 denotes

the radius of the granules (0.4×10^{-3} m), Z represents an integer, and k_p denotes the diffusion rate constant (L/s).

When the rate of adsorption is controlled by the liquid film diffusion, Eq. (8) can be used (Liu et el. 2008).

$$-\ln\left(1 - X_{(t)}\right) = k_{li}t = \left[\frac{3D_f C_e}{r_0 \delta C_s}t\right] \tag{8}$$

$$\text{with } D_f = \frac{k_d r_0 \delta C_s}{3C},$$

where D_f (m^2/s) denote the film diffusion coefficient in the liquid phase, k represents the diffusion rate constant (L/s), C_s (mg/L) denotes the equilibrium concentration of MB and CV in the solid phase (granules), and δ denotes the film thickness, which was estimated to 10^{-5} (m) (Yu & Luo 2014).

The graphs of $-\ln\left(1 - X_{(t)}{}^2\right)$ and $-\ln\left(1 - X_{(t)}\right)$ were used to determine the values of K_p and K_f, respectively, for different concentrations of MB and CV dyes in the binary dye mixture, and the slopes of the fitted lines were used to determine the effective diffusion coefficient D_p (m^2/s) and D_f (m^2/s).

Modeling of kinetic and isotherm data

The experimental kinetic data were fitted to the pseudo-first-order and pseudo-second-order kinetic models (Eqs. (9) and (10), respectively) (Brahmi et al. 2024).

$$q_t = q_e \times \left[1 - \exp\left(-k_1 t\right)\right], \tag{9}$$

$$q_t = q_e - \frac{q_e}{k_2 q_e t + 1}, \tag{10}$$

where k_1 (min^{-1}) denotes the pseudo-first-order rate constant and k_2 (g/(mg × min)) denotes the pseudo-second-order rate constant.

Three adsorption isotherm models, Langmuir, Freundlich, and Redlich–Peterson, were used to interpret the equilibrium data (Eqs. (11), (12), and (13), respectively) (Brahmi et al. 2024).

$$q_e = \frac{q_{\max} K_L C_e}{K_L C_e + 1}, \tag{11}$$

$$q_e = K_F C_e^{\frac{1}{n}}, \tag{12}$$

$$q_e = \frac{K_R C_e}{a_R C_c^{\beta} + 1}, \tag{13}$$

where $q_{\max}$ (mg/g) denotes the Langmuir monolayer adsorption capacity, K_L (L/mg) denotes the Langmuir adsorption constant, and K_F($mg^{1-\frac{1}{n}} \times L^{\frac{1}{n}}$/g) and $\frac{1}{n}$ denote the Freundlich constants and the partitioning coefficient, respectively, related to surface heterogeneity; K_R (L/g), a_R (L/mg), and β denote the Redlich–Peterson isotherm constants.

Furthermore, the validity of the data fitting to the isotherm models was evaluated using the root mean square error (RMSEC).

$$\text{RMSEC} = \sqrt{\frac{\sum_{i=1}^{n}\left(q_i^{\exp} - q_i^{\text{pred}}\right)^2}{N}}, \tag{14}$$

where $q_i^{\exp}$ and q_i^{pred} denote the obtained and predicted values of the adsorption amounts, respectively, and N represents the number of experiments. A lower RMSEC value indicates a good prediction capability of the model.

Box–Behnken optimization of regeneration parameters

The regeneration experiments were conducted using acetic acid for the G-PEG/SDS (L) granules and MB dye. The regeneration parameters were optimized using the BBD design while minimizing granule mass loss during the regeneration. Three independent variables were investigated: the acetic acid concentration (0.2–1 mol/L) (x_1), temperature (294–338 K) (x_2), and contact time (30–180 min) (x_3). The regeneration efficiency was calculated as weight-% of desorbed dye. The mass loss (as weight-%) was calculated after drying the regenerated granules overnight at 313 K.

Results and discussion

Morphological, microstructure, and mechanical properties of G-PEG/SDS granules

The FTIR spectra of HAP, MK-GP, and the granules prepared using PEG and SDS (solid or aqueous solution) are shown in Fig. 1. Each granule sample exhibits the characteristic absorption bands of both HAP (Meski et al. 2011; Ziani et al. 2014) and MK-GP (Luukkonen et al. 2019; Zenabou et al. 2019; Medri & Ruffini 2011). Furthermore, the peaks at 2841 and 1083 cm^{-1} (in the spectrum of G-PEG/SDS (S and L)) represent the symmetric stretching vibrations of the C–H bond and the stretching vibrations of the S = O bond of SDS (Zhang et al. 2023). This indicates that SDS was integrated into the granule structure and not removed during granule cleaning. The addition of SDS as a solid powder caused the stretching vibration of PO_4 tetrahedral units in HAP to shift from 1200 toward 1250 cm^{-1}, as observed in the spectra of G-PEG/SDS (S). Moreover, the XRF data show a slight decrease in the P content of the granule (Table S1, supporting information).

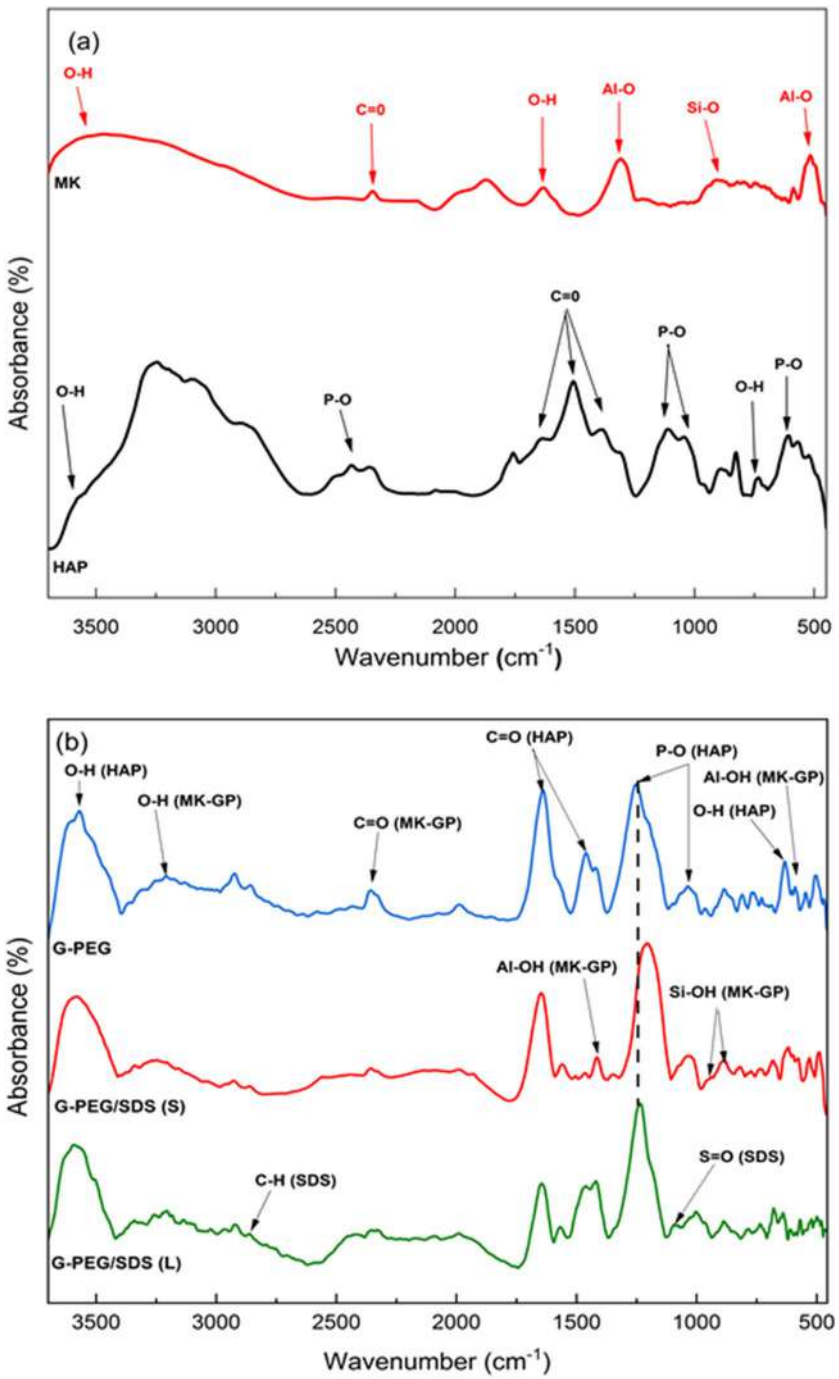

Fig. 1 FTIR spectra of **a** HAP and MK-GP powders and **b** G-PEG, G-PEG/SDS (S), and G-PEG/SDS (L) granules

This may be due to the dissolution of SDS during granule preparation by the addition of deionized water as a granulation fluid, resulting in an interaction between PO_4 groups of HAP and SO_4 groups of SDS.

Understanding how the elaborated granules react to temperature changes is critical for ensuring reliability, performance, and safety in a wide range of industrial applications. Moreover, it allows consideration of the appropriate approach to regenerate these granules (i.e., physical, chemical, or a combination of the two). The TGA and differential scanning calorimetry (DSC) thermograms shown in Fig. 2a, b illustrate the thermal behavior of HAP and MK-GP powders and the different elaborated granules.

According to the figures, the DSC and TGA thermograms of HAP powder (Fig. 2a) show two weight losses (12 and 9 wt%), accompanied by endothermic peaks

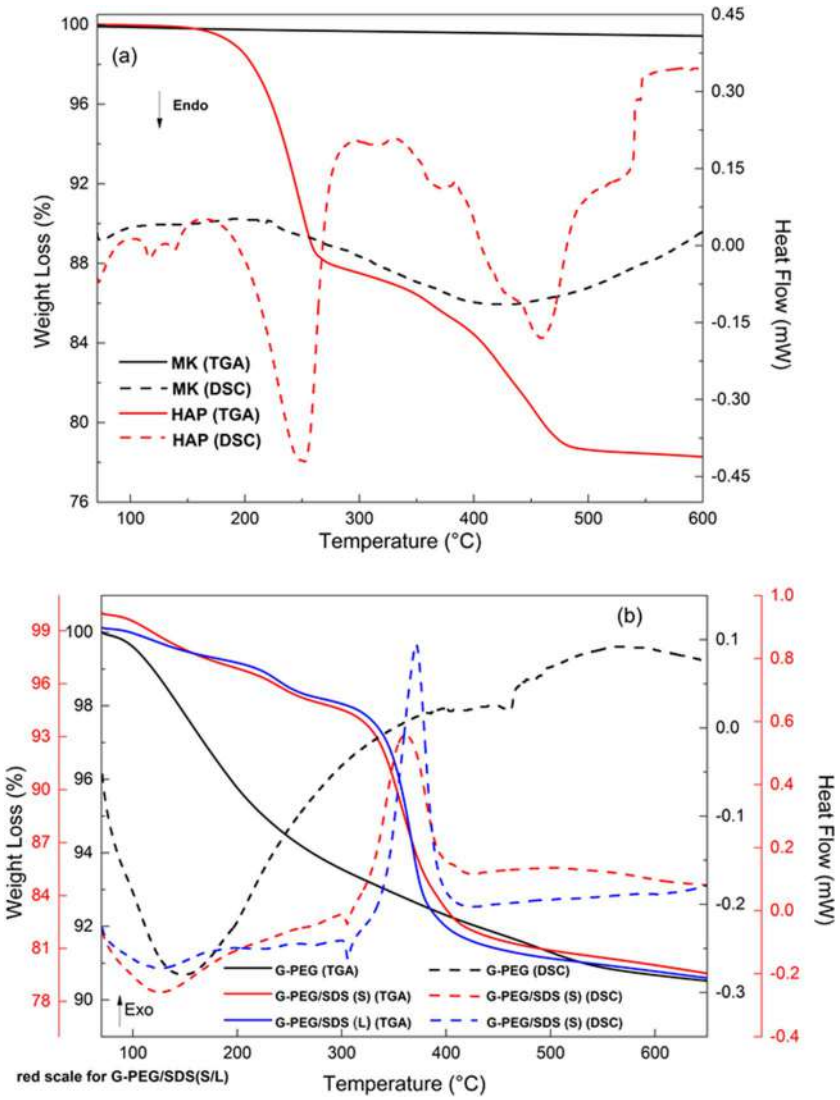

Fig. 2 TGA and DSC of **a** HAP and MK-GP powders and **b** G-PEG, G-PEG/SDS (S), and G-PEG/SDS (L) granules under nitrogen atmosphere

(at 250 °C and 470 °C). These weight losses are due to the evaporation of physisorbed and chemisorbed water molecules and the departure of synthesis residues. Above 480 °C, HAP generates a stable phase unlike MK, which records this stability throughout the range of heating temperature variation.

Moreover, as shown in Fig. 2b, the addition of SDS, either in liquid or solid form, to the G-PEG elaborated granules increases their decomposition by 8.79%. The increase in mass loss is mostly due to the disappearance of the long alkyl chain from SDS molecules (Lun et al. 2014). The presence of SDS reduces the surface tension of water, which can enhance its uniform dispersion into granules, thereby improving the process of removing PEG present in the granules and resulting in the elaboration of high-porosity granules.

The G-PEG/SDS (S/L) granules decompose in two steps: the first with 4 wt% in the 100–280 °C range, with an endothermic DSC signal at 120 °C, and the second with 14.5 wt%, with endothermic and exothermic DSC signals at 300 °C, 350 °C (the G-PEG/SDS (S)), and 370 °C (the G-PEG/SDS (L)). This is due to the loss of chemisorbed water molecules and the disappearance of the long alkyl chain from SDS molecules (Zhang et al. 2023). These findings suggest that chemical methods should be used to regenerate G-PEG/SDS (S/L) granules to prevent the breakdown of SDS.

The morphology of granules prepared using PEG and SDS (S or L) was assessed using SEM and optical microscopy. The results (Fig. 3) reveal highly porous granules with an asymmetric structure with a dense top layer and a porous sublayer with different pore sizes and forms.

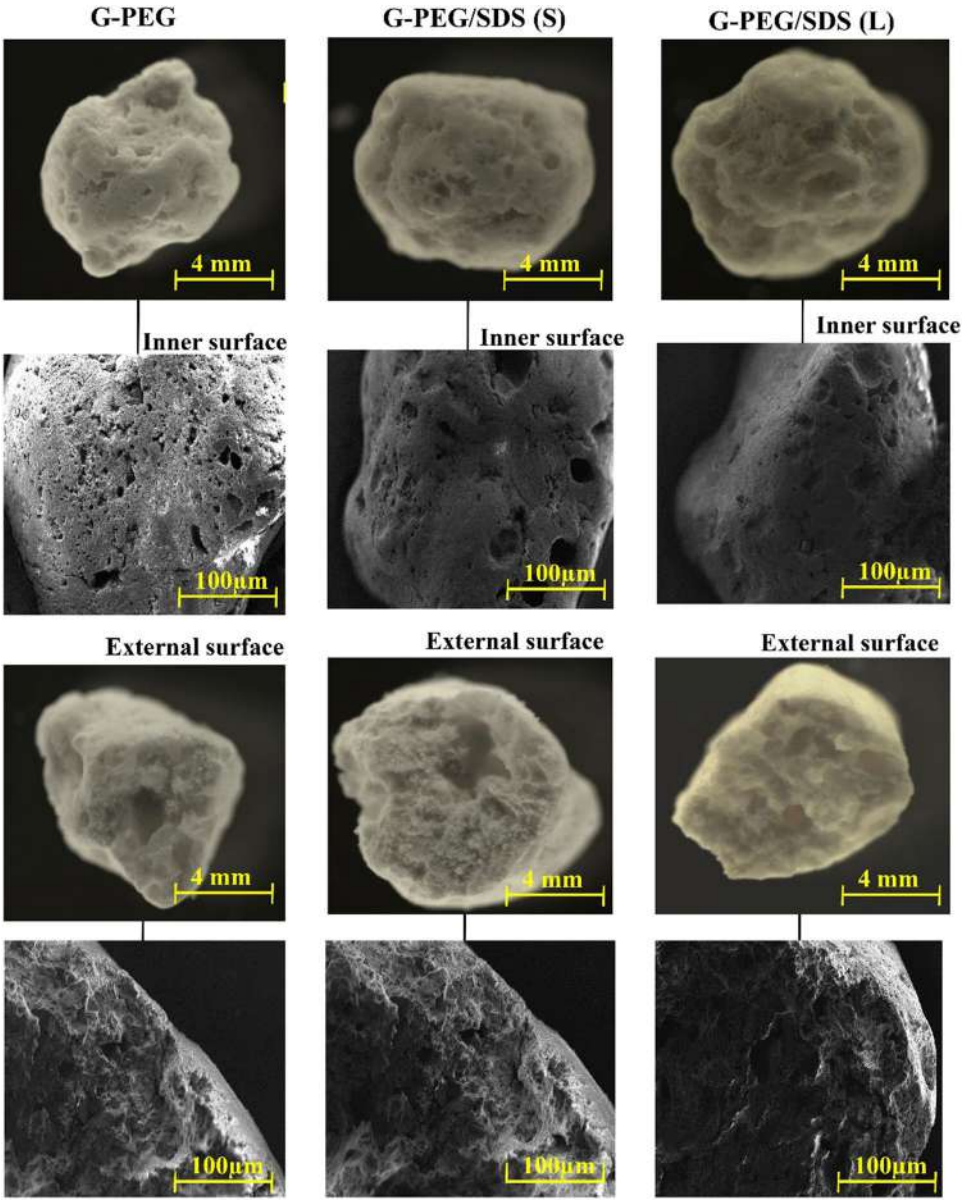

Fig. 3 SEM micrographs and optical microscope photographs of elaborated granules

The pore structure can be explained using the PEG removal process (described in the "Preparation of porous HAP-MK-PEG/SDS granules" section): at 358 K, PEG in the granules undergoes liquefaction, resulting in the formation of pores within the granules.

The N_2 adsorption/desorption isotherms and BJH pore size distribution for the HAP, MK, G-PEG, and G-PEG/SDS (S/L) granules are shown in Fig. S3 and Table 2, respectively.

The isotherms shown in Fig. S3 can be classified as type IV, indicating capillary condensation, and exhibit type H3 hysteresis, characteristic of mesoporous materials with irregular-shaped pores (Brahmi et al. 2024). This illustrates that the adsorption by the elaborated granules gradually increases from low pressures (approximately 0.01–0.45) and then sharply increases from 0.45 and above because of significant particle porosity. Comparing the volume adsorbed and the broadest desorption branch, the granules yield identical values and shapes.

However, the BJH pore size distribution (Fig. S3: inset) confirms that the mesopores (between 2 and 50 nm) dominate the pore structure of the granules (Brahmi et al. 2024).

Moreover, the granulation of the HAP and MK powders significantly affected their physical characteristics, altering particle arrangement, causing pore formation, influencing particle packing, and potentially creating a more complex

Table 2 Specific surface area, porosity, and mechanical parameters of HAP, MK, and the elaborated granules

Samples	G-PEG	G-PEG/SDS (S)	G-PEG/SDS (L)	HAP	MK
Average diameter d_0 (mm)	4.2 ± 0.1	4.1 ± 0.1	4.2 ± 0.1	–	–
Specific surface area (m^2/g)	73.08	85.25	97.89	31.20	10.74
Total pore volume (cm^3/g)	0.30	0.33	0.32	0.065	0.05
Mean pore diameter (nm)	16.79	15.89	13.27	11.82	21.82
F_{max} (N)	46.83 ± 0.4	44.31 ± 0.3	42.03 ± 0.6	–	–
Compressive strength (σ) (MPa)	0.91 ± 0.2	0.85 ± 0.4	0.81 ± 0.1	–	–
Deformation at F_{max} (%)	3.08 ± 0.3	4.26 ± 0.3	4.62 ± 0.4	–	–
Young's modulus (MPa)	16.69 ± 0.3	15.23 ± 0.2	15.08 ± 0.4	–	–

structure, which contributes to the observed increase in the specific surface area (Table 2 and Fig. S3).

Furthermore, the results reported in Table 2 indicate that the incorporation of SDS, either in liquid or solid form, into the G-PEG granules reduces the pore size and increases the surface area (an increase of 16% when solid SDS is used and 33% when dissolved SDS is used compared with granules without SDS). In general, a larger surface area implies improved adsorption properties.

The results of the mechanical compression test for the granules are displayed in Table 2. The G-PEG granules had the highest compressive strength and Young's modulus of 0.81 and 15.56 MPa, respectively. The higher mechanical strength is due to their lower porosity than that of the other granules (G-PES/SDS (S or L)).

Adsorption of MB and CV onto granules

The results of the comparative study between HAP, MK-GP, and the granules and the effect of SDS (S/L) on G-PEG granules are presented in Fig. 4. The results reveal that HAP alone does not adsorb either MB or CV dye. Conversely, MK-GP has an affinity to remove both dyes because of its negative surface charge. The granulation process of HAP and MK without SDS decreased the absorbed amount of MB and CV dyes compared with MK-GP. This can be explained by the decreased amount of MK-GP in the granules compared with that of MK-GP, which decreased the number of responsible active sites for MB and CV absorption.

However, the incorporation of SDS by dissolving it to a granulation fluid (i.e., G-PEG/SDS (L) granules) resulted in a synergistic increase in the adsorption of both MB and CV dyes compared with using HAP or MK-GP alone. Using the SDS solution as a granulation fluid reduces the

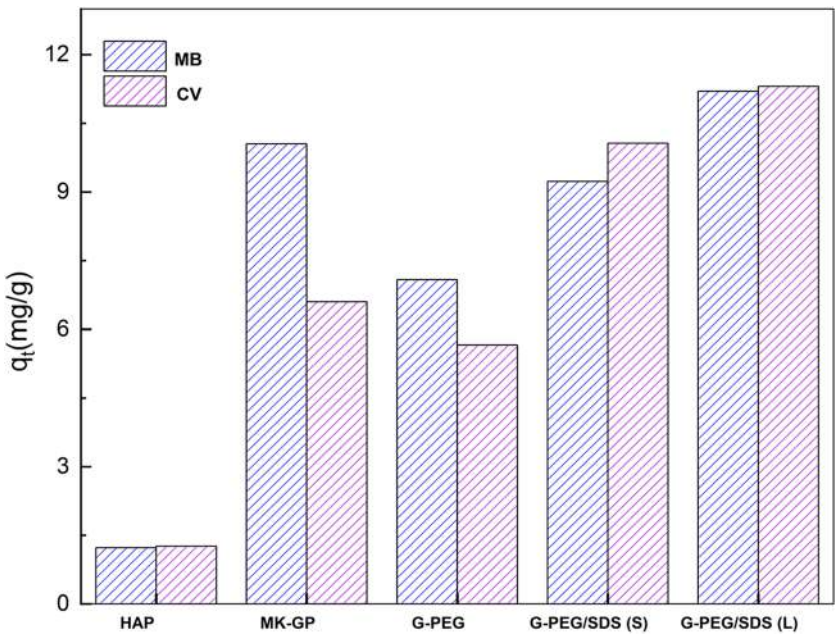

Fig. 4 Adsorption capacity of HAP, MK-GP, and elaborated granules for MB and CV dyes alone in aqueous solution. Conditions: $[dye]_0$ = 25 mg/L, granules mass = 2 g/L, pH of dye, $d_{granules}$ = 4 mm, agitation speed = 250 rpm, time = 90 min, and T = 298 K

surface tension of water, which can enhance its uniform dispersion into the forming granules, thereby leading to more efficient dissolution of sodium metasilicate and GP binder formation (Ramimoghadam et al. 2012). Moreover, this enhanced the porosity and surface area of the granules (Table 2) and improved the adsorption performance.

MB and CV dyes are weak bases with pK_a values of 2.6 and 9.4, respectively (i.e., they exist in the mono protonated (BH^+) and di-protonated (BH^{2+}) forms) (Lun et al. 2014; Li et al.2022). As pH increased, MB and CV uptake increased, reaching its maximum at pH = 8(Fig. 5a). This is due to the increased electrostatic attraction between the negatively charged granule surface (pH_{pzc} = 7.23 (Fig. 5b), i.e., the granules have a negative surface charge at pH higher than pH_{pzc}) and cationic MB and CV molecules.

Adsorption capacity and removal efficiency are influenced by the adsorbent dosage. Figure 5c shows that as the dosage increases from 1 to 3 g/L, the adsorption capacity increases to 18.6 and 23.3 mg/g for MB and CV, respectively.

Effect of dye concentration on adsorption

As shown in Fig. 6a, the adsorption of MB and CV dyes was faster during the first 5 min, and equilibrium was reached after 30 min. The quick equilibration time can be explained by the high porosity and specific surface area of the G-PEG/SDS (L) granules (as demonstrated by the SEM and BET/BJH results). Moreover, the adsorption amount of dyes significantly increased (from 7.3 to 34.8 mg/g for MB and from 7.4 to 45.2 mg/g for CV) as the initial dye concentration was increased. This can be ascribed to an increase in the driving power required to transport dye molecules from the solution to the solid surface (Bensedira et al. 2022).

Selectivity of G-PEG/SDS (L) granules toward dyes

The binary solutions of MB and CV dyes at different concentrations (15–100 mg/L, the original concentration ratio of each mixed dye in the solution was set to be 1:1) were used to evaluate the selectivity of G-PEG/SDS (L) granules for cationic dye adsorption under the aforementioned optimal conditions. The adsorption efficiency in the dye mixture solutions decreased compared with that in the individual solutions of each dye. This observed deviation is explained by the fact that both MB and CV dyes compete to occupy the available adsorption sites on the material surface. Moreover, the results indicate that, especially at concentrations higher than 50 mg/L, the granules had a stronger affinity for adsorbing CV than MB (Fig. 6b). This behavior can be attributed to the lower diffusion coefficient of CV than MB, as indicated in Table S2. When the dye concentrations are lower than 50 mg/L, both MB and CV have the same diffusion coefficients, because of less steric hindrance and a large concentration gradient; both MB and CV molecules are expected to move more swiftly within the

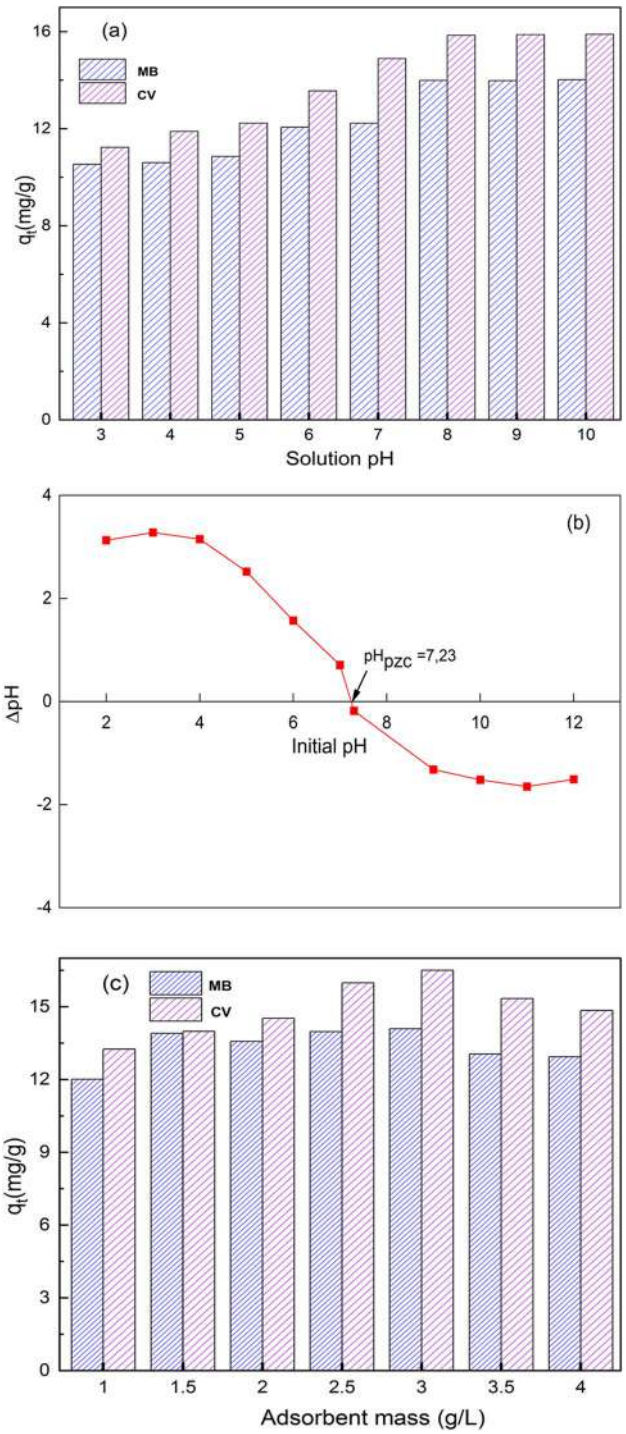

Fig. 5 **a** Effect of pH of solution on adsorption, **b** pH_{pzc} of granules, and **c** effect of granule mass per water volume on adsorption of MB and CV dyes alone in aqueous solution onto G-PEG/SDS (L). Conditions: $[dye]_0$ = 50 mg/L, $d_{granules}$ = 4 mm, agitation speed = 250 rpm, time = 90 min, and T = 298 K

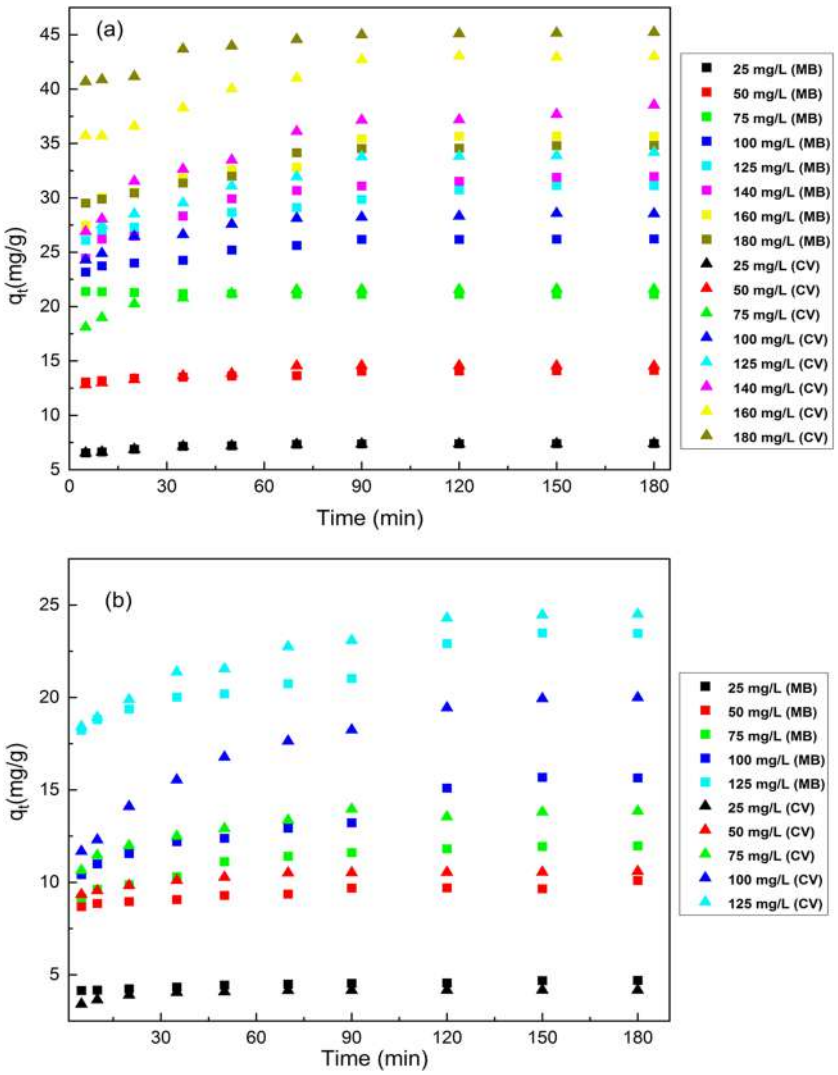

Fig. 6 Effect of initial concentration of MB and CV dyes on the adsorption amount onto G-PEG/SDS (L) granules. **a** Each dye alone in aqueous solution and **b** in binary dye mixtures. Conditions: pH = 8, adsorbent mass = 3 g/L, $d_{granules}$ = 4 mm, agitation speed = 250 rpm, time = 180 min, and T = 298 K

solution, leading to similar adsorption behaviors. However, as the concentration increases beyond 50 mg/L, the diffusion coefficient of CV dye becomes lower than that of MB dye, making it more difficult for MB molecules to diffuse through the solution and reach the granule surface. This can be attributed to the fact that the positively charged sites of CV molecules may interact more easily with the negatively charged surfaces of the granules compared with MB groups, facilitating CV diffusion.

Moreover, the separation factor values (Table 3) demonstrate that the granules have a stronger affinity for CV dye from a binary mixture than for MB dye.

Fitting of kinetic and adsorption isotherm models to data

Figure 7 and Table 4 illustrate the fitting of kinetic and isotherm models to the adsorption data on G-PEG/SDS (L) granules. The results indicate that the adsorption of MB and CV dyes, individually or in a binary mixture, onto the G-PEG/SDS (L) granules follows the pseudo-second-order kinetic model and Langmuir or Redlich–Peterson isotherms.

Table 3 Separation factors (α) for CV and MB in binary dye solution at various dye concentrations. Conditions: pH = 8, granule mass = 3 g/L, $d_{granules}$ = 4 mm, agitation speed = 250 rpm, time = 180 min, and T = 298 K

The initial concentrations of MB and CV in binary dye mixtures (mg/L)	$\alpha_{MB/CV}$	$\alpha_{CV/MB}$
25	0.95	0.97
50	1.02	1.12
75	0.41	2.38
100	0.49	2.01
125	0.89	1.11

MB/CV MB in binary dye mixture, *CV/MB* CV in binary dye mixture

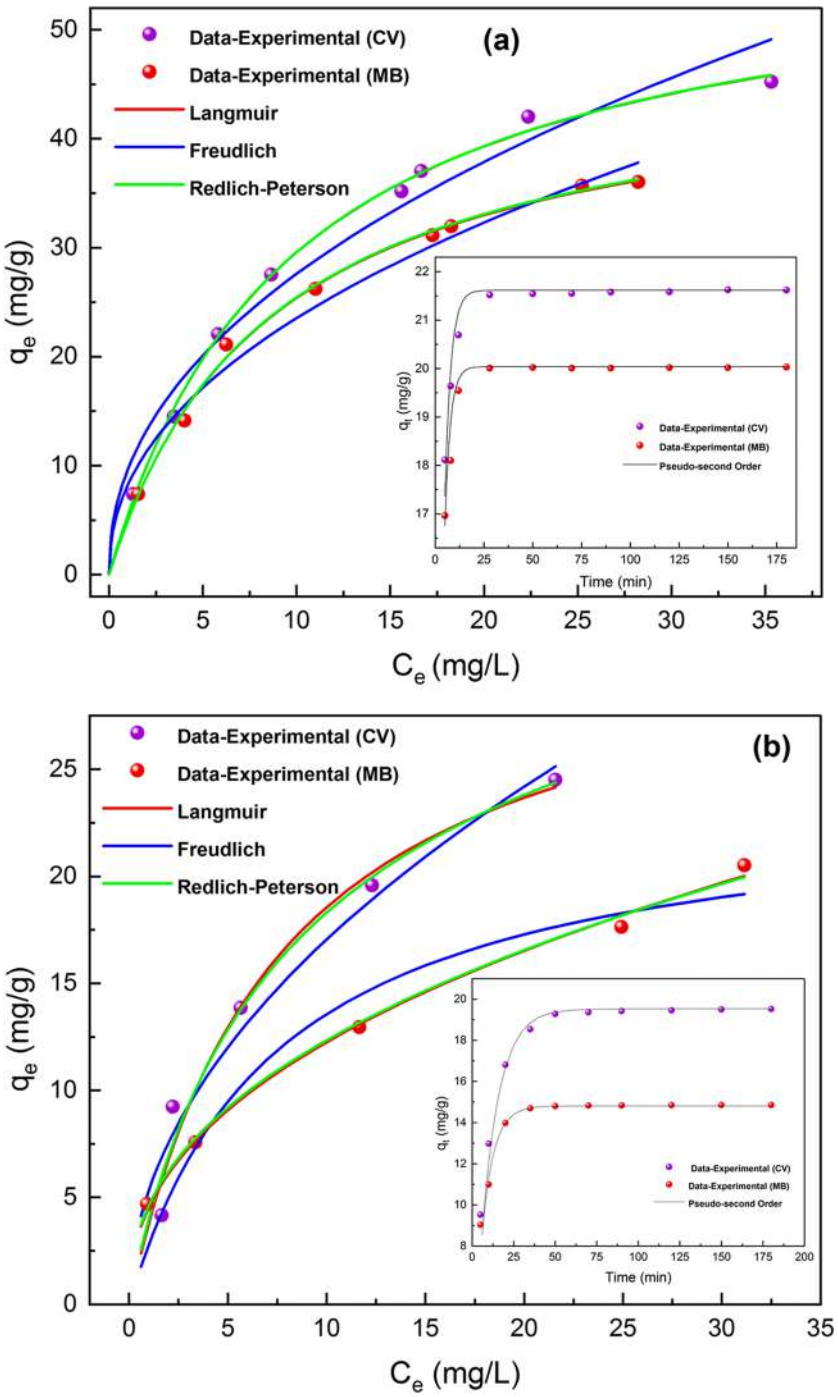

Fig. 7 Isotherm and kinetic models fitting to experimental data for MB and CV dyes **a** individually in aqueous solution and **b** in binary mixture. Conditions: pH = 8, adsorbent mass = 3 g/L, $d_{granules}$ = 4 mm, agitation speed = 250 rpm, time = 180 min, and T = 298 K

These findings suggest that the surface of the G-PEG/SDS (L) granules is homogeneous. All sites are equivalent, and each site can hold at most one cationic dye molecule (monolayer coverage only). There are no interactions between sorbate molecules on adjacent sites (Brahmi et al. 2024).

Experimental design and statistical analysis

Modeling of G-PEG/SDS (L) granule regeneration efficiency response

Statistical modeling was performed to investigate the effects of independent variables (i.e., acetic acid concentration, time, and temperature) and their mutual

Table 4 Kinetic and isotherm parameters for MB and CV dyes individually and in binary mixtures. Conditions: pH = 8, adsorbent dose = 3 g/L, $d_{granules}$ = 4 mm, agitation speed = 250 rpm, time = 180 min, and T = 298 K

		MB	MB/CV	CV	CV/MB
Kinetic model	Kinetic parameters				
Pseudo-first-order	q_{exp}(mg/g)	20.083	14.879	21.612	20.596
	q_{cal}(mg/g)	19.683	14.135	21.160	28.669
	k_1(min^{-1})	0.373	0.162	0.350	0.116
	R^2	0.973	0.943	0.956	0.963
Pseudo-second-order	q_{exp}(mg/g)	20.083	14.879	21.612	20.596
	q_{cal}(mg/g)	20.123	14.799	21.792	20.510
	k_2(mg/(g×L))	0.053	0.017	0.039	0.081
	R^2	0.992	0.995	0.990	0.994
Isotherm model		Equilibrium parameters			
Freundlich	$K_F(mg^{1-\frac{1}{n}}.L^{\frac{1}{n}}/g)$	8.216	4.531	9.634	5.328
	n^{-1}	0.457	0.436	0.451	0.550
	R^2	0.913	0.861	0.893	0.903
	RMSEC	0.383	0.170	0.623	0.210
Langmuir	K_L(mg/g)	0.116	0.136	0.102	0.130
	q_{max}(mg/g)	47.130	28.826	58.068	32.712
	R^2	0.992	0.991	0.997	0.998
	RMSEC	0.094	0.105	0.032	0.071
Redlich–Peterson	K_R(L/g)	5.510	2.897	5.618	4.765
	a_R(L/mg)	0.220	0.193	0.078	0.10
	B	0.983	0.884	1.001	0.992
	R^2	0.991	0.993	0.991	0.992
	RMSEC	0.194	0.189	0.138	0.081

MB/CV MB in binary mixtures (MB/CV), *CV/MB* CV in binary mixtures (MB/CV).

interactions on the regeneration efficiency of G-PEG/SDS (L) granules. In this context, a mathematical second-order quadratic polynomial model based on the RSM–BBD modeling was established using the experimental results of Table 5.

According to the analysis of variance data (Table S3), the adequacy of the proposed model to describe G-PEG/SDS (L) regeneration efficiency was confirmed by a small p-value (<0.05). Thus, the regression polynomial model for G-PEG/SDS (L) regeneration efficiency can be expressed as follows (Eq. (15), see Table 5 for the explanation of x_1, x_2, and x_3):

$$\hat{y} = 91.97 + 2.70x_1 - 3.76x_2 + 3.36x_3 - 1.86x_1x_2 - 12.32x_1x_3 - 4.36x_1^2 - 3.06x_2^2 - 4.37x_3^2. \quad (15)$$

Fig. S4 (a) illustrates the relationship between the measured and predicted G-PEG/SDS (L) regeneration efficiency. The data were distributed around a straight line ($R^2 = 0.99$), which unambiguously demonstrates the adequate correlation between the experimental and statistically predicted responses (AitAli et al. 2023). Furthermore, residual analysis, as shown in Fig. S4 (b), indicates that the predicted values and the residues have no relationship. Thus, the prediction model (Eq. (15)) can be used to explain the statistical results and predict the optimum conditions using RSM.

Study of model

The model discovered that all variables have an effect on granule regeneration ($p < 0.05$). The acetic acid concentration (x_1) and contact time (x_3) have a positive influence on desorption efficiency with coefficients $b_1 = 2.70$ and $b_3 = 3.36$, respectively, whereas the temperature has a negative influence ($b_2 = -3.76$). High temperatures accelerate the degradation of the granules, decreasing their structural integrity and performance.

Moreover, the regression model revealed the existence of slightly negative interactions between acetic acid concentration and temperature (x_{12}) and contact time (x_{13}).

To improve comprehension of the results, the predicted model (Eq. (15)) derived from BBD is illustrated in Fig. 8 as three-dimensional response surface plots. These plots, generated using MATLAB, serve to identify the optimal values of the operating parameters that yield the highest G-PEG/SDS (L) regeneration efficiency.

Figure 8a shows that an increase in acetic acid concentration (x_1) and contact time (x_3) positively influences the response, leading to an increase in G-PEG/SDS (L) regeneration efficiency. Extended contact times and elevated concentrations of acetic acid increased the diffusion of acetic acid within the granules, enhancing regeneration processes.

Furthermore, according to the curves shown in Fig. 8b, c, at high temperatures ($x_2 > 313$ K), it is recommended to minimize the contact time ($x_3 < 180$ min) and work with

Table 5 Experimental design matrix developed using RSM-based BBD model: variables, levels, and response

Values of parameters (coded experiment matrix)			Measured response	Predicted response	Residue
x_1, acetic acid concentration (mol/L)	x_2, temperature (K)	x_3, time (min)	y (%)	$\hat{y}$(%)	E
0.2 (−1)	298 (0)	180 (0)	90.36	89.86	0.5
0.2 (−1)	313 (0)	120 (−1)	64.25	64.83	−0.58
0.2 (−1)	313 (0)	240 (1)	95.86	96.21	−0.35
0.2 (−1)	328 (1)	180 (0)	86.53	86.07	0.46
0.6 (0)	298 (−1)	120 (−1)	90.56	90.46	0.1
0.6 (0)	298 (−1)	240 (1)	98.25	98.38	−0.13
0.6 (0)	313 (0)	180 (0)	92.69	91.97	0.72
0.6 (0)	313 (0)	180 (0)	91.25	91.97	−0.72
0.6 (0)	313 (0)	180 (0)	91.89	91.97	−0.08
0.6 (0)	313 (0)	180 (0)	92.05	91.97	0.08
0.6 (0)	328 (1)	120 (−1)	84.26	84.12	0.14
0.6 (0)	328 (1)	240 (1)	89.56	89.65	−0.09
1 (1)	298 (−1)	180 (0)	98.56	99.01	−0.45
1 (1)	313 (0)	120 (−1)	95.25	94.89	0.36
1 (1)	313 (0)	240 (1)	77.56	76.97	0.59
1 (1)	328 (1)	180 (0)	87.25	87.74	−0.49

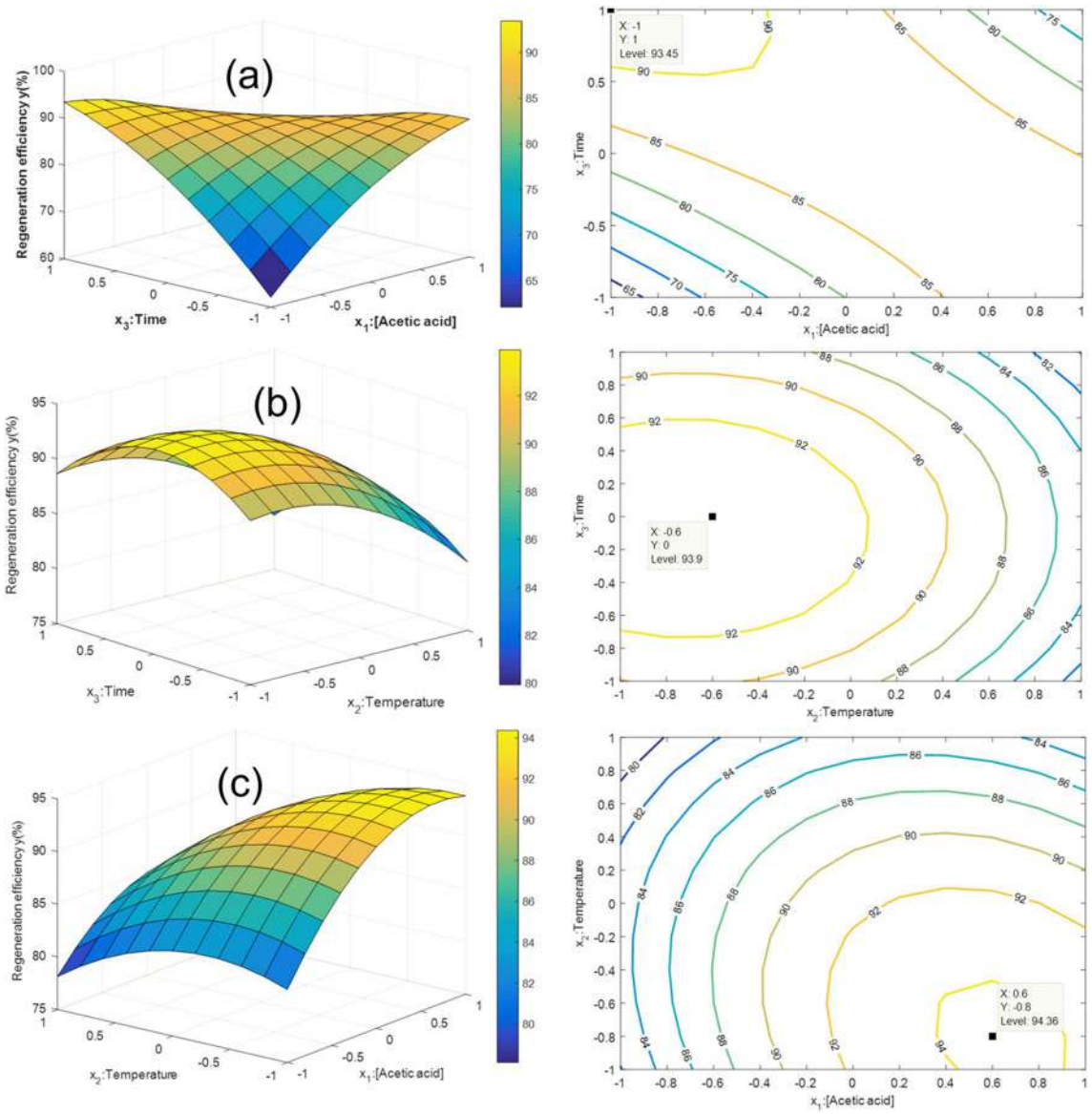

Fig. 8 Response surface and iso-response plots showing the effects of **a** acetic acid concentration and contact time, **b** temperature and contact time, and **c** acetic acid concentration and temperature on MB dye regeneration efficiency

a low acetic acid concentration ($x_1 < 0.6$ mol/L). As the temperature (x_2) and contact time (x_3) increase, the ratio of acetic acid inside the granules increases rapidly. This can cause a new reaction between the granule components (SDS, HAP, and MK-GP) and acetic acid, decreasing the number of active sites responsible for MB adsorption, thereby reducing regeneration efficiency. The optimal values were determined at an acetic acid concentration of 0.72 mol/L, a temperature of 323 K, and a contact time of 173.22 min. Duplicate confirmatory experiments were conducted using the optimized parameters. These parameters resulted in a measured regeneration rate of approximately 93.86% compared with the predicted granule regeneration rate of 90.89%.

G-PEG/SDS (L) granules were regenerated up to eight times without significant degradation (Fig. 9). However, after the eighth cycle, the rate of degradation increased because of treatment conditions, probably causing HAP dissolution.

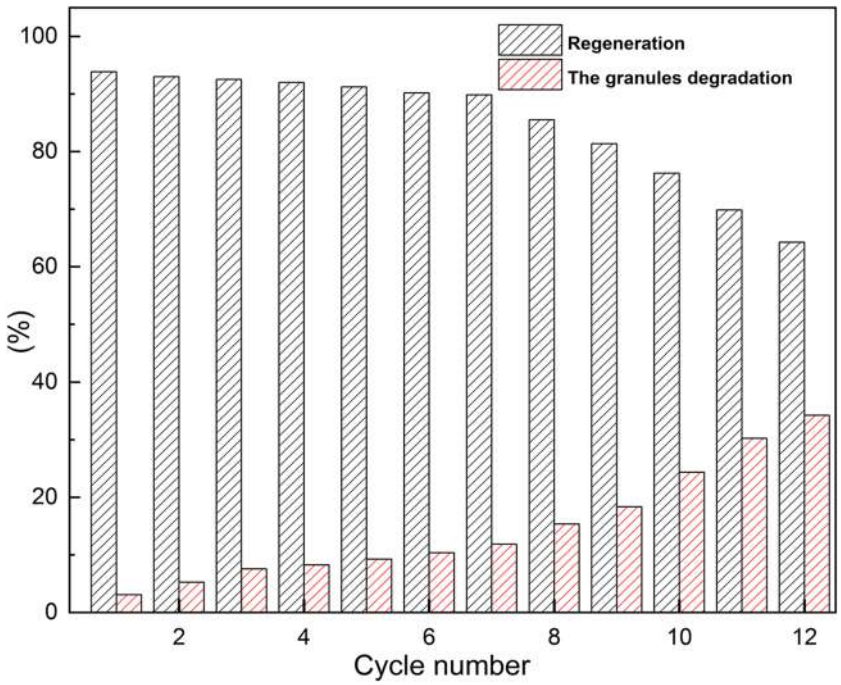

Fig. 9 Regeneration efficiency and granule degradation under optimal conditions: acetic acid concentration of 0.72 mol/L, temperature of 323 K, and contact time of 173.22 min

Comparison of the obtained granules with the previously developed adsorbents in the literature

This section compares the properties (i.e., surface area (SAA), adsorption capacity (q_{max}), and regeneration potential) of G-PEG/SDS (L) developed granules to traditional powdered adsorbents like MK-GP and HAP, as well as other relevant adsorbents in the literature. Table 6 summarizes the comparative analysis performed.

The results (Table 6) indicate that the G-PEG/SDS (L) developed granules have a high surface area and are cost-effective, making them a viable choice for industrial water treatment when compared to traditional powdered adsorbents, as well as

Table 6 Comparison of the properties of G-PEG/SDS (L) granules with the previously developed adsorbents in the literature

Adsorbent	Type	dyes	SAA (m^2/g)	q_{max}(mg/g)	Equilibrium time (min)	Regeneration	Ref
MK, HAP, PEG, SDS	Granules (4 mm)	MB	50–98	35	30 (298 K)	MB (8 cycle) CV (N/A)	This study
		CV		45			
MK, potassium-disilicate activating solution	Granules (2 mm)	MB	16	3–5	N/A	N/A	Medri et al. (2020)
Metakaolin and slag	Powder	MB	45	5	120 (298 K)	N/A	Feng et al. (2021)
MK-GP	Solid monolith	CV	27–62	27	120 (328 K)	N/A	Barbosa et al. (2018)
HAP	Powder	MB	N/A	26–38	20 (298 K)	N/A	Aaddouz et al. (2023)
Biochar-supported HAP	Powder	MB	26–127	21	800 (298 K)	4 cycles	Li et al. (2018)
Bio-HAP/MgO	Powder	CV	154	43	40 (298 K)	5 cycles	Foroutan et al. (2020)
Unmodifed HAp	Powder	CV	N/A	1	90 (298 K)	N/A	Amer Ali et al. (2023)
Other adsorbents							
Palm kernel fiber	Powder	CV	N/A	80	60 (298 K)	N/A	El-Sayed (2011)
		MB		95			
Zirconium silicate, SDS	Powder	CV	4–6	39	30 (298 K)	N/A	Mahmoud et al. (2019)
		MB		38			
Montmorillonite/magnetic Ni-Fe_2O_4-amine-functionalized chitosan	Powder	CV	N/A	118	30 (298 K)	10 cycles	Gomaa et al. (2022)
		MB		137			
CaO/g-C_3N_4-based nanocomposite	Powder	CV	N/A	458	240 (298 K)	N/A	Younis et al. (2016)
		MB		612			

other adsorbents. While some of these alternatives demonstrate superior adsorption capacity for removing MB and CV dyes, they face limitations in industrial applications primarily due to the challenges associated with handling powders. In addition, unlike G-PEG/SDS (L) granules, these alternative adsorbents can only be regenerated five times maximum.

MK metakaolin, *HAP* hydroxyapatite, *SDS* sodium dodecyl sulfate, *PEG* polyethylene glycol, *MB* methylene blue, *CV* crystal violet, *N/A* not variable

Conclusions

In this study, a novel granulation procedure was developed to obtain granules suitable for an adsorption application. The granulation method utilizes metakaolin geopolymer as a reactive binder for hydroxyapatite powder. The novel aspects are the use of PEG as a porogen agent and SDS dissolved in the granulation fluid (i.e., deionized water) which enhanced the granulation by reducing water surface tension. It should be noted that the proposed preparation method is versatile and can be applied to various geopolymers and alkali-activated materials, including lightweight artificial sound-absorbing acoustic panels, filtration materials, biofilm carrier materials, and catalyst support materials. It is expected to be simpler to scale and implement compared to previous methods (Valentina et al. 2020; Brahmi et al. 2024), and granule properties can be easily adjusted.

The adsorption selectivity study revealed that the G-PRG-SDS (L) granules exhibited higher adsorption toward CV than for MB. The maximum adsorption capacities (q_{max}) were 34.8 mg/g for MB and 45.2 mg/g for CV when the dyes were in present alone in an aqueous solution. In contrast, the maximum adsorption capacities were 23.5 mg/g for MB and 25.5 mg/g for CV when they were present together in a binary dye solution. Moreover, their adsorption either individually or in binary dye solutions followed the Langmuir isotherm model. The adsorption kinetic data indicated that the adsorption followed the pseudo-second-order kinetic model and was governed by film diffusion ($D_f = 1.37 \times 10^{-10}$ and 2.34×10^{-11} m^2/s for CV and MB dyes, respectively).

The optimization of the regeneration process of granules with acetic acid revealed that increasing the acid concentration and contact time improved the regeneration efficiency. The optimal values were 0.72 mol/L acetic acid concentration, 323 K, and 173 min contact time. Duplicate confirmatory experiments showed a regeneration rate of 94%, compared to the predicted rate of 91%. The granules could be regenerated for up to eight times without significant degradation. These results suggest that the porous granules prepared in this study have potential to be used in industrial wastewater treatment.

Recommendations for future work

The future research on the developed adsorbent granules should consider the following aspects:

- The granulation method could be still further developed by combining both PEG and SDS in the granulation fluid.
- The regeneration process by combining a chemical and thermal approach could be explored.
- The adsorption capacity of the granules may be too low if treating wastewater containing a high load of dyes. Thus, adsorption alone may not be sufficient as a treatment process. Therefore, combining adsorption with other methods such as electrocoagulation (Al-Qodah et al. 2024), biological treatment and others should be considered for future studies to enhance the treatment efficiency.

Supplementary Information The online version contains supplementary material available at https://doi.org/10.1007/s11356-024-34001-6.

Author contributions Aghilas Brahmi: conceptualization, formal analysis, investigation, methodology, validation, visualization, and writing—original draft. Salima Ziani: methodology, supervision, writing—review and editing, and conceptualization. Salima AitAli: conceptualization, methodology, supervision, and writing—review and editing. Hafit Khireddine: review and editing. Tero Luukkonen: conceptualization, funding acquisition, methodology, resources, supervision, and writing—review and editing.

Data availability Not applicable.

Declarations

Ethics approval Not applicable.

Consent to participate Not applicable.

Consent for publication Not applicable.

Conflict of interest The authors declare no competing interests.

References

Aaddouz M, Azzaoui K, Akartasse N, Mejdoubi E, Hammouti B, Taleb M, Sabbahi R, Alshahateet SF (2023) Removal of methylene blue from aqueous solution by adsorption onto hydroxyapatite nanoparticles. J Mol Struct 1288:135807. https://doi.org/10.1016/j.molstruc.2023.135807

AitAli S, Ziani S, Yahiaoui I, Brahmi A, Boudrahem F, Aissani-Benissad F (2023) Application of central composite design and response surface methodology for the study of extraction of gentian violet dye in aqueous solution by polystyrene membrane modified with oleic acid. Environ Prog Sustain Doi. https://doi.org/10.1002/ep.14200

Al-Qodah Z, Al-Zghoul TM, Jamrah A (2024) The performance of pharmaceutical wastewater treatment system of

electrocoagulation assisted adsorption using perforated electrodes to reduce passivation. Environ Sci Pollut Res 31:20434–20448. https://doi.org/10.1007/s11356-024-32458-z

Amer Ali D, Saad FA, Elsawy H (2023) Kinetics and isotherm studies for adsorption of gentian violet dye from aqueous solutions using synthesized hydroxyapatite (T Liu, Ed.). J Environ Res Public Health 2023:1–15. https://doi.org/10.1155/2023/7418770

Barbosa TR, Foletto EL, Dotto GL, Jahn SL (2018) Preparation of mesoporous geopolymer using metakaolin and rice husk ash as synthesis precursors and its use as potential adsorbent to remove organic dye from aqueous solutions. Ceram Int 44:416–423. https://doi.org/10.1016/j.ceramint.2017.09.193

Benamor M, Bouariche Z, Belaid T, Draa MT (2008) Kinetic studies on cadmium ions by Amberlite XAD7 impregnated resins containing di(2-ethylhexyl) phosphoric acid as extractant. Separation Purification Technol 59:74–84. https://doi.org/10.1016/j.seppur.2007.05.031

Boyd GE, Adamson AW, Myers LS (1947) The exchange adsorption of ions from aqueous solution by organic zeolites. II Kinetics. J Am Chem Soc 69:2836–2848. https://doi.org/10.1021/ja01203a066

Chen Y (2023) Key factors improving the stability and the loading capacity of nitrogen removal in a hydroxyapatite (HAP)-enhanced one-stage partial nitritation anammox process. Chem Eng J 452:139589. https://doi.org/10.1016/j.cej.2022.139589

El-Sayed GO (2011) Removal of methylene blue and crystal violet from aqueous solutions by palm kernel fiber. Desalination 272:225–232. https://doi.org/10.1016/j.desal.2011.01.025

Feng X, Yan S, Jiang S, Huang K, Ren X, Du X, Xing P (2021) Green synthesis of the metakaolin/slag based geopolymer for the effective removal of methylene blue and Pb (II). SILICON 14:6965–6979. https://doi.org/10.1007/s12633-021-01439-z

Foroutan R, Peighambardoust SJ, Aghdasinia H, Mohammadi R, Ramavandi B (2020) Modification of bio-hydroxyapatite generated from waste poultry bone with MgO for purifying methyl violet-laden liquids. Environ Sci Pollut Res 27:44218–44229. https://doi.org/10.1007/s11356-020-10330-0

Huang B, Xiong D, Zhao T, He H, Pan X (2016) Adsorptive removal of PPCPs by biomorphic HAP templated from cotton. Water Sci Technol 74:276–286. https://doi.org/10.2166/wst.2016.209

Li Y, Zhang Y, Zhang Y, Wang G, Li S, Han R, Wei W (2018) Reed biochar supported hydroxyapatite nanocomposite: characterization and reactivity for methylene blue removal from aqueous media. J Mol Liq 263:53–63. https://doi.org/10.1016/j.molliq.2018.04.132

Li Y, Otsubo M, Kuwano R (2022) Interpretation of static and dynamic Young's moduli and Poisson's ratio of granular assemblies under shearing. Computers and Geotechnics 142:104560. https://doi.org/10.1016/j.compgeo.2021.104560

Liu N, Wang H, Weng C, Hwan C (2008) Adsorption characteristics of Direct Red 23 azo dye onto powdered tourmaline. Sep Purif Technol 59:74–84. https://doi.org/10.1016/j.arabjc.2016.04.010

Lun H, Ouyang J, Yang H (2014) Enhancing dispersion of halloysite nanotubes via chemical modification. Phys Chem Minerals 41:281–288. https://doi.org/10.1007/s00269-013-0646-9

Luukkonen T, Heponiemi A, Runtti H, Pesonen J, Lassi U (2019) Application of alkali-activated materials for water and wastewater treatment: a review. Rev Environ Sci Biotechnol 18:271–297. https://doi.org/10.1007/s11157-019-09494-0

Mahmoud ME, Nabil GM, Khalifa MA, El-Mallah NM, Hassouba HM (2019) Effective removal of crystal violet and methylene blue dyes from water by surface functionalized zirconium silicate nanocomposite. J Environ Chem Eng 7:103009. https://doi.org/10.1016/j.jece.2019.103009

Manatunga DC, De Silva RM, De Silva KMN, De Silva N, Premalal EVA (2018) Metal and polymer-mediated synthesis of porous crystalline hydroxyapatite nanocomposites for environmental remediation. R Soc Open Sci 171557:1–15. https://doi.org/10.1098/rsos.171557

Medri V, Ruffini A (2011) The influence of process parameters on in situ inorganic foaming of alkali-bonded SiC based foams. Ceram Int 38:3351–9. https://doi.org/10.1016/j.ceramint.2011.12.045

Medri V, Papa E, Lizion J, Landi E (2020) Metakaolin-based geopolymer beads: production methods and characterization. J Clean Prod 244:118844. https://doi.org/10.1016/j.jclepro.2019.118844118844

Meski S, Ziani S, Khireddine H, Boudboub S, Zaidi S (2010) Factorial design analysis for sorption of zinc on hydroxyapatite. J Hazard Mater 186:1007–1017. https://doi.org/10.1016/j.jhazmat.2010.11.087

Meski S, Ziani S, Khireddine H, Yataghane F, Ferguene N (2011) Elaboration of the hydroxyapatite with different precursors and application for the retention of the lead. J Water Sci Technol 63:2087–2096. https://doi.org/10.2166/wst.2011.210

Panneerselvam K, Arul KT, Warrier AR (2019) Rapid adsorption of industrial pollutants using metal ion doped hydroxyapatite. AIP Conf Proc 2117:020004. https://doi.org/10.1063/1.5114584

Peng X, Chen W, He Z, Li D, Liu H, Jin H, Zhou G, Xu F (2019) Removal of Cu (II) from wastewater using doped HAP-coated-limestone. Journal of Molecular Liquids 293:111502. https://doi.org/10.1016/j.molliq.2019.111502

Ramimoghadam D, Mohd ZBH, Yun HTY (2012) The effect of sodium dodecyl sulfate (SDS) and cetyltrimethylammonium bromide (CTAB) on the properties of ZnO synthesized by hydrothermal method Int. J. Mol. Sci. 13:13275–13293. https://doi.org/10.3390/ijms131013275

Shen J, Wang X, Zhang L, Yang Z, Yang W, Tian Z, Chen J, Tao T (2018) Size-selective adsorption of methyl orange using a novel nano-composite by encapsulating HKUST-1 in hyper-crosslinked polystyrene networks. J Clean Prod 184:949–958. https://doi.org/10.1016/j.jclepro.2018.03.015

Teymouri A (2018) Hydroxyapatite and dittmarite precipitation from algae hydrolysate. Algal Research 29:202–211. https://doi.org/10.1016/j.algal.2017.11.030

Wang Y, Hu L, Zhang G, Yan T, Yan L, Wei Q, Du B (2017) Removal of Pb(II) and methylene blue from aqueous solution by magnetic hydroxyapatite-immobilized oxidized multi-walled carbon nanotubes. J Colloid Interface Sci 494:380–388. https://doi.org/10.1016/j.jcis.2017.01.105

Younis CA, Abd-Elaziz A, Hashem AI (2016) Utilization of a pyrrole derivative based antimicrobial functionality impregnated onto CaO/g-C3N4 for dyes adsorption. RSC Adv 6:89367–89379. https://doi.org/10.1039/C6RA10143G

Yu L, Luo YM (2014) The adsorption mechanism of anionic and cationic dyes by Jerusalem artichoke stalk-based mesoporous activated carbon. J Environ Chem Eng 2:220–229. https://doi.org/10.1016/j.jece.2013.12.016

Zhang X, Bai C, Qiao Y, Wang X, Jia D (2021) Porous geopolymer composites: a review. Composites Part A 150:106629. https://doi.org/10.1016/j.compositesa.2021.106629

Ziani S, Meski S, Khireddine H (2014) Characterization of magnesium-doped hydroxyapatite prepared by sol-gel process. Int J Appl Ceram 11:83–91

Al Natsheh A, Gray A, Luukkonen T (2022) Drivers and barriers for productization of alkali-activated materials in environmental technology, in: T. Luukkonen (Ed.), Alkali-Activated Materials in Environmental Technology Applications, Woodhead Publishing, Sawston, pp. 407–426, 10.1016/B978-0-323-88438–9.00008–9

Bensedira A, Haddaoui N, Doufnoune R, Meziane O, Labidi NS (2022) Study of methylene blue dye elimination from water using polyaniline (PANI) and PANI/SiO_2 composite. J Polym PolymCompos 30. https://doi.org/10.1177/09673911221141747

Brahmi A, Ziani S, AitAli S, Benkhaoula BN, Yu Y, Hania A, Khireddine H, Luukkonen T (2024) Porous metakaolin geopolymer as a reactive binder for hydroxyapatite adsorbent granules in dye removal. Hybrid Advances. https://doi.org/10.1016/j.hybadv.2023.100134

Gomaa H, Abd El-Monaem E M, Eltaweil A S, Omer AM (2022) Efficient removal of noxious methylene blue and crystal violet dyes at neutral conditions by reusable montmorillonite/NiFe2O4@amine-functionalized chitosan composite. Sci Rep 12. https://doi.org/10.1038/s41598-022-19570-1.

Luukkonen T, Yliniemi J, Sreenivasan H, Ohenoja K, Finnilä M, Franchin G, Colombo P (2020) Ag-or Cu-modified geopolymer filters for water treatment manufactured by 3D printing, direct foaming, or granulation. Sci Rep 101–14. https://doi.org/10.1038/s41598-020-64228-5

Zenabou NNM, Benoit-ali N, Zekeng S, Rossignol S, Melo UC, Tchamba AB (2019) Improving insulation in metakaolin based geopolymer: Effects of metabauxite and metatalc 23:403–15. https://doi.org/10.1016/j.jobe.2019.01.012.

Zhang J, Qi Y, lv T, Niu X, Tai B (2023) Effects of sodium dodecyl sulfate on nano carbon black-filled cement paste: performance and microstructure. J Mater Res Technol 24: 1706 e 1715. https://doi.org/10.1016/j.jmrt.2023.03.055

Authors and Affiliations

Aghilas Brahmi[1,2] · Salima Ziani[1,3] · Salima AitAli[1,3] · Hafit Khireddine[3] · Tero Luukkonen[2,4]

✉ Aghilas Brahmi
a.brahmi@univ-bouira.dz

[1] Laboratoire Des Matériaux Et Développement Durables (LMDD), Département de Génie Des Procédés, Faculté Des Sciences Et Des Sciences Appliquées, Université A.M.O, Bouira 10000, Algeria

[2] Fibre and Particle Engineering Research Unit, University of Oulu, P.O. Box 4300, Oulu 90014, FI, Finland

[3] Laboratoire de Génie de LEnvironnement (LGE), Faculté de Technologie, Université A. MIRA, Route de Targua Ouzemour, Bejaia 06000, Algeria

[4] Department of Chemical Engineering Technology, University of Johannesburg, P.O. Box 17011, Doornfontein 2088, South Africa

Surfaces and Interfaces 71 (2025) 106925

Contents lists available at ScienceDirect

Surfaces and Interfaces

journal homepage: www.sciencedirect.com/journal/surfaces-and-interfaces

Synthesis of hydroxyapatite-Fe_3O_4 nanocomposite modified with *Urtica dioica* extract for the removal of anionic dyes from aqueous solutions

Aghilas Brahmi [a,b,*], Salima Ziani [a,c,*], Salima AitAli [a,c], Yanis Zakaria Lakehal [a], Tero Luukkonen [b,d,*]

[a] Laboratoire des Matériaux et Développement Durable (LMDD), Département de Génie des Procédés, Faculté des Sciences Appliquées, Université de Bouira, 10000, Algérie
[b] University of Oulu, Fibre and Particle Engineering Research Unit, P.O. Box 4300, FI-90014, Finland
[c] Laboratoire de Génie de l'Environnement (LGE), Faculté de Technologie, Université A. MIRA, Route de Targua Ouzemour, 06000, Bejaia, Algérie
[d] Department of Chemical Engineering Technology, University of Johannesburg, P.O Box 17011, Doornfontein, 2088, South Africa

ARTICLE INFO

Keywords:
Hydroxyapatite
Iron oxide
Urtica dioica extract
Wastewater treatment
Central composite design
Response surface methodology

ABSTRACT

This study explores an innovative approach to enhance the adsorption capacity of hydroxyapatite (HAP) for organic pollutants, specifically anionic dyes Alizarin Red S (ARS) and Direct Red 23 (DR23). Fe_3O_4 (iron oxide) and *Urtica dioica extract* were incorporated into the HAP structure using a co-precipitation method. Characterization via various techniques demonstrated significant improvements in HAP's surface area (59.98 m^2/g) and porosity (0.30 cm^3/g), as confirmed by Brunauer-Emmett-Teller (BET) and Barrett-Joyner-Halenda (BJH) analyses. Scanning Electron Microscopy-Energy Dispersive X-ray (SEM-EDX) confirmed the successful integration of Fe_3O_4 and its homogeneous distribution within the HAP matrix, enhancing its adsorption potential. Additionally, Vibrating Sample Magnetometry (VSM) revealed strong magnetic properties (saturation magnetization = 10.93 emu/g), making the composite ideal for both adsorption and recovery applications.

The adsorption of ARS and DR23 dyes was optimized using Central Composite Design and Response Surface Methodology, resulting in a regression model with $R^2 = 0.99$. Kinetic and isotherm analyses indicated that adsorption was endothermic, spontaneous, and monolayer in nature. The process followed the Extended Langmuir isotherm and pseudo-second-order kinetic models, with maximum adsorption capacities of 47.96 mg/g for ARS and 56.15 mg/g for DR23. These findings demonstrate that HAP-Fe-*Urtica dioica extract* is a highly effective and sustainable material for wastewater treatment, especially for dye mixtures.

1. Introduction

Hydroxyapatite (HAP) is a mineral having the formula $Ca_{10}(PO_4)_6(OH)_2$, it belongs to the calcium apatite group [1]. Calcium in the HAP structure can be replaced by other cations such as Al^{3+}, Cu^{2+} or Ag^{+}, while the hydroxyl group can be substituted by anions such Cl^{-} or F^{-} [2]. Similarly, the phosphate group of HAP can be substituted by oxyanions such as VO_4^{3-} or SiO_4^{2-} [3]. This versatility of the HAP modification makes it suitable for various biological applications, including tissue repair, soft tissue regeneration, drug delivery systems, antimicrobial membranes, tissue engineering and wastewater treatment [4,5]. HAP may be produced from natural sources containing calcium and phosphorus such as egg and mussel shells [6] or fish, chicken and mammal bones [7–9], respectively. The use of the secondary materials eliminates the need for phosphate rock (which is defined as a critical raw material in the EU [10]).

As an adsorbent, HAP has a high adsorption capacity for metals such as zinc ($q_e = 450$ mg/g) [11], lead ($q_e = 505$ mg/g) [9] or copper ($q_e = 91$ mg/g) [2]. However, HAP has a low affinity for organic compounds in aqueous solutions, such as dyes. To address these limitations and enhance its adsorption performance, HAP-based composite materials have been developed by substituting various ions (i.e. Zn^{2+}, Mg^{2+}, and Fe^{2+}) into HAP's crystal lattice [12,13], or by introducing different adsorbents, such as chitosan [14], graphene oxide [15], activated carbon [16] or magnetic nanoparticles like Fe_3O_4[17], into the HAP structure. These modifications have further enhanced its adsorption capacity and ease of recovery via magnetic separation, particularly for organic contaminants .They have also contributed to significant

* Corresponding authors.
E-mail addresses: a.brahmi@univ-bouira.dz (A. Brahmi), s.ziani@univ-bouira.dz (S. Ziani), tero.luukkonen@oulu.fi (T. Luukkonen).

https://doi.org/10.1016/j.surfin.2025.106925
Received 3 October 2024; Received in revised form 28 May 2025; Accepted 10 June 2025
Available online 11 June 2025

improvements in its structural integrity and functional properties [18]. In particular, Fe_3O_4 nanoparticles offer notable advantages, including a large surface area, biocompatibility, non-toxicity, easy synthesis, and supermagnetic properties [19,20]. When combined with HAP, these nanoparticles provide a highly effective composite material with enhanced adsorption capacity. This combination facilitates and optimizes the recovery process, making the removal of organic pollutants and heavy metals from aqueous solutions more efficient [17].

Urtica dioica (common nettle), is known for its widespread distribution and adaptability and is rich in antioxidants such as polyphenols, flavonol glycosides, phenolic acids, amino acids, carotenoids, and chlorophyll [21]. Notably, its polyphenol content is higher that of many other plants [22]. If immobilized on a solid surface, these antioxidant molecules can interact with functional groups of dyes during the adsorption process, enhancing the adsorption capacity of the base material. Despite its recognized medicinal properties, there is limited research on the potential of *Urtica dioica* in material science, especially regarding its effects on surface area, porosity, and adsorption capacity.

Over 100,000 synthetic dyes are used in the textile industry, displaying diverse chemical structures, including azo, anthraquinone, and sulfur dyes. Their concentrations in textile industry wastewaters can vary widely, depending on the specific processes involved. However, due to the low fixing levels of dyes on the textile fibers, the discharge rate of dyes and pigments from the dye bath unit typically ranges between 10 % and 60 % [23,24]. Today, azo and anthraquinone derivatives are the most commonly used dyes in the industry [25]. Azo dyes, including Direct red 23 (DR23), are water-soluble and electron-deficient xenobiotics, making them challenging to remove using several methods procedures including biological degradation, electrolysis, flocculation and membrane filtration [26]. Anthraquinone dyes, like Alizarin Red S (ARS), are also water-soluble and stable; however, they are also known to be mutagenic and carcinogenic, causing toxic effects on aquatic organisms when present at concentrations exceeding 30 mg/L [27]. Thus, the efficient removal of these dyes from industrial wastewaters is a major environmental priority. In this context, adsorption is a promising technique that has recently attracted growing interest thanks to its effectiveness and ease of application. In this perspective, this study proposes an innovative, eco-friendly approach using iron oxide-doped magnetic hydroxyapatite (HAP-Fe) composites, enhanced with *Urtica dioica* extract, as an adsorbent for removing organic dyes from industrial wastewater.

Doping HAP with magnetic nanoparticles not only facilitates its recovery, but can also induce surface modifications and the addition of specific functionalities. These changes can significantly improve the adsorption capacity of the composite compared with unmodified HAP. However, the addition of *Urtica dioica* extract further modifies the surface of HAP, introducing various organic functions likely to improve its effectiveness as an adsorbent. Thus, this innovative combination aims to combine sustainability and efficiency in wastewater treatment. Moreover, the study emphasizes the optimization of adsorption conditions using the central composite design and response surface methodology (CCD-SRM) to evaluate its performance with a binary anionic dye solution composed of ARS and DR23. The adsorption efficiency for each dye in the binary solution is compared to the average efficiency of both dyes in the solution, providing deeper insights into the selectivity and behavior of the composite. A regression model is developed to relate the adsorption conditions to the removal efficiency of dyes, thus establishing a predictive tool for optimizing dye removal from complex wastewater matrices. This study highlights the potential of HAP-Fe-*Urtica dioica* ext composites as a promising, sustainable solution for the removal of organic dyes, with both industrial and environmental applications.

2. Materials and methods

2.1. Chemicals

Analytical grade chemicals, $Ca(NO_3)_2 \cdot 4H_2O$ (99 %, Biochem Chemopharma, canada), $(NH_4)_2HPO_4$ (99.2 %, Sigma-Aldrich, Germany), and Fe_3O_4 (97%, Aldrich, USA) were utilized to synthesize magnetic hydroxyapatite nanocomposites.*HCl* (0.1 N) and *NaOH* (0.1 N) solutions were purchased from VWR (Belgium) and used to adjust the solution pH. *Urtica dioica* leaves were collected from a woodland located in Bejaia (Amizour-Smaoun), Algeria. DR23 (33 %, Sigma-Aldrich, China), ARS (99 %, Sigma-Aldrich, Germany) textile dyes were employed in the adsorption experiments; their chemical structures, as well as absorption spectra, are provided in Fig. S1.

2.2. Preparation of Urtica dioica leaves extract

The *Urtica dioica* leaves were harvested and subsequently dried shielded from light to prevent any oxidation reactions that might alter the components of the plant. 10 g of leaves were added to 250 mL of distilled water and heated to 100 °C for 30 min. The solution ($V = 150$ mL) was then filtered, and the volume of organic extract was reduced to <30 mL at 55 °C using a rotary evaporator. The resulting *Urtica dioica* extract (abbreviated *Urtica dioica* ext) was stored in a refrigerator at 4 °C until use.

2.3. Preparation of HAP, HAP-Fe, and HAP-Fe- Urtica dioica ext nanocomposite

The HAP powder was synthesized by a conventional aqueous co-precipitation method. To obtain HAP with a Ca/P molar ratio of 1.67, the $(NH_4)_2HPO_4$ (0.30 mol/L) solution was added dropwise to the $Ca(NO_3)_2$ (0.50 mol/L) solution. After stirring for 45 min, *NaOH* (0.1 M) was added to the mixture until the pH reached the value of 10. The suspension was maintained at room temperature for 12 h. The resulting HAP was then filtered, thoroughly washed with deionized water to remove any impurities, and subsequently dried in an oven at 80 °C for 24 h to remove residual moisture and ensure the formation of a dry powder.

Magnetite hydroxyapatite (HAP-Fe) and magnetite hydroxyapatite *Urtica dioica* (HAP-Fe-*Urtica dioica* ext) composite were prepared by adding $(NH_4)_2HPO_4$(0.30 mol/L) solution dropwise to a mixture of Fe_3O_4 (0.5 g) and $Ca(NO_3)_2$ (0.50 mol/L) solution and to a mixture of Fe_3O_4 (0.5 g), *Urtica dioica* extract (30 mL), and $Ca(NO_3)_2$ (0.50 mol/L) solution, respectively.

The deposition mechanism of *Urtica dioica* extract on the HAP surface relies on forming chelates or complexes withCa^2 + ions [28]. *Urtica dioica* is rich in antioxidants, such as polyphenols, which act as precursors for complexation through reactive functional groups like terpenoids, flavonoids, and amino groups ($R - CH(NH_2) - COOH$)that contain -*COOH*, − *OH*, and carboxyl derivatives, under favorable pH conditions (pH = 9), these reactive groups form strong electrostatic interactions with Ca^2 + ions present in HAP, aiding in Ca-chelate formation. The resulting Ca-complex reacts with the phosphate precursor PO_4^{3-} [29], resulting in adsorption and deposition of *Urtica dioica* extract on the HAP surface.

2.4. Material characterization methods

The functional groups of the samples were identified by Fourier transform infrared spectroscopy FTIR (range: 400–4000 cm^{-1}, spectral resolution: 200). Analyses were performed using a Bruker Vertex v80 instrument equipped with a Harrick Praying Mantis DRIFT cell.

An X-ray diffraction (XRD) analysis was performed using a Rigaku Smart Lab diffractometer (9 kW Co Kα X-ray source) in the range of 2θ from 20° to 70° at 4°/min scan speed and a step width of 0.02° The

results were evaluated using the HighScore Plus software.

A thermogravimetric (TGA) analysis for samples was performed using an SDT 650 simultaneous thermal analyzer-heatingheating rate of 10 °C/min under nitrogen atmosphere.

Specific surface area and pore size were determined using a Micromeritics ASAP2020 instrument and calculated using the Brunauer-Emmett-Teller (BET) isotherm and the Barrett-Joyner-Halenda (BJH) method. Before the measurement, samples were degassed at 70 °C for 24 h.

The microstructural morphology and composition of the samples were determined using a field emission scanning electron microscope equipped with an energy dispersive X-ray spectroscope (FE-SEM-EDS, Zeiss Ultra Plus). The samples were imaged and placed on a two-sided tape and coated with carbon.

The magnetic properties of the samples were determined using a vibrating sample magnetometer (VSM) analysis (EV11 vibrating sample magnetometer, MicroSense, USA).

2.5. Batch adsorption experiments

2.5.1. Single adsorption system

In order to investigate the effect of $Fe_3O_4$and *Urtica dioica* extract on the removal performance of HAP towards anionic dyes, three adsorption experiments were conducted using HAP, HAP-Fe, and HAP-Fe-*Urtica dioica* ext as adsorbents to remove ARS and DR23 dyes individually from aqueous solutions under the following conditions: pH of dye (i.e., 5.83 for DR23 dye and 4.89 for ARS dye), $[dyes]_0 = 20mg/L$, time = 90 min, T = 21 °C, agitation speed = 200 rpm and adsorbent dose = 1 g/L. The dye solution was separated from the adsorbent by centrifuging (Beckman Coulter J326XPI-IM-1) at 8000 rpm for 6 min, and then analyzed using a UV-6300 PC spectrophotometer (VWR, China). The concentration of ARS and DR23 dyes was determined by measuring the absorbance at maximum wavelengths ($\lambda_{ARS} = 259nm$, $and\lambda_{DR23} = 505nm$) (Fig. S1). The percentage of the adsorbed dyes and adsorption amount per adsorbent mass were calculated using Eq. (2) and Eq. (3), respectively.

$$y(\%) = \frac{C_0 - C_t}{C_0} \times 100 \tag{2}$$

$$q_t = (C_0 - C_t) \times \frac{V}{W} \tag{3}$$

Where$y(\%)$ is removal efficiency of dyes, q_t (mg/g) is the amount of dyes adsorbed per adsorbent mass at time t, V (L) is the volume of dyes solution, and W (g) is the weight of adsorbent, C_0 (mg/L) and C_t (mg/L) are the initial concentration and concentration at time t of dyes, respectively.

The adsorption behavior and selectivity of HAP-Fe-*Urtica dioica* ext were evaluated by comparing its effectiveness for anionic dyes (Congo red (CR) and rhodamine B (RhB)) and cationic dyes (crystal violet (CV), brilliant green (BG), and methylene blue (MB)). Experiments were conducted under conditions: pH of the dye solution, $[dyes]_0 = 20mg/L$, time = 90 min, T = 21 °C, agitation speed = 200 rpm and adsorbent dose = 1 g/L. Dye concentrations were analyzed using a UV-6300 PC spectrophotometer (VWR, China) at specific wavelengths ($\lambda_{CR} = 494nm$, $\lambda_{Rhb} = 554nm$, $\lambda_{CV} = 586nm$, $\lambda_{BG} = 624nm$, $\lambda_{MB} = 664nm$). The percentage of dye adsorption was calculated using Eq. (2).

2.5.2. Binary adsorption system

The HAP-Fe-*Urtica dioica* ext was then chosen for the selective performance studies due to its high adsorption capacity. The selective adsorption dyes was carried out in a batch system in binary solution (ARS/DR23) dyes, under the following conditions: pH = 6.4, $[ARSandDR23]_0 = 20mg/L$, time = 90 min, T = 21 °C, agitation speed = 200 rpm and fixed $dose_{HAP-Fe-Urticadioicaext}$= 1 g/L. The concentration of ARS, and DR23 dyes in the binary solution (ARS/DR23) was determined using the analogous equations (Eq. (4) and Eq. (5)) [30,31].

$$C_1 = \frac{(K_{b2}A_1 - K_{b1}A_2)}{(K_{a1}K_{b2} - K_{a2}K_{b1})} \tag{4}$$

$$C_2 = \frac{(K_1A_2 - K_{a2}A_1)}{(K_{a1}K_{b2} - K_{a2}K_{b1})} \tag{5}$$

WhereK_{a1}, K_{a2},$K_{b1}$and K_{b2} are the calibration constants for ARS and DR23 at wavelengths $\lambda_1 = \lambda_{ARS}$ = 259 nm and $\lambda_2 = \lambda_{DR23}$ = 505 nm (Fig. S1), A_1 and A_2 are measured absorbance values of binary system at λ_1 = 259 nm andλ_2 = 505nm, respectively.

2.5.3. Central composite design and response surface methodology (CCD-RSM)

The CCD-RSM was employed in this work to optimize the adsorption efficiencies of ARS and DR23 in binary dye solution and the average adsorption efficiency of ARS and DR23 (Eq. (2)) in the binary dyes solution (y_{avg}(%)Eq. (6)) onto HAP-Fe-*Urtica dioica* ext. The effects of three variables: dose of HAP-Fe-*Urtica dioica* ext (x_1), pH of solution (x_2), and the agitation speed (x_3) were investigated (Table 1) at the conditions: $[ARS]_0 = [DR23]_0 = 20mg/L$, time = 90 min, and T = 21 °C. A regression model described by a second-order polynomial Eq. (7) [25] was used to establish the relationship between operational parameters and response.

$$y_{avg}(\%) = \frac{y_{ARS}(\%) + y_{DR23}(\%)}{2} \tag{6}$$

$$\widehat{y} = b_0 + \sum_{j=1}^{3} b_j x_j + \sum_{j=1}^{3} \sum_{u \neq j}^{3} b_{uj} x_u x_j + \sum_{j=1}^{3} b_{jj} x_j^2 + \varepsilon \tag{7}$$

$$with\ x_j = \frac{Z_j - Z_j^0}{\Delta Z_j},\ j = 1, 2, 3$$

where $y_{ARS}andy_{DR23}$ are the adsorption efficiency of ARS and DR23 dyes in the binary dye solution, respectively. $\widehat{y}$ represents the predicted response, b_0 is the value of the fitted response at the central point of the design; $b_j b_{uj}$, and $b_{jj}$are the linear, interaction and quadratic terms respectively, ε is the residual term, Z_j is the natural value of parameter j, ΔZ_j is the step size; Z_j^0 is the value of Z_j at the centeral point of the investigating domain

The Design Expert software (JMP Pro 13) was used for all the considered experimental data and parameters.

2.5.4. Binary-component kinetic, isotherm modeling and thermodynamic study

The experimental kinetic data were fitted to the pseudo-first-order and pseudo-second-order kinetic models (Eq. (10) and Eq. (11), respectively) [30].

$$q_t = q_e \times [1 - \exp(-k_1 t)] \tag{10}$$

$$q_t = q_e - \frac{q_e}{k_2 q_e t + 1} \tag{11}$$

Where, k_1 (min^{-1}) is the pseudo-first order rate constant and k_2 [g/(mg × min)] is the pseudo-second order rate constant.

Single component isotherm models are inadequate to study the binary component solution, and thus the extended versions of these models are employed. Specifically, the extended Langmuir (Eq. (12)) is used to interpret the equilibrium data [32].

$$q_{e,i} = \frac{q_{m,i}\ K_{L,i}\ C_{e,i}}{1 + \sum_{j=1}^{N} K_{L,j}\ C_{e,j}} \tag{12}$$

With $q_{e,1} = \frac{q_{m,1}\ K_{L,1}\ C_{e,1}}{1+K_{L,1}\ C_{e,1}+K_{L,2}\ C_{e,2}}$ and $q_{e,2} = \frac{q_{m,2}\ K_{L,2}\ C_{e,2}}{1+K_{L,1}\ C_{e,1}+K_{L,2}\ C_{e,2}}$

Where compounds 1 and 2 present ARS and DR23 dyes, respectively. $q_{e,1}$ and $q_{e,2}$ (mg/g) are the equilibrium amounts adsorbed, $q_{m,1}$ and $q_{m,2}$(mg/g) are the maximum amounts adsorbed of the extended-

Table 1
Experimental design matrix for the adsorption efficiency of ARS and DR23 dyes: Variables, levels, and response at conditions:$[ARS]_0 = [DR23]_0 = 20mg/L$, time = 90 min, and $T = 21$ °C.

Coded experiments matrix				Measured response			Predicted response		
N	Dose of HAP-Fe-*Urtica dioica* ext (g/L) (x_1)	pH of solution (x_2)	Agitation speed (rpm) (x_3)	y_{ARS} (%)	y_{DR23} (%)	y_{avg} (%)	$\hat{y}_{ARS}$ (%)	$\hat{y}_{DR23}$ (%)	$\hat{y}_{avg}$ (%)
1	2 (−1)	4 (−1)	170 (−1)	72.149	90.26	81.20	75.69	87.47	80.77
2	3 (1)	4 (−1)	170 (−1)	32.45	49.50	40.97	32.93	50.2	41.96
3	2 (−1)	7.5 (1)	170 (−1)	90.23	94.2	92.21	89.86	96.37	92.97
4	3 (1)	7.5 (1)	170 (−1)	71.56	84.23	77.89	71.91	84.94	78.93
5	2 (−1)	4 (−1)	250 (1)	40.02	55.63	47.82	39.39	56.35	46.71
6	3 (1)	4 (−1)	250 (1)	79.25	89.02	84.13	75.86	87.47	80.77
7	2 (−1)	7.5 (1)	250 (1)	75.37	86.25	80.81	75.11	85.74	80.14
8	3 (1)	7.5 (1)	250 (1)	77.19	87.26	82.22	78.04	86.74	81.62
9	2.5 (0)	5.75 (0)	210 (0)	72.6	80.02	76.31	72.22	81.88	76.83
10	2.5 (0)	5.75 (0)	210 (0)	72.93	80.26	76.59	72.25	81.88	76.83
11	2.5 (0)	5.75 (0)	210 (0)	44.6	56.25	50.42	44.46	55.74	51.62
12	2.5 (0)	5.75 (0)	210 (0)	23.05	39.25	31.15	23.64	37.28	31.39
13	2.5 (0)	5.75 (0)	210 (0)	21.86	34.02	27.94	21.77	34.76	29.23
14	2.5 (0)	4.75 (0)	210 (0)	75.87	84.02	79.94	76.53	84.59	80.17
15	3.30 (+ α)	4.75 (0)	210 (0)	93.26	98.78	96.02	93.01	97.72	95.36
16	1.68 (-α)	4.75 (0)	210 (0)	62.57	76.25	69.41	62.63	76.97	69.76
17	2.5 (0)	8.60 (+ α)	210 (0)	76.03	84.23	80.13	76.37	84.59	80.17
18	2.5 (0)	2.89 (- α)	210 (0)	64.13	72.36	68.24	65.08	71.31	68.09
19	2.5 (0)	4.75 (0)	145 (- α)	49.01	56.25	52.63	47.72	56.99	52.76
20	2.5 (0)	4.75 (0)	275 (+ α)	76.9	88.12	82.51	76.49	87.07	82.42

Langmuir model,$K_{L,1}$ and $K_{L,2}$ are the Langmuir constants (L/mg), and $C_{e,1}$, $C_{e,2}$ are the ARS and DR23 dyes equilibrium concentrations in the solution (mg/L).

The separation factor R_L (Eq. (13)) was used to explain the adsorption nature of ARS and DR23 dyes in binary solution as follows; favorable ($0 < R_L < 1$), unfavorable ($R_L > 1$), linear ($R_L = 1$) and irreversible ($R_L = 0$) [33]. Additionally, it was used to compare the degree of favorable adsorption of ARS and DR23 onto HAP-Fe-*Urtica dioica* ext, with a lower R_L value indicating more favorable adsorption.

$$R_{Li} = \frac{1}{1 + K_{Li}C_{0i}} \tag{13}$$

To investigate the effect of temperature and evaluate the diffusion process governing the adsorption of ARS and DR23 dyes onto HAP-Fe-*Urtica dioica* ext in a binary solution, the diffusion coefficient D (m^2/s) of these adsorbate/adsorbent systems were estimated at different temperatures (from 21 to 40 °C). These estimations were performed using the homogeneous particle diffusion model (HPDM) as shown in Eq. (14), introduced by Michelson *et al.* [34]. The model describes the rate-limiting step, which can be usually controlled by either an intra-particle diffusion D_p (Eq. (16)) or a film diffusion mechanism D_f (Eq. (17)) [34].

$$X_{(t)} = \frac{q_t}{q_e} = 1 - \frac{6}{\pi^2}\sum_{z=1}^{\infty}\frac{1}{Z^2}\exp\left[\frac{-Z^2\pi^2 D_p t}{r_0^2}\right] \tag{14}$$

For $0 < X_{(t)} < 1$ and when adsorption takes place on spherical particles, Eq. (14) can be simplified to Eq. (15) and 16 [34].

$$X_{(t)} = \left[1 - \exp\left[\frac{-\pi^2 D_p^2 t}{r_0^2}\right]\right]^{0.5} \tag{15}$$

$$-ln\left(1 - X_{(t)}{}^2\right) = 2K_p t = \frac{2\pi^2 D_p}{r_0^2}t \tag{16}$$

where $X_{(t)}$ is the fractional attainment at time t, $D_p = \frac{K_p r_0^2}{\pi^2}$ (m^2/s)is the effective diffusion coefficient, r_0 is the radius of HAP-Fe-*Urtica dioica* ext assumed to be spherical (6.451×10^{-6}m), Z is an integer, K_p is the diffusion rate constant (L/s), which was used for the calculation of effective intra-particle diffusivity from the experimental data.

If the rate of adsorption is controlled by liquid film diffusion [34], the analogous expression Eq. (17) may be used.

$$-ln(1 - X_{(t)}) = K_{li}t = \left[\frac{3D_f C_e}{r_0 \delta C_s}t\right] \; where \; D_f = \frac{K_f r_0 \delta C_s}{3C_e} \tag{17}$$

$D_f = \frac{K_f r_0 \delta C_s}{3C}$ (m^2/s) is the film diffusion coefficient in liquid phase, K_f is the diffusion rate constant (L/s), C_e and C_s (mol/L) are equilibrium concentrations of ARS and DR23 dyes in solution and solid phase, and δ is the film thickness; it is estimated to 10^{-5}(m), according to Liu et *al.* (2018) [35].

To evaluate the spontaneity of the ARS and DR23 dyes adsorption in a binary solution onto HAP-Fe-*Urtica dioica* ext, thermodynamic quantities, Gibbs free energy$\Delta G^{\circ}(kJ/mol)$, enthalpy$\Delta H^{\circ}(kJ/mol)$, and entropy$\Delta S^{\circ}(kJ/mol.K)$, were calculated using Eq. (18), Eq. (19), and Eq. (20), respectively [36].

$$\Delta G^{\circ} = -RTln\, K_d \tag{18}$$

$$\Delta G^{\circ} = \Delta H^{\circ} - T\Delta S^{\circ} \tag{19}$$

$$lnK_d = -\frac{\Delta G^{\circ}}{RT} = \frac{\Delta S^{\circ}}{R} - \frac{\Delta H^{\circ}}{RT} \tag{20}$$

Where R is the universal gas constant (8.314462 J / ($K \times$ mol), T is the absolute temperature (K), and K_d is the equilibrium adsorption constant.

2.6. Regeneration and reusability of HAP-Fe-Urtica dioica ext adsorbent for anionic dyes studies

Regeneration is a critical factor in adsorption studies, as it directly influences the economic viability of the process. In this study, the reusability of the HAP-Fe-*Urtica dioica* ext adsorbent was evaluated for the removal of the binary DR23 and ARS anionic dyes, over seven consecutive adsorption-desorption cycles. Each cycle started with adsorption equilibration under the following conditions: $[ARSandDR23]_0 = 20mg/L$,Time = 120 min, pH solution = 3.15,$dose_{Hap-Fe-Urticadioicaext} = 2.60g/L$, $T = 21$ °C, and agitationspeed = 260*rpm*. After adsorption, the dye-loaded adsorbent was rinsed with distilled water for 120 min to remove any unbound dye residues, dried at 100 °C for 3 h, and then subjected to desorption in a 0.1 *NaOH* solution. The desorption process was carried out at agitationspeed = 260*rpm*, Time = 120 min, and $T = 21$ °C. Following desorption, the adsorbent was rinsed

again with distilled water to remove any residual dye before being reused in subsequent cycles. All experiments were performed in duplicate, and the results are reported as mean values, with error bars representing the variability shown in the plots.

3. Results and discussion

3.1. Characterizations of adsorbent

Fig. 1 depicts FTIR spectra of HAP, HAP-Fe, and HAP-Fe-*Urtica dioica* ext, both spectra of HAP and HAP-Fe are in good agreement with the literature reports [3,8]. The band at 3440 cm^{-1} correspond to stretching vibrations of the O—H structural group of HAP. The strong stretching band at 1024 cm^{-1} and the band at 590–605 cm^{-1} correspond to bending vibrations of P-O bonds in the tetrahedral units. The bands observed at about 1370 and 1632 cm^{-1} could be assigned to the CO_3^{2-} group. Additionally, the FTIR spectra of HAP-Fe reveal new absorption peaks at 593cm^{-1}, corresponding to Fe-O stretching vibrations, confirming the presence of iron oxide [37].

The spectrum of HAP-Fe-*Urtica dioica* ext reveals new absorption peaks at 1081, 2932, and 3375 cm^{-1} corresponding to bending vibrations of the C—O and C—H bonds of phenolic compounds [38], and the bands belonging to amino groups (i.e. primary (I) and secondary (II)) at 1404 and 1613 cm^{-1} which define the active components in *Urtica dioica* extract such as histamine, serotonin, acetylcholine terpenoids, and flavonoids, [39]. Moreover, spectrum also exhibits a shift and decrease in intensity within HAP bands, with significant changes in bands at 598 to 649cm^{-1}, 1024 to 1079cm^{-1}, and 1370 to 1354cm^{-1} This is probably attributed to the deposition of *Urtica dioica* extract on the HAP surface, leading to the formation of new interactions between HAP phosphate and hydroxide groups with the functional groups of *Urtica dioica* extract.

X-ray diffraction (XRD) was used to investigate the influence of Fe_3O_4 and *Urtica dioica* ext on the crystal structure of HAP. Fig. 2 displays the acquired findings in the 2θ range of [20°−70°].

The HAP-Fe and HAP-Fe-*Urtica dioica* ext are composed of two distinct phases: HAP hexagonal structure with a spatial group of P63/m, andFe_3O_4 spinel-like Fd-3 m cubic structure with a spatial group number of 74. Moreover, a comparison of the HAP diffractogram with those of HAP-Fe and HAP-Fe-*Urtica dioica* ext reveals a slight shift in the position of the characteristic peaks of HAP towards lower angles . Conversely, the characteristic Fe_3O_4 peaks show an increase in intensity, especially in the HAP-Fe-*Urtica dioica* ext diffractogram. This is likely due to the higher amount of Fe_3O_4 impregnated on the HAP surface, which may result in increased crystallinity of the Fe_3O_4 phase. The observed increase in peak intensity, characteristic of the Fe_3O_4 structure in the HAP-Fe-*Urtica dioica* ext, can also be attributed to the presence of *Urtica dioica* extract, which may facilitate the impregnation of Fe_3O_4 onto the HAP surface.

The thermal behavior (TGA and DTG) of HAP, HAP-Fe, and HAP-Fe-*Urtica dioica* ext is illustrated in Fig. 3, demonstrating that $Fe_3O_4$and *Urtica dioica* extract influence the thermal stability of HAP.

The thermal decomposition of all three samples occurs within a single phase, spanning the temperature range of 100 °C to 800 °C, with variable weight loss observed across this interval. For HAP, the DTG peaks at 178 °C and 400 °C can be attributed to the loss of physically adsorbed water and chemisorbed water, respectively, the latter being stabilized within inter crystalline sites by capillary forces that require elevated decomposition temperatures (T ≃ 500 °C) [40]. In contrast, the incorporation of Fe_3O_4 and *Urtica dioica* extract in HAP-Fe and HAP--Fe-*Urtica dioica* ext results in the appearance of a third DTG peak at 590 °C, which attributed to the thermal transformation of the magnetite phase (T ≃ 600 °C), likely associated with the breakdown of iron oxide (Fe^{2+}). Furthermore, the DTG profile of HAP-Fe-*Urtica dioica* ext shows significantly higher peak intensities at 400 °C and 590 °C compared to HAP-Fe. This could be explained by to the decomposition of organic matter derived from the *Urtica dioica* extract like carboxylic groups, present in *Urtica dioica* ext decompose, leading to a reduction in mass (HAP-Fe- *Urtica dioica* ext) [41], which contributes additional thermal

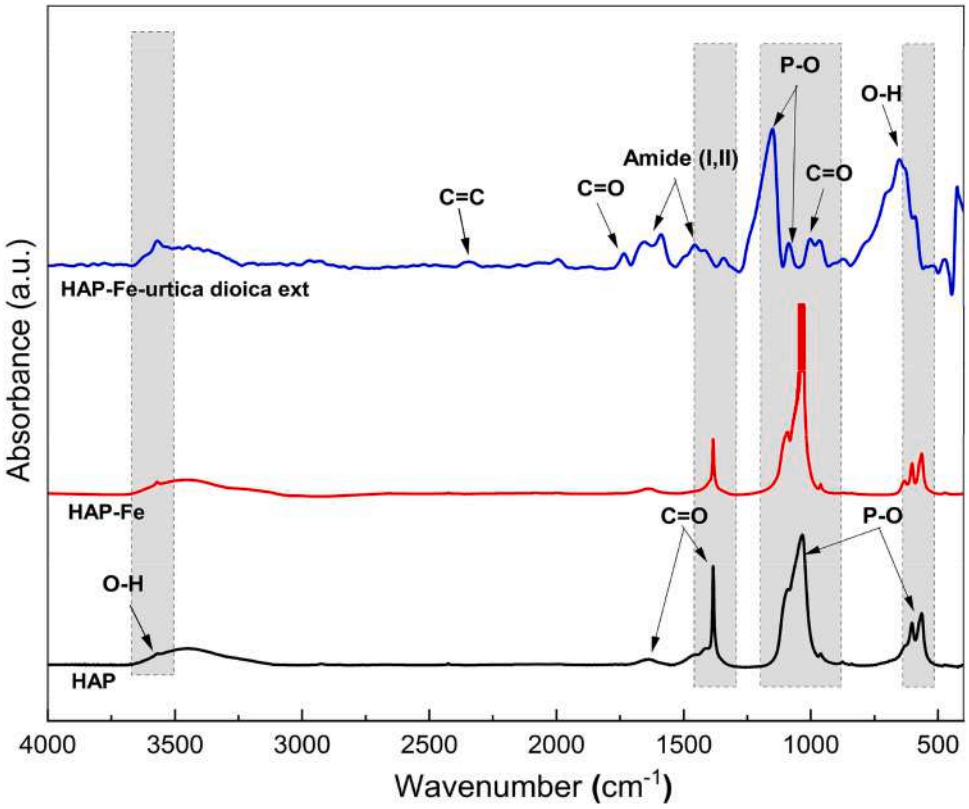

Fig. 1. FTIR spectra of HAP, HAP-Fe and HAP-Fe-*Urtica dioica* ext.

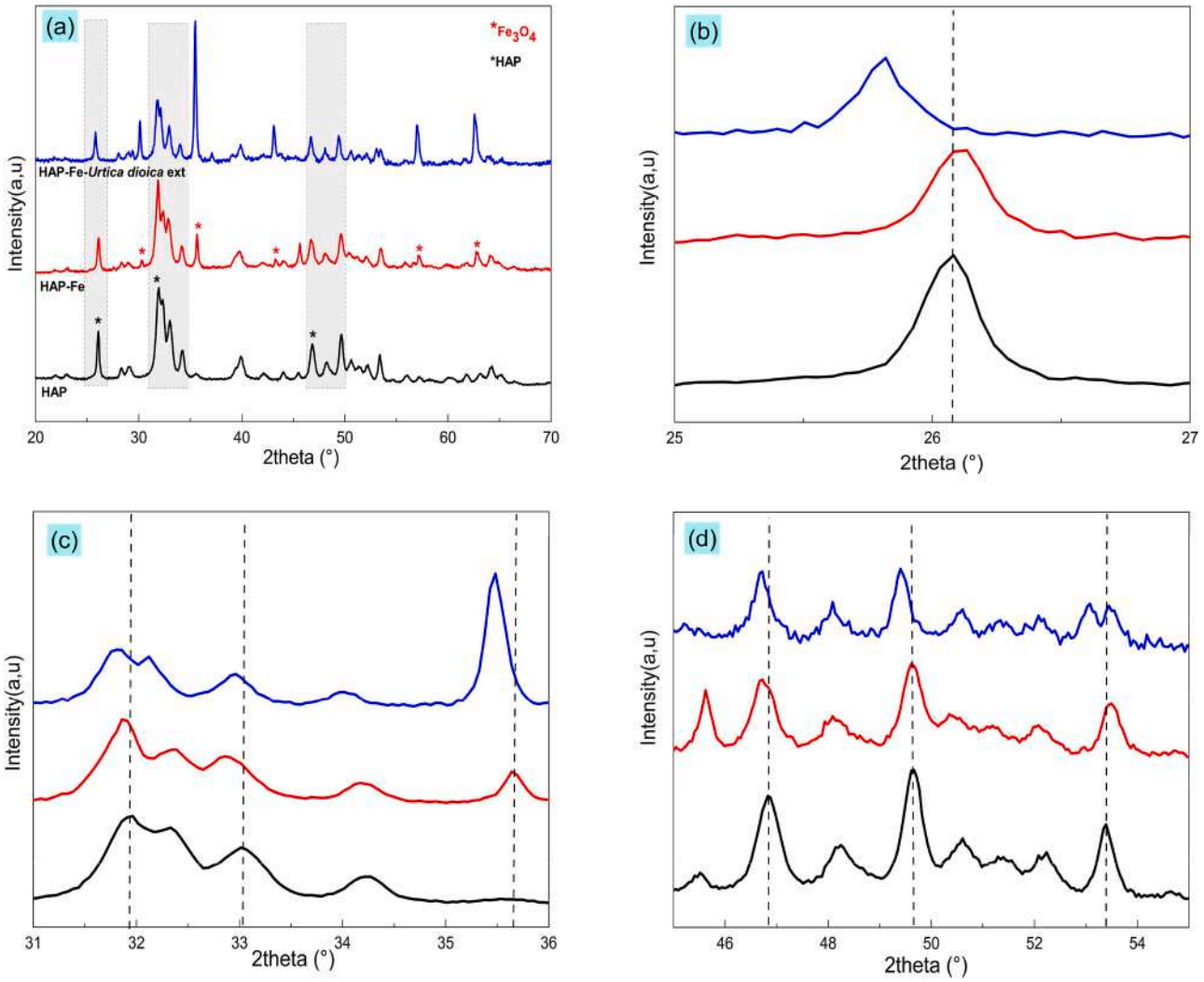

Fig. 2. (a) XRD diffractograms and (b, c, d) their zoomed-in views at different 2θ (°) angles for HAP, HAP-Fe and HAP-Fe-*Urtica dioica* ext.

degradation pathways.

The N_2 adsorption/desorption isotherms and BJH pore size distribution were employed to investigate the effect of incorporating either Fe_3O_4or a combination of $Fe_3O_4$with *Urtica dioica* extract into HAP during synthesis on its surface properties, specifically surface area and mesoporous structure. The results are shown in Fig. S2 and Table 2, respectively. A Type IV isotherm [40] was observed for all samples (Fig. S2), indicative of mesoporous materials with pore diameters ranging from 2 to 50 nm (Fig. S2b), which correspond to medium capillary pores critical for ion transport within pore networks [30]. Moreover, this isotherm is characterized by an initial adsorption region at low relative pressures ($P/P_o = 0$ to 0.045), resembling Type II isotherms and associated with monolayer and multilayer adsorption on the pore walls. This is followed by a sharp increase in adsorption at higher relative pressures ($P/P_o > 0.045$), attributed to capillary condensation at intermediate pressures, indicating mesoporous filling [42].

The results reveal that the incorporation of Fe_3O_4 or combined incorporation with *Urtica dioica* extract into HAP during its synthesis slightly improves its surface properties and porosity (Table 2), HAP-Fe-*Urtica dioica* ext powder has the highest specific surface area (SSA) ($SSA_{HAP-Fe-Urticadioicaext} = 59.98 m^2/g$) and the highest adsorbed volume (Fig. S2) compared to HAP and HAP-Fe ($SSA_{HAP} = 30.85 m^2/g$and$SSA_{HAP-Fe} = 53.85 m^2/g$, respectively). According to the BJH, pore size distribution (Fig. S2 (b) and Table 2), HAP-Fe and HAP-Fe-*Urtica dioica* ext have larger porosity (total pore volume $> 0.30 cm^3/g$) than HAP (Total pore volume $= 0.087 cm^3/g$). This results can be attributed to the synergistic effects of Fe_3O_4, which enhances pore formation and surface roughness, and *Urtica dioica* extract, which facilitates the development of a more open and porous network. These combined effects result in an expanded surface area, thereby improving the material's capacity for adsorption.

Fig. 4 depicts scanning electron micrographs (SEM) of the HAP and HAP-Fe and HAP-Fe-*Urtica dioica* ext at different size micrometers (100 μm and 20 μm). The SEM images show that all of the particles have irregular-shaped rough surface morphology and pores of various sizes, which supports our BET/BJH study findings (Table 2). Furthermore, the SEM analysis reveals that when Fe_3O_4 is added alone, the particles are less defined, and their size decreases compared to HAP. However, when Fe_3O_4 is added with the *Urtica dioica* extract, the particles appear to be more defined, and the size appears to be bigger than pure HAP, This can be attributed to the incorporation of Fe ions into the HAP crystal structure and polyphenols attach to the HAP surface, enhancing steric hindrance and electrostatic repulsion, thereby preventing particle aggregation.

The SEM-EDS analysis, which evaluates the elemental distribution of Fe_3O_4 on the surface of HAP, shows an even distribution of Ca, P, and Fe on the sample surfaces (Fig. S3). This indicates that Fe_3O_4 is well dispersed on the surface of HAP. The dispersion of Fe_3O_4on HAP enhances the material's potential for adsorption applications by combining the high adsorption capacity of HAP with the magnetic properties of

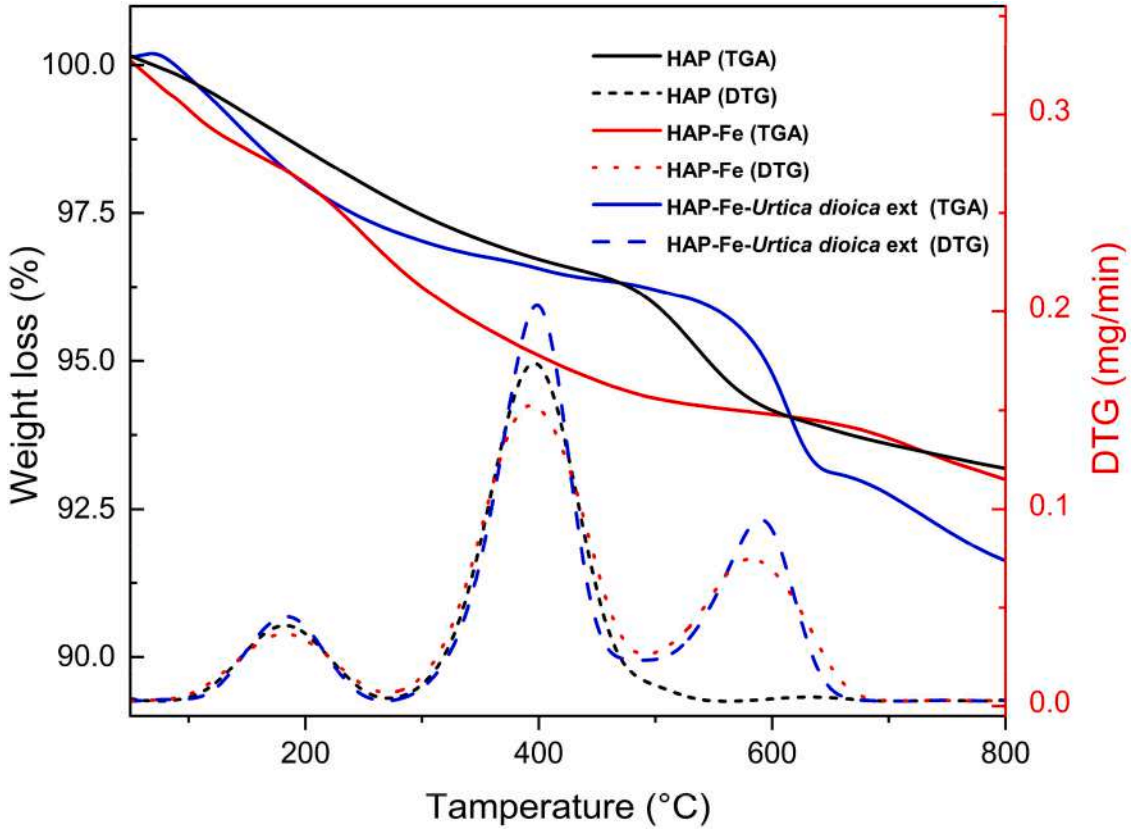

Fig. 3. TGA and DTG curves of HAP, HAP-Fe and HAP-Fe-*Urtica dioica* ext.

Table 2
BET/BJH parameters of HAP, HAP-Fe and HAP-Fe-*Urtica dioica* ext.

Samples	HAP	HAP-Fe	HAP-Fe-*Urtica dioica ext*
Specific surface area (m^2/g)	30.12	53.85	59.98
Total pore volume (cm^3/g)	0.09	0.32	0.30
Mean pore diameter (nm)	11.20	23.44	19.89

Fe_3O_4,allowing for easy separation and recovery.

The vibrating sample magnetometer (VSM) analysis was conducted at room temperature to investigate the magnetic properties of HAP, HAP-Fe, and HAP-Fe-*Urtica dioica* ext powder. The results are illustrated in Fig. 5. The data indicate that the saturation magnetization value of HAP is 0.0073 emu/g, suggesting that HAP does not exhibit significant magnetic properties. However, upon the addition of Fe_3O_4 and *Urtica dioica* extract, the magnetic properties of HAP have improved significantly. The hysteresis curves in Fig. 5 demonstrate that both HAP-Fe and HAP-Fe-*Urtica dioica* ext exhibit superparamagnetic characteristics, with saturation magnetization values of 10.32 emu/g and 10.92 emu/g, respectively [43]. This indicates that they have high magnetic susceptibility, can be easily magnetized, and can be recovered after adsorption experiments for regeneration purposes.

3.2. Adsorption studies

The results of the effect of $Fe_3O_4$and *Urtica dioica* extract on the removal efficiency of HAP towards anionic dyes, displayed in Fig. 6a, show that HAP-Fe-*Urtica dioica* ext outperforms HAP-Fe and HAP in terms of adsorption effectiveness for ARS and DR23 dyes. The presence of *Urtica dioica* extract on the surface of HAP-Fe increases its porosity and surface area (Table 2) and enhances electrostatic attraction. The *Urtica dioica* extract contains terpenoids, flavonoids, and amino groups ($R - CH(NH_2) - COOH$)that contain $-COOH$,$-OH$ and carboxyl derivatives (Fig. 1). These components form hydrogen bonds with NH, SO_3 groups, and n-π interactions benzene rings in the DR23 molecules, thereby improving adsorption effectiveness.

Likewise, the selectivity (Fig. 6b) of HAP-Fe-*Urtica dioica* ext towards ARS and DR23 dyes reveals that DR23 exhibits higher adsorption efficiency in individually and binary dye solution compared to ARS dye. This selectivity can be attributed to the significant charges of the DR23 dye structure compared to ARS dye, which may react electrostatically with the HAP-Fe-*Urtica dioica* ext. In addition, the presence of DR23 in aqueous solution also enhanced the adsorption of ARS dye in the binary solution (78.78 in binary solution vs 72.60 individually). This can be possibly explained by electrostatic interactions between the surface groups of HAP-Fe- *Urtica dioica* ext and DR23 dye groups, which may, in turn, interact with ARS dye groups.

The results of the comparative adsorption study (Fig. 7) indicate that HAP-Fe-*Urtica dioica* ext demonstrates relatively low selectivity for the removal of cationic dyes, such as MB, CV, and RhB. In contrast, the adsorption of anionic dyes (i.e., ARS, CR, and DR23) was significantly higher. This discrepancy can be attributed to the surface properties of the material, as well as the molecular size and chemical structure of the dyes, which influence their interactions with the adsorbent.

3.3. Modeling and optimization based on CCD-RMS design

3.3.1. Assessment of regression models

Eq. (12) is proposed based on the results of ANOVA analysis, means, and standard deviations of the experimental data obtained for each dye at its maximum wavelength, as illustrated in Table S1 and S2. The findings, including standard deviations, F-value (2.886) and p-value (0.098) of inner-group and intra-class formed from the combined results of both experiments (40 experiments), indicate the level of agreement among the experimental data and allow an objective comparison of the different dyes in terms of adsorption efficiency and other operating

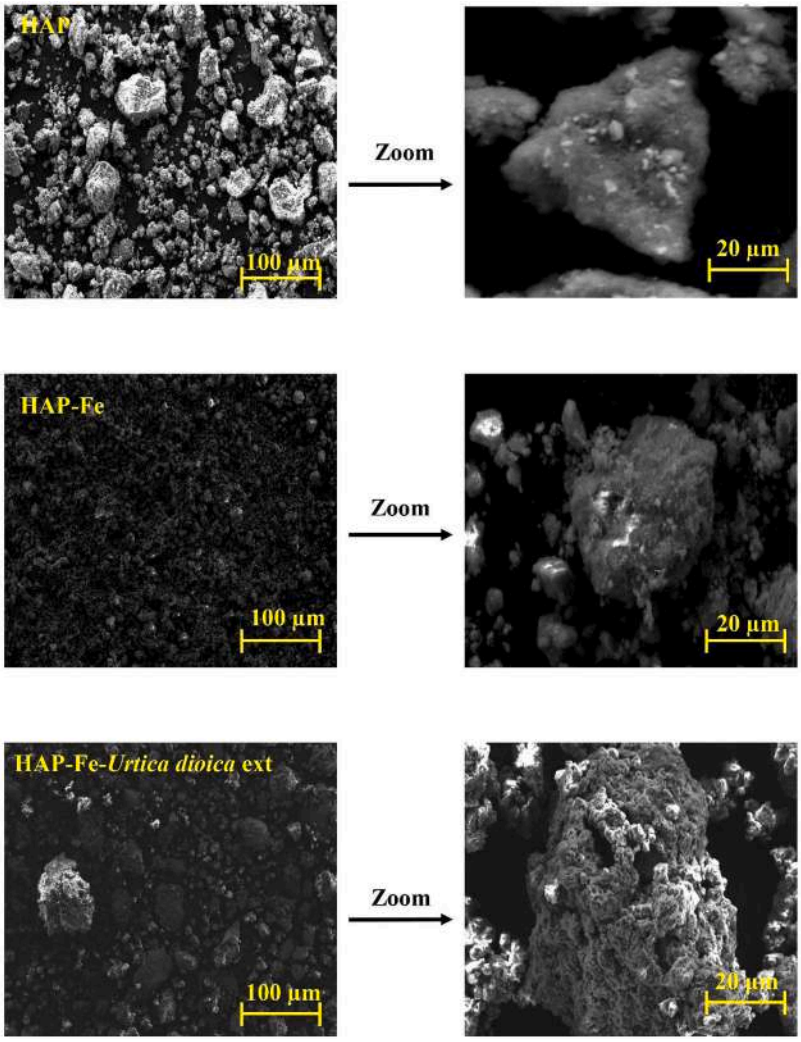

Fig. 4. SEM images of HAP, HAP-Fe, and HAP-Fe-*Urtica dioica* ext.

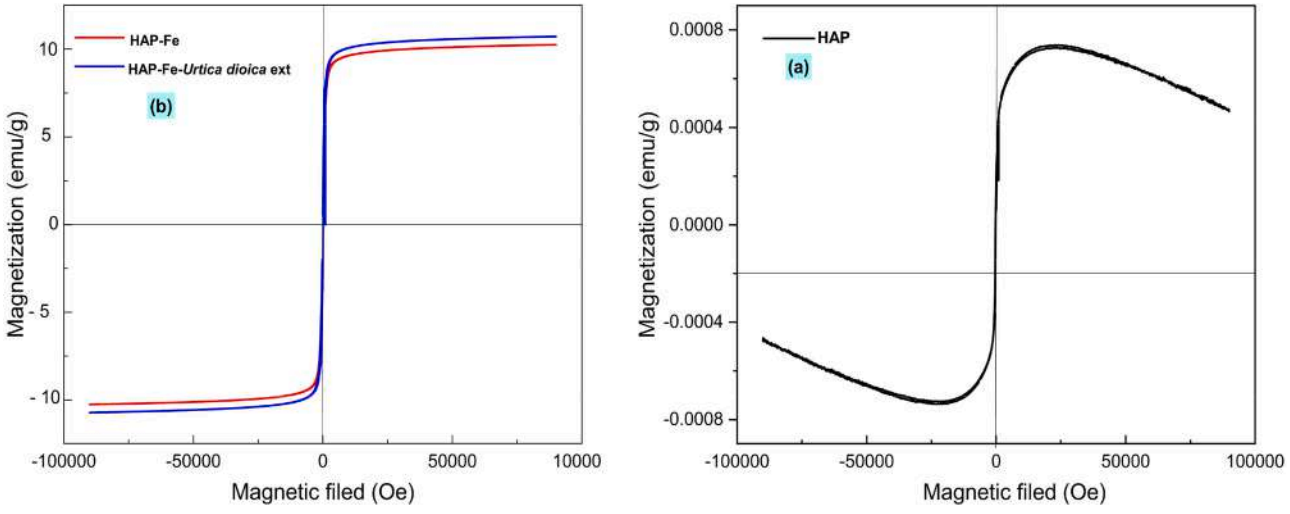

Fig. 5. Magnetization curve of HAP, HAP-Fe, and HAP-Fe-*Urtica dioica* ext.

parameters [14]. As shown in Table S2, the correlations between the factors and responses were found to be reasonable and suitable for forecasting ARS and DR23 binary solution dyes adsorption, as expressed by the experimental second-order polynomial equations, denoted Eqs. (21), 22, and 23.

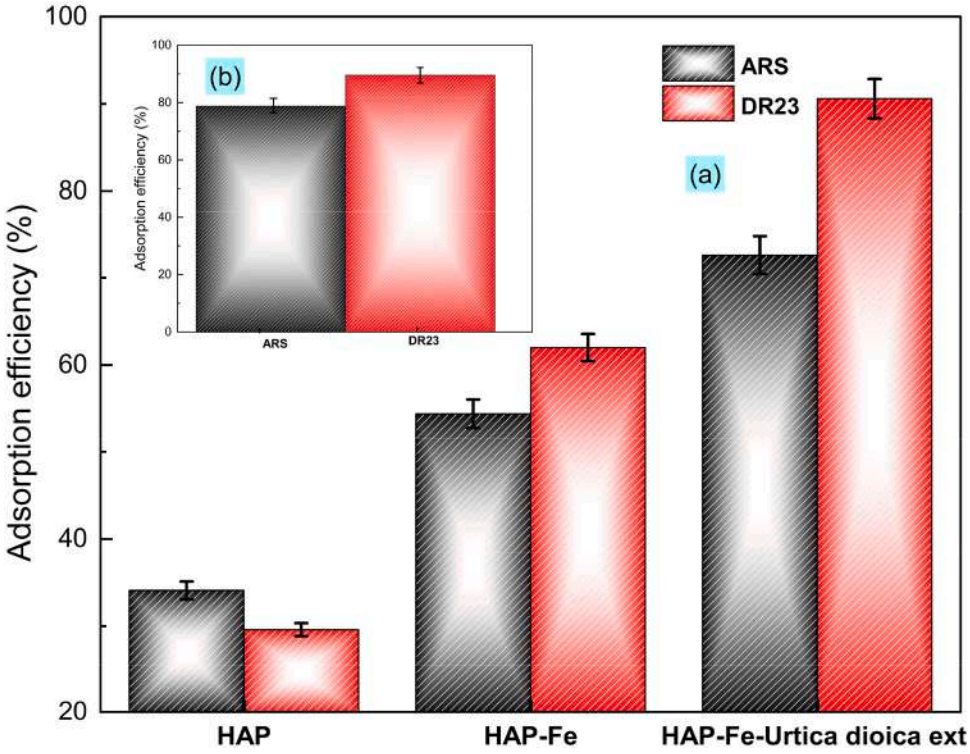

Fig. 6. (a) Effects of *Urtica dioica* extract and Fe_3O_4 on HAP adsorption efficiency for ARS and DR23 dyes individually, and (b) The selectivity of HAP-Fe-*Urtica dioica* ext for removing anionic (ARS/DR23) dyes in binary solution under the conditions: pH of dye, $[ARS]_0 = [DR23]_0 = 20mg/L$, time = 90 min, T = 21 °C, agitation speed = 200 rmp and $dose_{adsorbent}$= 1 g/L.

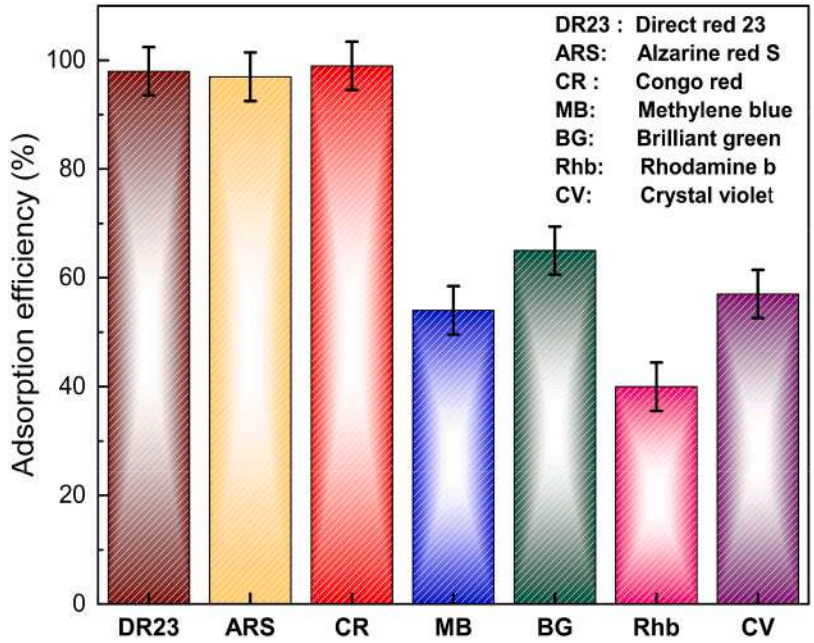

Fig. 7. Comparative study of the adsorption efficiency of HAP-Fe-*Urtica dioica* ext with different dyes the conditions: pH of dye, $[dyes]_0 = 20mg/L$, time = 90 min, T = 21 °C, agitation speed = 200 rmp and $dose_{adsorbent}$= 1 g/L.

$$\widehat{y}_{ARS} = 74.82 + 5.29\ x_1 - 21.81\ x_2 + 4.34\ x_3 - 7.48\ x_1^2 - 7.11\ x_2^2 - 2.54\ x_3^2 \quad (21)$$

$$\widehat{y}_{DR23} = 84.65 + 4.37\ x_1 - 19.27\ x_2 + 3.09\ x_3 + 1.77\ x_1\ x_2 - 7.66\ x_1^2 - 6.88\ x_2^2 \quad (22)$$

$$\widehat{y}_{Avg} = 79.74 + 4.84\ x_1 - 20.54\ x_2 + 3.27\ x_3 + 1.65\ x_1x_2\ - 7.57\ x_1^2 - 6.99\ x_2^2 - 1.75\ x_3^2 \quad (23)$$

The analysis ANOVA (Table S2) shows that both the linear and the quadratic terms of all parameters are statistically significant, with p-values $\langle$ 0.0001 and F-values listed in Table S2. A p-value $<$ 0.05 indicates robust evidence of statistical significance at the 95 % confidence level; while F-values $\rangle$ 5 confirm that, the models are well fitted, underscoring the importance of these variables in predicting adsorption efficiency.

The high estimated F-values reported for the quadratic model developed for each dye, as well as their average ($F_{ARS\ -\ values} = 202.03$, $F_{DR23\ -\ values} = 151.10$, and $F_{Avg\ -\ values} = 481.51$), demonstrate that Eqs

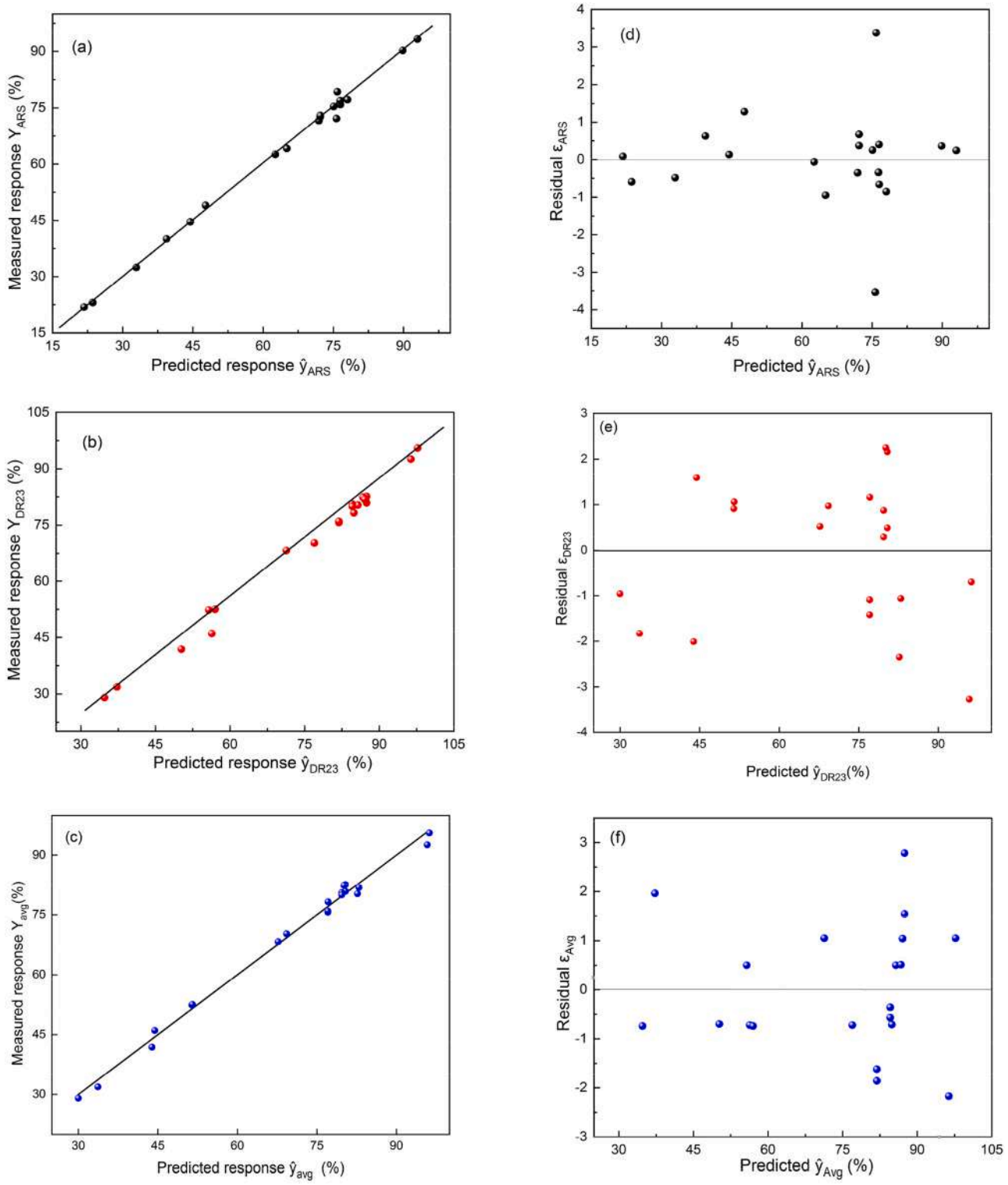

Fig. 8. (a), (b) and (c) Correlations between experiments and predicted adsorption efficiency, (d), (e), and (f) Residuals versus predicted response for ARS, DR23, and their average adsorption efficiency in the binary dye solution onto HAP-Fe-*Urtica dioica* ext.

(13), 14, and 15 accurately represent the measured responses. The probability that the variance of each model is of the same order of magnitude as the variance of its residuals (experimental error and lack of fit) is <0.0001, confirming the robustness and suitability of the models (they adequately summarize all the measured responses) [39]. The low coefficients of variation (CV) of 2.71, 3.03, and 1.73 of ARS, DR23, and avg models, respectively, suggest that the measurements are more precise and the results are reproducible and reliable [24].

The relationship between measured and predicted values of adsorption efficiency for ARS and DR23 in binary solution closely follows straight lines (Fig. 8a, b, and c). The data points do not deviate from the first bisector, indicating strong correlations and good fits between predicted values and experimental data points. This have supported by high coefficients of determination (R^2) and adjusted (R^2_{adj}) values, approximately 99.5 % and 98.8 %, respectively, for each model. These high values suggest that 99.5 % of the variations in ARS and DR23 adsorption efficiency are explained by the independent variables. Furthermore, residual analysis (Fig. 8e, and 8f) reveal no correlation between expected values and residuals for the ARS and DR23 models, as well as for their average adsorption efficiency in the binary dye solution model. The plots (Fig. 8) confirm the adequacy and reliability of the fitted models, demonstrating their strong predictive accuracy and robust performance [44].

3.3.2. Validation of the models

The predicted regression models for the adsorption efficiency of ARS and DR23 in a binary dye solution, along with their average values (Eqs. (13), 14, and 15), exhibit similar behavior.

They comprise essentially the same terms with identical signs, but with a slight variation in the coefficients values. All variables affect the responses studied. The responses are primarily influenced by pH (x_2) with a negative effect, while HAP-Fe-Urtica diodica ext dose (x_1)and agitation speed (x_3) have a positive effect. To confirm the results of the regression models, the effects of HAP-Fe-*Urtica diodica* ext dose (x_1) [from 1 to 3 g/L], pH solution (x_2)[from 3 to 7.5], and agitation speed (x_3) [from 145 to 275 rpm] on the adsorption of ARS and DR23 in a binary solution were studied under the following conditions: $[ARS]_0 = [DR23]_0 = 20mg/L$, time = 90 min, and $T = 21$ °C . The results are shown in Fig. 9.

Fig. 9a and 9b demonstrate that increasing the HAP-Fe-*Urtica dioica* ext dose (x_1) and agitation speed (x_3) enhances the adsorption efficiency of ARS and DR23 in a binary solution (positive effect). This is due to more available adsorption sites and moderate turbulence at agitation speeds between 145 and 275 rpm, which leads to more collisions with dye molecules and reduces film barrier around the HAP-Fe-*Urtica dioica* ext, resulting in greater mass transfer [40]. The optimal dose and agitation speed are 2.5 g/L and 250 rpm, respectively. Conversely, Fig. 9c shows that higher pH levels decrease the adsorption of ARS and DR23, with a pH of 3 being optimal. This is due to the reduced electrostatic attraction between the positively charged HAP-Fe-*Urtica dioica* ext surface (pH_{PZC} = 7.77(Fig. 9d)) and the negatively charged dye groups.

3.3.3. Optimization of significant process variables

The second-order polynomial models given by Eqs. (13), 14, and 15 were used to create 3D response surfaces and 2D contour plots to analyze

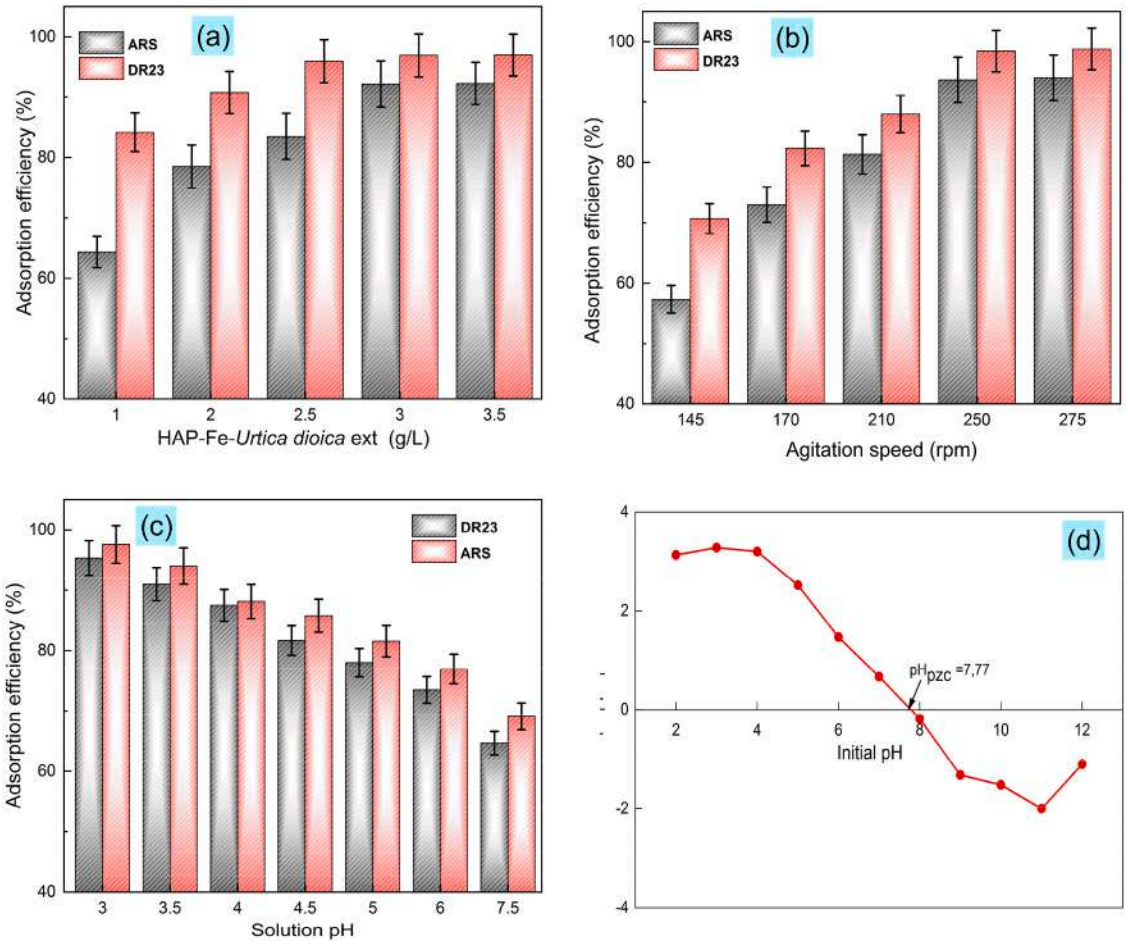

Fig. 9. Effects of (a) HAP-Fe-*Urtica dioica* ext dose, (b) Agitation speed, (c) pH solution and (d) pH_{pzc}, on the adsorption efficiency of ARS and DR23 in the binary dye solution onto HAP-Fe-*Urtica dioica* ext under the conditions:$[ARS]_0 = [DR23]_0 = 20mg/L$, time = 90 min, and $T = 21$ °C.

the correlation between independent process parameters and the response (Figs. S4, S5, and 10, respectively), as well to identify the optimal values of the operating parameters for achieving the highest ARS and DR23 adsorption efficiency. As illustrated in Fig. 9a-f, an adsorption efficiency exceeding 90 % can be obtained under the following conditions: pH solution = 3.15,$dose_{Hap-Fe-Urticadioicaext}$ = 2.60g/L, These optimal conditions are identical to those obtained with the other models (Fig S4 and Fig S5).

3.4. Effect of dye concentrations in binary solution on their adsorption efficiency onto HAP-Fe- Urtica dioica ext

Fig. 11a illustrates the effect of initial concentrations of ARS and DR23 in a binary dye solution on their adsorption efficiency onto HAP-Fe-*Urtica dioica* ext, with concentrations ranging from 20 to 180 mg/L. The study was conducted under the optimal conditions determined by CCD-RSM: time = 120 min, pH of solution = 3.15,$dose_{Hap-Fe-Urticadioicaext}$ = 2.60g/L, temperature = 21 °C, and agitationspeed = 260rpm. The results show that the adsorption of ARS and DR23 dyes is faster within the first 20 min, reaching equilibrium after 60 min due to the high specific surface area of HAP-Fe- *Urtica dioica* ext (Table 2). Moreover, it is indicated that HAP-Fe- *Urtica dioica* ext exhibits a similar adsorption efficiency for ARS and DR23 dyes within the concentration range of 20 to 100 mg/L. However, at concentrations of $[dyes]_0 \geq 100$ mg/L, HAP-Fe- *Urtica dioica* ext shows a higher affinity for DR23 compared to ARS dyes.

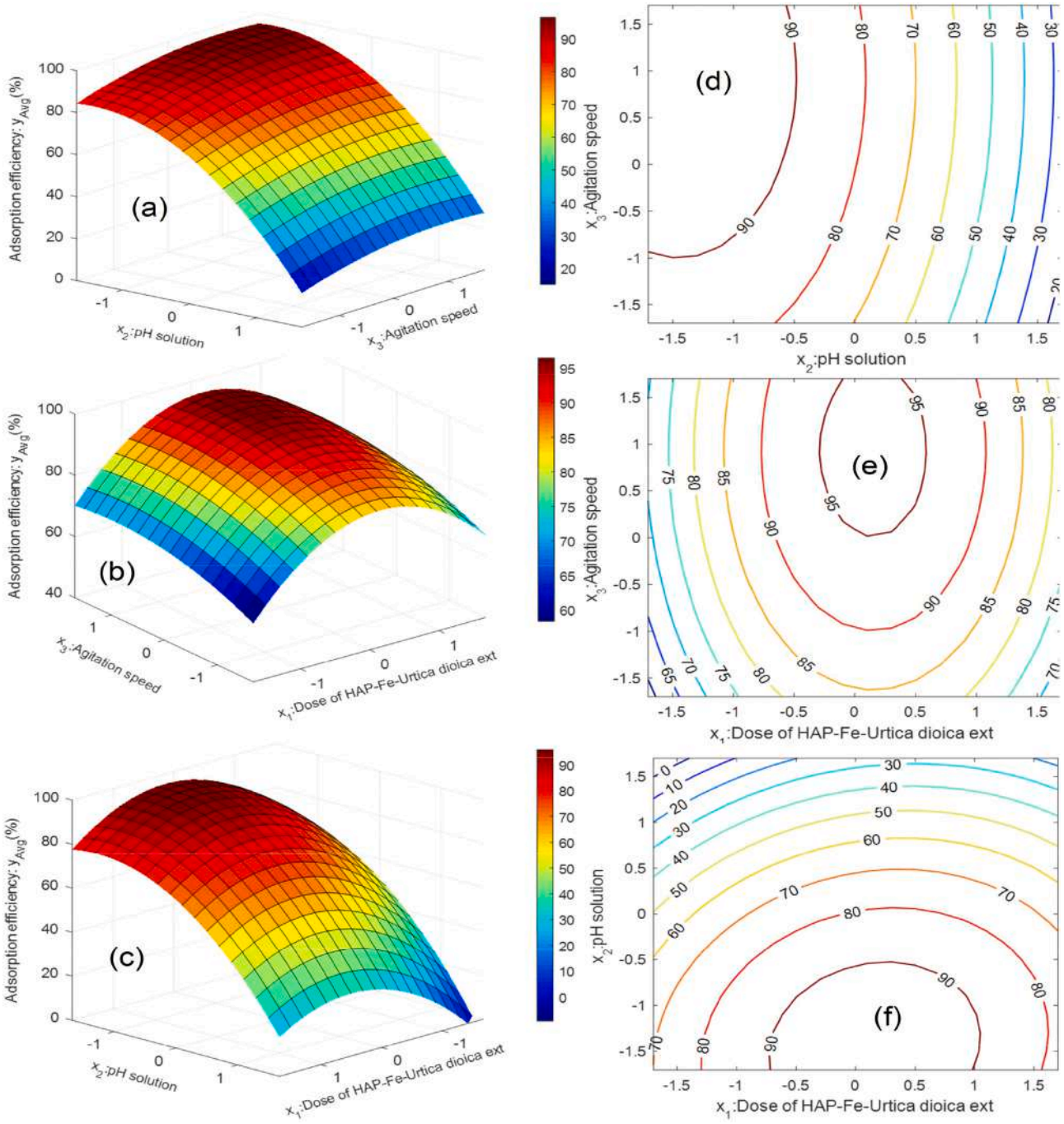

Fig. 10. 2D contour plots and 3D response surfaces of adsorption of ARS and DR23 in binary solution onto HAP-Fe-*Urtica dioica* ext under the conditions:$[ARS]_0$ = $[DR23]_0$ = 20mg/L, time = 120 min, pH solution = 3.15,$dose_{Hap-Fe-Urticadioicaext}$ = 2.60g/L, T = 21 °C, andagitationspeed = 260rpm.

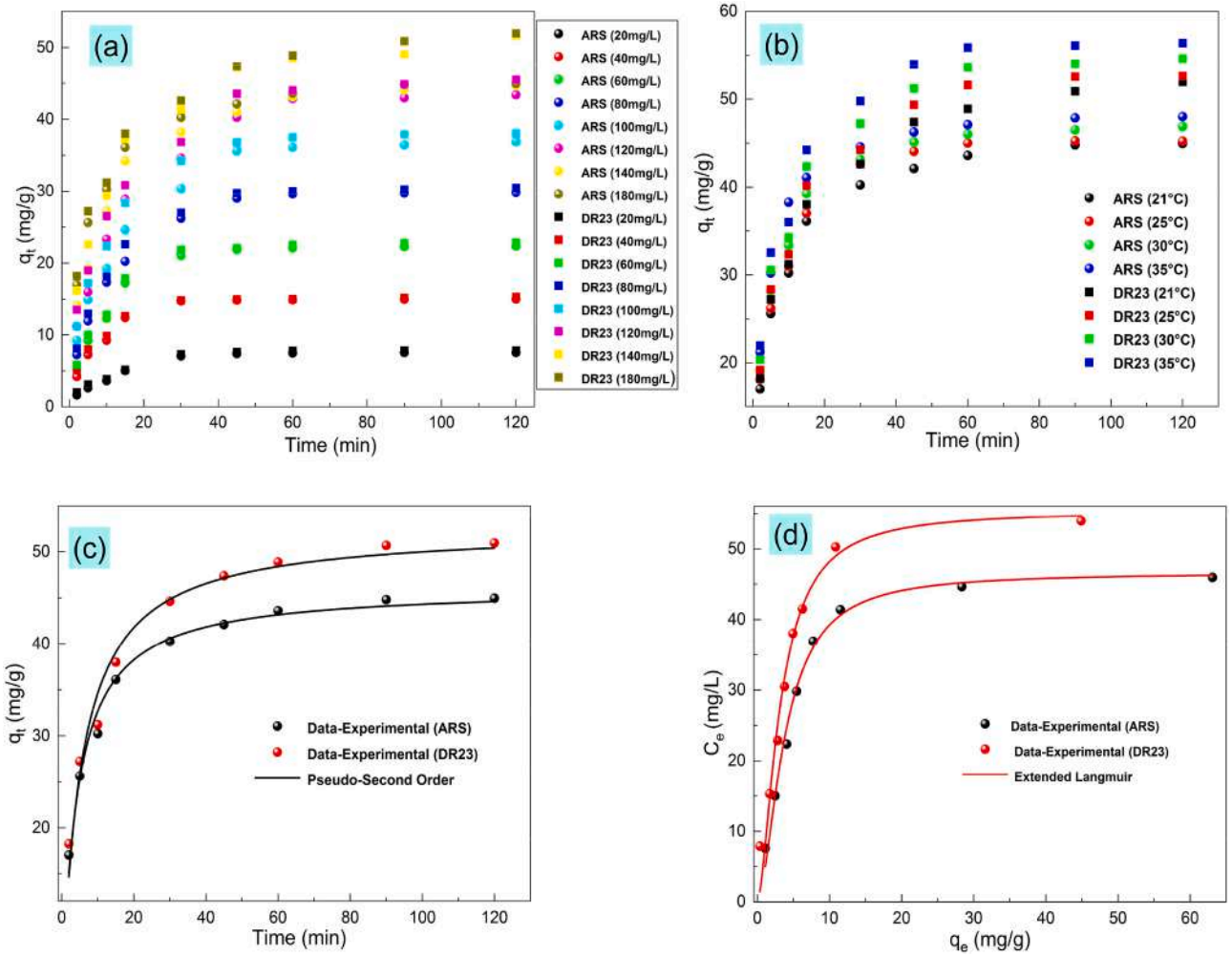

Fig. 11. (a) Effect of initial concentrations of (ARS and DR23) in binary solution, (b) Effect of the temperature's on ARS and DR23 dyes molecules' adsorption process, (c) Isotherm and (d) kinetic models fitting to experimental data for ARS and DR23 dyes in binary solution, under the optimized conditions determined by CCD-RSM.

At lower concentrations, the adsorption sites of HAP-Fe-*Urtica dioica* ext may not be fully utilized, allowing similar adsorption rates for both ARS and DR23 dyes. At concentrations over 100 mg/L, surface sites may become saturated more quickly with DR23 due to stronger electrostatic interactions with HAP-Fe-*Urtica dioica* ext, favoring DR23 adsorption. According to Heravi et *al.* (2024) [45], the number of SO_3 groups present in their structure influences the adsorption capacity for anionic dyes. Dyes with a higher number ofSO_3 group's exhibit superior adsorption efficiency. In this study, DR23 has more SO_3 groups compared to ARS (Fig. S1), resulting in more favorable and stronger electrostatic interactions with HAP-Fe-*Urtica dioica* ext, leading to enhanced performance.

3.5. Effects of temperature, thermodynamic and the homogeneous particle diffusion model (HPDM) studies

The impact of temperature on the adsorption process of ARS and DR23 dye molecules was studied under the optimized conditions determined by CCD-RSM; time = 120 min, pH = 3.15,$dose_{Hap-Fe-Urticadioicaext}$ = 2.60*g/L*, and agitationspeed = 260*rpm*. The results are displayed in the Fig. 11b and reveal that higher temperatures increase the amount of dyes adsorbed, leading to faster diffusion of dyes into HAP-Fe-*Urtica dioica* ext. As shown by the diffusion coefficient data (Table S3), a rise in diffusion coefficient occurs for all dyes with increasing temperature. According to Michelson et al. [34] and the results of the homogenous model (HPDM) (Table S3) reveal that the intra-particle diffusion controls ARS and DR23 dye uptake onto HAP--Fe-*Urtica dioica* ext.

The thermodynamic quantities (Table S3) show that the adsorption process for ARS and DR23 dyes onto HAP-Fe-*Urtica dioica* ext are spontaneous and endothermic, with positive ΔS° values and negative ΔG° values. Furthermore, The DR23 dye exhibits higher ΔH° values (ΔH° = 66.44kJ/mol) above 40kJ/mol, indicating chemisorption, while ARS dye have lower values, indicating physisorption [24].

3.6. Fitting of kinetic and adsorption isotherm models

Fig. 11c and Table 3 present the fitting of kinetic and extended Langmuir isotherm models for the adsorption data of ARS and DR23 dyes onto HAP-Fe-*Urtica dioica* ext. The results indicate that the adsorption process of ARS and DR23 dyes in a binary solution onto HAP-Fe-*Urticadioica*ext, follow the pseudo-second-order kinetic model and the extended Langmuir isotherm. These findings suggest homogeneous monolayer adsorption, where each site can hold at most one anionic dye molecule. This occurs at a finite number of identical sites with no lateral interaction or steric hindrance between sorbed molecules on adjacent sites, with constant enthalpies and sorption activation energy, and equal affinity for the adsorbate at all sites, indicating serial adsorption [40]. Moreover, the $R_L$values indicate that the adsorption of both dyes onto HAP-Fe- *Urtica dioica* ext is favorable. Additionally, the smaller $R_L$value

Table 3
Kinetic and isotherm parameters of ARS and DR23 dyes in binary solution. Conditions: Time = 120 min, pH solution = 3.15, $dose_{Hap-Fe-Urticadioicaext}$ = 2.60*g/L*, T = 21 °C, and agitationspeed = 260*rpm*.

Kinetic model	Kinetic parameters	dye		Isotherm model	
		ARS	DR23	Extended-Langmuir (ARS)	
Pseudo-First Order	q_{exp} (mg/g)	44.960	51.052	q_m(mg/g)	59.013
	q_{cal} (mg/g)	41.579	48.139	$K_{L,1}$(L/mg)	0.057
	k_1 (min^{-1})	0.141	0.133	$K_{L,2}$(L/mg)	0.201
	Δq(mg/g)	3.381	2.913	$R_{L,1}$	0.495
	R^2	0.91	0.88	$R_{L,2}$	0.199
				R^2	0.991
Pseudo-Second Order	q_{exp}(mg/g)	44.960	51.052	**Extended-Langmuir (DR23)**	
	q_{cal} (mg/g)	45.122	52.113	q_m(mg/g)	64.416
	Δq(mg/g)	−0.162	−1.061	$K_{L,1}$(L/mg)	0.020
				$K_{L,2}$(L/mg)	0.261
	k_2 (mg/(g × L))	0.003	0.005	$R_{L,1}$	0.714
	R^2	0.993	0.991	$R_{L,2}$	0.160
				R^2	0.993

for DR23 indicates that HAP-Fe has a higher affinity for adsorbing DR23 than ARS in binary dye solution [33].

3.7. Possible adsorption mechanisms of DR23 and ARS dyes into HAP-Fe-Urtica dioica ext

The adsorption mechanism of DR23 and ARS dyes onto the HAP-Fe-*Urtica dioica* ext involves a combination of different physical and chemical interactions between the dyes functional groups and the active sites on the HAP-Fe-*Urtica dioica* ext surface.

BET and BJH characterization data (Table 2) confirm that HAP-Fe-*Urtica dioica* ext has a well-developed mesoporous structure, with a high surface area and substantial pore volume. These structural features are crucial for promoting effective mass transfer of dye molecules from the bulk DR23/ARS dye solution. The mesopores provide sufficient space for dye molecules to diffuse into, enhancing interaction with the adsorbent surface. The presence of both micropores and mesopores contributes to a high adsorption capacity by accommodating a variety of dye molecules, thereby improving the overall adsorption efficiency.

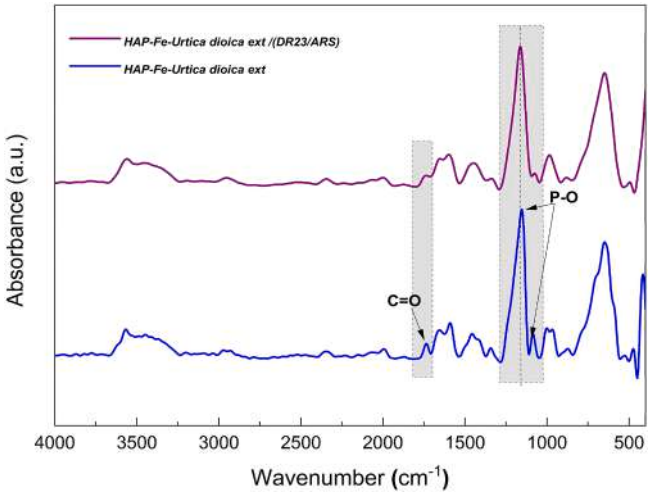

Fig. 12. FTIR spectrum of HAP-Fe-*Urtica dioica* ext before and after the adsorption of DR23 and ARS dyes, under conditions: $[DR23/ARS]_0$ = 180*mg/L*, Time = 120 min, pH solution = 3.15, $dose_{Hap-Fe-Urticadioicaext}$ = 2.60*g/L*, T = 21 °C, and agitationspeed = 260*rpm*.

FTIR (Fig. 12) analysis reveals a shift in the P-O band from 1146 cm^{-1} to 1165 cm^{-1}, accompanied by a reduction in intensity at 1069 cm^{-1}. Moreover, the decreased intensity of the carboxylic ($C=O$) groups in *Urtica dioica* extract after dye adsorption suggests a change in the electronic environment of the $C=O$ bond. This alteration can be attributed to interactions between the PO_4^{3-} and $C=O$ groups with functional groups such as hydroxyl (OH), sulfonate (SO_3^-) and amino (NH) in the ARS and DR23 dyes, involving hydrogen bonding and electrostatic interactions (Fig. 13) [46–48].

The calcium ions (Ca^{2+}) on the HAP surface can form chelate complexes with the carbonyl ($C=O$) and sulfonate (SO_3^-) groups of the ARS and R23 dyes (Fig. 13) [49]. Additionally, Fe_3O_4 can form hydrogen bonds with functional groups such as (SO_3^-) and OH in the dye molecules and engage in electrostatic interactions with the azo bonds (-$N=N$-) and amino (NH) groups in the DR23 dye (Fig. 13) [50].

3.8. The regeneration and reusability of HAP-Fe-Urtica dioica ext

The regeneration and reusability of HAP-Fe-*Urtica dioica* ext, as illustrated in Fig. 14, demonstrate that the adsorbent remains effective for a limited number of cycles, with optimal performance observed for approximately four cycles. This gradual decline in efficiency is primarily attributed to pore blockage caused by the accumulation of residual DR23 and ARS dyes, which obstruct adsorption sites and hinder the diffusion of new dye molecules. As these dye molecules become more embedded within the adsorbent matrix, their removal during desorption becomes increasingly difficult. Additional factors, such as potential chemical transformations due to interactions between the functional groups of HAP-Fe-*Urtica dioica* ext and the DR23 and ARS dyes, as well as possible degradation of the adsorbent under harsh regeneration conditions, further exacerbate the decline in performance. To enhance the material's longevity and reusability, alternative regeneration techniques, such as thermal degradation of residual dyes or advanced chemical treatments, may offer promising solutions.

The environmental impact and disposal of the spent HAP-Fe-*Urtica dioica* ext after its adsorption capacity is exhausted are critical considerations. Spent adsorbents that retain residual dyes can pose significant environmental hazards, as the adsorbed dyes may desorb or leach into the surrounding environment under specific conditions, leading to potential contamination of soil and water resources. Furthermore, the dopants used in the material, such as Fe3O4 and components derived from Urtica dioica extract, may introduce additional environmental risks if not properly managed.

To address these challenges, several strategies for the safe disposal or repurposing of the spent adsorbent are proposed. Thermal treatment, such as incineration at elevated temperatures, can effectively degrade the adsorbed dyes and minimize the risk of leaching. Immobilization of the exhausted material in inert matrices, such as cement or composite materials, offers a potential pathway for safe long-term storage or reuse. Additionally, integrating spent adsorbents into secondary applications, such as in construction materials or as precursors for other functional composites, may further enhance the environmental sustainability of the process.

Future research should focus on evaluating the long-term environmental stability of the spent adsorbent under varying conditions, such as pH, temperature, and microbial activity, to identify potential risks associated with its disposal. Moreover, the development of innovative disposal and recycling methods will be essential to ensure that the implementation of HAP-Fe-*Urtica dioica* ext in industrial and wastewater treatment applications aligns with environmental sustainability goals.

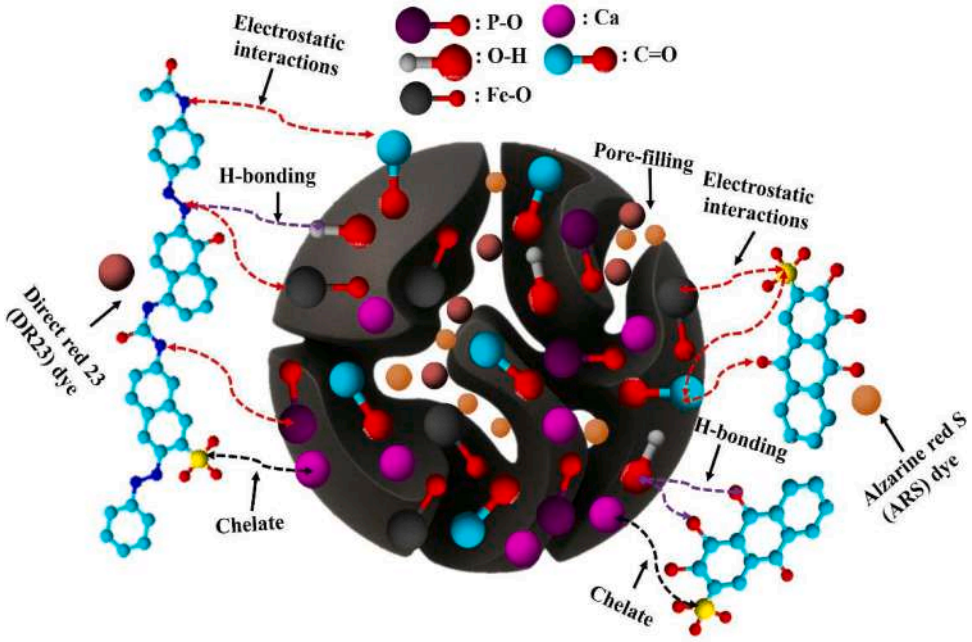

Fig. 13. Proposal mechanism of adsorption of DR23 and ARS dyes into HAP-Fe-*Urtica dioica* ext.

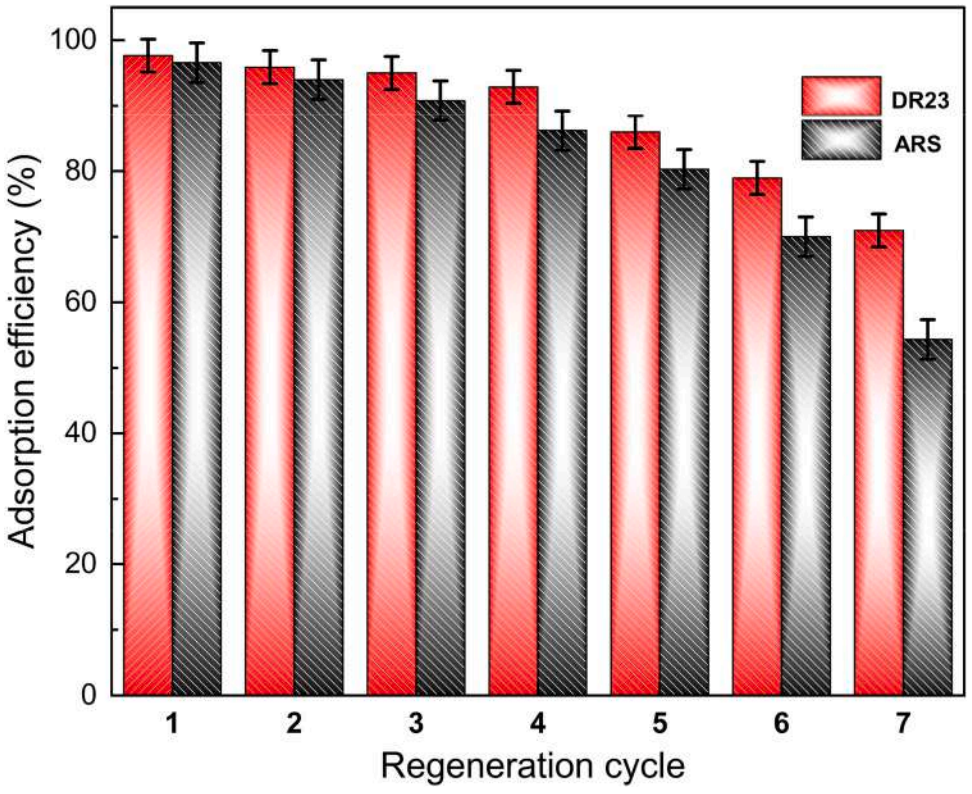

Fig. 14. Regeneration and reusability of HAP-Fe-*Urtica dioica* ext Adsorbent for the adsorption of binary DR23 and ARS dyes.

3.9. Comparison of HAP-Fe-Urtica dioica ext with the previously developed adsorbents in the literature

The comparison of HAP-Fe-*Urtica dioica* ext with other advanced adsorbents, based on parameters such as surface area, pore volume, kinetic behavior, and adsorption performance, offers valuable insights into its efficacy as a dye adsorbent. Table 4 presents a comparative analysis of the adsorption capacities for both DR23 and ARS dyes in binary mixtures (DR23/ARS), as well as in single dye systems, highlighting the distinct advantages of HAP-Fe-*Urtica dioica* ext.

Under optimized experimental conditions (Table 4) HAP-Fe-*Urtica dioica* ext exhibits substantial adsorption capacity for both DR23 and ARS dyes. In comparison with conventional adsorbents such as activated carbon/cynara cardunculus [51], Corn stalk [54], Magnetite talc (Fe_3O_4 @Talc) nanocomposite [56], and APTES-grafted vermiculite [59] (Table 4), HAP-Fe-*Urtica dioica* ext demonstrates a fast adsorption

Table 4
Comparative Insights into the Adsorption Efficiency and Surface Characteristics of HAP-Fe-*Urtica dioica* ext and Other Advanced Adsorbents.

Adsorbent	q_{max} (mg/g)	pH solution	Equilibrium time (min)	ref
Comparing DR23 Dye Adsorption Capacity of HAP-Fe-*Urtica dioica* ext in the Other Adsorbents				
HAP-Fe-*Urtica dioica* ext	56.15	pH = 3.15	60	This study
Activated carbon, Cynara cardunculus,	47.5	pH = 1.5	120	[51]
Nanoclay	166.6	pH = 2	30	[52]
Polyaniline coated activated carbon	109.8	pH = 3	90	[53]
Corn stalk	52	pH=3	10	[54]
Comparing ARS Dye Adsorption Capacity of HAP-Fe-*Urtica dioica* ext in the Other Adsorbents				
HAP-Fe-*Urtica dioica* ext	47.96	pH = 3.15	60	This study
Untreated Typha Grass	77.99	8	120	[55]
Magnetite talc (Fe_3O_4@Talc) Nanocomposit	11.76	3	60	[56]
Fe_3O_4@BC-KC composite	174.9	2	150	[57]
APTES grafted vermiculite	18.2	1	40	[58]
Comparing HAP-Fe-*Urtica dioica* ext surface characterization with other developed HAP based materials and other materials				
Adsorbent	**SAA (m^2/g)**	**Total pore volume (cm^3/g)**	**Mean pore diameter (nm)**	**Ref**
HAP-Fe-*Urtica dioica* ext	59.98	0.30	19.89	This study
HAP-1 % Go	35.61	0.054	6.08	[59]
Ag/Mg/Zn-HAP	0.63	0.007	2.06	[60]
(ZAB) bio-adsorbent	729.93	0.378	1	[61]
activated carbon/ γ-Fe_3O_4 nano-composite	347.8	N/A	N/A	[62]
carbon-bridge-doped g-C3N4/ Fe_3O_4 magnetic	62.98	0.30	17.74	[63]

process, reaching equilibrium within 60 min. This contrasts with adsorbents like activated carbon/cynara cardunculus [51], which require longer equilibrium times (up to 120 min). Although certain adsorbents, such as Fe_2O_3@BC-KC [58] and nenoclay [52] may exhibit superior individual adsorption capacities for DR23 and ARS dyes in isolation, HAP-Fe-*Urtica dioica* ext maintains a competitive edge due to its enhanced adsorption efficiency in more complex binary systems. This suggests that HAP-Fe-*Urtica dioica* ext not only offers substantial dye uptake potential but also retains its effectiveness in the presence of mixed dye solutions, which is crucial for real world applications involving multiple dyes. In this regard, its superior performance in mixed systems demonstrates its versatility and robustness, making it more reliable than adsorbents that may struggle with multi-component systems.

A comparative analysis of the surface characteristics of HAP-Fe-*Urtica dioica* ext with other HAP-based materials and adsorbents (Table 4) reveals HAP-Fe-*Urtica dioica* ext exhibits a surface area of 59.98 m^2/g, a total pore volume of 0.30 cm^3/g, and a mean pore diameter of 19.89 nm, indicating a well-developed porous structure ideal for effective dye adsorption. In contrast, materials such as HAP-1 % Go [59] and Ag/Mg/Zn-HAP [60] exhibit much lower surface areas (33.61 m^2/g and 0.63 m^2/g, respectively), reduced pore volumes (0.054 cm^3/g and 0.007 cm^3/g, respectively), and smaller pore diameters, which may limit their efficiency in adsorbing larger dye molecules or handling complex systems. On the other hand, advanced materials like carbon-bridge-doped g-C3N4/Fe_3O_4 [62] magnetic materials show surface areas of 62.98 m^2/g, with corresponding pore volumes of 0.30 cm^3/g. While suitable for various adsorption tasks, these materials still fall short when compared to HAP-Fe-*Urtica dioica* ext, especially in terms of pore diameter. The larger pores of HAP-Fe-*Urtica dioica* ext can accommodate a broader range of dye molecules, enhancing its overall adsorption efficiency. The surface and structural attributes of HAP--Fe-*Urtica dioica* ext, particularly its balanced combination of surface area, pore volume, and pore size distribution, make it a competitive and versatile adsorbent. These characteristics position it as an effective material for dye removal in both single and mixed systems.

4. Conclusions

In this study, a novel method for enhancing the adsorption properties of hydroxyapatite (HAP) was explored using the co-precipitation technique with iron oxide (Fe_3O_4) both with and without *Urtica dioica* extract as a dopant. Characterization through BET/BJH, XRD, SEM, VSM, and FTIR revealed that incorporating Fe_3O_4 and *Urtica dioica* extract during HAP synthesis is an effective and practical strategy for industrial applications. This approach improves various properties, including surface area, porosity, magnetic characteristics, and adsorption capacity for anionic dye.

Moreover, the study employed the central composite design and response surface methodology (RSM-CCD) to optimize the adsorption process from a binary anionic (ARS/BR23) dye solutions. This approach compares the adsorption efficiency of each dye in the binary solution to the average efficiency of the two dyes. The reliability of the method was confirmed by high estimated F-values, low coefficients of variation, strong correlations between measured and predicted values, and high coefficients of determination, supported by residual analysis.

Optimal conditions for maximum removal of ARS and DR23 dyes in binary solution were a pH of 3.15, a dose of 2.6 g/L of HAP-Fe-*Urtica dioica* ext, and an agitation speed of 250 rpm. Under these conditions, maximum adsorption capacities reached 59.01 mg/g for ARS and 64.40 mg/g for DR23. Equilibrium and kinetic studies indicated that adsorption followed the extended Langmuir isotherm and pseudo-second-order kinetic model. Thermodynamic analysis revealed that both adsorption processes were favorable, endothermic, involving physisorption and chemisorption for ARS and DR23, respectively. These findings suggest that HAP-Fe-*Urtica dioica* ext could serve as a sustainable solution for treating wastewater-containing solutions of dyes through effective adsorption.

CRediT authorship contribution statement

Aghilas Brahmi: Writing – original draft, Validation, Software, Methodology, Investigation, Formal analysis, Data curation, Conceptualization. **Salima Ziani:** Writing – review & editing, Supervision, Conceptualization, Investigation. **Salima AitAli:** Writing – review & editing, Investigation, Conceptualization. **Yanis Zakaria Lakehal:** Investigation, Conceptualization, Writing – review & editing. **Tero Luukkonen:** Writing – review & editing, Supervision, Resources, Conceptualization, Funding acquisition, Investigation.

Declaration of competing interest

The authors declare the following financial interests/personal relationships which may be considered as potential competing interests: AGHILAS BRAHMI reports administrative support, article publishing charges, equipment, drugs, or supplies, statistical analysis, travel, and writing assistance were provided by University of Bouira. AGHILAS BRAHMI reports a relationship with University of Bouira that includes: employment. If there are other authors, they declare that they have no known competing financial interests or personal relationships that could have appeared to influence the work reported in this paper.

Supplementary materials

Supplementary material associated with this article can be found, in the online version, at doi:10.1016/j.surfin.2025.106925.

Data availability

Data will be made available on request.

References

[1] M.K. Alam, M.S. Hossain, M. Kawsar, N.M. Bahadur, S. Ahmed, Synthesis of nano-hydroxyapatite using emulsion, pyrolysis, combustion, and sonochemical methods and biogenic sources: a review, RSC Adv. 14 (5) (2024) 3548–3559, https://doi.org/10.1039/d3ra07559a.

[2] S. Meski, S. Ziani, H. Khireddine, F. Yataghane, N. Ferguene, Elaboration of the hydroxyapatite with different precursors and application for the retention of the lead, Water Sci. Technol. 63 (10) (2011) 2087–2096, https://doi.org/10.2166/wst.2011.210.

[3] S. Ziani, S. Meski, H. Khireddine, Characterization of Magnesium-Doped Hydroxyapatite Prepared by Sol-Gel Process, Int. J. Appl. Ceramic Technol. 11 (1) (2013) 83–91, https://doi.org/10.1111/ijac.12093.

[4] R. Kumar, S. Mohanty, Hydroxyapatite: a versatile bioceramic for tissue engineering application, J. Inorg Organomet Polym. Mater. 32 (12) (2022) 4461–4477, https://doi.org/10.1007/s10904-022-02454-2.

[5] A. Nayak, B. Bhushan, Hydroxyapatite as an advanced adsorbent for removal of heavy metal ions from water: focus on its applications and limitations, Mater. Today Proc. 46 (2021) 11029–11034, https://doi.org/10.1016/j.matpr.2021.02.149.

[6] N.M. Pu'ad, J. Alipal, H. Abdullah, M. Idris, T. Lee, Synthesis of eggshell derived hydroxyapatite via chemical precipitation and calcination method, Mater. Today: Proc. 42 (2021) 172–177, https://doi.org/10.1016/j.matpr.2020.11.276.

[7] A. Pal, S. Paul, A.R. Choudhury, V.K. Balla, M. Das, A. Sinha, Synthesis of hydroxyapatite from Lates calcarifer fish bone for biomedical applications, Mater. Mater. Lett. 203 (2017) 89–92, https://doi.org/10.1016/j.matlet.2017.05.103.

[8] D. Shi, H. Tong, M. Lv, D. Luo, P. Wang, X. Xu, Z. Han, Optimization of hydrothermal synthesis of hydroxyapatite from chicken eggshell waste for effective adsorption of aqueous Pb(II), Environ. Sci. Pollut. Res. Int. 28 (41) (2021) 58189–58205, https://doi.org/10.1007/s11356-021-14772-y.

[9] S. Meski, S. Ziani, H. Khireddine, S. Boudboub, S. Zaidi, Factorial design analysis for sorption of zinc on hydroxyapatite, J. Hazard. Mater. 186 (2–3) (2011) 1007–1017, https://doi.org/10.1016/j.jhazmat.2010.11.087.

[10] A. Hosseinian, A. Pettersson, J. Ylä-Mella, E. Pongrácz, Phosphorus recovery methods from secondary resources, assessment of overall benefits and barriers with focus on the Nordic countries, J. Mater. Cycles Waste Manag. 25 (5) (2023) 3104–3116, https://doi.org/10.1007/s10163-023-01747-z.

[11] X. Peng, W. Chen, Z. He, D. Li, H. Liu, H. Jin, G. Zhou, F. Xu, Removal of Cu(II) from wastewater using doped HAP-coated-limestone, J. Mol. Liq. 293 (2019) 111502, https://doi.org/10.1016/j.molliq.2019.111502.

[12] C. Oliveira, A.L.M. De Oliveira, L. Chantelle, R. Landers, S. Medina-Carrasco, M. Del Mar Orta, E.C.S. Filho, M.G. Fonseca, Zinc (II) modified hydroxyapatites for tetracycline removal: zn (II) doping or ZnO deposition and their influence in the adsorption, Polyhedron 194 (2020) 114879, https://doi.org/10.1016/j.poly.2020.114879.

[13] C. Oliveira, A.L.M. De Oliveira, L. Chantelle, G.R. Cavalcanti, R. Landers, S. Medina-Carrasco, M. Del Mar Orta, E.C.S. Filho, M. Jaber, M.G. Fonseca, Functionalization of the hydroxyapatite surface with ZnO for alizarin immobilization, Appl. Surf. Sci. 593 (2022) 153412, https://doi.org/10.1016/j.apsusc.2022.153412.

[14] Aghilas Brahmi, Maissa Agsous, Bachir Nadir Benkhaoula, Salima Ziani, Hafit Khireddine, Salima AitAli, M.M.S. Abdullah, Boon Xian Chai, Ahmed Belaadi, Fluoro-hydroxyapatite/chitosan composites as an eco-friendly adsorbent for direct red 23 dye removal: optimization through response surface methodology, J. Mol. Struct. (2024), https://doi.org/10.1016/j.molstruc.2024.140212.

[15] K. Mizar, S. Mulyati, S. Aprilia, M.P. Aulia, N. Arahman, Preparation of tungsten trioxide/graphene oxide/hydroxyapatite (WO3/GO/HAp) for photocatalytic removal of methylene blue under visible light, Case Stud. Chem. Environ. Eng. 10 (2024) 100870, https://doi.org/10.1016/j.cscee.2024.100870.

[16] V. Bhuvaneshwari, C.G. Jinitha, S. Sonia, Synergistic biocomposites (HAp/AC) of rice husk-based activated carbon (AC) and turkey bone-derived hydroxyapatite (HAp) for degradation of toxic dyes, antibacterial efficacy, and in vitro evaluation of anticancer activity in human hepatocellular carcinoma HepG2 cell line, Biomass Convers. Bioref. (2024), https://doi.org/10.1007/s13399-024-05931-5.

[17] B. Bhushan, S. Kotnala, A. Nayak, Biogenic magnetic nanocomposite of hydroxyapatite and dextran: synthesis, characterization, and enhanced removal of 2,4-D from aqueous environment, Environ. Sci. Pollut. Res. 31 (27) (2024) 39331–39349, https://doi.org/10.1007/s11356-024-33819-4.

[18] E. Forgacs, T. Cserháti, G. Oros, Removal of synthetic dyes from wastewaters: a review, Environ. Int. 30 (7) (2004) 953–971, https://doi.org/10.1016/j.envint.2004.02.001.

[19] G.T. Canbaz, Fe3O4@Granite: a novel magnetic adsorbent for dye adsorption, Processes 11 (9) (2023) 2681, https://doi.org/10.3390/pr11092681.

[20] Z. Shen, Y. Kuang, S. Zhou, J. Zheng, G. Ouyang, Preparation of magnetic adsorbent and its adsorption removal of pollutants: an overview, TrAC Trends Anal. Chem. 167 (2023) 117241, https://doi.org/10.1016/j.trac.2023.117241.

[21] A. Ammarellou, Extraction of nettle (*Urtica dioica* L.) toxins under natural biting conditions, Sci. Rep. 12 (1) (2022), https://doi.org/10.1038/s41598-022-09916-0.

[22] I. Tarasevičienė, M. Vitkauskaitė, A. Paulauskienė, J. Černiauskienė, Wild Stinging Nettle (Urtica dioica L.) Leaves and Roots Chemical Composition and Phenols Extraction, Plants 12 (2) (2023) 309, https://doi.org/10.3390/plants12020309.

[23] F. Bessaha, G. Bessaha, A. Benhouria, B. Benalioua, F. Bendahma, F. Boucif, N. Mahrez, S. Ziane, A. Çoruh, A. Khelifa, Highly efficient batch adsorption of anionic dye in wastewater using nanocomposite: experimental and theoretical studies, Desalinat. Water Treat. 317 (2024) 100292, https://doi.org/10.1016/j.dwt.2024.100292.

[24] S. AitAli, S. Ziani, I. Yahiaoui, A. Brahmi, F. Boudrahem, F. Aissani-Benissad, Application of central composite design and response surface methodology for the study of extraction of gentian violet dye in aqueous solution by polystyrene membrane modified with oleic acid, Environ. Prog. Sust. Energy 42 (6) (2023), https://doi.org/10.1002/ep.14200.

[25] W.A. Al-Amrani, M.A.K.M. Hanafiah, A.H.A. Mohammed, A comprehensive review of anionic azo dyes adsorption on surface-functionalised silicas, Environ. Sci. Pollut Res. Int. 29 (51) (2022) 76565–76610, https://doi.org/10.1007/s11356-022-23062-0.

[26] H. Megherbi, H. Runtti, S. Tuomikoski, A. Heponiemi, T. Hu, U. Lassi, A. Reffas, The effect of phosphoric acid on the properties of Activated Carbons made from Myrtus communis Leaves: textural characteristics, surface chemistry, and capacity to adsorb Methyl orange, J. Mol. Struct. (2024) 140038, https://doi.org/10.1016/j.molstruc.2024.140038.

[27] A.K. Moorthy, S.P. Shukla, R.B. Govindarajan, K. Kumar, V.S. Bharti, Application of Microalgal Physiological Response as Biomarker for Evaluating the Toxicity of the Textile Dye Alizarin Red S, Bull. Environ. Contam. Toxicol. 109 (2) (2022) 401–408, https://doi.org/10.1007/s00128-022-03525-3.

[28] K. Alorku, M. Manoj, A. Yuan, A plant-mediated synthesis of nanostructured hydroxyapatite for biomedical applications: a review, RSC Adv. 10 (67) (2020) 40923–40939, https://doi.org/10.1039/d0ra08529d.

[29] R. Zhou, S. Si, Q. Zhang, Water-dispersible hydroxyapatite nanoparticles synthesized in aqueous solution containing grape seed extract, Appl. Surf. Sci. 258 (8) (2012) 3578–3583, https://doi.org/10.1016/j.apsusc.2011.11.119.

[30] R. Ghemit, A. Makhloufi, N. Djebri, A. Flilissa, L. Zerroual, M. Boutahala, Adsorptive removal of diclofenac and ibuprofen from aqueous solution by organobentonites: study in single and binary systems, Groundw. Sust. Devel. 8 (2019) 520–529, https://doi.org/10.1016/j.gsd.2019.02.004.

[31] H. Ganji, H. Ganji, Efficient adsorption of Lead and Copper from water by modification of sand filter with a green plant-based adsorbent: adsorption kinetics and regeneration, Environ. Res. (2024) 119529, https://doi.org/10.1016/j.envres.2024.119529.

[32] J. Zolgharnein, M. Bagtash, T. Shariatmanesh, Simultaneous removal of binary mixture of Brilliant Green and Crystal Violet using derivative spectrophotometric determination, multivariate optimization and adsorption characterization of dyes on surfactant modified nano-γ-alumina, Spectrochim. Acta A Mol. Biomol. Spectrosc. 137 (2015) 1016–1028, https://doi.org/10.1016/j.saa.2014.08.115.

[33] R. Lamari, B. Benotmane, S. Mezali, Zeolite imidazolate framework-11 for efficient removal of Bromocresol Green in aqueous solution, isotherm kinetics, and thermodynamic studies, Desalinat. Water. Treat. 224 (2021) 407–420, https://doi.org/10.5004/dwt.2021.27183.

[34] Michelsen, D.L., Gideon, J.A., Griffith, G.P., Pace, J.E., & Kutat, H.L. (1975). Removal of soluble mercury from waste water by complexing techniques. http://hdl.handle.net/10919/25731.

[35] N. Liu, H. Wang, C.H. Weng, C.C. Hwang, Adsorption characteristics of Direct Red 23 azo dye onto powdered tourmaline, Arab. J. Chem. 11 (8) (2018) 1281–1291, https://doi.org/10.1016/j.arabjc.2016.04.010.

[36] T. Saeed, A. Naeem, I.U. Din, M. Farooq, I.W. Khan, M. Hamayun, T. Malik, Synthesis of chitosan composite of metal-organic framework for the adsorption of dyes; kinetic and thermodynamic approach, J. Hazard. Mater. 427 (2021) 127902, https://doi.org/10.1016/j.jhazmat.2021.127902.

[37] S. Mondal, P. Manivasagan, S. Bharathiraja, M.S. Moorthy, V. Nguyen, H. Kim, S. Nam, K. Lee, J. Oh, Hydroxyapatite coated iron oxide nanoparticles: a promising nanomaterial for magnetic hyperthermia cancer treatment, Nanomaterials 7 (12) (2017) 426, https://doi.org/10.3390/nano7120426.

[38] M. Izadi, T. Shahrabi, B. Ramezanzadeh, Synthesis and characterization of an advanced layer-by-layer assembled Fe 3 O 4 /polyaniline nanoreservoir filled with Nettle extract as a green corrosion protective system, J. Ind. Eng. Chem. 57 (2018) 263–274, https://doi.org/10.1016/j.jiec.2017.08.032.

[39] S. Prabha Dubey, A. Dhar Dwivedi, M. Lahtinen, C. Lee, Y.N. Kwon, M. Sillanpaa, Spectrochim, Acta A 103 (2013) 134.

[40] A. Brahmi, S. Ziani, S. AitAli, H. Khireddine, T. Luukkonen, Preparation of porous hydroxyapatite–metakaolin geopolymer granules for adsorption applications using polyethylene glycol as porogen agent and sodium dodecyl sulfate as anionic surfactant, Environ. Sci. Pollut. Res. Int. (2024), https://doi.org/10.1007/s11356-024-34001-6.

[41] S. Otles, B. Yalcin, Phenolic compounds analysis of root, stalk, and leaves of nettle, Sci. World J. 2012 (2012) 1–12, https://doi.org/10.1100/2012/564367.

[42] A. Brahmi, S. Ziani, S. AitAli, B.N. Benkhaoula, Y. Yu, H. Ahouari, H. Khireddine, T. Luukkonen, Porous metakaolin geopolymer as a reactive binder for hydroxyapatite adsorbent granules in dye removal, Hybrid Adv. 5 (2024) 100134, https://doi.org/10.1016/j.hybadv.2023.100134.

[43] X. Wei, Y. Wang, J. Chen, Z. Liu, F. Xu, X. He, H. Li, Y. Zhou, Fabrication of di-selective adsorption platform based on deep eutectic solvent stabilized magnetic polydopamine: achieving di-selectivity conversion through adding CaCl2, Chem. Eng. J. 421 (2021) 127815, https://doi.org/10.1016/j.cej.2020.127815.
[44] F. Boudrahem, S. Ziani, F. Aissani-Benissad, Application of response surface methodology based on central composite design for optimization of yellow bezacryl sorption on shoe soles waste, Environ. Prog. Sustain Energy 38 (s1) (2018), https://doi.org/10.1002/ep.13073.
[45] M. Heravi, V. Srivastava, A. Ahmadpour, V. Zeynali, M. Sillanpää, The effect of the number of SO3− groups on the adsorption of anionic dyes by the synthesized hydroxyapatite/Mg–Al LDH nanocomposite, Environ. Sci. Pollut Res. Int. 31 (11) (2024) 17426–17447, https://doi.org/10.1007/s11356-024-32192-6.
[46] R. Jiang, G. Yu, P. Ndagijimana, Y. Wang, F. You, Z. Xing, Y. Wang, Effective adsorption of Direct Red 23 by sludge biochar-based adsorbent: adsorption kinetics, thermodynamics and mechanisms study, Water Sci. Technol. 83 (10) (2021) 2424–2436, https://doi.org/10.2166/wst.2021.126.
[47] N.I. Normi, A.S. Abdulhameed, A.H. Jawad, S.N. Surip, R. Razuan, M.L. Ibrahim, Hydrothermal-Assisted Grafting of Schiff base Chitosan by Salicylaldehyde for Adsorptive Removal of Acidic Dye: statistical Modeling and Adsorption Mechanism, J. Polym. Environ. 31 (5) (2022) 1925–1937, https://doi.org/10.1007/s10924-022-02730-9.
[48] A. Nayak, B. Bhushan, S. Kotnala, Evaluation of hydroxyapatite-chitosan-magnetite nanocomposites for separation of pharmaceuticals from water: a mechanistic and comparative approach, J. Hazardous Mater. Adv. 10 (2023) 100308, https://doi.org/10.1016/j.hazadv.2023.100308.
[49] T. Moriguchi, K. Yano, S. Nakagawa, F. Kaji, Elucidation of adsorption mechanism of bone-staining agent alizarin red S on hydroxyapatite by FT-IR microspectroscopy, J. Colloid Interface Sci. 260 (1) (2003) 19–25, https://doi.org/10.1016/s0021-9797(02)00157-1.
[50] G.R. Chaudhary, P. Saharan, A. Kumar, S.K. Mehta, S. Mor, A. Umar, Adsorption studies of cationic, anionic and azo-dyes via monodispersed Fe3O4 Nanoparticles, J. Nanosci. Nanotechnol. 13 (5) (2013) 3240–3245, https://doi.org/10.1166/jnn.2013.7152.
[51] S. Wang, H. Nam, H. Nam, Preparation of activated carbon from peanut shell with KOH activation and its application for H2S adsorption in confined space, J. Environ. Chem. Eng. 8 (2) (2020) 103683, https://doi.org/10.1016/j.jece.2020.103683.
[52] A.H. Mahvi, A. Dalvand, Kinetic and equilibrium studies on the adsorption of Direct Red 23 dye from aqueous solution using montmorillonite nanoclay, Water Qual. Res. J. 55 (2) (2019) 132–144, https://doi.org/10.2166/wqrj.2019.008.
[53] N. Gopal, M. Asaithambi, P. Sivakumar, V. Sivakumar, Adsorption studies of a direct dye using polyaniline coated activated carbon prepared from Prosopis juliflora, J. Water Process Eng. 2 (2014) 87–95, https://doi.org/10.1016/j.jwpe.2014.05.008.
[54] Fathi, A. Asfaram, A. Farhangi, Removal of Direct Red 23 from aqueous solution using corn stalks: isotherms, kinetics and thermodynamic studies, Spectrochimica Acta Part a Mol. Biomol. Spectrosc. 135 (2014) 364–372, https://doi.org/10.1016/j.saa.2014.07.008.
[55] N.A. Muhammad, N.S. Musa, Study on adsorption of alizarin red S and eriochrome black t dyes by untreated typha grass as a low cost adsorbent, UMYU Scientifica 1 (1) (2022) 155–165, https://doi.org/10.56919/usci.1122.020.
[56] A.A. Nayl, A.I. Abd-Elhamid, I.M. Ahmed, S. Bräse, Preparation and Characterization of Magnetite Talc (Fe3O4@Talc) Nanocomposite as an Effective Adsorbent for Cr(VI) and Alizarin Red S Dye, Materials 15 (9) (2022) 3401, https://doi.org/10.3390/ma15093401.
[57] P.E. Ohale, K. Chukwudi, J.N. Ndive, M.E. Michael, M.N. Abonyi, M.M. Chukwu, C. C. Obi, C.E. Onu, C.A. Igwegbe, C.O. Azie, Optimization of Fe2O3@BC-KC composite preparation for adsorption of Alizarin red S dye: characterization, kinetics, equilibrium, and thermodynamic studies, Results Surf. Interf. 13 (2023) 100157, https://doi.org/10.1016/j.rsurfi.2023.100157.
[58] N. Ali, F. Ali, A. Said, T. Begum, M. Bilal, A. Rab, Z.A. Sheikh, H.M.N. Iqbal, I. Ahmad, Characterization and Deployment of Surface-Engineered Cobalt Ferrite Nanospheres as Photocatalyst for Highly Efficient Remediation of Alizarin Red S Dye from Aqueous Solution, J. Inorg. Organomet Polym Mater. 30 (12) (2020) 5063–5073, https://doi.org/10.1007/s10904-020-01654-y.
[59] A. Mahanty, D. Shikha, Design of a new Ag/Mg/Zn alloyed doped hydroxyapatite hybrid biomaterial, Mater. Chem. Phys. 311 (2023) 128553, https://doi.org/10.1016/j.matchemphys.2023.128553.
[60] N.S. Ali, H.N. Harharah, I.K. Salih, N.M.C. Saady, S. Zendehboudi, T.M. Albayati, Applying MCM-48 mesoporous material, equilibrium, isotherm, and mechanism for the effective adsorption of 4-nitroaniline from wastewater, Sci. Rep. 13 (1) (2023), https://doi.org/10.1038/s41598-023-37090-4.
[61] P. Maiti, H. Siddiqi, U. Kumari, A. Chatterjee, B. Meikap, Adsorptive remediation of azo dye contaminated wastewater by ZnCl2 modified bio-adsorbent: batch study and life cycle assessment, Powder. Technol. 415 (2022) 118153, https://doi.org/10.1016/j.powtec.2022.118153.
[62] M. Fayazi, M. Ghanei-Motlagh, M.A. Taher, The adsorption of basic dye (Alizarin red S) from aqueous solution onto activated carbon/γ-Fe2O3 nano-composite: kinetic and equilibrium studies, Mater. Sci. Semicond. Process. 40 (2015) 35–43, https://doi.org/10.1016/j.mssp.2015.06.044.
[63] X. Zhang, B. Ren, X. Li, B. Liu, S. Wang, P. Yu, Y. Xu, G. Jiang, High-efficiency removal of tetracycline by carbon-bridge-doped g-C3N4/Fe3O4 magnetic heterogeneous catalyst through photo-Fenton process, J. Hazard. Mater. 418 (2021) 126333, https://doi.org/10.1016/j.jhazmat.2021.126333.